UNIVERSITY
OF OSLO

Stine Hverven Thon

Image Quality Enhancement in Medical Ultrasound

Detecting Point Scatterers

Thesis submitted for the degree of Philosophiae Doctor

Department of Informatics
Faculty of Mathematics and Natural Sciences

2023

Series of dissertations submitted to the
Faculty of Mathematics and Natural Sciences, University of Oslo
No. 2631

ISSN 1501-7710

Cover: UiO.
Print production: Graphic Center, University of Oslo.

"I was taught that the way of progress is neither swift nor easy."
– Marie Curie

To my daughters Eline and Cecilie,
without whom this thesis would
have been completed years earlier.
Thank you for giving me new purpose
and keeping me on my toes.

To my husband Bjørn Olav,
for being my anchor in rough waters
and keeping me grounded.

Preface

This thesis is submitted for the degree of *Philosophiae Doctor* at the University of Oslo. The research presented here was conducted at the University of Oslo under the supervision of Professor Andreas Austeng and Professor Roy Edgar Hansen. This work was funded by the faculty as part of the strategic research initiative MEDIMA.

The thesis is a collection of five papers, presented according to the research work process order. The main topic of this thesis is how to enhance and detect point scatterers in an ultrasound image. The papers are preceded by an introduction providing background information and motivation for the work. It describes the relation between the papers.

Acknowledgments

I am deeply grateful for the help and support of people around me. My sincere gratitude and appreciation go first and foremost to my wonderful supervisors for providing me with the guidance and counsel I needed to succeed in the Ph.D. program. My main supervisor, Professor Andreas Austeng, always has his office door ajar, and he always welcomes any academic discussions or casual coffee talk. It amazes me how quickly he can dive into specific details of the problem at hand. Professor Roy Edgar Hansen became my supervisor halfway into my Ph.D. His entrance marked a change in the work process, and it was a joy to experience the fruitful discussions that followed. There have been many long discussions over video due to the Covid-19 pandemic. It amazes me how long my supervisors can have detailed and rapid discussions without a break. I have been fortunate to have supervisors who care so much about my work and appreciate me as their colleague.

The research group Digital Signal Processing and Image Analysis (DSB) at the University of Oslo has been a friendly and inspiring work environment. I am grateful to the other Ph.D. students who shared office with me and became my friends. I want to thank Ole Marius for his collaboration and many research discussions. I am also grateful to Sten Roar Snare, who co-lectured the Bachelor/Master course in Signal Processing with me for two semesters.

Finally, I want to thank my family for their support. My husband, Bjørn Olav, deserves much praise for keeping me grounded. He tries to understand my research problems and lifts my spirits when things are tough. My daughter Eline motivates me to be present and enjoy the most important things in life. My heart fills with love when you smile and giggle. A final thanks to our future baby, for providing extra motivation to finish and the promises of many more smiles and giggles to come.

Stine Hverven Thon
Oslo, April 2022

List of Papers

Paper I

Hverven, Stine Myhre, Rindal, Ole Marius Hoel, Rodriguez-Molares, Alfonso, and Austeng, Andreas “The Influence of Speckle Statistics on Contrast Metrics in Ultrasound Imaging” in *IEEE International Ultrasonics Symposium (IUS)*, Washington, DC, 2017, pp. 1-4, DOI: 10.1109/ULTSYM.2017.8091875.

Paper II

Thon, Stine Hverven, Hansen, Roy Edgar, and Austeng, Andreas “Detection of Point Scatterers in Medical Ultrasound” in *IEEE Transactions on Ultrasonics, Ferroelectrics, and Frequency Control*, Feb. 2022, 69 (2): 617-628. DOI: 10.1109/TUFFC.2021.3129619.

Paper III

Hverven, Stine Myhre, Rindal, Ole Marius Hoel, Hunter, Alan Joseph, and Austeng, Andreas “Point scatterer enhancement in ultrasound by wavelet coefficient shrinkage” in *IEEE International Ultrasonics Symposium (IUS)*, Washington, DC, 2017, pp. 1-4, DOI: 10.1109/ULTSYM.2017.8092971.

Paper IV

Thon, Stine Hverven, Hansen, Roy Edgar, and Austeng, Andreas “Point Detection in Ultrasound Using Prewhitening and Multilook Optimization” in *IEEE Transactions on Ultrasonics, Ferroelectrics, and Frequency Control*, June 2022, 69 (6): 2085-2097. DOI: 10.1109/TUFFC.2022.3167923.

Paper V

Thon, Stine Hverven, Austeng, Andreas, and Hansen, Roy Edgar “Point Detection in Textured Ultrasound Images” in *Elsevier Ultrasonics*, May 2023, volume 131, pages 106968. DOI: 10.1016/j.ultras.2023.106968.

Contents

Chapter 1

Introduction

This thesis addresses image quality enhancement in medical ultrasound with special focus on detection of point scatterers. In ultrasound images, peaks in the surrounding background of point targets can often make point detection difficult. Imaging of breast microcalcifications, kidney stones, microbubbles, and point tracking are example applications where point detection is important. These applications would greatly benefit from methods that are able to enhance and detect point scatterers in ultrasound images.

The improvements in hardware processing power have made it possible to incorporate software beamforming into medical ultrasound systems, such as the GE Vingmed Ultrasound Vivid system. With increasing software processing power, we can apply different advanced methods to reconstruct ultrasound images. We typically compare such new adaptive beamforming techniques to conventional Delay-and-Sum (DAS) beamforming, but thorough studies are required to examine their effect. Post-processing techniques are commonly performed in software. A fair comparison between post-processing methods also requires a statistical image quality evaluation. This thesis raises the research questions of how new software methods affect the statistics of the ultrasound image and how to assess improvement in point detection performance. Inspired by techniques common in the radar and sonar communities, it suggests new methods to improve point scatterer detection in ultrasound images.

1.1 Research Questions

The primary research question of this thesis is how to enhance and detect point scatterers in an ultrasound image. The following questions concretize this research question:

- How should we measure and evaluate the detection performance of point scatterers in ultrasound images?

- How do advanced beamforming techniques influence the statistics of an ultrasound image, and do common ultrasound techniques affect point scatterer detection?

- Inspired by the wavelet shrinkage method presented in [HV14], can the method also be applied to medical ultrasound images to enhance point scatterers?

- Can we get inpiration from other methods in radar and sonar imaging to find new methods that improve point scatterer detection in ultrasound images?

1.2 Claims

This thesis explores various aspects of medical ultrasound techniques and post-processing image analysis. In this thesis, I explore how to measure the point detection performance of different methods. I present a strategy for assessing and evaluating the detection performance of point scatterers in ultrasound images. I determine how modern beamformers and techniques affect point detection. Inspired by multilook techniques in radar and sonar, I explore methods that optimize the spatial frequency spectrum of the ultrasound image. I study if the wavelet coefficient shrinkage method can enhance point targets in ultrasound. I apply the normalized matched filter (NMF) technique to ultrasound images using a two-dimensional (2-D) multilook method, and assess if this can improve point scatterer detection. Finally, this thesis presents new post-processing methods to improve point detection performance in ultrasound images.

1.3 Scope

The scope of this thesis is within medical ultrasound and the associated processing chain, image analysis post-processing, and image quality evaluation.

1.4 Thesis Outline

The background chapters in this thesis present different topics addressed in the papers. Chapter 2 briefly presents medical ultrasound imaging, from acquisition to software processing and image evaluation. This chapter introduces the results from Paper I on how adaptive beamforming techniques influence speckle statistics. Chapter 3 presents how to evaluate the detection performance of point scatterers, starting out with the classical binary detection problem. The presented methodology is from Paper II. The paper demonstrated how common ultrasound techniques such as apodization, speckle reduction, and adaptive beamformers affect point detection.

Chapter 4 presents the wavelet coefficient shrinkage method applied in Paper III. This is a method which enhances point scatterers while suppressing speckle background. Chapter 5 presents the whitening transform, and the effect prewhitening can have on point detection performance, as studied in Paper IV. Chapter 6 presents how we can simulate textured ultrasound images and correct for the texture before point detection. Paper V studies the effect of prewhitening prior to texture correction and point detection.

Chapter 7 presents the multilook technique applied in Paper IV and Paper V. The technique is widely used on synthetic aperture radar (SAR) images to reduce speckle. In this chapter, I present the three new multilook methods called *normalized matched filter weighted* (NMFW), *multilook coherence factor* (MLCF), and *multilook coherence factor weighted* (MLCFW), as first presented in Paper IV. Chapter 8 summarizes and discusses the findings in the papers in relation to the main research question. I compare the detection performance of the multilook methods with prewhitening and the original Delay-and-Sum (DAS) image, on both uniform and textured backgrounds.

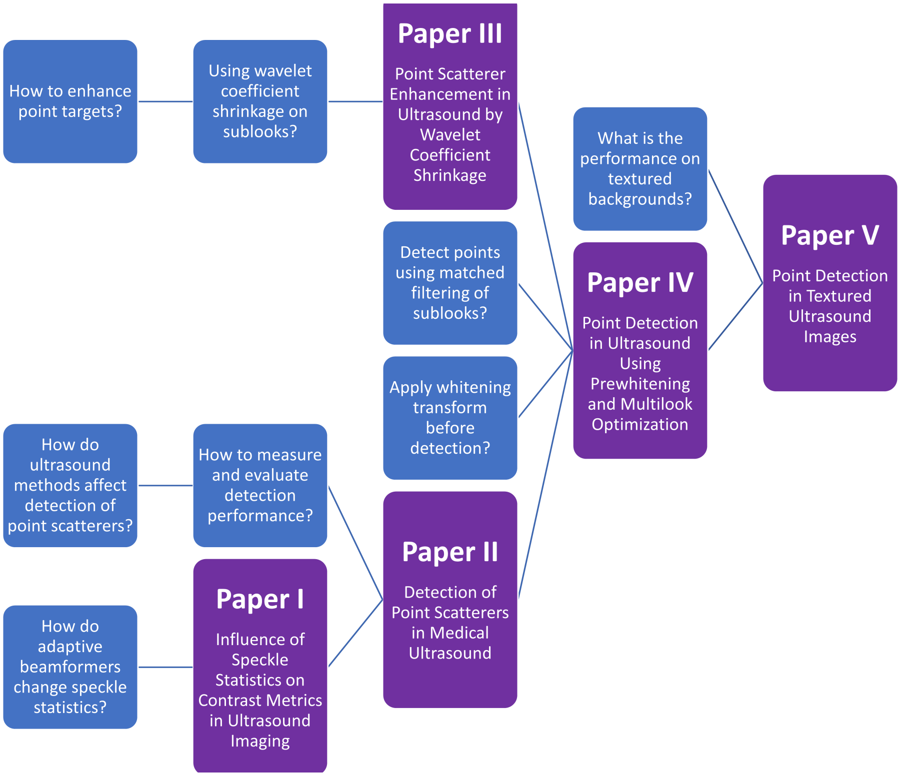

Figure 1.1: Outline of the research work process and papers in this thesis

Chapter 9 summarizes the main contributions of the work, discusses the implications, and suggests further research possibilities.

1.5 Summary of Publications

Figure 1.1 outlines the research work process and papers in this thesis. Here follows a short summary of each of the papers.

Paper I presents how different adaptive beamformers influence the statistics of the speckle background in the ultrasound image. Conventional DAS imaging of fully developed speckle has a Rayleigh amplitude distribution. This publication shows that some adaptive beamformers alter the speckle statistics. Since the statistical distribution affects the contrast metrics used to evaluate the beamformers, it is essential to know how the beamformer alters the speckle statistics. If not, the alterations of the speckle statistics allow for cherry-picking contrast metrics. *Published in IEEE International Ultrasonics Symposium (IUS), Washington, DC, 2017, pp. 1-4, DOI: 10.1109/ULTSYM.2017.8091875.*

Paper II presents the effect of common ultrasound techniques on the detection performance of point scatterers. The publication presents an overview of the detection of point scatterers in ultrasound images and suggests strategies for evaluating and measuring the detection performance. The paper evaluates how common imaging techniques affect point target detectability using many Field II [Jen+06; Jen96; JS92] simulations of a point scatterer in speckle background. Different adaptive beamformers, speckle reduction methods, apodization windows, and adaptive aperture sizes are studied. The publication discusses how to compare the performance of the methods and calculate confidence intervals. *Published in IEEE Transactions on Ultrasonics, Ferroelectrics, and Frequency Control, Feb. 2022, 69 (2): 617-628. DOI: 10.1109/TUFFC.2021.3129619.*

Paper III presents a wavelet coefficient shrinkage method to enhance point scatterers in an ultrasound image. The method uses a random block grid to create sublooks combined with coherence-based wavelet coefficient shrinkage. The algorithm separates coherent point targets from incoherent background speckle. Field II ultrasound simulations show how the algorithm retains the point scatterers and increases their conspicuity. *Published in IEEE International Ultrasonics Symposium (IUS), Washington, DC, 2017, pp. 1-4, DOI: 10.1109/ULTSYM.2017.8092971.*

Paper IV presents how optimization in the spatial frequency spectrum can improve the detectability of point scatterers. An optimized whitening transform can increase the spatial resolution of the image. The coherent properties of a point scatterer can be exploited by splitting an image's frequency spectrum into many subsets using the multilook technique. The publication studies the effect on the detection performance using prewhitening, the normalized matched filter (NMF) multilook technique, and three new multilook methods called NMFW, MLCF, and MLCFW. *Published in IEEE Transactions on Ultrasonics, Ferroelectrics, and Frequency Control, June 2022, 69 (6): 2085-2097. DOI: 10.1109/TUFFC.2022.3167923.*

Paper V presents how optimization of the spatial frequency spectrum can improve the detectability of point scatterers in *textured* ultrasound images. The publication evaluates the detection performance of prewhitening and the four multilook methods in Paper IV on ultrasound images with randomly textured backgrounds. The multilook methods NMF and MLCF are normalized methods that do not require any texture correction prior to detection analysis. The results show that texture size affects the optimal number of sublooks for the multilook methods. *Published in Elsevier Ultrasonics, May 2023, volume 131, pages 106968. DOI: 10.1016/j.ultras.2023.106968.*

Chapter 2

Ultrasound Imaging

2.1 Ultrasound Wave Physics

Ultrasound waves are longitudinal pressure waves capable of traveling through solids, liquids, and gases. The waves are high-frequency sound waves that are above the human ear's audible range of up to 20 kHz. Medical ultrasound typically lies in the frequency range of 1 to 15 MHz [Sza14, ch. 1.8.2], but specialized investigations use even higher frequencies. Ultrasound imaging is based on the principle of pulse-echo ranging, where we can estimate the position of an object by measuring the time it takes for the echoes to return from it. The distance d to the object is

$$d = \frac{ct}{2}, \tag{2.1}$$

where c is the speed of sound in the medium. The total time between transmission of a pulse and the received echo is t. We divide by a factor of two since the pulse travels back and forth.

Pulse-echo ranging has been used in many applications throughout the years. Some of the papers in this thesis are inspired by techniques from the sonar and radar communities. Sonar is an acronym for *sound navigation and ranging*. It can for example be used to navigate, measure distances (ranging), and detect objects. Active sonar is pulse-echo ranging applied underwater, while passive sonar listens to acoustic sound. Sonar was developed during World War I as a method for warships to detect submarines [Sza14, ch. 1.1.2]. During World War II, pulse-echo ranging applied to electromagnetic waves became radar, an acronym for *radio detection and ranging* [CGM95, ch. 1]. The development of medical ultrasound follows the development of sonar and radar. Today, we use ultrasound in medical applications as well as in other fields such as the construction industry and the oil, gas, and maritime sectors. For example, ultrasound can be used for non-destructive testing of a material's quality, detection of erosion or sand in wellbores, counting fish, and monitoring babies in the womb. Prenatal ultrasound evaluates the baby's growth and development and is a classic example of medical ultrasound. Figure 2.1 shows two sonograms of a ten-week-old and six-month-old fetus. Ultrasound is especially beneficial for fetal imaging as it is non-invasive, low in cost, and has widespread availability. Ultrasound is a useful way of examining many of the body's internal organs, such as the abdomen or the heart. A high skill level is needed to obtain good diagnostic images with medical ultrasound.

If we approximate the medium as lossless , the propagation of sound waves is described by the lossless wave equation [Hol19, ch. 1]

$$\nabla^2 u = \frac{1}{c^2}\frac{\partial^2 u}{\partial t^2}. \tag{2.2}$$

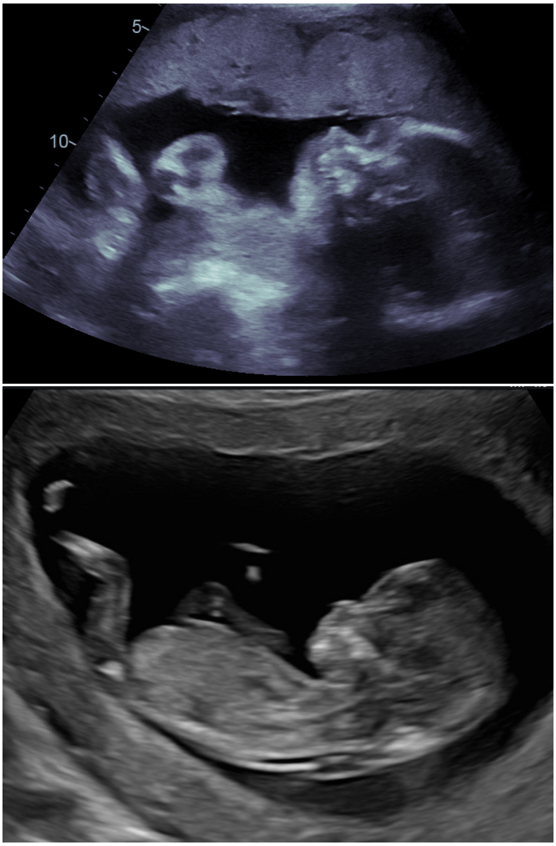

Figure 2.1: Two fetal ultrasound images. The top image shows my eldest daughter as a six-month-old fetus. The baby's gestational age can be estimated by measuring the head circumference. The bottom image shows my youngest as a ten-week-old fetus. Notice how the contrast of the baby's nose and head is especially distinct because of the boundary with the amniotic fluid. Even at this early stage, measuring the distance between the crown and rump provides a very good estimate of the due date.

Here $u(x, y, z, t)$ is the displacement vector associated with the compression and expansion of the acoustic wave, and $\nabla^2 = \frac{\partial^2}{\partial x^2} + \frac{\partial^2}{\partial y^2} + \frac{d^2}{\partial z^2}$ is the Laplacian operator. A solution to the wave equation (2.2) is a time-harmonic plane wave with propagation speed c,

$$\mathbf{u}(\mathbf{x}, t) = Ae^{i(\omega t - k_x x - k_y y - k_z z)} = Ae^{i(\omega t - \mathbf{kx})}. \tag{2.3}$$

Here $\mathbf{k}$ is the wave vector, $|\mathbf{k}|$ is the wavenumber, and ω is the angular frequency. The amplitude remains constant throughtout the propagation in a lossless medium. In the lossless case, the dispersion relation is simply [Hol19, ch. 1]

$$k = \frac{\omega}{c} = \frac{2\pi f}{c} = \frac{2\pi}{\lambda}, \tag{2.4}$$

where f is the frequency and λ is the wavelength.

Attenuation is the reduction in wave intensity as the wave travels through a medium [Cob07, ch. 1.8]. Waves with higher frequencies experience a higher amount of attenuation. Some of the beam is absorbed or scattered by the medium through which it travels. The amount of absorption depends on the type of medium. Bone is an example of a strong absorber, while water absorbs very little.

The viscous wave equation includes an extra term to model viscous loss [Hol19, ch. 1]

$$\nabla^2 u - \frac{1}{c^2}\frac{\partial^2 u}{\partial t^2} + \tau\frac{\partial}{\partial t}\nabla^2 u = 0. \tag{2.5}$$

The time constant τ characterizes the viscous loss, which causes a frequency-dependent attenuation. An attenuating wave is characterized by a complex wavenumber, where the real part represents the propagation and phase velocity and the imaginary part represents the attenuation [Hol19, ch. 2.3.1].

The amplitude attenuation depends on frequency, temperature, and pressure. The attenuation in soft tissue has a frequency-dependence with a power-law exponent in the range from 1 to 2 [Cob07, ch. 1.8.1] [NH13]. An ultrasound beam with a higher frequency has better resolution but cannot penetrate as far into the medium. Ultrasound imaging is thereby a trade-off between resolution and penetration.

Acoustic impedance describes how much the medium opposes the flow of the sound wave. The acoustic impedance Z of a medium is given by [Sza14, ch. 1.2]

$$Z = \rho c, \tag{2.6}$$

where ρ is the density and c is the speed of sound in the medium. In typical soft tissue, the sound speed is 1540 m/s and the density is 1060 kgm^{-3}.

When an ultrasound beam meets a boundary, it can be reflected or transmitted. Refraction involves a change in the wave direction as it passes from one medium to another. Snell's law describes the relationship between the transmitted wave's direction θ_t and the angle of incidence θ_i at a distinct boundary [Cob07, p. 52],

$$\frac{\sin\theta_t}{\sin\theta_i} = \frac{c_1}{c_2}. \tag{2.7}$$

Here c_1 and c_2 are the sound speeds in the first and second medium.

The difference in impedance across the boundary decides how much of the wave is reflected. The reflection coefficient R describes how much of the intensity is reflected compared to the incident intensity,

$$R = \frac{(Z_2 - Z_1)^2}{(Z_2 + Z_1)^2} = \frac{(\rho_2 c_2 - \rho_1 c_1)^2}{(\rho_2 c_2 + \rho_1 c_1)^2}. \tag{2.8}$$

The reflection coefficient for a soft tissue/muscle interface is small, whereas a bone/soft tissue interface reflects around 40 %. Since bone is such a strong reflector, ultrasound imaging through bone can be difficult. Any boundary with air results in almost 100 % reflection, so we cannot use ultrasound to image beyond air gaps such as the lungs. Figure 2.1 shows a songoram where the image quality of the body structures under study improves due to a distinct fluid boundary. In general, only a tiny part of the transmitted ultrasound signal will be reflected or scattered back to the probe.

Scattering is when the wave energy is redirected by a scattering object or structure, mostly along paths different from the incident wave. The scattered energy can be subsequently absorbed, and multiple scattering can occur [Cob07, p. 70]. Most echoes from ultrasound imaging arise from scattering. There are three types of scattering, and they depend on the size of the scattering object compared to the sound wavelength [Sza14, ch. 8.2]. Specular scattering occurs when the object is much larger than the wavelength. Diffractive scattering occurs when the size is comparable to the wavelength. Diffusive or Rayleigh scattering occurs when the object is much smaller than the wavelength. Diffusive scattering has important implications in ultrasound imaging since many small scatterers cause multiple scattering and create a granular pattern called speckle.

2.2 The Ultrasound Probe

Piezoelectric crystals are capable of converting mechanical energy into electrical energy through the piezoelectric effect [Cob07, ch 6.1]. Ultrasound is both generated and detected through oscillations in piezoelectric crystals. An ultrasound transmitter applies an alternating voltage to make the crystal vibrate and emit a pressure wave. An ultrasound receiver monitors the piezoelectric voltage developed across the crystal when it vibrates due to returning echos. In medical ultrasound, the waves are transmitted into the body using a probe consisting of an array of piezoelectric elements.

The ultrasound probe can have different array designs. Arrays of individual elements can be both focused and steered. This concept is used in ultrasound, radar, and sonar imaging. The development of ultrasound array has benefited from advances in the radar and sonar fields. During World War II, developing one-dimensional (1-D) and two-dimensional (2-D) antenna array designs was especially important for radar and communication systems. In this thesis, I present methods that use the array design to enhance the point targets.

A modern 1-D ultrasound transducer typically has a linear, phased, or convex array. A 2-D ultrasound array is used for 3-D imaging. Figure 2.2 shows the GE Vivid E95 ultrasound scanner (GE Vingmed Ultrasound) equipped with a linear and phased probe and two bottles of ultrasound gel. The ultrasound gel minimizes the immediate reflection caused by air between the patient and the transducer.

2.2.1 Linear probe

Most of the ultrasound images used in this thesis were imaged with a linear probe. This section will go through how we get the mathematical expression for the beampattern of a linear array. The beampattern determines the amplitude and phase of the beamformed signal when the wavefield consists of a single plane (far-field) wave [JD93, ch. 4.2.1]. The beampattern is essential in further discussions on resolution.

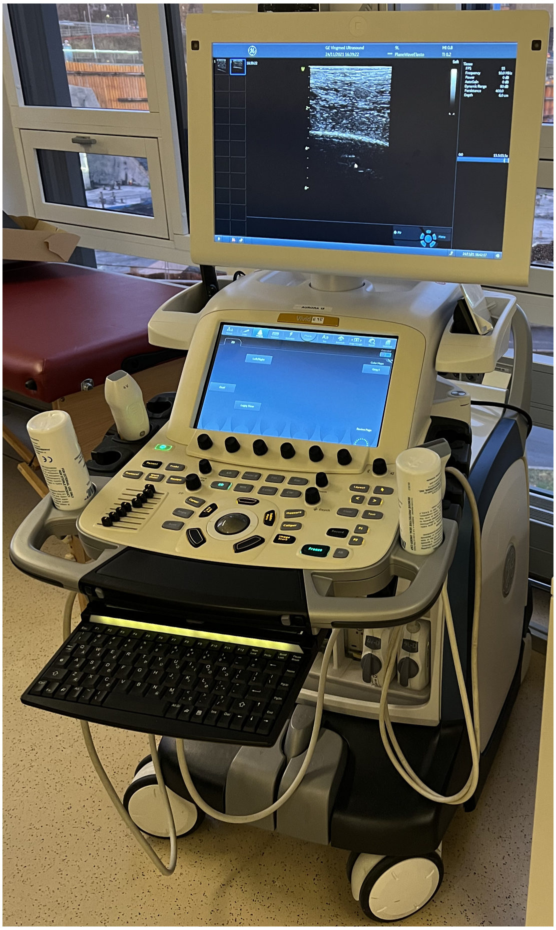

Figure 2.2: The GE Vivid E95 ultrasound scanner from GE Vingmed Ultrasound. A phased probe is placed in a holder to the left, and a linear probe is in a holder to the right behind a bottle of ultrasound gel.

A *continuous* linear aperture has an aperture function that is nonzero only along the finite length D of the array,

$$w(x) = \begin{cases} 1, & \text{if } |x| < \frac{D}{2} \\ 0, & \text{otherwise.} \end{cases} \tag{2.9}$$

Because the linear aperture lies along the x-axis, its aperture smoothing function depends only on k_x, the x-component of the wavenumber [JD93, ch. 3.1.1]

$$W(\mathbf{k}) = \frac{\sin(k_x D/2)}{k_x/2}. \tag{2.10}$$

$W(\mathbf{k})$ is calculated by the Fourier transform of the weighting sequence w. The resulting sinc-function has mainlobe of height D. The mainlobe width is $4\pi/D$, and the infinite number of sidelobes have decreasing amplitude. If the incoming wave has an incident angle θ with respect to the broadside of the array, $k_x = -k \sin\theta$ [JD93, p. 32].

The linear probes used in ultrasound imaging are not continuous but consist of many sensor elements. The discrete aperture smoothing function can be used to calculate the beampattern. A linear aperture with M uniform sensor elements has the discrete aperture smoothing function [JD93, p. 88]

$$W(\mathbf{k}) \equiv \sum_{m=0}^{M-1} w_m e^{jk_x x_m} = \frac{\sin(k_x M d/2)}{\sin(k_x d/2)}, \tag{2.11}$$

where the sensor position for element m is $x_m = md$. The element weight is w_m and the pitch or distance between the point elements is d. The derivation assumes point elements. If the elements have a width, the element's aperture smoothing function will be multiplied with the array's aperture smoothing function. The distance between the elements and not the element width affect the beampattern's mainlobe the most. Unlike the case of a continuous linear aperture, the aperture smoothing function for the linear array is a periodic sinc-function of k_x. It is illustrated in Figure 2.3. The spectrum has period $k_x = 2\pi/d$. Each period of $W(k)$ consists of a *mainlobe* and a number of smaller amplitude peaks called *sidelobes*. The mainlobe height $W(0)$ for a linear array with uniform element weighting equals the number of sensor elements in the array, M. The first zero of $W(k)$ occurs at $2\pi/Md$, so the mainlobe width is $\frac{4\pi}{Md}$.

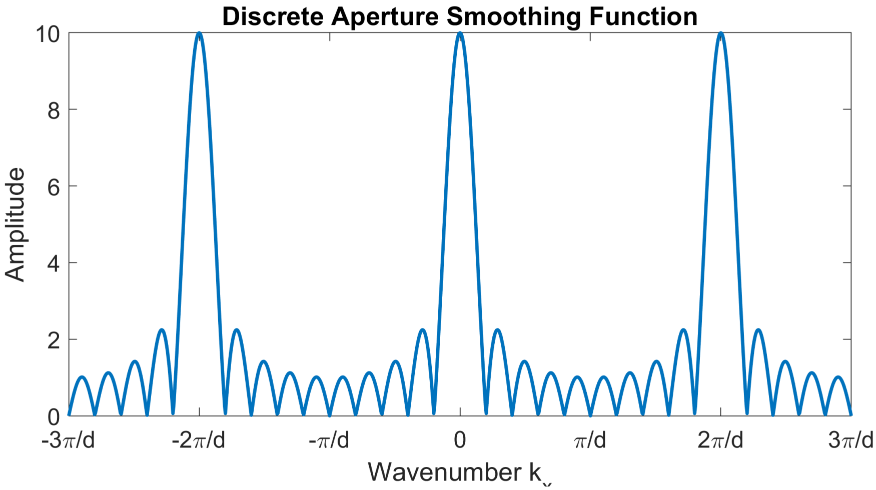

Figure 2.3: The magnitude of the discrete aperture smoothing function $|W(k)|$ for a linear array with $M = 10$ sensor point elements. The spectrum's period is $2\pi/d$. The "secondary" mainlobes not located at the origin are called grating lobes. The sidelobes are the small amplitude peaks between the mainlobe and the grating lobes. The visible region is $-2\pi/\lambda \leq k_x \leq 2\pi/\lambda$. The first zero of $W(k)$ occurs at $2\pi/Md$.

The beampattern's width is often used to characterize the spatial resolution, as discussed in Section 2.3. In ultrasound imaging, we first transmit a pulse and then receive the reflected signal. The two-way beampattern is a product of the beampattern in each direction. Assuming the full array is used for both transmit and receive, the two-way beampattern is [JD93, ch. 3.1.1]

$$W(\mathbf{k})_{\text{two-way}} = W(\mathbf{k})_{\text{transmit}} W(\mathbf{k})_{\text{receive}} = W(\mathbf{k})^2_{\text{one-way}}. \tag{2.12}$$

The linear array used in Paper II, Paper IV, and Paper V was the Verasonics L11-4v transducer (Verasonics Ltd). It consists of 128 elements with an element height of 5 mm. The pitch, or distance between the center of the elements, is 0.30 mm. The kerf, or gap between the elements, is 0.03 mm. The width of the elements is then simply the difference between the pitch and the kerf, i.e., 0.27 mm. The aperture size of the probe is 38.1 mm. The L11-5v is a mid-to-high-frequency, linear broadband array. If we use a 5.13 MHz center frequency f_0 at 1540 m/s sound speed, we get λ pitch since the wavelength $\lambda = c/f_0 = 0.3$ mm. The bandwidth of the transmitted pulse was 65 $\%$ of the center frequency f_0.

Figure 2.4 shows an image of a linear probe and a breast phantom with applied ultrasound gel. The GE 9L is a linear array ultrasound transducer probe from GE Healthcare. The GE 9L probe has a frequency range of 2.5 to 8.0 MHz. It is used for vascular, abdomen, neonatal, pediatric, obstetrics, and gynecology applications.

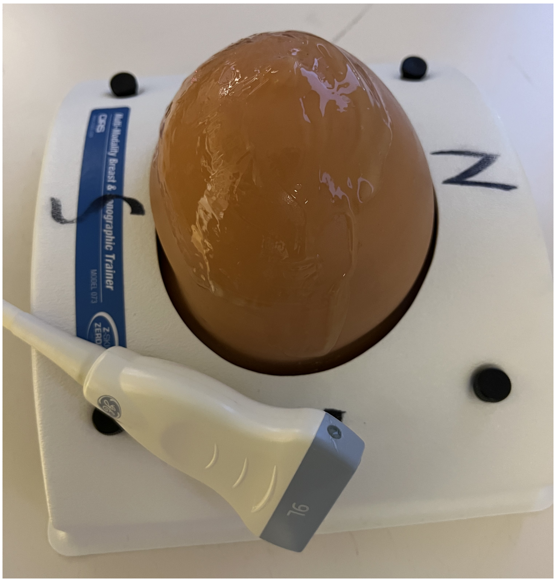

Figure 2.4: The GE 9L is a linear array ultrasound transducer. It is shown together with a tissue-mimicking breast phantom (CIRS M073), applied with ultrasound gel.

2.2.2 Phased and 3-D imaging probes

The phased probe shown in Figure 2.2 is a GE 4V-D probe with a bandwidth of 1.5 to 4 MHz. The size of the probe is smaller than the linear probe, which gives a lower image resolution. Since the probe is used for cardiography, its size must be small enough to fit between the ribs. The cardiac probe has a lower center frequency than the linear probe GE 9L since the beam must penetrate deep enough to image the heart. By transmitting several focused beams at specific steered angles, we can obtain a sector scan of the heart.

The GE 6VT-D probe from GE Vingmed Ultrasound is a 4-D volume cardiac probe (3-D + time) with a center frequency of 5 MHz. It is designed for transesophageal echocardiography (TEE) and must be small enough to go inside the esophagus. The frequency bandwidth is 3 to 8 MHz. The probe was used to image the breast phantom in Figure 2.4. The probe is too tiny to be optimal for breast imaging, but we wished to obtain 3-D data to test the wavelet shrinkage method presented in Paper III.

2.3 Spatial Resolution

Spatial resolution is important for the image quality and the detectability of point scatterers. There are many different definitions of resolution. A common definition in several fields of study is using the full width half maximum (FWHM) of the beampattern mainlobe, corresponding to -6 in dB-scale [Sza14, p. 230]. The angular resolution can be approximated depending on the array geometry and the applied apodization. The -6 dB angular resolution of the discrete Fourier transform (DFT) of a rectangular window is given by F. Harris in [Har78] as approximately 1.21 bins, where a bin corresponds to the fundamental frequency resolution. For a linear array with rectangular apodization, we correspondingly get

$$\theta_{\text{-6 dB}} \approx \frac{1.21\lambda}{D}. \tag{2.13}$$

Here D is the probe size and λ is the wavelength. A large array corresponds to high resolution. The -6 dB lateral spatial resolution $x_{\text{-6 dB}}$ at a certain depth z can be found by small angle approximation as

$$x_{\text{-6 dB}} = \theta_{\text{-6 dB}} z = \frac{1.21\lambda}{D} z. \tag{2.14}$$

In ultrasound imaging, we first transmit a pulse and then receive the reflected signal. We are therefore actually interested in the *two-way* lateral resolution. Taking the square root of the one-way beampattern reduces the mainlobe width such that the -6 dB width of the two-way beampattern equals the -3 dB width of the one-way beampattern. The -6 dB angular *two-way* resolution is [Rin19, App. A]

$$\theta_{\text{-6 dB two-way}} = \frac{\theta_{\text{-6 dB one-way}}}{\sqrt{2}} \approx \frac{1.21\lambda}{\sqrt{2}D}. \tag{2.15}$$

The lateral resolution in an ultrasound image at depth z is thereby

$$x_{\text{res}} = \frac{1.21\lambda z}{\sqrt{2}D}. \tag{2.16}$$

The ratio between imaging depth z and size of the *active* aperture D^* is termed *F-number* or $f_\#$,

$$f_\# = \frac{z}{D^*}. \tag{2.17}$$

We can ensure uniform resolution by having a constant $f_\#$. A constant $f_\#$ ensures a range-independent beamwidth by increasing the active aperture with increasing range z [Sza14, p. 381]. Since the physical aperture has finite size, pixels close to the edges will be illuminated by an active aperture of smaller size. Inserting a constant $f_\#$ into (2.16), we can express the -6 dB lateral resolution as

$$x_{\text{res}} = \frac{1.21}{\sqrt{2}} \lambda f_\#. \tag{2.18}$$

We can also calculate the resolution in the elevation direction, y_{res}. For a 1-D array, it depends on the element height. For a 2-D array, it depends on the size of the array of sensor elements in the elevation direction.

The axial resolution z_{res} depends on the transmitted pulse bandwidth B and speed of sound c [Cob07, ch. 8.3.1],

$$z_{\text{res}} = \frac{c}{2B}. \tag{2.19}$$

A large pulse bandwidth corresponds to high spatial resolution.

2.4 Apodization

In medical ultrasound, applying an apodization window is standard practice for reducing sidelobe levels [Sza14, p. 178] [JD93, p. 322]. A rectangular apodization means that each element on the aperture is used and weighed equally. Windowing is always a trade-off between resolution and contrast [Har78]. The choice of apodization window influences the spatial resolution. A nonuniform window suppresses some elements at the edges of the aperture and effectively reduces the active aperture size. Apodization on linear arrays is accomplished by exciting the individual elements with different voltage amplitudes [Sza14, p. 178]. For a linear array with Hamming apodization, the -6 dB angular resolution is [Har78]

$$\theta_{\text{-6 dB, Hamming}} \approx \frac{1.81\lambda}{D}. \tag{2.20}$$

In Paper II, we applied three different apodization methods to study the effect on detection: rectangular, Hamming only on transmit, and Hamming on both transmit and receive. Transmit apodization is applied over the elements when transmitting the ultrasound wave.

2.5 Spatial Frequency Limits

Paper III, Paper IV, and Paper V apply techniques to the ultrasound image in the spatial frequency domain. The spatial frequency support for an ultrasound imaging system is defined by the finite aperture size and the bandlimited pulse. It is centered on $2k_0 = 4\pi f_0/c$ [AT00, ch. 3]. In Figure 2.5, the imaging pulse is bandpass filtered ($f_L \leq f \leq f_H$) and demodulated by $k_D \approx 2k_0$. The Point Spread Function (PSF) is the response of an ultrasound system to a point source and describes the system's image quality.

To discuss and illustrate the spatial frequency limits, we consider a linear array with a point scatterer placed in the center of the image scene. The PSF is the system's impulse response, and its shape resembles a slice cut of a circular arc, as illustrated in Figure 2.5. The PSF is horizontally symmetric when the point scatterer is located in the center, but asymmetric when the point is located to the side [Che+20]. The support region is bounded by the aperture function in the k_x direction. The lateral width increases linearly with increasing frequency. In Figure 2.5, the spectrum has been demodulated and normalized such that

$$\max \kappa_z = \frac{k_H - k_D}{k_D} = \frac{2\pi}{c} \frac{f_H - f_D}{f_D}. \tag{2.21}$$

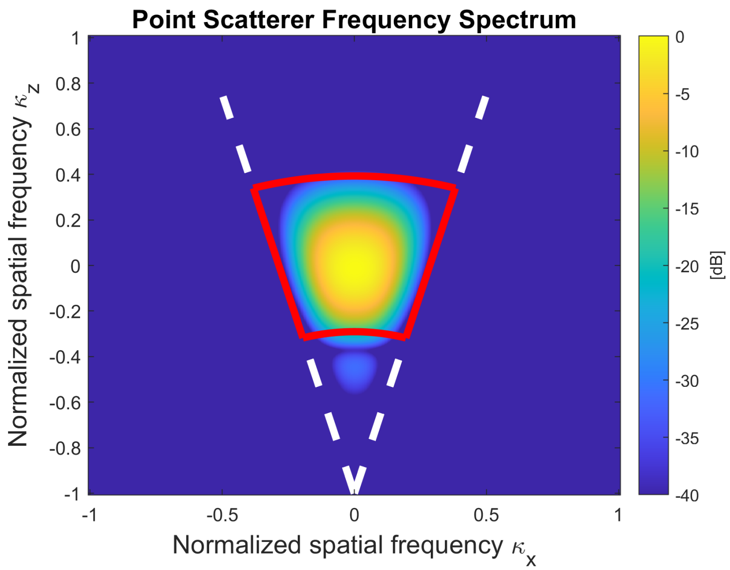

Figure 2.5: The frequency spectrum of a point scatterer is shown with a 40 dB dynamic range. The spatial frequencies are normalized by the estimated center frequency k_D ($\approx 2k_0$). The spatial frequency limits are shown in red. The critical angle and frequency bandwidth define the limits. The critical angle α is 16°. The point scatterer is located in the center of the image scene and is imaged using a linear array with constant $f_{\#}$.

The receiving angle is the angle between the depth z and the lateral distance from the origin x. The *critical* angle is the largest probe-to-object angle the system can image. The aperture defines it with $x_{\max} = D/2$. We can define the limits of the lateral spatial frequency k_x using the critical angle. For the PSF shown in Figure 2.5, I applied an adaptive aperture setting using constant $f_{\#}$ to ensure uniform image resolution. With equal transmit and receive aperture D^*, the critical angle α is [Gol+21][Den+13]

$$\alpha = \operatorname{atan}\left(\frac{D^*/2}{z}\right) = \operatorname{atan}\left(\frac{1}{2f_{\#}}\right). \tag{2.22}$$

Reducing the $f_{\#}$ increases the width of the frequency response in the k_x-direction. Figure 7.2 illustrates the critical angle α and the normalized spatial frequency limits κ_x and κ_z. The lower limit for κ_z is

$$\min \kappa_z = \frac{k_L \cos(\alpha) - k_D}{k_D}. \tag{2.23}$$

The limits for the normalized lateral spatial frequency k_x are

$$-\frac{k_H \sin(\alpha)}{k_D} < \kappa_x < \frac{k_H \sin(\alpha)}{k_D}. \tag{2.24}$$

2.6 Pulse-Echo Transmission and Scan Types

Since ultrasound imaging uses pulse-echo ranging, the next wave cannot be transmitted before the probe has received the first wave. The time between transmits must be larger than the two-way travel time for the deepest pixel position in the image. Several transmitted beams construct each final ultrasound image, affecting the imaging frame rate. Common imaging modalities in ultrasound are Focused Imaging (FI), Plane Wave Imaging (PW), Diverging Wave Imaging (DW), and Synthetic Transmit Aperture Imaging (STAI).

Focused imaging is a common ultrasound scan where the transmission converges towards a focal point and expands afterward. Figure 2.6 illustrates how one transmit corresponds to an axial scan line and how several scan lines can be created by shifting the location of the focal point. Figure 2.6 illustrates a focused linear and sector scan. It is worth mentioning that software techniques such as multiple line acquisition (MLA) and retrospective beamforming (RTB) can improve the image quality by synthetically recreating a focus in overlapping transmit regions and coherently compounding them. However, we will not go further into the details here.

Figure 2.6 illustrates a plane wave fired at two different angles. We can create an angled plane wave by applying specific transmit delays to the elements according to the wanted angle. In 2009, Montaldo et al. [Mon+09] achieved high-quality images by coherently compounding many plane wave images. They showed that a high frame rate is possible using plane wave transmits. A plane wave illuminates a large area and reduces the required number of transmits to produce an acceptable image quality. Denarie et al. discuss the required number of plane waves to cover the critical angle α and achieve equivalence with conventional imaging in [Den+13]. In Paper III, a Coherently Compounded Plane Wave (CPWC) ultrasound image was acquired with the Verasonics Vantage system using a linear probe (Philips L7-4, 128 elements, 75 angles, 5.2 MHz, $f_{\#} = 1.75$).

A diverging sector scan grows with depth and yields a resolution that decreases with increasing depth. The virtual source for a diverging wave lies before the aperture.

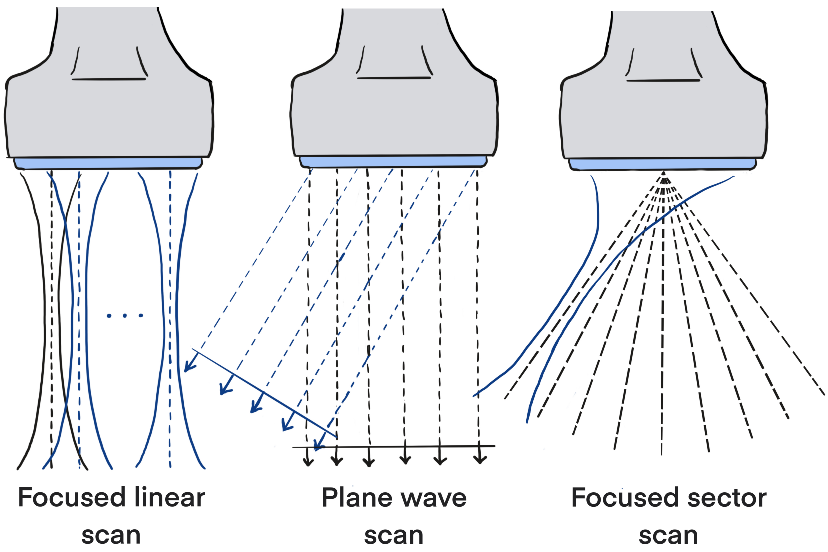

Figure 2.6: Schematic of a focused linear scan, a plane wave scan, and a focused sector scan.

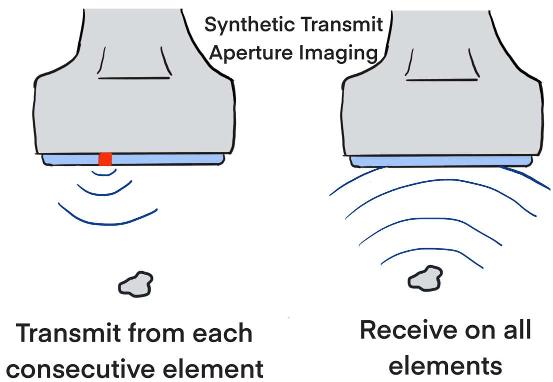

Figure 2.7: Schematic of synthetic transmit aperture imaging.

We acquired synthetic transmit aperture datasets to get images with uniform resolution for all pixels in Paper I - Paper V. STA imaging creates images with high spatial resolution since we for each transmit fire from one specific element and receive on the entire array, as illustrated in Figure 2.7. After transmitting from every consecutive element, we synthesize focus at every pixel. A drawback of STA imaging is that transmitting from a single element limits the beam energy and makes second harmonic imaging and imaging of moving structures more challenging.

2.7 Tissue-mimicking Phantoms

Figure 2.8: The tissue-mimicking phantom 054GS from CIRS embedded with several cysts and wire targets.

Figure 2.9: The Multi-Modality Breast Biopsy and Sonographic Trainer M073 from CIRS. The phantom accurately mimics the heterogeneous appearance of breast tissue under ultrasound, mammography, and MRI. It has cystic and dense lesions with 100-300 micron microcalcifications.

The background of much of this Ph.D. work is that point scatterers, such as kidney stones or microcalcifications in breasts, are often obscured by background speckle. Figure 2.8 shows the tissue-mimicking phantom 054GS from CIRS. The phantom was used in Paper III and Paper V. It is embedded with hyperechoic and anechoic cysts and several wire targets that appear as point scatterers in the final ultrasound image. We can test spatial resolution or contrast using such phantoms.

Figure 2.9 shows a tissue-mimicking breast phantom embedded with cysts with microcalcifications. Microcalcifications are tiny calcium deposits within the breast tissue, and they appear as small white spots on a mammogram or an ultrasound image. They are usually benign, but specific patterns can signify cancer. A 3-D ultrasound image of the breast phantom is analyzed for probable locations of microcalcifications in Section 4.7.

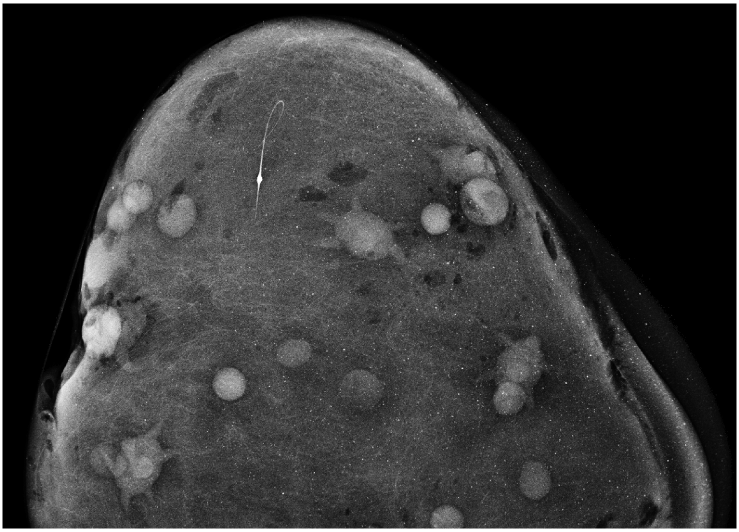

Figure 2.10: X-ray image or mammogram of the breast phantom.

Figures 2.10 – 2.12 illustrate the differences in image quality between Computed Tomography (CT), Magnetic Resonance Imaging (MRI), and ultrasound imaging. Microcalcifications appear as small white spots on a mammogram, an X-ray picture of the breast. Figure 2.10 shows a mammogram of the breast phantom. I obtained a 3-D Magnetic Resonance Imaging (MRI) scan of the phantom, and Figure 2.11 shows a slice near the center of the breast. Figure 2.12 shows an ultrasound image of the same phantom. I also imaged the phantom with the tiny transesophageal 4-D probe (3-D + time), shown in Figure 2.13. This 3-D image is analyzed further in Section 4.7.

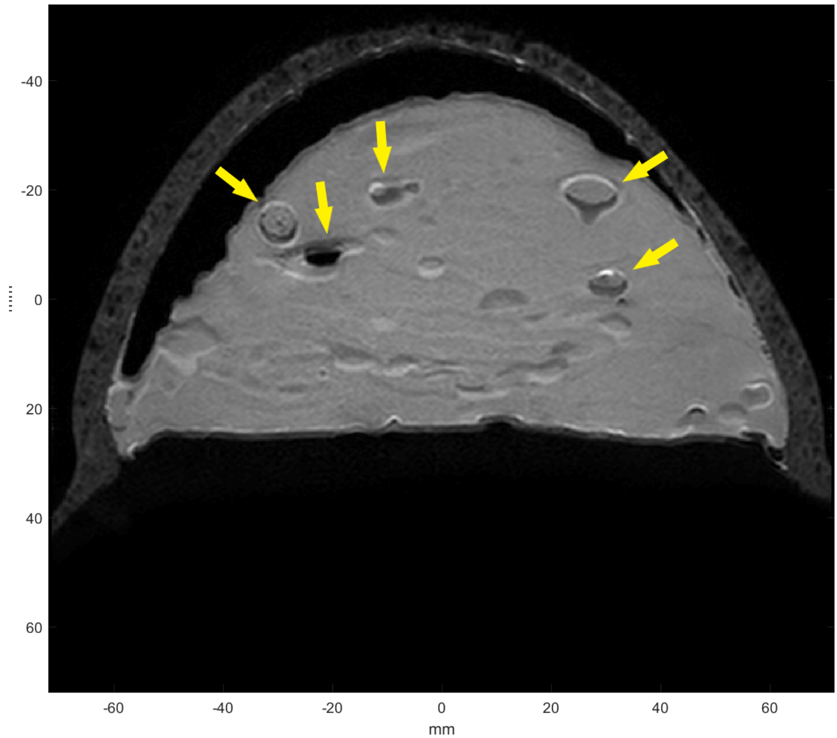

Figure 2.11: MRI slice of the breast phantom with clearly visible cysts, as indicated with the yellow arrows. The small microcalcifications within the cysts can be seen if studied closely.

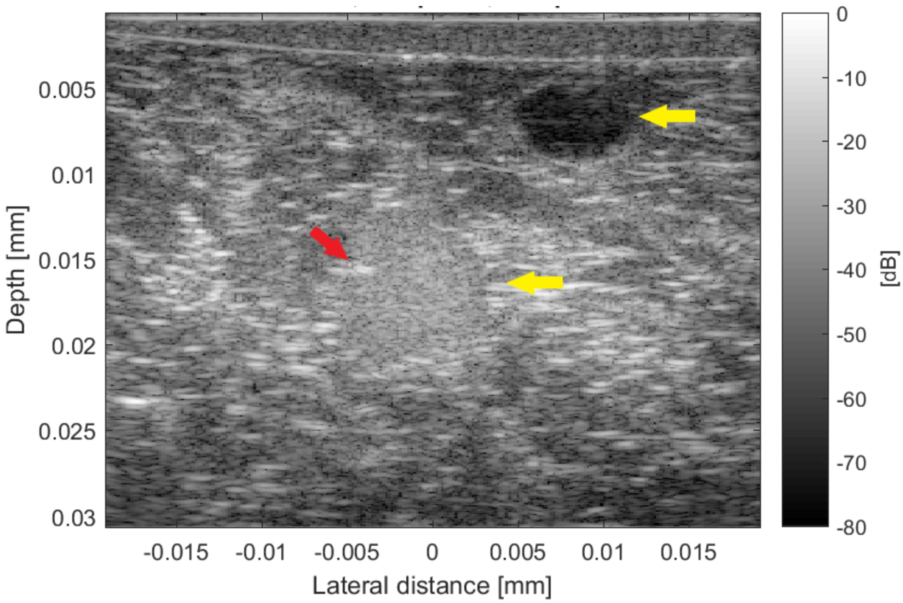

Figure 2.12: An ultrasound image of the breast phantom imaged using the linear 2-D probe GE 11L. We see a hyperechoic cyst and an anechoic cyst, as indicated by the yellow arrows. The red arrow indicates a possible microcalcification inside the hyperechoic cyst.

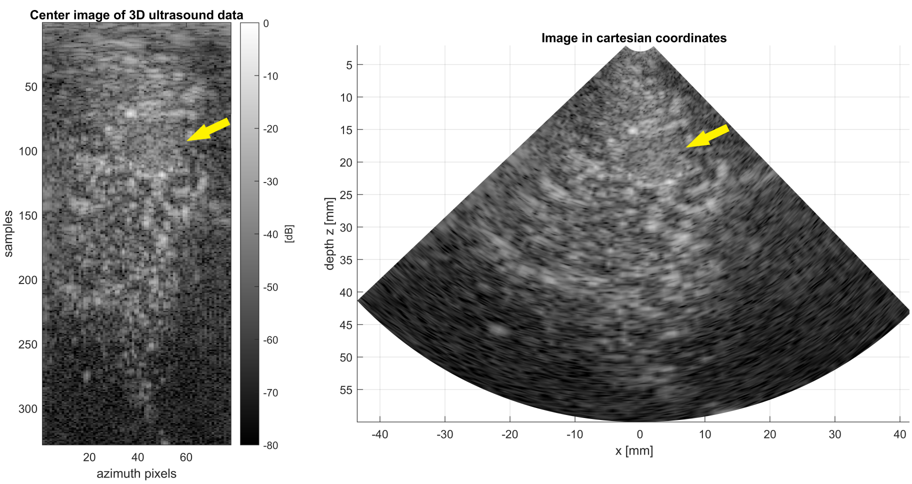

Figure 2.13: An ultrasound image of the breast phantom imaged using a GE 6VT-D ultrasound transducer. The yellow arrow shows the location of a cyst. This is a 4-D volume cardiac transesophageal transducer and thus not ideal for breast imaging.

2.8 The Conventional Beamformer

In this section, I describe how the received ultrasound signal is converted to the final image. We start with the channel data received by each probe element. We convert the data to an analytical signal, demodulate it, and combine the signals using a beamformer. This thesis uses methods that analyze the data at different stages in the image processing chain.

2.8.1 Channel Data

The probe elements record the reflected ultrasound signals. Figure 2.14 shows the signal received from one element. The received data is commonly referred to as radio frequency (RF) channel data. According to the Nyquist sampling theorem, we must sample the data at a frequency at least twice the highest frequency to avoid unwanted aliasing [MI11, p. 340]. Figure 2.15 shows the frequency spectrum of the channel data example.

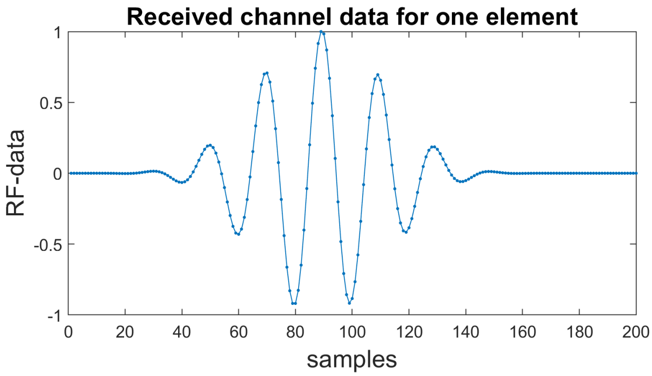

Figure 2.14: The received signal from a single probe element, normalized by its maximum value.

A Hilbert transform can be used to convert the channel data to a complex, analytical signal [MI11, p. 542]. The final image displayed on a medical ultrasound machine is the envelope of the received signal, i.e., simply the magnitude of the analytical signal. The Ultrasound Toolbox (USTB) [Rod+17] is an open software processing framework for ultrasound signals and was extensively used in this Ph.D. project. It uses the analytical signal throughout the beamforming and detects the envelope after beamforming.

2.8.2 IQ-Channel Data

Since the received channel data is bandlimited, we want to demodulate it. Demodulation is a common approach because it enables decimation, i.e., reducing the number of samples [MI11, ch. 6.6]. The original RF-channel data is centered around a center frequency f_0. By multiplying the data with a complex sinusoidal carrier signal of

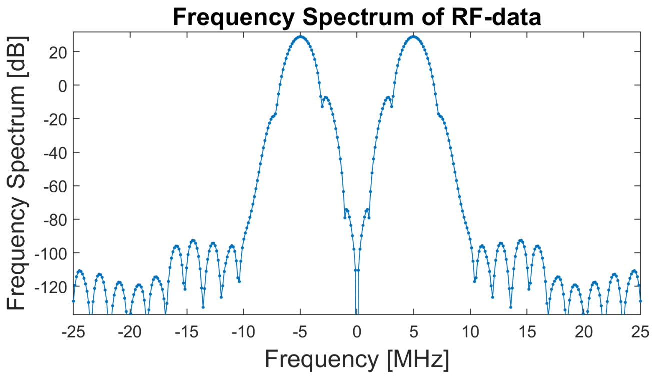

Figure 2.15: The frequency spectrum of the channel data. The center frequency is around 5 MHz.

frequency f_{demod}, we can move the frequency spectrum correspondingly [MI11, p. 181]. If $f_{\text{demod}} \approx f_0$, the new spectrum is centered around the origin. Low-pass filtering the resulting spectrum ensures we only retain the frequencies within the valid bandwidth. The resulting spectrum is asymmetrical and thereby complex. We now have what is known as the In-phase Quadrature (IQ) signal. Many of the methods in this Ph.D. thesis use IQ-data instead of RF-data as input.

2.8.3 The Delay-and-Sum (DAS) Beamformer

Beamforming converts the recorded channel data into an image containing the combined estimate of all the received reflections. We calculate delays to adjust for the wave's travel time to and from each pixel position in the tissue to each probe sensor. The beamformer then combines the delayed signals. Paper I and Paper II study the effect of different beamformers. The Delay-and-Sum (DAS) beamformer coherently combines the pixel values received by all elements from all transmits. Paper II presents the DAS beamformer as follows:

> Conventional DAS consists of applying a delay and an amplitude weight to the output of each sensor, then summing the resulting signals [JD93, ch. 4.1]. DAS for image pixel $[z, x]$ is defined as
>
> $$S_{\text{DAS}}[z,x] = \sum_{m=0}^{M-1} w_m y_m[z,x], \tag{2.25}$$
>
> where M is the number of elements, $y_m[z,x]$ is the delayed signal received at element m, and w_m is a predefined weight. DAS is the oldest and simplest array signal processing algorithm but remains a powerful approach today [JD93, ch. 4.1].
>
> *Paper II*

2.9 Adaptive Beamforming

Paper I presents how different adaptive beamformers affect the speckle statistics of an ultrasound image. Paper II studies how different adaptive beamformers affect point detection performance. Since the papers introduce the theory for the different beamformers, I introduce them here as presented in the papers. The USTB [Rod+17] implements all six adaptive beamformers presented here.

2.9.1 Capon's Minimum Variance (MV)

Capon's Minimum Variance (MV) [Cap69] calculates for each pixel a data dependent set of weights $\boldsymbol{w} = [w_0, w_1, \ldots, w_{M'-1}]^T$ that minimizes power while maintaining unity gain in the steering direction [SAH07]. To calculate the weights, the spatial covariance matrix needs to be estimated for each pixel. To do this, we apply spatial averaging with subarrays $\boldsymbol{y}_l[z,x] = [y_l, y_{l+1}, \ldots, y_{l+L-1}]^T$, $l \in [0, M'-L-1]$, where M' is the length of the active receive aperture and $L = M'/2$. We apply time averaging with 1.5λ range (λ being the wavelength), a diagonal loading factor of $1/100$, and the steering vector as a vector of ones [SAH09]. The MV weights are used in (2.25) and the final image becomes

$$S_{\text{MV}}[z,x] = \frac{1}{M'-L+1} \sum_{l=0}^{M'-L} \boldsymbol{w}^H[z,x]\, \boldsymbol{y}_l[z,x]. \tag{2.26}$$

MV can achieve low sidelobe levels and a narrow beamwidth, increasing the spatial resolution of closely spaced point scatterers. See [SAH09] for a discussion on the parameters.

2.9.2 Mallart-Fink Coherence Factor (CF)

The Coherence Factor (CF) calculates the ratio between coherent and incoherent energy across the aperture [MF94]

$$\text{CF}[z,x] = \frac{\left|\sum y_m[z,x]\right|^2}{M \sum \left|y_m[z,x]\right|^2}. \tag{2.27}$$

It has the potential to give increased contrast and resolution when applied as an adaptive weight to the DAS image [LL03]

$$S_{\text{CF}} = S_{\text{DAS}}[z,x]\ \text{CF}. \tag{2.28}$$

2.9.3 Camacho-Fritsch Phase Coherence Factor (PCF)

The Phase Coherence Factor (PCF) [CPF09b] calculates for each pixel an adaptive weight based on the phase of the receive data. It is a method proposed to improve resolution [CPF09a]

$$\text{PCF}[z,x] = \max\left\{0, 1 - \frac{\gamma^*}{\sigma_0} f[z,x]\right\}, \tag{2.29}$$

where γ^* is a parameter *provided to adjust the sensitivity of PCF to out-of-focus signals* [CPF09b], and $\sigma_0 = \pi/\sqrt{3}$ is the STD of a uniform distribution between $-\pi$ and π [Rod+17]. The function $f[z,x]$ calculates the minimum STD of the instantaneous phase across the aperture. PCF is applied as an adaptive weight to the DAS image

$$S_{\text{PCF}} = S_{\text{DAS}}[z,x]\ \text{PCF}. \tag{2.30}$$

Paper II

2.9.4 Generalized Coherence Factor (GCF)

The Generalized Coherence Factor (GCF) beamformer is an extension of CF which utilizes the Fourier-spectrum over the receive aperture of the delayed channel data [LL03]. The GCF is calculated as the ratio between the energy in a small angular sector around the direction of interest divided by the total energy of the Fourier-spectrum.

Paper I

Li and Li introduced the GCF in [LL03]. It can be expressed as

$$\text{GCF}[z,x] = \frac{\left|\sum_{p<M_0} Y_p[z,x]\right|^2}{M\sum_{p=-M/2}^{M/2-1} |Y_p[z,x]|^2}, \tag{2.31}$$

where Y_p is the M-point frequency spectrum over the aperture of the received channel data y_m. The spatial frequency index p lies in the range $p \in [-\frac{M}{2}, \frac{M}{2}-1]$. The low frequency region is specified by the cutoff frequency M_0 and $M_0 \in [0, \frac{M}{2}-1]$. In Paper I, we used 11 out of a total of 128 Fourier coefficients. The GCF simplifies to CF if $M_0 = 0$. GCF is applied as an adaptive weight to the DAS image

$$S_{\text{GCF}} = S_{\text{DAS}}[z,x]\ \text{GCF}. \tag{2.32}$$

2.9.5 Eigenspace Based Minimum Variance (EBMV)

The Eigenspace Based Minimum Variance (EBMV) beamformer is an extension of the MV beamformer which utilizes the eigenstructure of the covariance matrix to enhance performance [AM10]. The covariance matrix is eigendecomposed into a signal and noise subspace, and the conventional MV weights are projected onto the signal subspace.

Paper I

Asl and Mahloojifar applied the EBMV beamformer to medical ultrasound in [AM10]. The signal subspace $\boldsymbol{E}_S$ consists of the eigenvectors corresponding to the largest eigenvalues,

$$\boldsymbol{E}_S = [\boldsymbol{v}_1, \boldsymbol{v}_2, ..., \boldsymbol{v}_{\text{Num}}], \tag{2.33}$$

where Num is the number of eigenvectors that demonstrate the signal subspace. We find the EBMV weights using the MV weights $\boldsymbol{w}_{\text{MV}}$ [AM10]

$$\boldsymbol{w}_{\text{EBMV}} = \boldsymbol{E}_S \boldsymbol{E}_S^H \boldsymbol{w}_{\text{MV}}. \tag{2.34}$$

In a similar fashion to the MV image, given by (2.26), we calculate the final EBMV image as

$$S_{\text{EBMV}}[z,x] = \frac{1}{M' - L + 1} \sum_{l=0}^{M'-L} \boldsymbol{w}_{\text{EBMV}}^H[z,x]\, \boldsymbol{y}_l[z,x]. \tag{2.35}$$

2.9.6 Delay-Multiply-And-Sum (DMAS)

> The Delay-Multiply-And-Sum (DMAS) [Mat+15] multiplies the delayed RF-signals using a "signed" square root. The sum of these signals is band-pass filtered around an "artificial second harmonic" signal before conventional envelope detection and log-compression of the signal results in the final image. It is not obvious that this is a "coherence based beamformer". However, it has been shown that "The DMAS enhances signal coherence and can be seen as an intermediate solution between the DAS beamformer and the coherence factor method" [Pri+17].
>
> *Paper I*

DMAS is also termed Filtered-DMAS (F-DMAS). Findings in [PRA18] show that the difference in image amplitude between DAS and F-DMAS can be partly explained by how signal coherence influences the beamformers. The nonlinear operation involves a pairwise multiplication and a square root before summation, and the final DMAS image is [PRA18]

$$S_{\text{DMAS}} = \sum_{q=0}^{M-1} \sum_{r=q+1}^{M} \text{sign}(y_q y_r)\sqrt{|y_q y_r|}. \tag{2.36}$$

2.10 Probability Distribution Functions (PDF)

The PDF describes the statistics of a distribution. In this section, I present three PDFs as background material for Paper I and Paper II. We use the PDF when estimating the probability of false alarm and detection, as discussed further in Chapter 3.

2.10.1 The Rayleigh Distribution

The *Rayleigh* PDF is important in ultrasound because it describes the speckle background. Conventional DAS beamforming gives speckle background with an amplitude Rayleigh distribution [Wag+83]. The Rayleigh PDF is obtained as the PDF of two normally distributed sequences with combined amplitude $A = \sqrt{x_1^2 + x_2^2}$.

Here x_1 and x_2 are independent variables with mean $\mu = 0$ and variance σ^2, so $x_1 \sim \mathcal{N}(0, \sigma^2)$ and $x_2 \sim \mathcal{N}(0, \sigma^2)$[Kay98, ch.2.2.6].

$$p(A)_{\text{Rayleigh}} = \begin{cases} \frac{A}{\sigma^2} \exp(-\frac{A^2}{2\sigma^2}) & \text{if } A > 0 \\ 0 & \text{if } A < 0. \end{cases} \tag{2.37}$$

Fig. 2.16 shows the PDF for a Rayleigh random variable with $\sigma^2 = 1$. σ is called the scale parameter of the Rayleigh distribution. The mean and variance of a Rayleigh

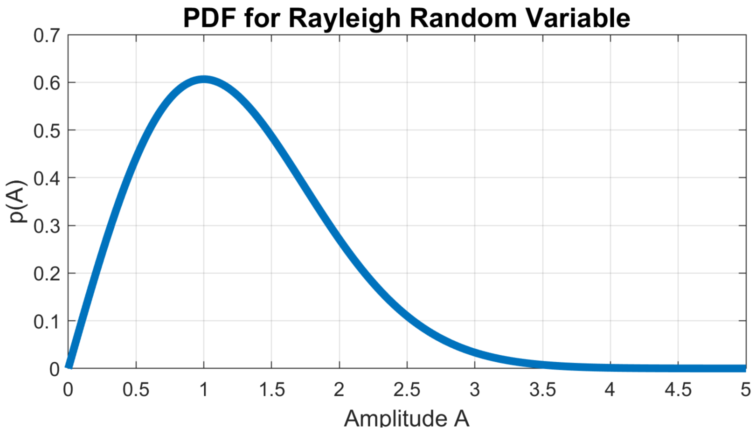

Figure 2.16: PDF for Rayleigh random variable A with $\sigma^2 = 1$.

distribution is

$$\mathrm{E}(A) = \sqrt{\pi\sigma^2/2} \tag{2.38}$$

$$\mathrm{Var}(A) = (2 - \pi/2)\sigma^2 \tag{2.39}$$

The signal-to-noise ratio (SNR) is commonly used in ultrasound to characterize imaging statistics

$$\mathrm{SNR} = \frac{\mathrm{E}(A)}{\sqrt{\mathrm{Var}(A)}}. \tag{2.40}$$

By inserting (2.38) and (2.39) into (2.40), we see that the theoretical Rayleigh distribution has SNR $= \sqrt{\frac{\pi/2}{2-\pi/2}} \approx 1.91$.

The right-tail probability is the probability of exceeding a given value γ. To get the expression for the probability, we integrate the PDF

$$Pr\{A > \gamma\} = \int_{\gamma}^{\infty} p(A)dA = \exp\left(\frac{-\gamma^2}{2\sigma^2}\right) \tag{2.41}$$

Following [Kay98, ch.2.2.6], the right-tail probability can also be written using the noncentral chi-squared PDF with two degrees of freedom (χ_2^2) by substituting the Rayleigh distributed amplitude A with a χ_2^2-distributed variable b as $A = \sqrt{\sigma^2 b}$ to get

$$\begin{aligned} Pr\{A > \sqrt{\gamma^*}\} =& Pr\{A/\sqrt{\sigma^2} > \sqrt{\gamma^*/\sigma^2}\} = Pr\{\sqrt{b} > \sqrt{\gamma^*/\sigma^2}\} \\ =& Pr\{b > \gamma^*/\sigma^2\} = \mathcal{Q}_{\chi_2^2}(\gamma^*/\sigma^2) \end{aligned} \tag{2.42}$$

The function $\mathcal{Q}(x)$ is the complementary cumulative distribution function. Since $\mathcal{Q}_{\chi_2^2}(t) = \exp(t/2)$, we can rewrite (2.42) as

$$Pr\{A > \gamma\} = \mathcal{Q}_{\chi_2^2}\left(\frac{\gamma^2}{\sigma^2}\right) = \exp\left(\frac{-\gamma^2}{2\sigma^2}\right). \tag{2.43}$$

2.10.2 The Negative Exponential Distribution

Ultrasound images are often shown in decibel (dB) scale. Squaring the amplitude of the signal changes the distribution. Intensity, i.e., the squared amplitude $i = A^2$ has a negative exponential distribution [Abr19, p. 261] [OQ98, p. 88][Cob07, p. 502]. The PDF for negative exponential random variable i is

$$p(i)_{\text{neg. exp.}} = \begin{cases} \frac{1}{\beta}\exp(-\frac{i}{\beta}) & \text{if } i > 0 \\ 0 & \text{if } i < 0. \end{cases} \tag{2.44}$$

Here β is the mean value $\mathrm{E}(i)$. If we compare with (2.38), it is clear that $\beta = 2\sigma^2$. Fig. 2.17 shows the PDF for a negative exponential random variable with $\beta = 2$.

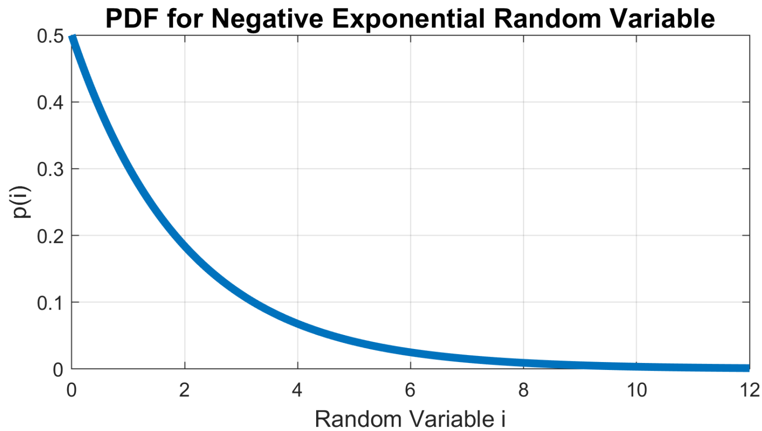

Figure 2.17: PDF for negative exponential random variable i with $\beta = 2$.

The right-tail probability of the PDF in (2.44) is

$$Pr\{i > \gamma\} = \mathcal{Q}_{\chi_2^2}\left(-\frac{\gamma}{\beta}\right) = \exp\left(-\frac{\gamma}{\beta}\right), \tag{2.45}$$

2.10.3 The Rician Distribution

The *Rician* PDF is important in Paper II when we add a point scatterer to the speckle background. The Rician PDF is the PDF of two normally distributed sequences with combined amplitude $A = \sqrt{x_1^2 + x_2^2}$. Here x_1 and x_2 are independent variables with different mean values but variance σ^2, so $x_1 \sim \mathcal{N}(\mu_1, \sigma^2)$ and $x_2 \sim \mathcal{N}(\mu_2, \sigma^2)$[Kay98, ch.2.2.6].

$$p(A)_{\text{Rician}} = \begin{cases} \frac{A}{\sigma^2} \exp\left(-\frac{(A^2+\alpha^2)}{2\sigma^2}\right) \mathrm{I}_0\left(\frac{\alpha A}{\sigma^2}\right) & \text{if } A > 0 \\ 0 & \text{if } A < 0, \end{cases} \tag{2.46}$$

where $\mathrm{I}_0(u)$ is the modified Bessel function of the first kind and zeroth order, and $\alpha^2 = \mu_1^2 + \mu_2^2$. If $\alpha^2 = 0$, the PDF reduces back to Rayleigh. Fig. 2.18 shows the PDF for a Rician random variable with $\sigma^2 = 1$ and varying values of α^2.

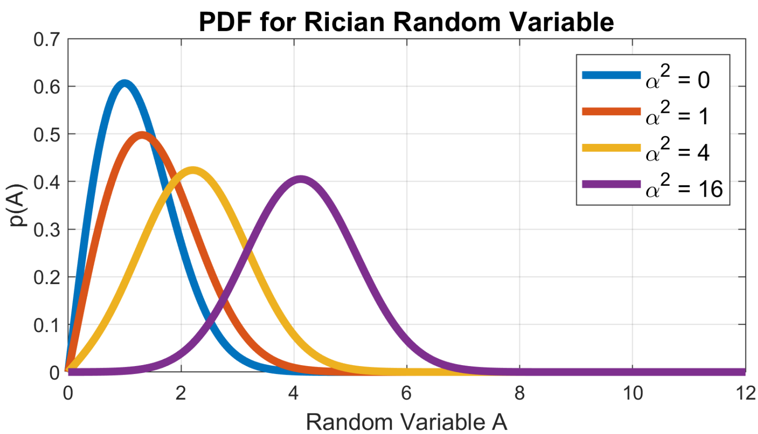

Figure 2.18: PDF for Rician random variable A with $\sigma^2 = 1$.

The right-tail probability can be shown to be related to that of the noncentral χ^2 random variable and must be evaluated numerically [Kay98, ch.2.2.7].

$$\begin{aligned} Pr\{A > \sqrt{\gamma'}\} =& Pr\left\{\sqrt{\frac{x_1^2 + x_2^2}{\sigma^2}} > \sqrt{\frac{\gamma'}{\sigma^2}}\right\} = Pr\left\{\frac{x_1^2 + x_2^2}{\sigma^2} > \frac{\gamma'}{\sigma^2}\right\} \\ =& \mathcal{Q}_{\chi_2'^2(\tau)}\left(\frac{\gamma'}{\sigma^2}\right), \\ \text{or} & \\ Pr\{A > \gamma\} =& \mathcal{Q}_{\chi_2'^2(\tau)}\left(\frac{\gamma^2}{\sigma^2}\right), \end{aligned} \tag{2.47}$$

where $\tau = (\mu_1^2 + \mu_2^2)/\sigma^2$. Appendix 2D in [Kay98] lists the MATLAB program *Qchipr2.m*. It determines the right-tail probability of a Rician random variable and was used to create theoretical estimates in Paper II.

2.11 Point Signal to Speckle Noise Ratio

As a measure of a point scatterer's intensity relative to the speckle background in Paper II, Paper IV, and Paper V, we calculate the point's SNR metric as

$$\text{point SNR} = 10 \log_{10} \left(\frac{i_p}{i_s} \right), \tag{2.48}$$

where i_p is the point scatterer intensity, and i_s is the average intensity of the speckle background without the point scatterer present.

2.12 Contrast Metrics

Claiming that one imaging method is better than another can be tricky. This thesis discusses how methods can be compared statistically. Contrast metrics are often used to describe the image quality. In Paper I, we discuss contrast metrics when benchmarking adaptive beamformers. In 1983, Smith et al. [Smi+83] developed a statistical model for image quality by connecting contrast and lesion detection. Lesion detectability using contrast is now well established in medical ultrasound [Dah+11; IH94; LPW04; Rod+20; SW84; Zem+05]. The most common contrast metrics are contrast ratio (CR) and contrast-to-noise ratio (CNR). CR is defined as [HTu+92]

$$\text{CR} = 20 \log_{10} \left(\frac{\mu_1}{\mu_2} \right), \tag{2.49}$$

where μ_1 and μ_2 are the mean intensity values of two speckle regions. It is often given in logarithmic dB-scale. CNR weights the intensity difference between the two regions with the average variance [PF83]

$$\text{CNR} = \frac{|\mu_1 - \mu_2|}{\sqrt{(\sigma_1^2 + \sigma_2^2)/2}}, \tag{2.50}$$

where μ_1 is the mean intensity value and σ_1^2 is the variance of region 1.

In [Rod+20], the generalized CNR metric (gCNR) is introduced. It is a contrast metric for lesion detectability that is resistant to dynamic range alterations. It can be used on all kinds of images, regardless of compression, scale, or output units [Rod+20].

2.13 Speckle Statistics of Adaptive Beamformers

Conventional DAS beamforming produces a speckle background with an amplitude Rayleigh distribution [Wag+83][Bur78] [OQ98, p. 88] [Kay98, p. 30]. The SNR ≈ 1.91 and the PDF is shown in Figure 2.16. Since speckle has a Rayleigh PDF in amplitude, the imaginary and real parts of the speckle signal have normal Gaussian distributions. The speckle pattern is considered well developed if the number of scatterers per resolution cell is larger than ten [Wag+83] [Rin19, ch. 2.9].

In Paper I, we show that certain adaptive beamformers alter the statistics of the speckle background. We simulated ultrasound image scenes with two speckle regions with 0 and −30 dB intensity. We created horizontal and vertical phantom orientations to see if the orientation of the boundary line had any influence on the results. Paper I presents figures of the measured PDFs of the seven beamformers for each speckle region. The SNR value for each beamformer indicates if there is a deviation from conventional DAS with SNR ≈ 1.91.

Table 2.1: Summary of findings on speckle statistics of adaptive beamformers

High intensity speckle region		Low intensity speckle region	
Rayleigh	Non-Rayleigh	Rayleigh	Non-Rayleigh
DAS, MV, EBMV and GCF	CF, PCF, and DMAS	DAS and MV	EBMV, CF, PCF, GCF and DMAS

Vertical boundary orientation	Horizontal boundary orientation
Speckle statistics for each region within the same image are similar.	EBMV, CF, GCF, PCF have increased variance for the low intensity region. DMAS has a deformed PDF with a 2nd peak at low intensity.

Table 2.1 summarizes the observed findings of how the adaptive beamformers alter the speckle statistics. The results show that the beamformers alter the statistics of the low and high intensity regions differently. The results also show that the beamformers alter the statistics of the two regions differently depending on the boundary orientation.

2.14 Speckle Reduction

Speckle reduction or noise suppression is often applied on medical ultrasound images to improve contrast [Sza14, ch. 8.4.6]. It can improve the contrast between grayscale tissue areas but simultaneously reduce the resolution of the point scatterer. In Paper II, we analyzed the effect of common denoising filters on the detection of point scatterers. We studied the following filters: Wiener [GW10, ch. 5.8], non-local means [BCM05], bilateral [TM98], anisotropic diffusion [PM90], and simple block averaging. Short descriptions of the different filters and the parameters we used can be found in Paper II.

Chapter 3

Detection of a Point Scatterer in Speckle

Detection of a point scatterer in speckle can be viewed as a classical binary detection problem [Abr19; EG05; Kay13; Kay98; Lev08]. This section presents the background theory for how we can measure and evaluate point detection performance in ultrasound images. In Paper II, we present an overview and framework for the detection of point scatterers in ultrasound images. In the paper, we discuss how to measure detection performance and calculate confidence intervals. The detection strategy and methodology presented in Paper II is relevant for Paper IV and Paper V. I therefore include the relevant background material in this section and reuse some of the formulations from Paper II.

3.1 Binary Detection Problem and the Likelihood Ratio Test

The objective is to decide between two possible scenarios; speckle background with or without a point signal present. We apply a binary hypothesis test to decide if I have speckle (hypothesis $\mathcal{H}_0$) or signal + speckle (hypothesis $\mathcal{H}_1$) [TRL15].

$$\begin{cases} \mathcal{H}_0: & \xi = \xi_w \\ \mathcal{H}_1: & \xi = \xi_a + \xi_w. \end{cases} \tag{3.1}$$

where ξ is the received signal, ξ_w is the signal from the speckle background, and ξ_a is the signal from the point scatterer.

The Neyman-Pearson theorem states that the probability of detection (P_{D}) is maximized for a given probability of false alarm (P_{FA}) by using the Likelihood Ratio Test (LRT) [Kay98, ch. 3.3]

$$L(t) = \frac{p(\xi; \mathcal{H}_1)}{p(\xi; \mathcal{H}_0)} > \gamma, \tag{3.2}$$

where p is the PDF for observation ξ for the test case with or without a signal present. The threshold γ can be found by integrating the PDF of hypothesis $\mathcal{H}_0$ to the chosen P_{FA} value [Kay98, p. 30]

$$P_{\mathrm{FA}} = \int_{\gamma}^{\infty} p(\xi; \mathcal{H}_0) d\xi. \tag{3.3}$$

The proof can be found in [Kay98, App. 3A]. The LRT is the optimal detector for a known signal in noise when the PDFs of both hypothesis are known. However, in our case we wish to detect a signal with unknown amplitude, phase and position in speckle background of unknown level. We can assume the shape of the PDFs to be known, but with unknown parameters. The generalized likelihood ratio test (GLRT) replaces the unknown parameters by their maximum likelihood estimates (MLEs) before performing hypothesis testing as in (7.7) [Kay98, ch. 6]. We will return to GLRT in Chapter 7.

To illustrate the detection theory, we consider ideal one-dimensional (1-D) sequences of a point scatterer with a random position in speckle. The speckle sequence is constructed as a complex sum of two normally distributed sequences. We add a point scatterer to the sequence with a chosen point SNR value and test many different point positions. As discussed in Paper II, the probability distribution of an ideal point in additive white Gaussian noise in complex sequences is statistically equivalent to an ideal point in a critically sampled, fully developed speckle scene. We estimate expressions for the detection probabilities using the ideal 1-D case. In the 1-D study, the mean speckle background intensity $i_s = 2$ as we set the scale parameter to $\sigma^2 = 1$.

The P_{FA} is estimated on images containing only speckle, while P_{D} is estimated on images containing one point scatter in speckle. To get P_{FA} and P_{D}, we count the number of detections and false alarms above a certain threshold γ. We get the final probabilities by comparing the respective numbers to the total number of realizations.

3.2 Probability of False Alarm

We return to the probability distributions presented in Section 2.10.1 and Section 2.10.2 and borrow some text from Paper II. The PDF for speckle in an ultrasound image is Rayleigh distributed in amplitude A [Bur78] [OQ98, p. 88] [Kay98, p. 30]. When presented with an ultrasound image, we assume that the most likely point target candidate is the point scatterer with the highest intensity. To find point target candidates, we apply a threshold on the intensity image [OQ98, ch. 10]. Intensity $i = A^2$ has a negative exponential PDF [Abr19, p. 261] [OQ98, p. 88][Cob07, p. 502]. The expression for P_{FA} is thus given by (2.45), with γ as the intensity threshold and β as the mean speckle intensity value $i_s = \beta$.

In Paper II, we suggest using the detection strategy that selects the maximum value within a search window for both false alarms and detections. Figure 3.1 from Paper II presents the theoretical $P_{\text{FA}}(\gamma)_{\max}$ for a speckle sequence of varying length or window size. Since we pick the maximum within the window, the number of false alarms increases with increasing window size.

> The maximum value of speckle increases with the number of independent pixels N considered. This increases or inflates the P_{FA} for a given threshold. Following [EG05, ch. 2.11], the probability is such that $Pr\{i_{\max} \leq \gamma\} = (Pr\{i \leq \gamma\})^N$. The P_{FA} for the maximum of N random independent variables then becomes [EG05, ch. 2.11], [Kay98, p. 283], [Abr19, p. 587]
>
> $$P_{\text{FA}}(\gamma)_{\max} = 1-(1-P_{\text{FA}}(\gamma))^N = 1-(1-\exp(-\gamma/\beta))^N. \tag{3.4}$$
>
> *Paper II*, slightly altered

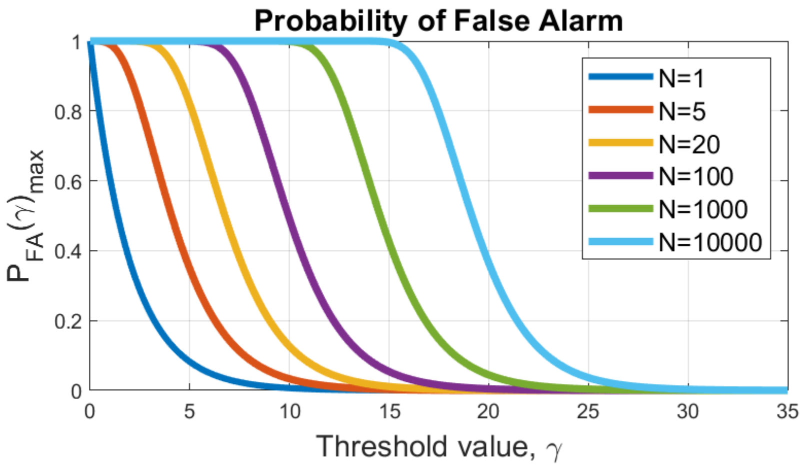

Figure 3.1: Theoretical $P_{\mathrm{FA}}(\gamma)_{\max}$ for a speckle sequence of varying length versus threshold values. The maximum value of a speckle sequence increases with sequence length. The theoretical mean value β is 2 since the scale parameter is set to $\sigma^2 = 1$. Figure borrowed from Paper II.

3.3 Probability of Detection

When a signal from a point scatterer is added to a speckle background, we get the Rician PDF presented in (2.46) [Kay98, p. 31], [OQ98, p. 113].

> The theoretical P_{D} for threshold γ can be estimated as [Kay98, p. 283]
>
> $$P_{\mathrm{D}}(\gamma) \approx \mathcal{Q}_{\chi_2'^2(\tau)}\left(\frac{2\gamma}{\beta}\right), \tag{3.5}$$
>
> where $\mathcal{Q}_{\chi_2'^2(\tau)}$ is the right-tail probability or complementary cumulative distribution function related to a noncentral χ^2 variable. It must be evaluated numerically [Kay98, App. 2-D] [Kay13, ch. 6.4]. P_{D} is estimated using $\tau = \frac{2i_p}{\beta}$, and it is therefore dependent on point SNR. By combining (2.45) with (3.5), P_{D} can be expressed in terms of P_{FA} as
>
> $$P_{\mathrm{D}}(\gamma) \approx \mathcal{Q}_{\chi_2'^2(\tau)}\left(2\ln\frac{1}{P_{\mathrm{FA}}(\gamma)}\right). \tag{3.6}$$
>
> *Paper II*, slightly altered

In [Kay98, App. 2-D], Steven Kay presents a program to compute the right-tail probability of a central or noncentral chi-squared PDF. The MATLAB function *Qchipr2.m* computes $\mathcal{Q}_{\chi_\nu'^2(\tau)}$, and inserting $\nu = 2$ gives the numerical estimate needed in 3.6. In [Kay98, ch.7.8], Kay derives the theoretical expressions for P_{D} and P_{FA} for active sonar/radar detection using the GLRT for the detection of a sinusoid of unknown amplitude, phase, frequency, and time of arrival in white Gaussian noise. Kay finds that the optimal detector evaluates the Fourier transform of the sequence and finds the maximum frequency bin. ”In essence we "pick the peak" of the spectrogram and compare it to a threshold” [Kay98, p.280]. Picking the maximum frequency bin is similar to picking the maximum intensity value in an image as the most likely point candidate.

We wish to pick the maximum within the search window for both false alarms and true positives. We therefore combine (3.4) with (3.5) to get P_{D} given by $P_{\mathrm{FA}}(\gamma)_{\max}$ as

$$P_{\mathrm{D}}(\gamma) \approx \mathcal{Q}_{\chi_2'^2(\tau)}\left(-2\ln\left(1-(1-P_{\mathrm{FA}}(\gamma)_{\max})^{\frac{1}{N}}\right)\right). \tag{3.7}$$

Finally, the P_{D} of the maximum value can be found as [Abr19, p. 588]

$$P_{\mathrm{D}}(\gamma)_{\max} = 1-(1-P_{\mathrm{D}}(\gamma))(1-P_{\mathrm{FA}}(\gamma)_{\max})^{\left(1-\frac{1}{N}\right)}. \tag{3.8}$$

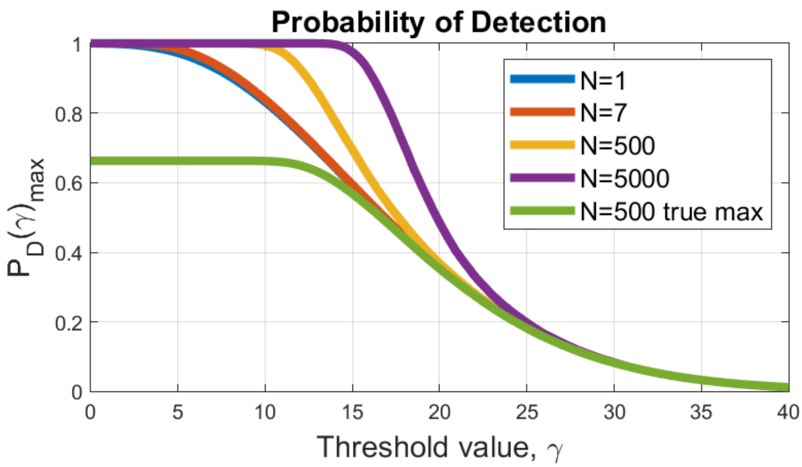

Figure 3.2: Theoretical $P_{\mathrm{D}}(\gamma)_{\max}$ vs. threshold values and varying sequence length. Point SNR is 12 dB. The mean speckle intensity value $\beta = 2$. $P_{\mathrm{D}}(\gamma)_{\max}$ finds the maximum intensity point within the sequence. $N = 1$ signifies P_{D} calculated using known true point position only, $N = 7$ corresponds to a ± 3 pixel search window, and $N = 500$ signifies picking the maximum out of 500 pixels. $P_{\mathrm{D}}(\gamma)_{\text{true max}}$ additionally checks if the found maximum has correct position, and for weak point scatterers it will not converge to 1. Figure borrowed from Paper II.

3.4 Evaluation of Detection Performance

3.4.1 Receiver Operating Characteristics (ROC) and Area Under the Curve (AUC)

A Receiver Operating Characteristics (ROC) curve displays detection performance. The ROC curve compares P_{D} to P_{FA} for a given threshold γ. If we increase γ, we lower P_{FA}, but then P_{D} will also decrease. All points on the ROC curve should satisfy $P_{\mathrm{D}} \geq P_{\mathrm{FA}}$ [Lev08, ch. 2.4.2] [Kay98, p. 74]. We present the detection performance of methods using ROC curves in Paper II, Paper IV, and Paper V. Since high P_{FA} values is not of much practical interest, we show the ROC curves for P_{FA} values up to 0.1

We also present detection performance results by tabulating Area Under the Curve (AUC) [Abr19, p. 315] values. AUC for a diagonal line with $P_{\mathrm{D}} = P_{\mathrm{FA}}$ is 0.5. We also tabulate P_{D} for a chosen P_{FA} value, which is another way to compare detection performance [Kay13, ch. 7.3.2]. When testing the detection performance of different methods, the SNR-range where P_{D} varies greatly is the most interesting to analyze. In Figure 3.3 from Paper II, we see that measured P_{D} values vary the most in the SNR-range of $[8, 14]$ dB.

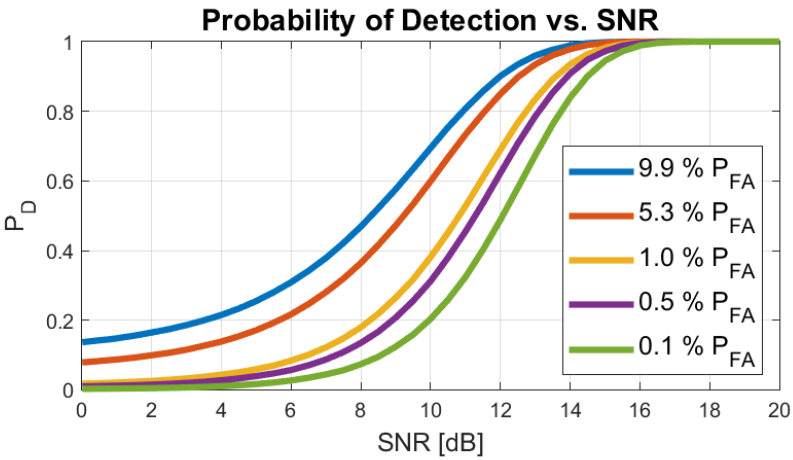

Figure 3.3: The P_{D} increases with point SNR. P_{D} is shown for five P_{FA} values. Figure borrowed from Paper II.

3.4.2 Number of Required Realizations and Confidence Interval for the AUC

The number of realizations R affect the accuracy of the measured results [Kay98, p. 37]. In Paper II, we discuss how to plot confidence intervals for the ROC curves, and how to compute confidence intervals for the AUC.

> If the true probability is small, for example $P_{\mathrm{FA}} = 0.1\%$, only one in a thousand realizations is expected to exceed the threshold. In such a case, R must be much larger than a thousand to ensure an accurate probability estimate. As presented in [Kay98, p. 37], if we wish to have a relative absolute error ϵ for probability P for $100(1-b)\%$ of the time, then the required number of realizations R_{req} is
>
> $$R_{req} \geq \frac{(\mathcal{Q}^{-1}(b/2))^2\ (1-P)}{\epsilon^2 P}. \tag{3.9}$$

Here $\mathcal{Q}^{-1}(b/2)$ is the inverse right-tail probability function of a standard normal distribution evaluated at $b/2$. For very small values such as $P_{\text{FA}} = 10^{-3}$, a 10% relative accuracy for 80% of the time requires $R = 164070$ and it can be difficult or impractical to get enough data. On the other hand, if we wish to analyze a probability of $P = 0.05$ for 80% of the time and have $R = 6500$, we get an error of $\epsilon = 7\%$. Confidence intervals for the ROC curve can be plotted by calculating the relative error for both P_{FA} and P_{D} at each threshold value using (3.9). The coefficient of variation of the estimated probability P, i.e. the ratio of the standard deviation (STD) to the mean of the estimate, is a similar quantity used to express R_{req} [Abr19, p. 314].

As presented by Hanley and McNeil [HM82], we can compute the confidence interval for the AUC. For large samples, the distribution of AUC is approximately normal. A $100(1-b)\%$ confidence interval for sample AUC-value θ may be computed using the standard error (SE) as follows

$$\theta \quad \pm \quad \mathcal{Q}^{-1}(b/2)\ \text{SE}(\theta), \tag{3.10}$$

where

$$\text{SE}(\theta) = \sqrt{\frac{\theta(1-\theta) + (R_p-1)(Q_1-\theta^2) + (R_s-1)(Q_2-\theta^2)}{R_s R_p}}.$$

It is worth noting that $\text{SE}(\theta)$ is inversely proportional to $\sqrt{R}$. Quadrupling R only reduces $\text{SE}(\theta)$ by a factor of two. $\text{SE}(\theta)$ is small for high θ values close to 1. The number of realizations with and without a point scatterer present is R_p and R_s respectively. Q_1 and Q_2 are distribution-specific quantities expressed as functions of θ and give a conservative estimate of $\text{SE}(\theta)$ [HM82].

$$Q_1 = \frac{\theta}{2-\theta}\,, \qquad Q_2 = \frac{2\theta^2}{1+\theta}. \tag{3.11}$$

Paper II

3.4.3 Choice of Point Target Detection Strategy

In Paper II, we discuss the pros and cons of five different detection strategies (A-E). Figure 3.4 presents theoretical ROC curves for the five strategies. The strategies were applied to a random vector of length 500 with a randomly positioned point scatterer with 12 dB SNR.

As discussed in Paper II, strategy C resembles a realistic, practical approach the most and gives valid ROC curves. We chose to use this strategy for the detection studies in Paper II, Paper IV, and Paper V. The strategy evaluates a search window around the known point location and picks the maximum value for both false alarm and detection. Figure 3.2 shows how P_{D} for a small search window only slightly deviates from P_{D} at the known point position. Strategy C applied a ± 3 pixel search window for the 1-D study, corresponding to $N = 7$ independent pixels. Increasing the number of pixels in the search window inflates P_{FA}, as shown in Figure 3.1. However, with a search window we can evaluate how a method affects the speckle background

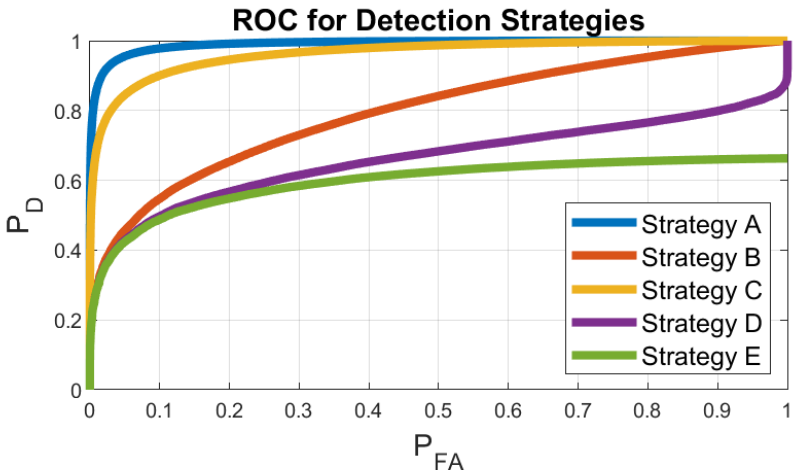

Figure 3.4: ROC curves for the different strategies for calculating point detection performance. Figure borrowed from Paper II.

and corresponding false alarms. In the 2-D study, the size of the search window was twice the −6 dB spatial resolution for the original DAS image. As discussed in Paper II, the probability of detecting the true point target as the maximum is high within such a small window. A window also counteracts the possible slight shift in pixel location caused scalloping loss or other imaging effects. The chosen size affects the possible separability of detected point scatterers.

3.5 Practical Detection Performance in Ultrasound Images

In Paper II, we list several factors in practical ultrasound imaging that affect the detection probabilities. The publication evaluates how common imaging techniques affect the detection performance of point scatterers.

> The theoretical formulae for detection performance in this section are for ideal signals in additive white Gaussian noise in complex sequences. This is statistically equivalent to ideal points in fully developed speckle. In practical ultrasound imaging, there are several factors that potentially affect detection:
>
> - Additive noise on channel data. The effect of noise causes the SNR to vary with depth.
> - Finite probe size causes targets positioned far off-center not to be as well represented as centered point targets.
> - The spatial resolution is determined by the aperture size and transmitted pulse bandwidth. It typically varies for depth and angle, and oversampling is common.

- Scalloping loss can cause a reduction in amplitude and leakage in energy to nearby pixels.
- Apodization changes resolution and reduces side lobes.
- Speckle reduction methods are often applied on ultrasound images and alter the statistics.
- Advanced beamforming methods alter both the speckle statistics [Hve+17] and the point-plus-speckle statistics.

Paper II, slightly altered

3.6 Numerical Experiments to Measure Point Detection

In Paper II ,Paper IV, and Paper V, we use many simulated images to experimentally measure the detection performance. The flow chart below summarizes the applied methodology in the papers. The approach is to measure the detection performance independent of knowledge of the PDFs to directly compare how they affect the point detectability. Applying a search window lets us evaluate and compare how the imaging method affects the speckle background and corresponding false alarms.

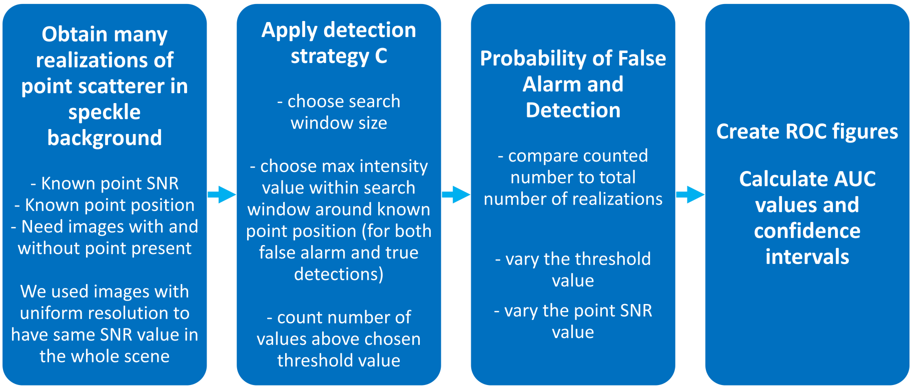

Figure 3.5: The flow chart of the applied detection methodology in this thesis.

The goal of the detection study is distinct from imaging. The results are not intended for visual assessment but rather to determine and evaluate the statistical detection performance of the suggested method. We need full-scale Monte Carlo simulations to get statistical results. To sufficiently evaluate the suggested method in Paper IV and Paper V, we create and analyze 28431 realizations for P_D and P_{FA} calculation. Since we require many images with specific point SNR and known point location, we need to use simulations. Fortunately, the Field II software beamformer produces ultrasound images with representative characteristics.

Chapter 4

The Wavelet Coefficient Shrinkage Method

The wavelet coefficient shrinkage method was used to find buried mines and large boulders on the seabed using sonar in [HV14]. On a sonar image, the mines appear as tiny dots on a sizeable speckled background of the seabed. In Paper III, we investigated if the method could be applied to ultrasound images to enhance point scatterers and suppress speckle background. This chapter presents the proposed algorithm in Paper III that uses shrinkage of incoherent wavelet coefficients. We categorize the algorithm into five steps. Figure 4.1 shows a flowchart of the algorithm.

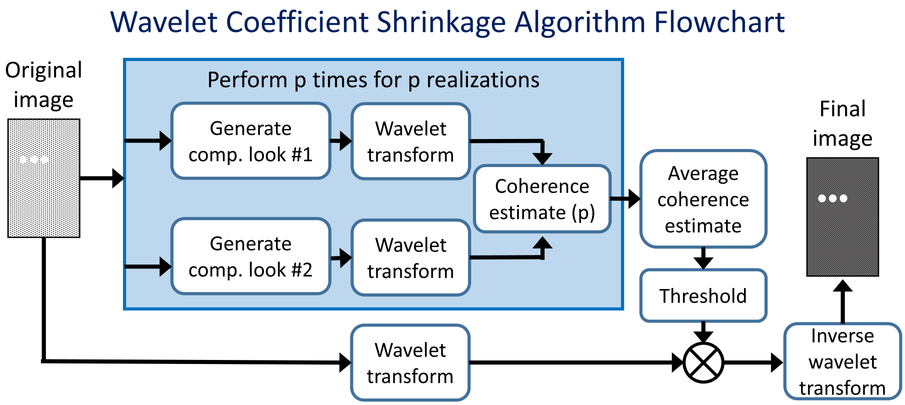

Figure 4.1: Flowchart of the wavelet coefficient shrinkage algorithm in Paper III. We first create two complementary looks and subsequently decompose them into wavelet coefficients. The algorithm then estimates the coherence between the wavelet transforms. An average estimate of the coherence is found by averaging p realizations. This estimate is further thresholded before multiplication with the wavelet transform of the original image. The final image is created after applying the inverse wavelet transform.

4.1 Step 1: Create complementary looks

The algorithm starts by partitioning the image's frequency spectrum to create *looks*. It creates two complementary random block grids to create a pair of looks. The following steps summarize the method:

- Take the 2-D Fourier transform of the image

- Create a random 2-D block grid and its inverse block grid.
- Multiply the Fourier image with each block grid.
- Take the inverse Fourier transform and end up with two images or looks.

The idea is that point scatterers are spread over all frequencies so that the points will be persistent in both looks. On the other hand, Speckle has ideally low coherence or similarity between the looks. The blocks in the 2-D grid are randomly assigned to either of the two sets, see Figure 4.2. We chose the size of the blocks so that we preserve the point target information over several blocks, whereas the speckle background is correlated on a much smaller scale than the block size [HV14]. The method is illustrated in Figure 4.3. It shows an example of the partitioning of the frequency spectrum due to multiplication with a block grid pair. Figure 4.4 shows the complementary looks of an actual ultrasound image.

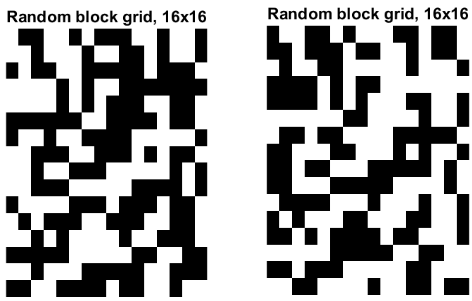

Figure 4.2: Two complementary random block grids.

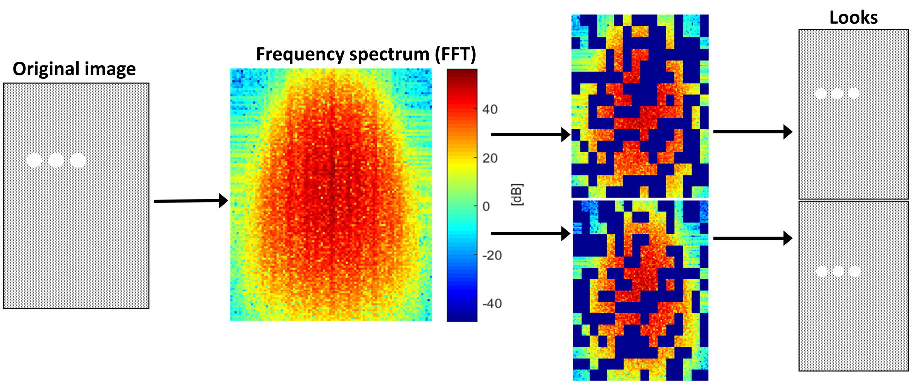

Figure 4.3: We create the complementary looks by first applying a 2-D Fourier transform to the original image. We then multiply the frequency spectrum with each of the 2-D random block grids. Applying the inverse Fourier transform again produces complementary looks.

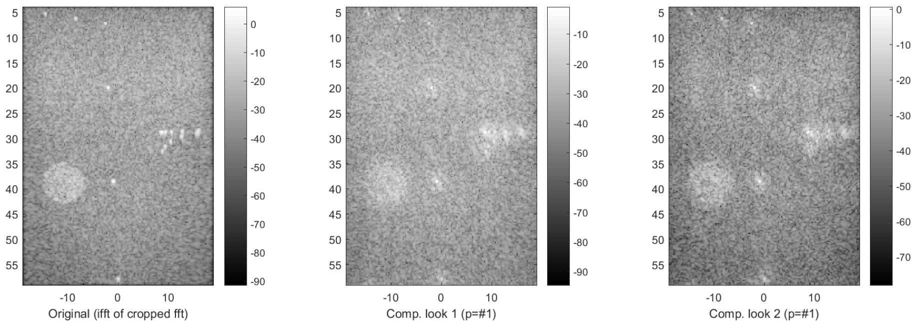

Figure 4.4: An example of two complementary looks. The original image is of a tissue-mimicking phantom and includes a cyst and several point scatterers. The image quality of the looks is degraded compared to the original image, but the point scatterers are included in both looks.

4.2 Step 2: Wavelet transform of looks

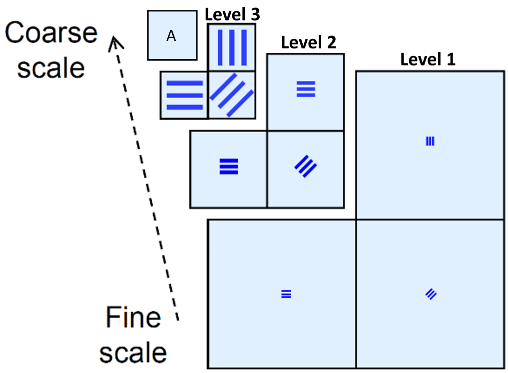

Figure 4.5: Illustration of the 2-D discrete wavelet transform. It decomposes an image into four coefficient images per decomposition level. The algorithm divides the image into high and low frequency bands. The algorithm also downsamples in horizontal and vertical directions to extend the wavelet transform to 2-D. The output is three detail images sensitive to vertical, horizontal, and diagonal frequencies. The low-pass filtered band is further downsampled to produce the three detail images of the next scale level.

Wavelet analysis can be used to compress or denoise an image while preserving the resolution. This is why standard image compression methods such as JPEG use wavelets. The target information can be described using a few wavelet coefficients, whereas noise is more evenly distributed [HV14]. Fourier analysis divides a signal into sine waves of various frequencies. A wavelet is a wave-like oscillation localized in time. Wavelet analysis divides a signal into shifted and scaled versions of the mother wavelet. In Paper III, we performed the multilevel 2-D wavelet decomposition using a symmetric biorthogonal wavelet base. We used the built-in functions *wavedec2* and *waverec2* in MATLAB with the bior mother wavelet. The scale defines how stretched or squished the wavelet is.

The wavelet transform decomposes an image into high and low frequencies *and* scale. The scale corresponds to the number of levels in the transform. The algorithm also downsamples the input in horizontal and vertical directions to extend the wavelet transform to 2-D. We create three detail images from the high-pass filtered image where each image describes local directional changes in the image. The output is denoted as the high-high (HH), high-low (HL), and low-high (LH) bands. The LH, HL, and HH bands are sensitive to vertical, horizontal, and diagonal frequencies at each scale. The low-pass filtered image is further downscaled and yields what is known as an approximation image. We can further high-pass filter the approximation image to produce the three smaller detail images of the next level. Figure 4.5 illustrates the process.

4.3 Step 3: Estimate coherence between looks

We estimate the coherence between the complementary looks while in the wavelet domain. We present the formula as presented in Paper III.

> The coherence between two looks is estimated as:
>
> $$\mathrm{C}(x,y,l,p) = \left| \frac{\sum_{m,n=-\frac{N-1}{2}}^{\frac{N-1}{2}} \mathrm{W}_1\mathrm{W}_2^*}{\sqrt{\sum_{m,n=-\frac{N-1}{2}}^{\frac{N-1}{2}} |\mathrm{W}_1|^2}\sqrt{\sum_{m,n=-\frac{N-1}{2}}^{\frac{N-1}{2}} |\mathrm{W}_2|^2}} \right|$$
>
> $$\text{given } \mathrm{W}_i = \mathrm{W}_i(x+m\Delta x, y+n\Delta y, l, p) \tag{4.1}$$
>
> where (x,y) is the pixel location in the wavelet transformed image, l is the decomposition level, p is the realization number, and Δx and Δy are the pixel dimensions. W_i is the wavelet transform of complementary look i and W_i^* denotes its conjugate. NxN is the sliding window size over which the coherence for pixel location (x,y) is calculated. A hanning window with $N = 5$ was used. A large window size will reduce variance, but also reduce spatial resolution. The average coherence estimate for each level l is obtained by averaging the coherence estimate between two looks over all P realizations.
>
> $$\mathrm{C}_{\mathrm{av}}(x,y,l) = \frac{1}{P}\sum_{p=1}^{P} |\mathrm{C}(x,y,l,p)| \tag{4.2}$$
>
> *Paper III*

Figure 4.6 shows an example of the calculated average coherence estimate for each decomposition level. Notice how the method encircles the boundaries of the cyst and the point scatterers.

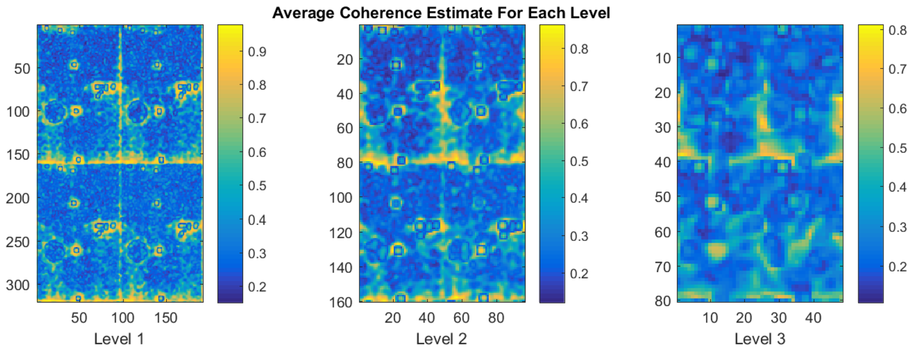

Figure 4.6: The average coherence estimate for three decomposition levels. The original image is of a tissue-mimicking phantom and includes a cyst and several point scatterers.

4.4 Step 4: Apply shrinkage to incoherent wavelet coefficients

The next step is to apply shrinkage to the incoherent wavelet coefficients of the average coherence estimate. We apply a simple weighting scheme where we completely suppress coefficients with values less than t_{min} and retain values greater than t_{max}. We apply a linear transition for values in between these threshold limits.

$$\mathrm{C}_{\text{th}}(x,y,l) = \begin{cases} 1, & \text{if } C_{\text{av}}(x,y,l) > t_{\text{max}} \\ 0, & \text{if } C_{\text{av}}(x,y,l) < t_{\text{min}} \\ \frac{\mathrm{C}_{\text{av}}(x,y,l)-t_{\text{min}}}{t_{\text{max}}-t_{\text{min}}}, & \text{otherwise} \end{cases} \tag{4.3}$$

Paper III

4.5 Step 5: Apply shrinkage to the wavelet transform of the original image

We now obtain the wavelet coefficient images of the original image. We multiply the thresholded coefficients after (4.3) with the wavelet coefficients of the original image. The inverse wavelet transform of these coefficients yields the final image.

4.6 Evaluation Criteria

We used the metrics conspicuity (Cp) and Peak$_{\text{point}}$-to-Peak$_{\text{speckle}}$ ratio (PP) in Paper III.

Cp is a measure of how clearly discernible a point is from the background at same depth and it is defined as [Dah+11]:

$$\text{Conspicuity} = \frac{\max_{\text{point}} - \mu_{\text{speckle}}}{\sigma_{\text{speckle}}}. \tag{4.4}$$

PP measures the intensity difference between the point scatterers and peaks in the speckle background:

$$\text{PP} = 20\log_{10}\left(\frac{\max_{\text{point}}}{\max_{\text{speckle}}}\right) \tag{4.5}$$

where $\max_{\text{point}}$ and $\max_{\text{speckle}}$ are the maximum intensity values.

Paper III

4.7 Additional steps for a 3-D image

In addition to the work presented in Paper III, I performed a preliminary study of the wavelet shrinkage method applied to 3-D images. If we have a 3-D image, we can exploit all three orthogonal directions to reduce the number of false alarms. When we have a 3-D input image, we perform steps 1-5 for each orthogonal direction. We then obtain three new 3-D data images from the azimuth, elevation, and depth direction run-throughs. We further calculate the coherence between these three direction estimates. Finally, we combine all three direction estimates and retain only the locations with high coherence values. Points present in all three direction estimates are more likely to be true point targets. The method suppresses point scatterer candidates and speckle points not present in all three directions.

Figure 4.7 shows an example of the process applied on a 3-D image of a breast phantom. It is difficult to ascertain which of the intensity peaks in the image are true microcalcifications (MCs). I tested the 3-D wavelet coefficient shrinkage method on such images. Figure 4.7 shows how we can drastically reduce the number of point target candidates if we exploit all three directions.

Figure 4.8 shows the original image together with the final wavelet shrunk image. The wavelet shrunk image determines probable locations of microcalcifications. For the image example in Figure 4.8, the method reduced the number of candidates from an average of 18 when using only one of the direction estimates to the final three candidates.

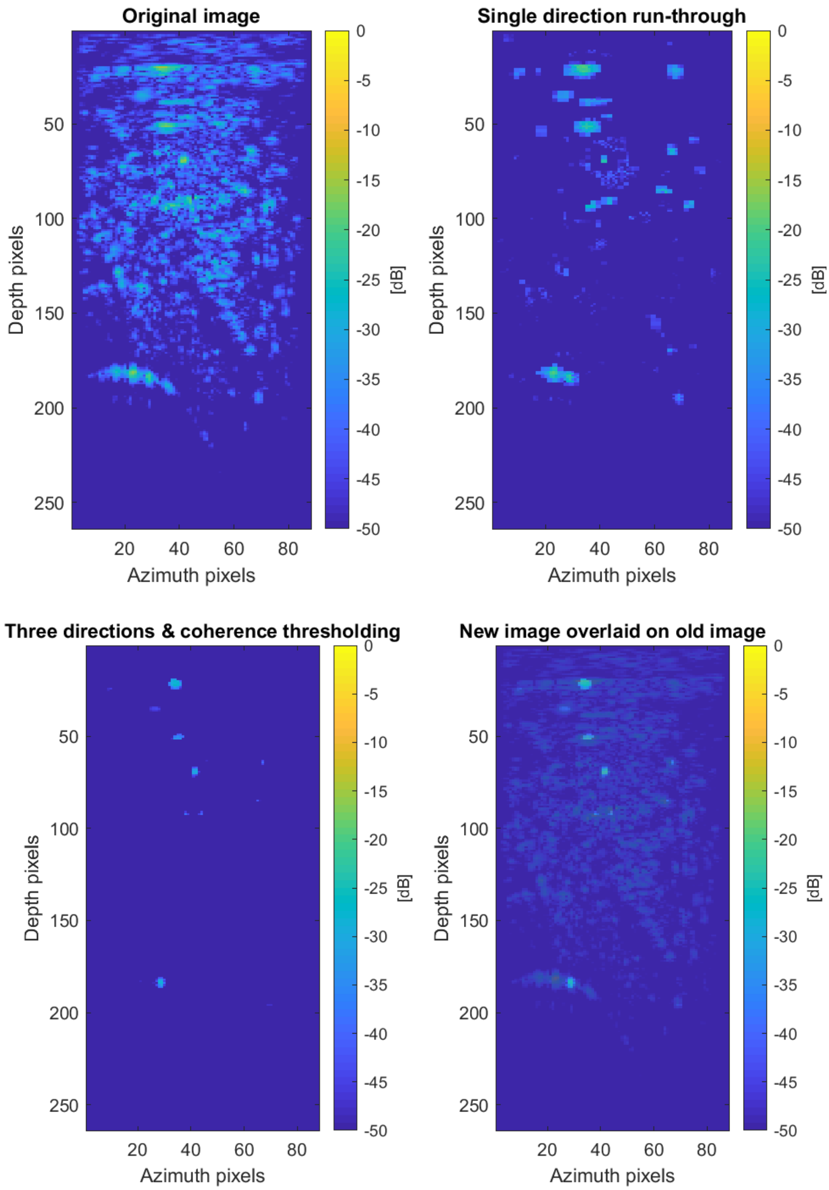

Figure 4.7: We create three direction estimates from a 3-D image of a breast phantom (top left). The image in the top right shows the image after a single direction run-through. The image to the bottom left is the result after running through all three directions and thresholding the coherence between the direction estimates. We drastically reduce the number of probable point targets by exploiting all three directions. The final image to the bottom right overlays the new wavelet shrunk image atop the original image to highlight the probable point targets. All images are shown in 2-D in a radial depth versus azimuth pixel plane. The images are all normalized by the maximum value to be comparable.

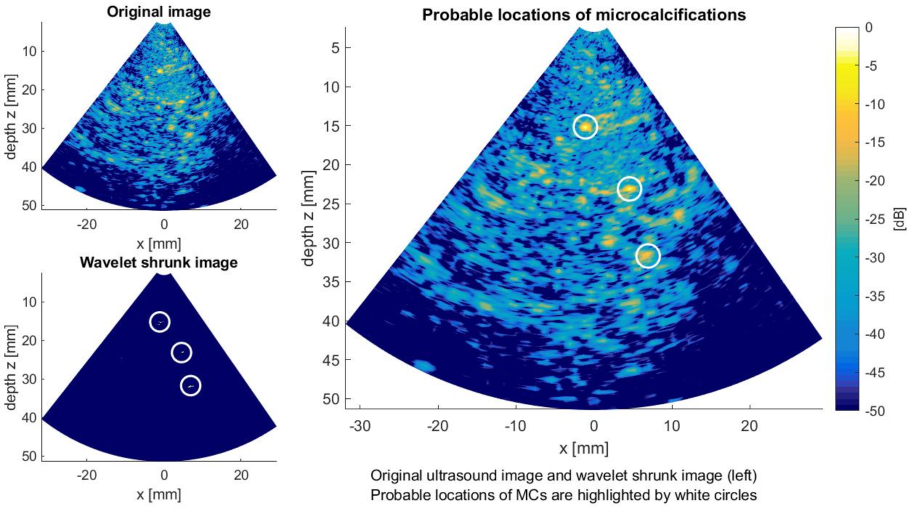

Figure 4.8: The original image of a breast phantom is shown together with the final wavelet shrunk image. The 3-D images are shown in a 2-D plane in cartesian coordinates. The wavelet shrinkage method reduces the number of probable microcalcifications. The image to the right shows the original image with small white circles indicating the probable locations.

Chapter 5

The Whitening Transform

A *whitening transform* converts a set of random variables having a known covariance matrix into a set of new random variables whose covariance is the identity matrix [Kel86; KK99; KLS18]. The transformation is called *whitening* because it changes the input vector into white noise. To obtain a whitening transform, we can estimate a smoothed average of the spatial frequency spectrum. We can calculate the estimate by applying an adaptive method or using secondary data. By applying the inverse of this estimate to the image's frequency spectrum, we boost the frequency amplitudes to the same average level. Regarding the methods presented in Chapter 7, we can also incorporate the whitening transform into the covariance matrix calculation [Kel86].

5.1 Prewhitening a 1-D Sequence

To study the effect of prewhitening on point detection in Paper IV, we started with ideal 1-D sequences of a point scatterer with a random position in speckle. Figure 5.1 shows the magnitude of the frequency response of such a sequence. The speckle vector in Figure 5.1 is oversampled by a factor of three. Its frequency spectrum has a similar shape to the spectrum of an oversampled, basebanded ultrasound signal in one direction.

To obtain a whitening filter, we first calculate a smoothed average of the magnitude of the 2-D Fourier transform of the speckle vector. We can calculate the average for all the complex speckle vectors if we have secondary data. In Paper IV, we used the magnitude of the 2-D Fourier transform, but we could have used the magnitude of the frequency power spectrum. The output is an estimate with real values, and the whitening filter is the inverse of this estimate. We set the whitening filter to zero outside the valid frequencies and smoothen the cutoffs slightly to reduce edge effects. The frequencies after whitening have the same mean amplitude level, but the transform retains the randomness. In this thesis, we call the resulting sequence in the image domain a *whitened* or *prewhitened* sequence.

Figure 5.2 shows the significant improvement in ROC by applying an optimized prewhitening of the data. The detection improvement depends on the signal spectrum and the noise spectrum. We use a priori knowledge of the spectrum shape to set the whitening filter limits. The sequences in the 1-D study are oversampled by a factor of three, and we accordingly set the whitening limits. However, the optimal limits depend on where we have both large bandwidth and positive point SNR. The shape of the frequency spectrum for a near-field, broadband signal will not have an ideal rectangular shape with clear cutoff limits between the signal and noise. The optimal cutoff limits, therefore, depend on the additive noise level. For high point SNR values, the optimal whitening limits are governed by the known oversampling as given in Figure 5.1. For weak point scatterers, the optimal wavenumber coverage of the whitening filter

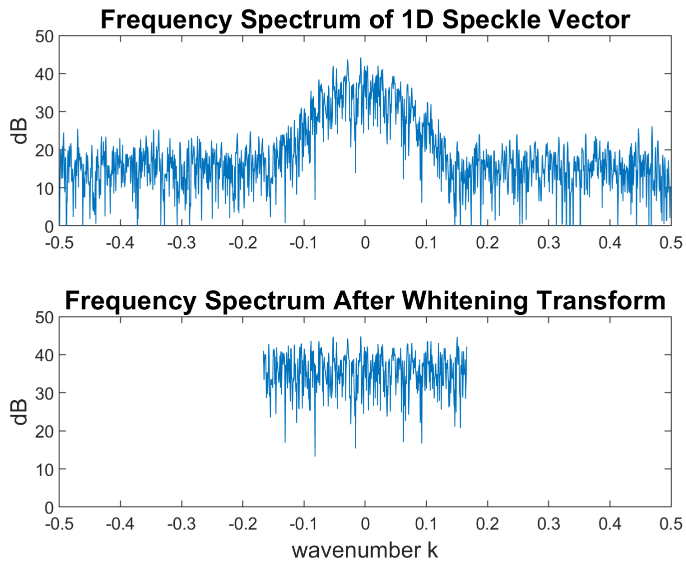

Figure 5.1: The spatial frequency spectrum of a bandpass filtered, oversampled 1-D speckle sequence with some added noise. The same spectrum is also shown after applying an optimized whitening transform, and the transform only retains and enhances the valid frequencies. Figure borrowed from Paper IV.

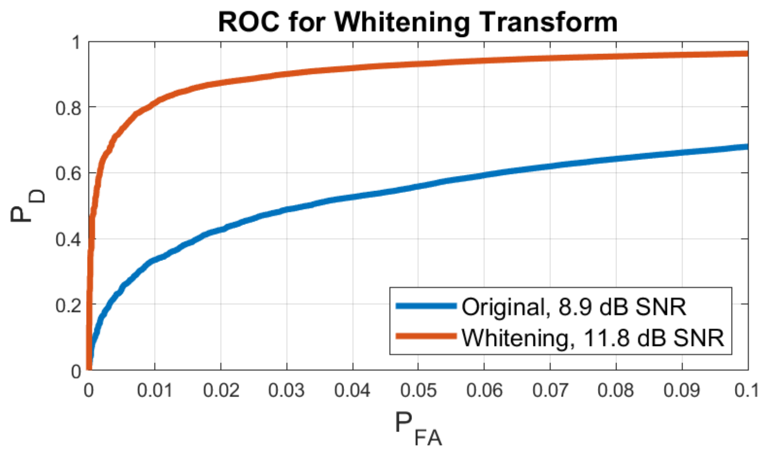

Figure 5.2: ROC for prewhitening applied on the 1-D sequences before point detection. Applying an optimized whitening increases the measured point SNR.

shrinks. The whitening filter that optimizes detection performance thus depends on both image resolution and point SNR since the spectrum is nonuniform. We discuss how P_{D} is proportional to *both* bandwidth B and point SNR in Paper IV.

5.2 2-D Whitening Limits

In the 2-D detection study in Paper IV, we applied the same whitening transform to all the DAS images. We estimated a smoothed average of the magnitude of the 2-D Fourier transform using all of the complex speckle images. We tapered the inverse estimate with a small Gaussian filter to reduce edge effects. As presented in Section 2.5, the limits for the spatial frequencies are defined by the critical angle α and the pulse bandwidth.

Figure 5.3 from Paper IV compares the ROC curves for the original and optimal α-whitened images for two different point SNR values. The results in Paper IV show that an optimized prewhitening can drastically increase the point SNR, as shown by the measured point SNR values in the legend. The ROC results in Figure 5.3 show that prewhitening the images has a *significantly* positive effect on point detection.

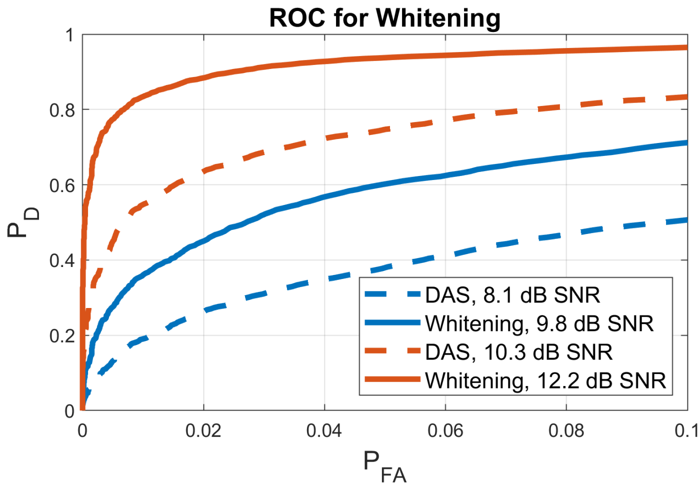

Figure 5.3: ROC curves for two point SNR values with or without α-whitening the 2-D ultrasound images before detection analysis. Figure borrowed from Paper IV.

Paper IV also studied suboptimal whitening limits by increasing or decreasing the applied critical angle or frequency bandwidth. The optimal whitening limits depend on the image resolution and the point SNR. Figure 5.4 illustrates the different whitening filter limits analyzed in Paper IV. Narrowing the limits can be beneficial in the presence of noisy backgrounds and weak point scatterers since we then suppress spatial frequency regions with low SNR values.

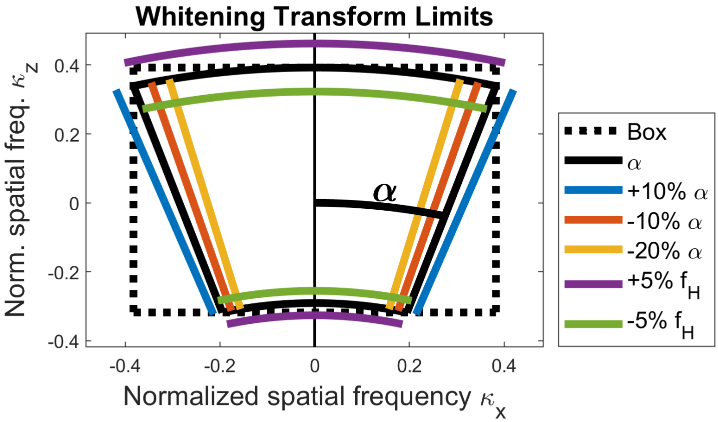

Figure 5.4: Illustration of seven whitening filter limits defined by the critical angle α and the pulse bandwidth. $+5\%$ f_H corresponds to a 5% increase in the maximum bandwidth limit f_H and -5% in the minimum bandwidth limit f_L. Figure borrowed from Paper IV.

Chapter 6

Texture Correction

Since ultrasound images typically include varying echo intensities in the tissue speckle, it is important to study nonuniform backgrounds when testing a method's point detection performance. Living tissue is full of movement and structure and is nonlinear both elastically and dynamically [Sza14, ch. 9.1]. An *inhomogenous* texture has predominantly the same type of tissue with small fluctuations about a mean value, while a region enclosing a group of contiguous regions with different characteristics is called *heterogeneous* [Sza14, ch. 9.2]. Transitions between interfaces or lines caused by anisotropic muscle fibers can create edges in an ultrasound image, making it more difficult to discern small point scatterers. A point scatterer detector, therefore, needs to handle nonuniform backgrounds. In Paper V, we created textured ultrasound images and applied texture correction prior to point detection performance.

6.1 Creating Textured Backgrounds

In Paper V, we model the tissue backgrounds with random texture fluctuations of a specific scale. The size of the texture was substantially larger than a point scatterer but much smaller than the image scene. We chose to model random Gaussian variations in an image scene, providing relevant texture fluctuations for an inhomogenous ultrasound background. We combined the DAS images with the random texture maps to simulate varying texture backgrounds. With such a method, the point scatterer retains its point SNR value compared to the immediate surrounding background. We applied a Gaussian profile with a maximum value in the center of the frequency spectrum to create a texture map. Figure 6.1 shows such a frequency spectrum with a Gaussian distribution. It is easy to set a specific scale for the texture blobs with a Gaussian texture profile. Since we use simulations, we can easily use the frequency spectrum to measure the size of the texture.

> “ The -6 dB width Δk_x in spatial frequency is related to the -6 dB width in the image domain
>
> $$\Delta x_{\text{texture}} = \frac{2\pi}{\Delta k_x}. \tag{6.1}$$
>
> *Paper V* ”

The texture size can also be estimated by measuring the autocorrelation of some realizations of the textured image scene. Averaging over some frames can improve the estimate.

The random texture map in Figure 6.1 is approximately 7 mm $\times$ 8 mm in size. The frequency spectrum has a steep Gaussian profile. We further multiply it with a complex random frequency spectrum. Inversion back to the image domain creates the amplitude texture map. We produce the final textured background by multiplying the original image with the texture map. We created texture with two different sizes in Paper V.

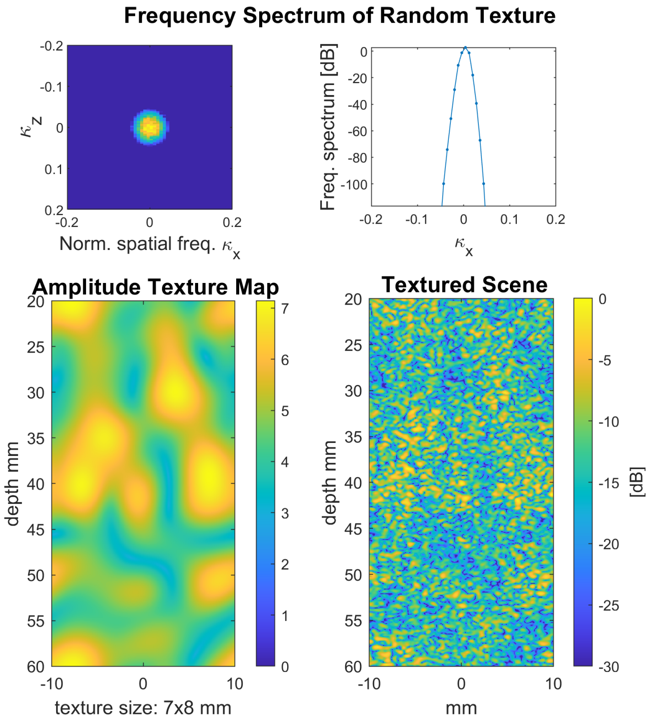

Figure 6.1: Example of a random texture map. A frequency spectrum with a Gaussian distribution is multiplied with a complex random frequency spectrum. Inversion back to the image domain creates the amplitude texture map. We multiply the texture map with the original image to produce a textured background. The final DAS image is normalized by its maximum value and shown with a −30 dB dynamic range.

6.2 Texture Estimation and Correction

Texture correction is a necessary step for simple threshold detection to work. It finds slowly varying changes in the amplitude of the textured image and removes them. We can estimate the texture by applying background smoothing with a sufficiently large window. In Paper V, we apply median filtering and continue with a 2D Gaussian smoothing kernel. We get the texture corrected image by dividing the original image with the estimate. Figure 6.2 shows the texture estimate of an image and the resulting texture corrected image.

The optimal texture correction depends on the scale and type of texture. Since the applied texture size in Paper V was known and the same in the whole image

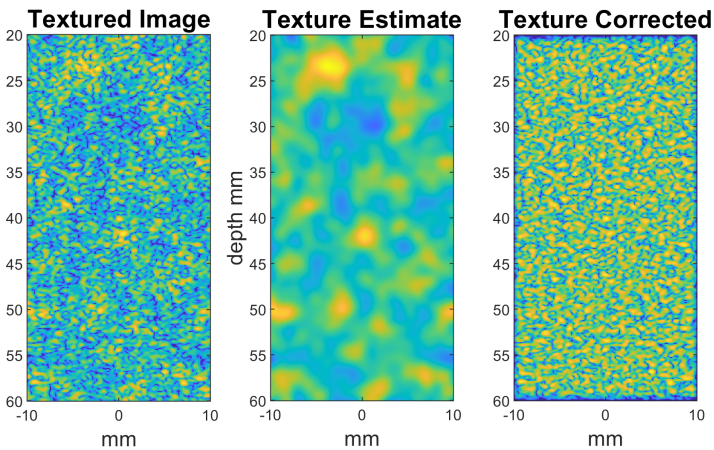

Figure 6.2: Texture correction of the DAS image ("DAS TC"). A texture estimate is first found by applying background smoothing with a large window. We obtain a texture corrected image by dividing the original image with the texture estimate. The texture estimate is shown with a -15 dB dynamic range, while the other images have -30 dB dynamic range. All images are normalized by their maximum value to be comparable.

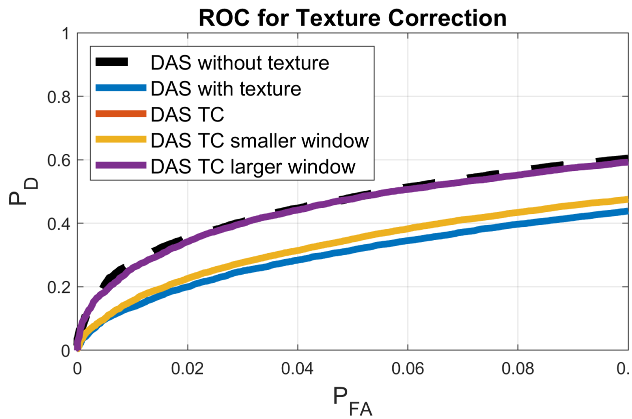

Figure 6.3: ROC for texture corrected (TC) images using three window filter sizes compared to original DAS *with* and *without* texture. P_{FA} is shown up to 0.1. The red curve signifies texture estimation with window size defined by the measured -6 dB texture size. The red curve lies directly beneath the purple curve. The purple ROC curve corresponds to 50% larger window size. Figure borrowed from Paper V.

scene, we could apply a relatively simple texture estimation. The window size must be larger than a point scatterer to ensure we only suppress the texture. However, if we apply a too large window, we can miss smaller texture variations. It is especially challenging to estimate aggressive and highly varying texture of small size. We ensured an optimal window size in Paper V by using the known -6 dB texture size combined with comparing ROC analysis using varying window sizes to the ROC results for the original DAS images *without* texture. Figure 6.3 from Paper V shows how texture degrades the ROC. As seen in the figure, we can improve the performance by applying texture correction, but it will not entirely restore the performance to the non-textured backgrounds. The yellow ROC curve in Figure 6.3 shows the ROC results when the window size used in the texture estimation is too small and consequently reduces P_{D}.

6.3 Prewhitening Before Texture Correction

Prewhitening changes the resolution of point scatterer and speckle blobs, as discussed in Chapter 5 and Paper IV. It does not change the size of the texture variations. In Paper V, we wanted to know if there is a difference in detection performance if we whiten the images *before* or *after* texture correction. Figure 6.4 shows a textured image that is whitened prior to texture correction and can be compared to Figure 6.2.

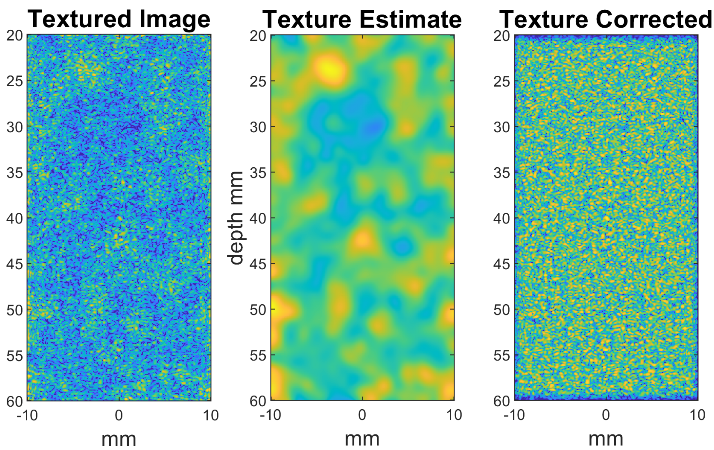

Figure 6.4: Texture correction on a whitened image ("Whitening + TC"). We obtain a texture corrected image by dividing the whitened image with the texture estimate. The texture estimate is shown with a -15 dB dynamic range, while the other images have -30 dB dynamic range. All images are normalized by their maximum value to be comparable.

Paper V compares the ROC results between prewhitening ("Whitening + TC") and whitening after texture correction ("TC + Whitening"). The results show how the ROC greatly improves when prewhitening is applied *prior* to texture correction.

Chapter 7

The Multilook Technique

In this section, we introduce the multilook technique, a technique widely used on synthetic aperture radar (SAR) images to reduce speckle [Jak+96, ch. 3.3] [Fer+03][OQ98, p. 29]. The technique splits the entire frequency bandwidth of the image into several adjacent subsets. Each subset has a different central frequency. We can create a separate image, known as a *sublook* or *look*, by computing the inverse Fourier transform of a subset. Splitting into L non-overlapping subsets reduces the frequency bandwidth by a factor L and thus similarly degrades the final image resolution of the looks. We can create several sublooks by either having independent subset bandwidths or allowing a partial overlap [San+15]. Paper IV introduces the multilook technique and three new multilook methods. We therefore reuse some formulations and text from Paper IV in this Chapter.

7.1 Point Signal Response in a Sublook

“

A point target is a coherent scatterer that is a dominant scatterer within a resolution cell. Some scattering loss occurs when the point scatterer is not in the center of the resolution cell. The Point Spread Function (PSF) describes the response of an imaging system to a point source. To obtain the PSF for each point position in the 1-D study, we started with the PSF of a point in the center, and then shifted the phase with respect to each pixel position. We can retrieve the response of a coherent scatterer in each sublook by adjusting the PSF for the sublook center frequency and bandwidth. We now evaluate the ideal 1-D point scatterer signal. The complex amplitude of this original point scatterer is $C = C_0 e^{j\phi}$ if we assume it is in the center of the resolution cell. Following [San+15], we start with a point scatterer positioned at a distance z_0 and its sinc-response

$$a_{\text{point}}(z) = C_0 e^{j\phi} e^{-j\frac{4\pi f_0}{c} z_0} \operatorname{sinc}\left(\frac{2B(z - z_0)}{c}\right). \tag{7.1}$$

Here f_0 is the transducer center frequency, c is the wave speed, and B is the frequency bandwidth. We create L sublooks of equal bandwidth $B_S = B/L$ by applying rectangular window filters over the different central frequencies $f_c^{(n)}$, for $n = 1, ..., L$. Each sublook response $a^{(n)}$ is thus

$$a^{(n)}(z) = \mathcal{F}^{-1}\left\{\mathcal{F}\{a_{\text{point}}(z)\}\text{rect}\left(\frac{f - f_c^{(n)}}{B_S}\right)\right\} \tag{7.2}$$

where $\mathcal{F}$ represents the Fourier transform. We can express the point signal response in each sublook n as [San+15]

$$a^{(n)}(z) = \frac{B_S}{B} C_0 e^{j\phi} e^{-j\frac{4\pi f_0}{c} z_0} e^{j\frac{4\pi f_c^{(n)}}{c}(z-z_0)} \operatorname{sinc}\left(\frac{2B_S(z-z_0)}{c}\right). \tag{7.3}$$

From the expression, we see that the new bandwidth B_S creates a broader sinc and thus degrades the range resolution to $\Delta z_S = c/(2B_S)$. The final 2-D response depends on the bandwidth in both directions. For the 2-D images in [San+15], the response in the other direction was similarly calculated and multiplied to the above expression.

Paper IV, slightly adapted

Paper IV further discusses how to obtain the PSF per pixel position. In [Che+20], Chen et al. presents a theoretical model to depict the PSF for varying point scatterer positions and apodization settings for plane-wave ultrasound imaging. The point scatterer's position, the transducer characteristics, and beamforming setting all affect the PSF. Since so many aspects affect the PSF, we chose to simulate the actual response of a point scatterer placed in each pixel to obtain the true PSF. The PSF was further whitened and divided into subsets. We tested 9×9, 13×13, 19×15, and 45×25 sublook divisions in Paper IV and Paper V.

7.2 Sublook Covariance Matrix

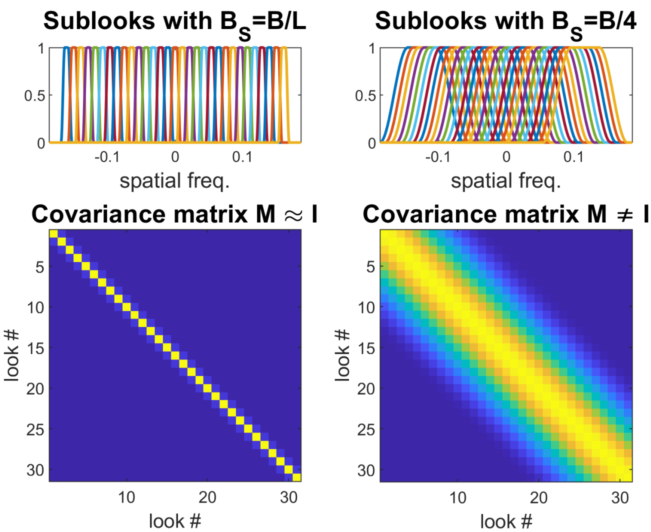

Figure 7.1: Sublook covariance matrices for independent and overlapping subset bandwidths. The covariance matrices shown here are for 1-D speckle sequences.

In the case of partially overlapping sublooks, i.e., subsets of bandwidth $B_S > B/L$, we must calculate the correlation among speckle samples belonging to the different sublooks. The correlation depends on the amount of bandwidth overlap compared to the total subset bandwidth. The normalized covariance matrix $M_{n,m}$ of the nth and mth rectangular subsets can be simplified to [San+15]

$$\mathrm{M}_{n,m} = \begin{cases} 1 - \frac{|f_c^{(m)} - f_c^{(n)}|}{B_S}, & \text{if } |f_c^{(m)} - f_c^{(n)}| < B_S \\ 0, & \text{otherwise.} \end{cases} \tag{7.4}$$

The correlation decreases when the distance between the center frequencies of the subsets increases. M is equal to the identity matrix I in the case of independent subsets. In the case of overlapping subsets, it depends on both the number of subsets L and the ratio between B_S and B, as depicted in Figure 7.1.

When considering 2-D subsets, the joint 2-D covariance matrix M is calculated as the Kronecker product of the matrices in each dimension [San14, p. 41],

$$\mathrm{M} = \mathrm{M}_z \otimes \mathrm{M}_x. \tag{7.5}$$

If we have L_z and L_x number of sublooks, the final dimension of M is $L_z L_x \times L_z L_x = L \times L$. We refer to L as the total number of sublooks.

7.3 Spatial Frequency Limits of Subset Division

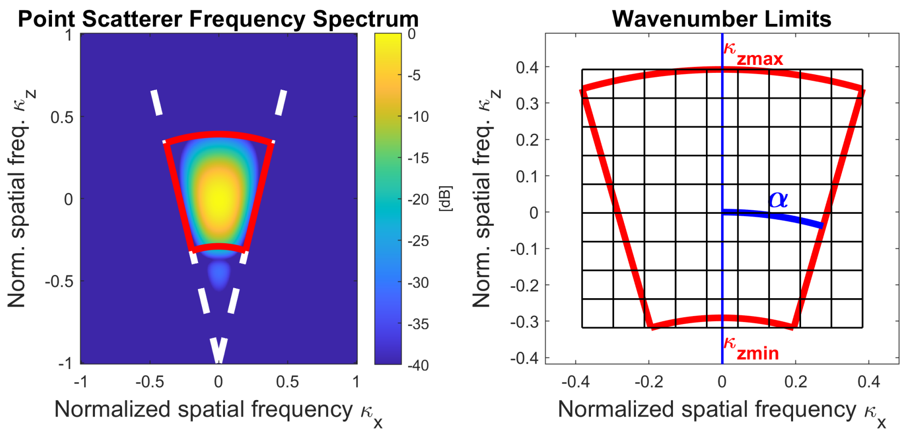

Figure 7.2: The frequency spectrum of a point scatterer, shown with a 40 dB dynamic range. The spatial frequencies are normalized by the estimated center frequency k_D ($\approx 2k_0$). The critical angle α is 16°. The region shown is divided into 9×9 subsets. Figure borrowed from Paper IV.

As described in Section 2.5, the spatial frequency support for an ultrasound imaging system is defined by the finite aperture size and the band-limited pulse. It is centered on $2k_0 = 4\pi f_0/c$ [AT00, ch. 3]. The imaging pulse is bandpass filtered ($f_L \leq f \leq f_H$) and demodulated by $k_D \approx 2k_0$. The PSF has a shape resembling a slice cut of a circular arc and is illustrated in Figure 7.2 from Paper IV. The support region is bounded by the aperture function in the k_x direction. The lateral width increases linearly with increasing frequency. In Figure 7.2, the spectrum has been demodulated and normalized. The region is then divided into rectangular subsets for the multilook technique. We create individual sublooks by applying the inverse Fourier transform on each subset.

7.4 The Generalized Likelihood Ratio Test (GLRT) for Sublooks

The Generalized Likelihood Ratio Test (GLRT) is the basis for the formulae for the multilook techniques. In Paper IV, we presented a detailed derivation of the solution to the GLRT for sublooks. Quite a lot of effort was spent in formulating a compact and complete derivation, so we will reuse the text from the Appendix in Paper IV here.

“ To give a complete and detailed presentation, we follow and combine the derivations in [Kel86], [CLR95], [San14, ch. 3.4.4], and [San+15], and fill in steps in between. We start with a binary test to decide if we have speckle (hypothesis $\mathcal{H}_0$) or signal + speckle (hypothesis $\mathcal{H}_1$) [TRL15]. The point scatterer is present in the pixel under test when the L-dimensional sublook vector $\boldsymbol{y}$ contains the point signal response $\boldsymbol{a}$.

$$\begin{cases} \mathcal{H}_0 : & \boldsymbol{y} = \boldsymbol{w} \\ \mathcal{H}_1 : & \boldsymbol{y} = C\boldsymbol{a} + \boldsymbol{w}. \end{cases} \tag{7.6}$$

The complex amplitude of the point scatterer is $C = C_0 e^{j\phi}$, and $\boldsymbol{w}$ signifies only speckle.

The Neyman-Pearson (NP) theorem states that the Likelihood Ratio Test (LRT) maximizes P_{D} for a given P_{FA} [Kay98, ch. 3.3]

$$\text{LRT}(\boldsymbol{y}) = \frac{p(\boldsymbol{y}; \mathcal{H}_1)}{p(\boldsymbol{y}; \mathcal{H}_0)} > \gamma, \tag{7.7}$$

where p is the probability density function (PDF) for observation $\boldsymbol{y}$. The threshold γ can be found by integrating the PDF for observation y of hypothesis $\mathcal{H}_0$ to the chosen P_{FA} value [Kay98, p. 30],

$$P_{\text{FA}} = \int_{\gamma}^{\infty} p(y; \mathcal{H}_0) dy. \tag{7.8}$$

If the speckle background is modeled as a zero-mean complex Gaussian random vector, the PDF of the sublook vector $\boldsymbol{y}$ given hypothesis $\mathcal{H}_0$ is [San+15]

$$p(\boldsymbol{y}; \mathcal{H}_0) = \frac{1}{\pi^L (\sigma^2)^L |\mathrm{M}|} \exp\left(-\frac{\boldsymbol{y}^H \mathrm{M}^{-1} \boldsymbol{y}}{\sigma^2} \right), \tag{7.9}$$

where $\boldsymbol{a}^H$ is the conjugate transpose of the point signal response and M is the normalized covariance matrix. Note that the notation in [San+15] refers to normalized covariance matrix, while the notations in [Kel86] and [CLR95] uses the covariance matrix $\mathrm{M} = 2\sigma^2\Sigma$ where Σ is the normalized covariance matrix after the whitening transformation ($|\mathrm{M}| = |2\sigma^2\Sigma| = (2\sigma^2)^L|\Sigma|$). Under the $\mathcal{H}_1$ hypothesis, the background $\boldsymbol{w}$ has the same PDF as under $\mathcal{H}_0$, and we find the PDF of $\boldsymbol{y}$ by substituting $\boldsymbol{w}$ with $\boldsymbol{y} - C\boldsymbol{a}$ [Kel86]

$$p(\boldsymbol{y};\mathcal{H}_1) = \frac{1}{\pi^L(\sigma^2)^L|\mathrm{M}|}\exp\left(\frac{-(\boldsymbol{y}-C\boldsymbol{a})^H\mathrm{M}^{-1}(\boldsymbol{y}-C\boldsymbol{a})}{\sigma^2}\right). \tag{7.10}$$

The LRT is thus the ratio between (7.10) and (7.9), and the NP test becomes a matched filter [San14, ch. 3.4].

The LRT is the optimal detector for a known signal in noise when the PDFs of both hypotheses are known. However, in our case, we wish to detect a signal with unknown amplitude, phase, and position in a speckle background of unknown level. Following classical detection theory [Kay98, ch. 6], the GLRT replaces the unknown parameters by their maximum likelihood estimates (MLE) before performing hypothesis testing as in (7.7). The GLRT takes the form

$$\mathrm{GLRT}(y) = \frac{\max\limits_{C,\sigma^2} \; p(\boldsymbol{y}|C,\sigma^2;\mathcal{H}_1)}{\max\limits_{\sigma^2} \; p(\boldsymbol{y}|\sigma^2;\mathcal{H}_0)} > \gamma, \tag{7.11}$$

where the speckle power σ^2 is the variance of the speckle and noise background, and C is the complex signal amplitude $C_0e^{j\phi}$. For simplicity, we assume the point scatterer inside the resolution cell is centered. In [San14, ch. 4.2.5], the formulae was extended to the case of unknown position, and the mismatch was shown to be small but noticeable for low point SNR values. The results indicate that using many sublooks decreases the mismatch and makes it possible to avoid optimizing the formulae for unknown position.

We now derive the maximizations in (7.11) using the PDFs in 7.10 and 7.9, and following [Kel86], [CLR95], [San14, ch. 3.4.4], and [San+15]. Even though the solution is derived in the case of white Gaussian background, the formulation remains valid also for the more complex case of compound-Gaussian clutter[San14, ch. 3.4.4]. To derive the GLRT, it is necessary to calculate the MLEs of the unknown parameters σ^2 and C.

We first derive the MLE of σ^2 under $\mathcal{H}_0$ and start by taking the natural logarithm of the PDF. The exponential function goes away and the expression becomes the sum

$$\ln(p(\boldsymbol{y};\mathcal{H}_0)) = -\ln\pi - L\ln\sigma^2 - \ln|\mathrm{M}| - \sigma^2\boldsymbol{y}^H\mathrm{M}^{-1}\boldsymbol{y}. \tag{7.12}$$

Derivation of (7.12) gives

$$\frac{d}{d\sigma^2}\left\{\ln(p(\boldsymbol{y};\mathcal{H}_0))\right\} = -\frac{L}{\sigma^2} - \boldsymbol{y}^H\mathrm{M}^{-1}\boldsymbol{y}. \tag{7.13}$$

By setting (7.13) equal to zero, we get the final expression for the MLE of σ^2 as

$$\hat{\sigma^2}\;|_{\mathcal{H}_0} = \frac{\boldsymbol{y}^H\mathrm{M}^{-1}\boldsymbol{y}}{L}. \tag{7.14}$$

Inserting M as the identity matrix in (7.14) simplifies the expression to $\boldsymbol{y}^H\boldsymbol{y}/L$. With the MLE $\hat{\sigma^2}$, the denominator in (7.11) becomes

$$\max_{\sigma^2} p(\boldsymbol{y};\mathcal{H}_0) = \frac{\exp(-L)}{\pi^L\left(\frac{\boldsymbol{y}^H\mathrm{M}^{-1}\boldsymbol{y}}{L}\right)^L|\mathrm{M}|}. \tag{7.15}$$

The MLEs under hypothesis $\mathcal{H}_1$ must also be found. We start by first supposing the parameter C is known [San14, ch. 3.4.4]. Using the same parameter substitution on (7.14) as we did moving from (7.9) to (7.10), the MLE under $\mathcal{H}_1$ can be expressed as

$$\hat{\sigma^2}\,|_{\mathcal{H}_1} = \frac{1}{L}(\boldsymbol{y}-C\boldsymbol{a})^H\mathrm{M}^{-1}(\boldsymbol{y}-C\boldsymbol{a}). \tag{7.16}$$

We now insert (7.16) into (7.10) to get

$$\max_{\sigma^2} p(\boldsymbol{y};\mathcal{H}_1) = \frac{\exp(-L)}{\pi^L(\frac{1}{L}(\boldsymbol{y}-C\boldsymbol{a})^H\mathrm{M}^{-1}(\boldsymbol{y}-C\boldsymbol{a}))^L|\mathrm{M}|}, \tag{7.17}$$

We must also obtain the MLE for $\hat{C}$ to maximize the PDF for C. To maximize this term, we follow the procedure E. J. Kelly presented in [Kel86] by rewriting

$$\begin{aligned}(\boldsymbol{y}-C\boldsymbol{a})^H\mathrm{M}^{-1}(\boldsymbol{y}-C\boldsymbol{a}) =&(\boldsymbol{y}^H\mathrm{M}^{-1}\boldsymbol{y}) + |C|^2(\boldsymbol{a}^H\mathrm{M}^{-1}\boldsymbol{a})\\ &- 2\mathrm{Re}\{C(\boldsymbol{y}^H\mathrm{M}^{-1}\boldsymbol{a})\}\\ &= (\boldsymbol{y}^H\mathrm{M}^{-1}\boldsymbol{y}) - \frac{|(\boldsymbol{a}^H\mathrm{M}^{-1}\boldsymbol{y})|^2}{(\boldsymbol{a}^H\mathrm{M}^{-1}\boldsymbol{a})}\\ &+ (\boldsymbol{a}^H\mathrm{M}^{-1}\boldsymbol{a})\times\left|C-\frac{(\boldsymbol{a}^H\mathrm{M}^{-1}\boldsymbol{y})}{(\boldsymbol{a}^H\mathrm{M}^{-1}\boldsymbol{a})}\right|^2.\end{aligned} \tag{7.18}$$

We maximize the PDF by minimizing the quantity in (7.18). The minimum is clearly attained when the positive term containing C is made to vanish [Kel86]. The MLE for C is therefore

$$\hat{C} = \frac{\boldsymbol{a}^H\mathrm{M}^{-1}\boldsymbol{y}}{\boldsymbol{a}^H\mathrm{M}^{-1}\boldsymbol{a}}. \tag{7.19}$$

Using this expression for $\hat{C}$, we can now find $\hat{\sigma^2}$ under hypothesis $\mathcal{H}_1$ by inserting (7.19) into (7.16) [San+15]. We get

$$\begin{aligned}\hat{\sigma^2}\,|_{\mathcal{H}_1} &= \frac{1}{L}(\boldsymbol{y}-\frac{\boldsymbol{a}^H\mathrm{M}^{-1}\boldsymbol{y}}{\boldsymbol{a}^H\mathrm{M}^{-1}\boldsymbol{a}}\boldsymbol{a})^H\mathrm{M}^{-1}(\boldsymbol{y}-\frac{\boldsymbol{a}^H\mathrm{M}^{-1}\boldsymbol{y}}{\boldsymbol{a}^H\mathrm{M}^{-1}\boldsymbol{a}}\boldsymbol{a})\\ &= \frac{1}{L}\left((\boldsymbol{y}^H\mathrm{M}^{-1}\boldsymbol{y}) - \frac{|(\boldsymbol{a}^H\mathrm{M}^{-1}\boldsymbol{y})|^2}{(\boldsymbol{a}^H\mathrm{M}^{-1}\boldsymbol{a})}\right).\end{aligned} \tag{7.20}$$

Finally, we have $\hat{\sigma^2}$ and $\hat{C}$ under $\mathcal{H}_1$ and we can rewrite the numerator in (7.11) as

$$\max_{\sigma^2,C} p(\boldsymbol{y};\mathcal{H}_1) = \frac{\exp(-L)}{\pi^L\left(\frac{1}{L}\left((\boldsymbol{y}^H\mathrm{M}^{-1}\boldsymbol{y})-\frac{|(\boldsymbol{a}^H\mathrm{M}^{-1}\boldsymbol{y})|^2}{(\boldsymbol{a}^H\mathrm{M}^{-1}\boldsymbol{a})}\right)\right)^L|\mathrm{M}|}. \tag{7.21}$$

Inserting (7.21) and (7.15) into (7.11), we express the GLRT as

$$\begin{aligned}\mathrm{GLRT}(\boldsymbol{y}) &= \frac{\left(\dfrac{\exp(-L)}{\pi^L\left(\frac{1}{L}\left((\boldsymbol{y}^H\mathrm{M}^{-1}\boldsymbol{y})-\frac{|(\boldsymbol{a}^H\mathrm{M}^{-1}\boldsymbol{y})|^2}{(\boldsymbol{a}^H\mathrm{M}^{-1}\boldsymbol{a})}\right)\right)^L|\mathrm{M}|}\right)}{\left(\dfrac{\exp(-L)}{\pi^L\left(\frac{\boldsymbol{y}^H\mathrm{M}^{-1}\boldsymbol{y}}{L}\right)^L|\mathrm{M}|}\right)}, \\ &= \frac{\left(\boldsymbol{y}^H\mathrm{M}^{-1}\boldsymbol{y}\right)^L}{\left((\boldsymbol{y}^H\mathrm{M}^{-1}\boldsymbol{y})-\frac{|(\boldsymbol{a}^H\mathrm{M}^{-1}\boldsymbol{y})|^2}{(\boldsymbol{a}^H\mathrm{M}^{-1}\boldsymbol{a})}\right)^L} > \gamma.\end{aligned} \tag{7.22}$$

Adjusting the threshold and simplifying (7.22) further gives

$$\mathrm{GLRT}(\boldsymbol{y}) = \frac{1}{\left(1-\frac{|(\boldsymbol{a}^H\mathrm{M}^{-1}\boldsymbol{y})|^2}{(\boldsymbol{y}^H\mathrm{M}^{-1}\boldsymbol{y})(\boldsymbol{a}^H\mathrm{M}^{-1}\boldsymbol{a})}\right)} > \gamma, \tag{7.23}$$

or equivalently [CLR95]

$$\mathrm{GLRT}(\boldsymbol{y}) = \frac{|\boldsymbol{a}^{\mathrm{H}}\mathrm{M}^{-1}\boldsymbol{y}|^2}{(\boldsymbol{y}^{\mathrm{H}}\mathrm{M}^{-1}\boldsymbol{y})(\boldsymbol{a}^{\mathrm{H}}\mathrm{M}^{-1}\boldsymbol{a})} > \gamma. \tag{7.24}$$

Paper IV, Appendix

7.5 The Multilook Methods NMF, MLCF, NMFW, and MLCFW

The GLRT detector is well-known in the radar community and known as the *normalized matched filter* (NMF) [CLR95; CLR96; DFP09]. It evaluates each specific image pixel and its corresponding L-dimensional sublook vector $\boldsymbol{y}$. The multilook method NMF and the three new multilook methods NMFW, MLCF and MLCFW are derived and presented in Paper IV. We borrow the presentation from Paper IV here.

The NMF decision rule with respect to threshold γ is [CLR95; CLR96; Kel86; San+15] [San14, ch. 3.4.4]

$$\mathrm{NMF}(\boldsymbol{y}) = \frac{|\boldsymbol{a}^{\mathrm{H}}\mathrm{M}^{-1}\boldsymbol{y}|^2}{(\boldsymbol{y}^{\mathrm{H}}\mathrm{M}^{-1}\boldsymbol{y})(\boldsymbol{a}^{\mathrm{H}}\mathrm{M}^{-1}\boldsymbol{a})} > \gamma. \tag{7.25}$$

Here $\boldsymbol{a}^{\mathrm{H}}$ is the Hermitian conjugate of the sublook vector of a theoretical point scatterer at the specific pixel position. The correlation among speckle samples belonging to the different sublooks is described by the sublook covariance matrix M. The whitening process can be incorporated into M as in [CLR95; CLR96; Kel86], but in this study we prewhiten the images prior to subset division and therefore M only depends on the subset bandwidth overlap [San+15]. M is equal to the identity matrix I in the case of independent, non-overlapping subsets. With $L = L_z L_x$ number of sublooks, the dimension of M is $L \times L$.

The numerator of (7.25) corresponds to the power output of matched filtering of the sublook vector $\boldsymbol{y}$ with the theoretical vector $\boldsymbol{a}$, calculated per pixel. Note that the numerator effectively is a weighted coherent sum of all looks such that we retain the full image resolution in the final image. The NMF method is a normalized method due to the denominator. The denominator is essential in the case of textured backgrounds, where the number and resolution of the sublooks influence how well the denominator estimates the background.

We simplify (7.25) for independent sublooks (M = I) and get

$$\mathrm{NMF}(\boldsymbol{y})\Big|_{\mathrm{M=I}} = \frac{|\boldsymbol{a}^{\mathrm{H}}\boldsymbol{y}|^2}{(\boldsymbol{y}^{\mathrm{H}}\boldsymbol{y})(\boldsymbol{a}^{\mathrm{H}}\boldsymbol{a})} > \gamma. \tag{7.26}$$

If we weight all sublooks equally, i.e., $\boldsymbol{a} = 1$'s, the numerator becomes a coherent sum of all looks. The numerator is then the same as only applying prewhitening. Again, the numerator ensures we retain the full image resolution in the final image. The test in (IV.11) changes to a ratio of the coherent and incoherent sum of all the sublooks. We term the new multilook method *multilook coherence factor* (MLCF).

$$\mathrm{MLCF}(\boldsymbol{y}) = \frac{|\mathbf{1}^{\mathrm{H}}\boldsymbol{y}|^2}{(\boldsymbol{y}^{\mathrm{H}}\boldsymbol{y})L} = \frac{|\sum_{n=1}^{L} y(n)|^2}{L\sum_{n=1}^{L}|(y(n)|^2} > \gamma. \tag{7.27}$$

The simplification of $\boldsymbol{a} = 1$'s drastically reduces the computational complexity as the method does not require prior knowledge of the theoretical point signal response per sublook. The ratio in MLCF is reminiscent of Coherence Factor (CF) beamforming in ultrasound. The CF *beamformer* calculates the ratio between coherent and incoherent energy across the aperture [MF94]. It is used as an adaptive weight to the DAS image [LL03]. This study takes the DAS image as its starting point and investigates methods to improve point detection. The MLCF method is a new 2-D CF method since we divide the spatial frequencies over two dimensions and calculate the coherence over the resulting sublooks. Traditional CF has overlapping spatial frequency areas, whereas MLCF has non-overlapping spatial frequency areas in both spatial direction and frequency.

The image weighting is inspired by adaptive coherence-based beamformers that apply weights to the DAS image. Since image weighting with the CF weights gave an improvement in the ROC results in [THA22], it was interesting to explore if we could obtain the same improvement using the multilook methods as weighting schemes. We therefore create two new multilook methods by applying NMF and MLCF as weighting schemes to the prewhitened image. NMF is not applied as an image weighting in the radar community. We term the new image created by NMF weighting as a *NMF weighted* image (NMFW).

$$\mathrm{NMFW}(\boldsymbol{y}) = \mathrm{NMF}(\boldsymbol{y}) \cdot \left|\sum_{n=1}^{L} y(n)\right| > \gamma. \tag{7.28}$$

We correspondingly apply MLCF as a weighting scheme and refer to the new multilook image as a *MLCF weighted* (MLCFW) image.

$$\text{MLCFW}(\boldsymbol{y}) = \text{MLCF}(\boldsymbol{y}) \cdot \left| \sum_{n=1}^{L} y(n) \right| > \gamma. \tag{7.29}$$

It should be noted that (7.25) and (7.27) produce normalized results, and (7.30) and (7.31) do not.

Paper IV

Table 7.1 from Paper IV summarizes the differences in computational complexity of the suggested methods.

Table 7.1: Computational Complexity of the Suggested Methods

Prewhitening	MLCF & MLCFW	NMF & NMFW
Low computational complexity. Preferable with prior knowledge of the critical angle and pulse bandwidth.	Medium computational complexity. Prewhitening and sublook division.	High computational complexity. Prewhitening and sublook division. Requires prior knowledge of the theoretical point signal response per sublook.

The inspiration for weighting the multilook images with the prewhitened image was that adaptive coherence-based beamformers calculate weights and apply these to the DAS image. The van Cittert–Zernike theorem postulates that speckle has a lower CF value than a point scatterer [MF94]. The DAS image includes the intensity of the point scatterer, while the CF weights can help differentiate the point and speckle. In Paper II, the CF weights alone do not improve the detection performance, but the CF weights used as image weighting to the DAS image performed well. Therefore, it was interesting to investigate if the same improvement could be the case for the multilook methods. The traditional CF beamformer calculates the coherence over the elements and has overlapping spatial frequency areas. MLCF has non-overlapping spatial frequency areas in both spatial direction and frequency. There is a difference between coherence over direction and coherence over time. Look direction is not the same as an array position. As such, CF is not just MLCF in one dimension.

The NMF and MLCF methods are calculated on prewhitened images and do *not* require any texture correction prior to detection analysis. Paper IV introduced the multilook methods NMFW and MLCFW as weighting schemes of NMF and MLCF to the prewhitened images. For homogenous backgrounds, the coherent sum of all sublooks is the same as the prewhitened DAS image. With the introduction of texture in Paper V, we refer to these multilook methods using the term $\text{DAS}_{\text{whitened+TC}}$ instead of the coherent sum of all looks.

We also apply NMF and MLCF as a weighting schemes to the prewhitened *and* texture corrected image, $\text{DAS}_{\text{whitened+TC}}$. We refer to these two methods as *NMF* *weighted* (NMFW) and *MLCF weighted* (MLCFW) images.

$$\mathrm{NMFW}(\boldsymbol{y}) = \mathrm{NMF}(\boldsymbol{y}) \cdot \mathrm{DAS}_{\mathrm{whitened+TC}}. \tag{7.30}$$

$$\mathrm{MLCFW}(\boldsymbol{y}) = \mathrm{MLCF}(\boldsymbol{y}) \cdot \mathrm{DAS}_{\mathrm{whitened+TC}}. \tag{7.31}$$

Paper V

Figure 7.3 shows an example ultrasound image scene with seven point scatterers. The same image scene is shown after prewhitening and the four multilook methods. The number of sublooks is 45×25 for the multilook methods, and optimal α-prewhitening is applied. From the image example, it would seem all the methods improve the point scatterer's visibility. The multilook methods seem to increase the threshold level between the point scatterers and the peaks in the speckle background. However, it could be that the methods stretch the dynamic range [Rin+19]. This is the reason a complete ROC analysis using many realizations is needed to fully evaluate the detection performance of a method.

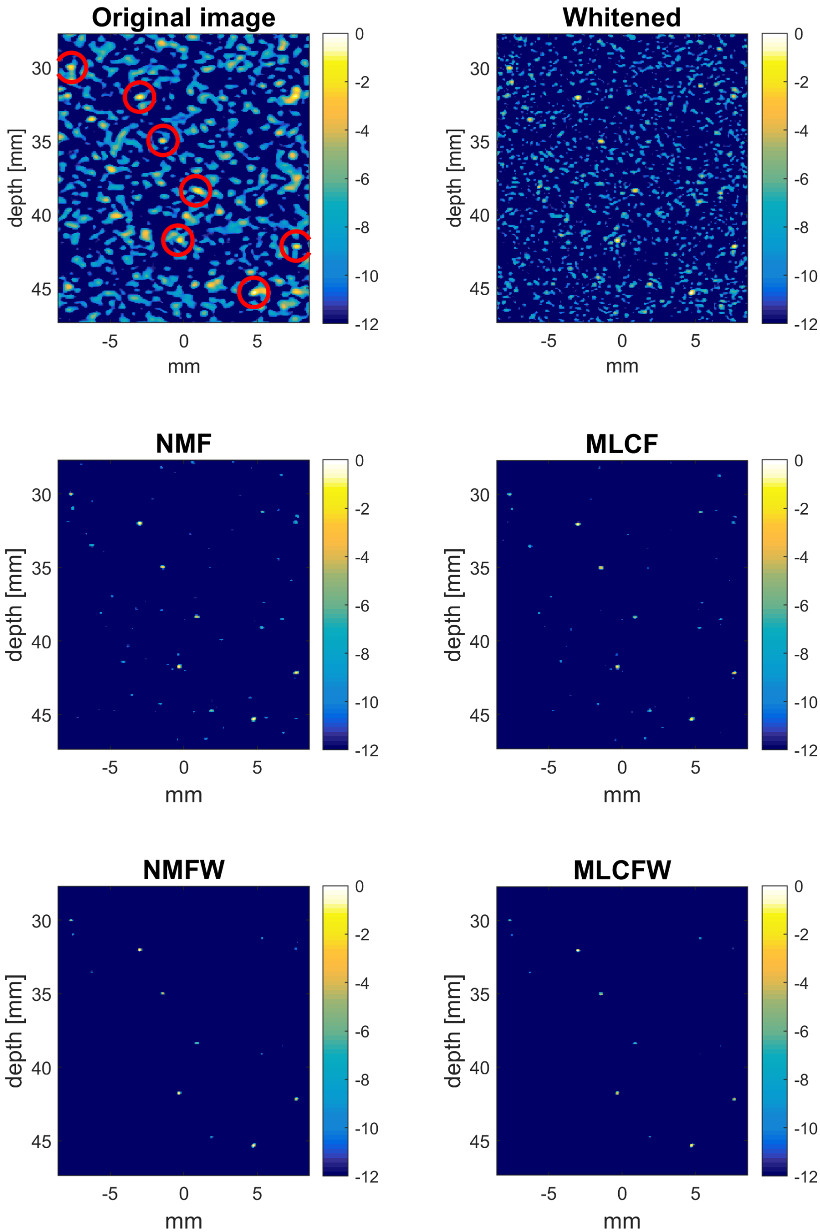

Figure 7.3: Example of how prewhitening and the multilook methods affect an ultrasound image scene with seven point scatterers in uniform speckle background. The number of sublooks is 45×25 for the multilook methods and optimal α-prewhitening is applied. All images are normalized by the maximum value to be comparable and shown with a 12 dB dynamic range.

Chapter 8

Summary and Discussion of Findings

This section summarizes and discusses the findings in the papers in relation to the main research question.

8.1 Measuring and Evaluating Point Detection Performance

Paper II presents a framework for how to measure and evaluate point detection performance in ultrasound images. I present and discuss the strategy and methodology from Paper II in Chapter 3 as it provides relevant background material for Paper IV and Paper V.

We used the detection strategy summarized in Section 3.6 for Paper II, Paper IV, and Paper V. To obtain ROC and AUC results with sufficient confidence intervals, we created many images using the Field II software. Real phantom data has challenges regarding wanted point SNR, point location, and varying speckle backgrounds. Standard tissue-mimicking phantoms often give images with brighter point targets, and slight deviations in the probe orientation can cause slight shifts in the assumed point locations. When evaluating detection performance, we are most interested in the point SNR range where the probability of detection P_{D} varies the most. Therefore we want images with weak point scatterers at known positions. We have complete control of the point scatterer's intensity and exact position in the image scene with simulated images.

We chose to obtain images with uniform resolution. We could then position point scatterers randomly and be ensured the same point SNR value. We used many point positions to ensure we average out possible artifacts from the simulations. We must compare point targets of equal size and point SNR value since the detection performance depends strongly on spatial resolution and point SNR. Another reason for choosing a large speckle scene is that this requires fewer speckle images, and many speckle images with fully developed speckle are computationally demanding to simulate. We could have created very small, focused speckle scenes with equal resolution, but this would require more realizations. To simulate such scenes, we could have chosen to use compound plane-wave imaging, retrospective transmit focusing, or even focused transmits for each pixel in the images. The results should be the same. We chose to use synthetic transmit aperture imaging with constant $f_{\#}$.

The theoretical formulae for the detection probabilities given in Chapter 3 assume a Rayleigh distributed speckle background. The presented detection study starts with a complex DAS image with uniform resolution and Rayleigh distributed speckle. We chose to have uniform apodization at receive. The resulting image still has Rayleigh distributed speckle if we wanted to receive with tapering. The second harmonic has Rayleigh distributed speckle even though the effective apodization is narrower

[Fed+03]. Therefore, the detection performance results are valid for both fundamental and second harmonic imaging. Our study concerns point in speckle, regardless of the frequency used. Focused imaging, as we have chosen, can produce such images with uniform resolution. So do imaging with a defocused beam, but the spatial resolution will then vary. It could drop or become range dependent. Images with varying spatial resolution require an adjustment to the detection strategy since the point SNR value then depends on where the point is located. The optimal size of the search window is also affected by the resolution and must be varied if the resolution is not constant.

8.2 Effect of common ultrasound techniques

8.2.1 Spatial Resolution and Apodization Affect Point Detection

Reducing the size of the aperture degrades the spatial resolution of the image. In Paper II, we compared three different $f_{\#}$ values to establish the effect of aperture size on detection performance. As seen from the ROC results in Paper II, increasing the $f_{\#}$ degrades the detection performance. The great difference between $f_{\#} = 7$ and $f_{\#} = 3.5$ illustrates how doubling the adaptive aperture greatly improves point detectability.

In Paper II, we also studied the effect of different apodization schemes: rectangular, Hamming only on transmit, and Hamming on both transmit and receive. We can conclude from the results that when we mainly wish to detect point scatterers, the ideal method is to apply uniform apodization. A uniform rectangular window gives the highest detection probability. Applying a nonuniform window suppresses some probe elements. It thereby reduces the resolution and the maximum point intensity value. In general, techniques that trade-off spatial resolution to obtain better contrast have lower probability of point detection.

8.2.2 Speckle Reduction Affects Point Detection

In Paper II, we analyzed the effect of common denoising filters on the detection of point scatterers. They alter the speckle statistics of the image. Applying any speckle reduction smooths the background, and also degrades the image resolution and consequently reduces the point SNR. The results in Paper II show that it is possible to smooth the speckle background while still having detection performance quite close to the original. The bilateral, Wiener, and non-local means filters managed to preserve relatively high performance even for a high degree of background smoothing.

8.2.3 Advanced Beamforming Methods Affect Point Detection

In Paper I, we show that certain adaptive beamformers alter the statistics of the speckle background. The altered speckle statistics allow cherry-picking of contrast metrics to describe the image quality and performance of the beamformer. The observed results and conclusions of Paper I can be summarized as follows:

- The adaptive beamformers CF, GCF, PCF, and DMAS have higher CR than DAS but concurrently lower CNR.

- Figures of the PDFs confirm that EBMV, CF, PCF, GCF, and DMAS have increased both the variance and the intensity difference between the regions.
- Several adaptive beamformers alter the speckle statistics, and the alteration is both spatially and intensity dependent.
- A beamformer may have high CR and simultaneously low CNR compared to DAS. This allows for cherry-picking of contrast metrics.
- When benchmarking a beamformer, we should present both CR and CNR and include a statistical discussion.

Paper I has inspired several other works. In 2017, the papers Paper I and [RRA17] compared seven beamformers and how they affect the image statistics. The findings in these initial studies elucidated why we need a generalized contrast metric to compare the image quality of different techniques when they deviate from conventional DAS speckle statistics. This inspired the publication [Rod+20], which introduces the generalized CNR metric (gCNR). With the new knowledge introduced in [Rod+20], the last finding in the above bullet list is less relevant since we now should use gCNR.

Advanced beamforming techniques and speckle reduction methods alter the statistics. They have different PDFs than DAS and will correspondingly affect the detection performance. The approach of Paper II is to measure the detection performance independent of knowledge of the PDFs to directly compare how they affect the point detectability. In Paper II, we analyzed the detection performance of the three advanced beamformers; MV, CF, and PCF. The input to all the methods was identical and the point SNR value was calculated from the corresponding DAS images. The tabulated P_{D}-results from Paper II are visually illustrated in Figure 8.1.

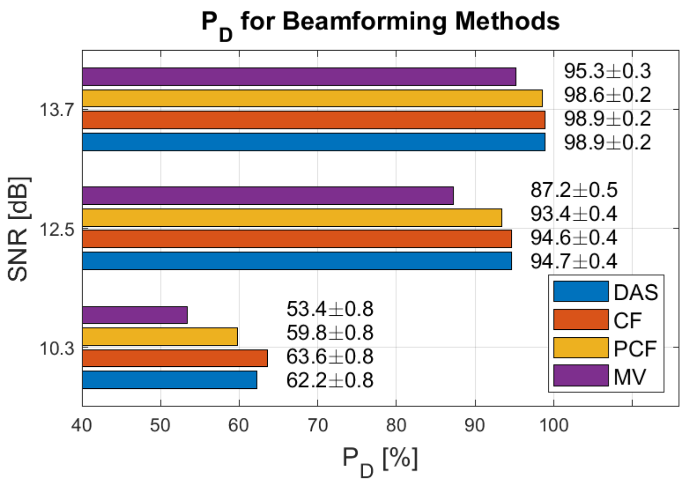

Figure 8.1: Tabulated P_{D} for the four beamformers, given 2 $\%$ P_{FA} and three SNR values. Error margins were calculated for P_{D} with 6500 realizations and 80% confidence.

Applying a search window lets us evaluate and compare how the imaging method affects the speckle background and corresponding false alarms. A search window is a good choice since the positions of the peaks of the speckle pattern remain more or less the same for CF and MV. For each direction, MV retains the energy in the specific direction and suppresses the energy from the other directions. MV has a narrower PSF than DAS. It calculates a weight per direction and depth. It uses the full DAS resolution for its calculations. We have more than 20 scatterers per cell in our simulated images. As presented in Chapter 2, fully developed speckle requires more than ten scatterers per resolution cell.

The results show how the CF weights provide a positive weighting to DAS at low SNR and P_{FA} values. Unweighted, original DAS is the best detector unless we include prior knowledge in the analysis. CF differentiates between coherent and incoherent energy across the aperture. Its weights thereby accentuate signals from coherent point scatterers. However, we do not have enough realizations to state that CF is statistically significantly better than DAS at low SNR and P_{FA} values since the confidence intervals partially overlap.

8.3 The Wavelet Coefficient Shrinkage Method

Paper III investigates if the wavelet coefficient shrinkage method can enhance point scatterers and suppress speckle background in ultrasound images. The results on the simulated images and the tissue-mimicking phantom in Paper III show that we can greatly increase the visibility and conspicuity of the point scatterers with the wavelet coefficient shrinkage method. The method retains the point scatterers even when peaks in the speckle background are almost at the same intensity level.

The 3-D breast phantom results show that the method is ideal for strong point scatterers. The results also show that we can drastically reduce the number of point target candidates if we exploit all three dimensions. I imaged the breast phantom with a tiny transesophageal probe, which is not ideal for point detection. A transducer with a higher center frequency and larger aperture size is better suited to find point scatterers. The 3-D wavelet shrinkage method illustrates the benefits of exploiting all available information and the possibility of using coherence to enhance signals from point scatterers. An obvious next step is to exploit fluctuations in time. Point targets should have high coherence over several image frames. Using several frames should then drastically reduce the number of false alarms.

To fully ascertain if the wavelet coefficient shrinkage method increases point detectability, we must perform a complete ROC analysis using many simulated images. The conference paper in 2017 was a preliminary study with promising results. The work in Paper III started a discussion on how to measure point target enhancement correctly and how the ultrasound community lacks a clear overview of how to statistically describe an improvement in point detectability. This discussion led to the work published some years later in Paper II. The work in Paper III also started a discussion on the possibility of partitioning the frequency spectrum in other ways than by creating look pairs. This discussion led to the work in Paper IV and Paper V where we partition the frequency spectrum into many sublooks. The algorithms we apply in these two papers also exploit the coherence information over the sublooks to enhance point targets.

8.4 Prewhitening Before Point Detection

Paper IV compares the ROC curves for the original and optimal α-whitened images. An optimized prewhitening can increase the measured point SNR value and the results show that prewhitening has a *significantly* positive effect on point detection.

In Paper IV and Paper V, we study suboptimal whitening limits by increasing or decreasing the applied critical angle or frequency bandwidth. The optimal whitening limits depend on the image resolution and the point SNR. Narrowing the limits can be beneficial in the presence of noisy backgrounds and weak point scatterers since we then suppress spatial frequency regions with low SNR values. For a point scatterer with increasing intensity compared to the background, the optimal angular limit converges towards α. The ROC curves in Paper IV show that the limits of the pulse bandwidth are a good estimate of the optimal frequency limits. Increasing or decreasing the frequency limits by only 5% degrades the overall detection performance in Paper IV.

Since the whitening transform increases the resolution, it increases the number of independent pixels within the applied search windows. In Paper II, we discuss how the number of independent pixels within a search window affects the detection performance. We found that the search window must be sufficiently large and include several independent pixels to provide a fair comparison between different methods. We also use an oversampled image to ensure we do not have straddle loss. We apply the 1-D and 2-D detection setups from Paper II in the studies in Paper IV and Paper V.

The images used in Paper IV and Paper V have uniform resolution and thereby the same wavenumber coverage for all pixels. It was then possible to calculate one whitening filter and use it on all the images. If we have an image with varying spatial resolution, the wavenumber coverage will vary at different pixel positions. We must then vary the prewhitening transform based on pixel position. The resolution will also affect the optimal size of the search window. In addition, the probability of detection will also vary due to the changes in resolution and consequently changes in point SNR values. We chose to use the most straightforward scenario in Paper IV and Paper V. We strongly believe that the results are transferable to images with varying spatial resolution. The detection strategy and the prewhitening method will then have to be adjusted.

In Paper V, we wanted to know if there is a difference in detection performance if we whiten the images *before* or *after* texture correction. The ROC results in Paper V show how the ROC greatly improves when prewhitening is applied *prior* to texture correction. Prewhitening achieves a higher performance since it reduces the size of the point scatterers and speckle blobs, but not the slowly varying texture. The scale difference between the point scatterers and the texture is larger after prewhitening. The texture estimation can therefore achieve a better estimate of the texture only. In general, a successful texture estimate is easier to achieve with slowly varying texture, such as illustrated in Figure 6.4. The results in Paper V show *significant* improvement in detection performance using optimized prewhitening on images where an optimal texture correction is easily obtained.

We use the Fourier transform to obtain a spectral estimate for the prewhitening method in the papers. The classical estimator requires that the input signal is stationary and ergodic [Ale16, p.399]. If the data has an amplitude trend in range, we can compensate by first applying a time-varying gain or depth correction to remove the transmission loss effects. The signal is strictly non-stationary even after depth correction when the spectrum shape changes with depth. A fixed prewhitening filter is then suboptimal, and we should instead apply a depth-dependent prewhitening filter. If we have considerable amplitude variations in the image, it may be beneficial to apply texture correction to achieve stationarity before applying prewhitening.

8.5 Multilook Methods and Point Detection

Paper IV introduces the multilook technique and three new multilook methods aiming to improve point detection. In this chapter, I discuss the findings on number of sublooks, suboptimal texture correction, suboptimal prewhitening, and dominant additive acoustic noise.

8.5.1 The Number of Sublooks

The optimal number of sublooks for the multilook methods varies depending on the image background. In Paper IV, we found that it was beneficial to divide the frequency spectrum into as many subsets as computationally possible. The numerator in (7.24) retains full image resolution regardless of the number of sublooks. However, Paper IV studied uniform speckle background images. With the introduction of texture in Paper V, the optimal number of sublooks changed. We found that the optimal number of sublooks for our scene with large texture was around 19×15, while the optimal for small texture was around 13×13 sublooks. Table 8.1 from Paper V summarizes the observed performance of the multilook methods using a varying number of sublooks. I include the table here to give a complete summary of the findings.

Table 8.1: Summary of Observed Performance Using Varying Number of Sublooks

Background	Number of sublooks			
	9x9	13x13	19x15	45x25
Homogenous	Poor	Poor	Moderate	Best
Large texture	Moderate	Good	Best	Poor
Small texture	Good	Best	Good	Poor

The results show that textured scenes require sublooks with higher image resolution than the uniform speckle backgrounds in Paper IV. The denominator in (7.24) improves its estimate of the background when the sublooks are many but also have high image resolution. Therefore, there is an optimal number of sublooks that depends on the texture size. A texture of small size requires subsets with larger bandwidth for it to be discernible in the resulting sublooks. If we have a texture of larger size, we can decrease the subset size slightly and thereby increase the number of sublooks. A larger texture is estimated more easily, which is why the multilook methods perform better on images with slowly varying textures.

8.5.2 Suboptimal Texture Correction

The results in Paper V show that the detection performance of the multilook methods compared to prewhitening is especially large for image backgrounds where optimal texture correction is difficult to obtain. Such a scenario is realistic, as optimal texture estimates can be difficult in ultrasound images with unknown or more aggressive textures. To simulate such a scenario, we applied a window size for the texture estimation that was smaller than the actual texture size.

Paper V presents the ROC results for the multilook methods on small texture with suboptimal texture correction. All the multilook methods perform better than prewhitening in this scenario. The image weighting methods NMFW and MLCFW perform best since the applied texture correction still provides some improvement to the detection performance. However, the NMF and MLCF methods show great potential when an optimal texture correction is difficult to obtain, or a normalized method is wanted.

8.5.3 Dominant Acoustive Noise

Paper V shows how the improvements in ROC for the multilook methods compared to prewhitening are significant when additive, acoustic noise dominates speckle. Acoustic noise is a realistic scenario as the imaging depth increases. For this detection study, we applied adaptive prewhitening of the images. The optimal whitening limits and window size for the texture correction were known. The images had slowly varying textures, and we used 19×15 sublooks. All four multilook methods perform better than prewhitening, but the NMFW and NMF methods perform exceptionally well.

8.5.4 Suboptimal Prewhitening

The results in Paper IV show that the detection performance of the multilook methods compared to prewhitening is high when optimal whitening limits are difficult to obtain. The multilook methods MLCF and MLCFW can be applied even when prior knowledge about the optimal prewhitening limits is unavailable. They do not require prior knowledge of the point signal response per sublook. The results in both Paper IV and Paper V show significant improvement in detection performance when we apply MLCF as an image weighting to the prewhitened image.

Paper IV compares *suboptimal* prewhitening and the four multilook methods NMF, NMFW, MLCF and MLCFW on speckle backgrounds that are without texture variations. The slightly wider whitening limits reduce the detection performance compared to the optimized α-whitening limits. The NMFW method performs better than MLCFW in the case of suboptimal whitening since it incorporates extra knowledge about the correct point signal response per sublook and can suppress more unwanted subsets at the edges of the spectrum.

When we expand to textured backgrounds, the results change a little. As discussed, textured backgrounds require sublooks with higher resolution, which causes the optimal number of sublooks to decrease. Consequently, the multilook methods cannot suppress as many unwanted subsets at the edges, and it cannot achieve the same amount of increase in the ROC results as found in Paper IV.

Paper V presents tabulates P_{D} given 3% P_{FA} for the multilook methods using slightly wide or very wide whitening limits. Figure 8.2 presents the ROC values for the multilook methods when using a suboptimal, slightly wider whitening filter. The ROC curves show how NMFW and MLCFW perform slightly better than prewhitening at low P_{FA} values. However, the results also show that prewhitening is robust even when applied suboptimal limits. The difference at low P_{FA} values is too small to give the multilook methods higher overall AUC values.

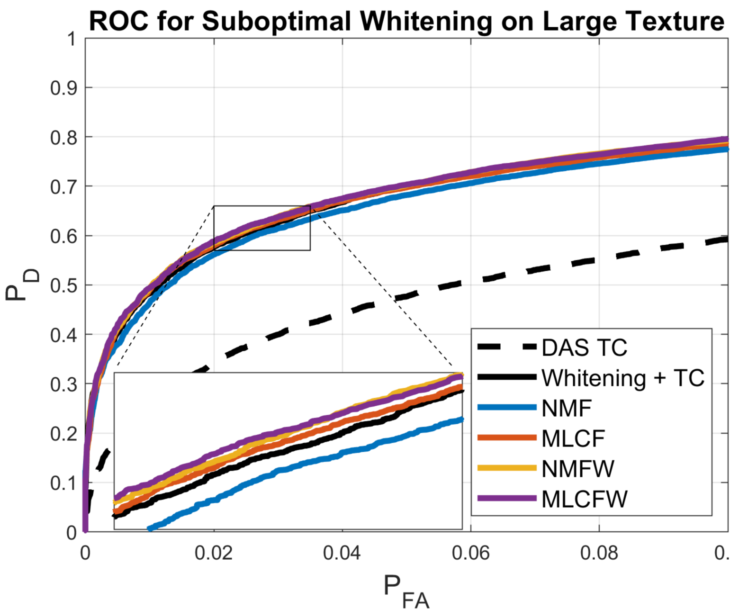

Figure 8.2: ROC for the multilook methods using 19×15 sublooks combined with suboptimal prewhitening and optimal texture correction (TC). The speckle backgrounds have slowly varying texture fluctuations. The multilook methods NMFW and MLCFW perform only slightly better than prewhitening at low P_{FA} values.

If the whitening limits are poorly estimated, the benefit of using the NMF weights increases. Figure 8.3 presents the ROC values for the multilook methods when used with a poor choice for the whitening limits. We chose extra-wide limits corresponding to a 30% increase in critical angle α and $\pm 10\%$ increase in the frequency bandwidth limits. The increased span in wavenumber coverage gives a larger area to divide into subsets. We increased the number of sublooks to keep the subset size the same as in the studies with α-prewhitening.

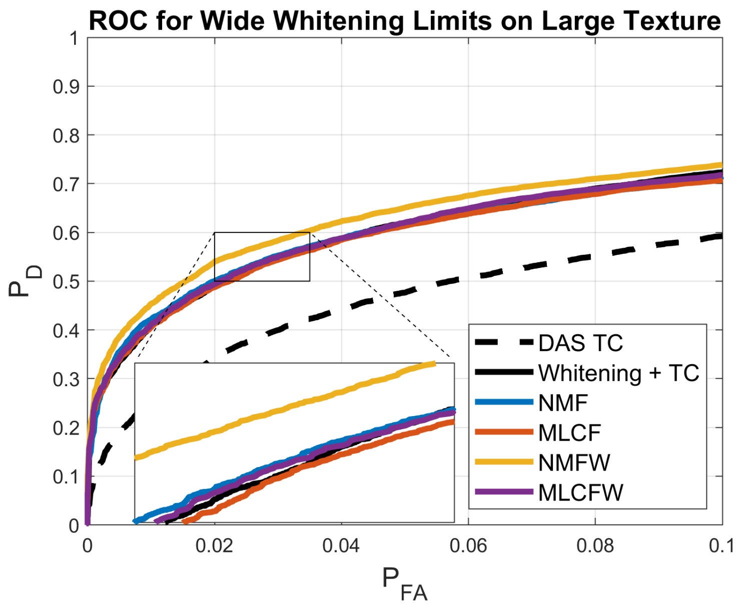

Figure 8.3: ROC for the multilook methods using 25×21 sublooks combined with too wide whitening limits. The speckle backgrounds have slowly varying texture fluctuations, and we applied optimal texture correction (TC). The multilook methods NMF and NMFW perform better than prewhitening at low P_{FA} values.

As discussed, we used DAS images with uniform resolution in Paper IV and Paper V as the starting images. An image with uniform resolution has the same wavenumber coverage for all pixels. If we have an image with varying spatial resolution, the wavenumber coverage will vary at different pixel positions. We must then adjust the detection strategy and the prewhitening method accordingly. The NMF method incorporates the theoretical PSF for each pixel position in the scene and has no problems with images with varying spatial resolution. The suboptimal prewhitening results show that the NMF and NMFW methods can improve the detection performance when the optimal prewhitening is unknown. The potential gain of the NMF weights is promising for images with varying resolution.

8.5.5 Table Summarizing the Observed Benefits and Setbacks of the Methods

Table 8.2 from Paper V summarizes the observed benefits and setbacks of prewhitening and the four multilook methods. I also include it here to give a complete summary of the findings from Paper IV and Paper V.

Table 8.2: Summary of Observed Benefits and Setbacks of the Multilook Methods

Scenario	Method				
	Prewhitening	MLCF	MLCFW	NMF	NMFW
Optimal whitening & optimal TC	Large improvement in detection performance.	Similar performance as whitening.	Similar performance as whitening. Slightly better than whitening in the case of large texture.	Setback compared to whitening.	Similar performance as whitening.
Suboptimal prewhitening wo/texture	Some reduction in detection performance, but still a robust method.	Performs slightly better than whitening.	Performs slightly better than whitening.	Performs slightly better than whitening.	Performs better than whitening.
Suboptimal prewhitening w/texture	Some reduction in detection performance, but still a robust method.	Similar performance as whitening.	Performs slightly better than whitening at low P_{FA} values.	Some setback compared to whitening.	Performs slightly better than whitening at low P_{FA} values.
Wide prewhitening w/texture	Reduction in detection performance.	Similar performance as whitening.	Similar performance as whitening.	Performs slightly better than whitening at low P_{FA} values.	Performs better than whitening.
Suboptimal TC	Much affected by suboptimal TC.	Not affected by TC.	Improvement due to weighting with MLCF.	Not affected by TC.	Improvement due to weighting with NMF.
Poor TC	Much affected by poor TC.	Not affected by TC.	Affected by poor TC.	Not affected by TC.	Affected by poor TC.
Dominant additive acoustic noise	Improvement compared to only TC, but method enhances much of the noise.	Method weights sublooks using coherence.	Method weights sublooks using coherence.	Method weights sublooks according to theoretical point signal response.	Method weights sublooks according to theoretical point signal response.
Computational complexity	Low	Medium	Medium	High	High

Color coding: Poor / Good / Great

Chapter 9

Concluding Remarks

9.1 Main Contributions of Thesis Work

The primary research question of this thesis is how to enhance and detect point scatterers in an ultrasound image. In this thesis, I explore how new software methods affect the statistics of the ultrasound image and how to evaluate possible improvements in point detection. I explore new and existing approaches to improve the detection of point scatterers by optimizing the spatial frequency spectrum. The following results answer the primary research question as concretized by the detailed questions presented in Chapter 1:

- **How should we measure and evaluate the detection performance of point scatterers in ultrasound images?**
  This thesis presents an overview and framework of detection of point scatterers in ultrasound images. It discusses different detection strategies for evaluating and measuring point detection performance. It presents a methodology for calculating detection performance and corresponding confidence intervals.

- **How do advanced beamforming techniques influence the statistics of an ultrasound image, and do common ultrasound techniques affect point scatterer detection?**
  Adaptive beamformers alter the speckle statistics and influence conventional contrast metrics in ultrasound imaging. A beamformer may have high CR and simultaneously low CNR compared to DAS. This allows for cherry-picking of contrast metrics. Phantom results show that the beamformers alter the statistics of two speckle regions differently depending on the orientation of the boundary between the regions.

  Common ultrasound techniques such as apodization, speckle reduction, and adaptive beamformers affect the detection of point scatterers. In general, methods that preserve spatial resolution have better detection performance of point scatterers. Results show that it is possible for a suitable and optimized method to smooth the speckle background and still preserve relatively high performance. Detection results show that the adaptive beamformer CF achieves slightly better detection performance than DAS for weak point scatterers.

- **Inspired by the wavelet shrinkage method presented in [HV14], can the method also be applied to medical ultrasound images to enhance point scatterers?**
  The wavelet coefficient shrinkage method can enhance the conspicuity of point targets in an ultrasound image. The phantom results show that we can enhance point scatterers by separating coherent point targets from incoherent background

speckle. However, a complete detection study is needed to statistically prove an improvement in point detection.

- **Can we get inpiration from other methods in radar and sonar imaging to find new methods that improve point scatterer detection in ultrasound images?**
  Optimized prewhitening can significantly improve point detection performance. Results show that optimized prewhitening before texture correction and point detection is a robust method that dramatically improves the detection.

  Point detection can be improved by dividing an image's spatial frequency spectrum into subsets and exploiting the coherent properties of point targets. The multilook technique NMF from the radar community is introduced to ultrasound in this thesis work. The work also introduced three new multilook methods called NMFW, MLCF, and MLCFW, and studied their effect on point detection. The multilook methods have the potential to improve the detection of weak point scatterers when a sufficient number of looks are used. The MLCF and MLCFW are more straightforward methods than conventional NMF. The new methods can be applied even when prior knowledge about the optimal prewhitening limits is unavailable and results show they can improve the point detection. The multilook methods are also very promising methods to apply on images where acoustic noise dominates the speckle background.

  The texture size affects the optimal number of sublooks for the multilook methods. The multilook methods NMF and MLCF are normalized methods that do not require texture correction prior to detection analysis. They are especially promising when optimal texture correction of the ultrasound images is difficult to obtain or a normalized method is wanted.

9.2 Implications and Further Research

Paper I explored how certain adaptive beamformers alter the speckle statistics and consequently allow cherry-picking of contrast metrics to describe the image quality. The findings elucidated why we cannot use the standard contrast metrics to compare the image quality of different techniques when they deviate from conventional DAS speckle statistics. This work is a part of the initial studies that raised awareness around the validity of image quality metrics and inspired later work on developing a generalized contrast metric [Rod+20].

As indicated by the third detailed research question, a part of the Ph.D. plan was to explore if the wavelet shrinkage method from [HV14] could be used to improve the detection of point scatterers in ultrasound images. The work in Paper III started a discussion on how the ultrasound community lacks a clear framework on how to statistically measure point detection, which led to the work in Paper II. Paper II presents an overview of how to measure and evaluate point detection performance. Many previous works used contrast metrics or similar to describe observed improvements in point detectability. With Paper II, we emphasize how we must evaluate detection performance using many realizations with known point scatterers to provide detection results with reliable accuracy. The work offers a framework for point detection in ultrasound.

Paper III shows promising results using the wavelet coefficient shrinkage method to enhance the conspicuity of point targets in ultrasound images. A possible further work is to perform a detection analysis using the detection strategy presented in Paper II on many wavelet shrunk images. The preliminary studies on 3-D images in Chapter 4 shows promising results when we exploit the coherence over all three dimensions. A further research possibility is to test the multilook methods in Paper IV on 3-D images and exploit all orthogonal directions.

The method in Paper III partitions the spatial frequency spectrum into many look pairs. It inspired the work in Paper IV and Paper V where we instead partition the spectrum into many sublooks. Paper IV and Paper V introduce the multilook methods to ultrasound. The work emphasizes how the detection performance can be drastically improved by prewhitening the images before point detection analysis. Applying a whitening transform is not computationally heavy for modern software systems. The increase in software processing power makes it possible to generate both the standard display image and images that are preferable for analysis. It is thereby possible to use the whitened image for the point detection analysis. An option could be to indicate the detected point scatterer locations on the standard display image. To the author's knowledge, using a whitened image is not standard practice in ultrasound. The work in this thesis illuminates the great potential improvement in point detection by using an optimized prewhitening method. It also raises awareness of how the whitening filter limits can affect point detection. The research has established the importance of prewhitening for the ultrasound community regarding point detection. The work has also inspired changes to supervisor Roy Hansen's work on underwater images, especially the importance of optimizing the whitening transform when detecting point scatterers.

The multilook methods from this thesis will be used in further work on detecting coherent scatterers in large sonar images [Han+22]. In [Han+22], the multilook coherence method is tested on real synthetic aperture sonar data collected by a HUGIN autonomous underwater vehicle. This thesis work has shown the potential of using multilook methods in the ultrasound community. It has provided a foundation for further studies on clinical images. The multilook methods will be tested on ultrasound heart images with scar tissue. The detection study on textured images in Paper V nears authentic, inhomogenous ultrasound images. Detection on clinical ultrasound images is the natural next step.

There are several applications in medical ultrasound in which point detection is essential, such as breast microcalcifications, kidney stones, and point tracking. For example, breast microcalcifications are often the first indication of cancer and consequently key to early cancer diagnosis. The latest report by the World Health Organization and International Agency for Research on Cancer showed that the incidence and mortality of breast cancer ranked first place among female cancer patients [Ouy+19]. In [Ouy+19], Ouyang et al. present a review summarizing the current ultrasonic detection methods for breast microcalcifications. There are some commercialized techniques and several others currently in the experimental stage. Ultrasound imaging is low-cost and has real-time capability. It does not include ionizing radiation as conventional mammography does. With the steady increase in software flexibility and equipment quality, it is possible that ultrasound imaging will be used as the early screening method in the future. This thesis shows promising potential for going further with the multilook methods on clinical images with known breast microcalcifications.

Bibliography

[Abr19] Abraham, D. A. *Underwater Acoustic Signal Processing: Modeling, Detection, and Estimation.* Springer, 2019.

[Ale16] Alessio, S. M. *Digital Signal Processing and Spectral Analysis for Scientists.* Cham, Switzerland: Springer, 2016.

[AM10] Asl, B. M. and Mahloojifar, A. "Eigenspace-based minimum variance beamforming applied to medical ultrasound imaging". In: *IEEE Trans. Ultrason., Ferroelectr., Freq. Control* vol. 57, no. 11 (Nov. 2010), pp. 2381–2390.

[AT00] Anderson, M. E. and Trahey, G. E. *A seminar on k-space applied to medical ultrasound.* Duke Univ., Apr. 2000.

[BCM05] Buades, A., Coll, B., and Morel, J.-M. "A Non-Local Algorithm for Image Denoising". In: *Proc. IEEE Comput. Soc. Conf. Comput. Vis. Pattern Recognit.* Vol. 2. June 2005, pp. 60–65.

[Bur78] Burckhardt, C. B. "Speckle in Ultrasound B-Mode Scans". In: *IEEE Trans. Sonics Ultrason.* vol. 25 (1 Jan. 1978), pp. 1–6.

[Cap69] Capon, J. "High-resolution frequency-wavenumber spectrum analysis". In: *Proc. IEEE* vol. 57 (8 Aug. 1969), pp. 1408–1418.

[CGM95] Carrara, W. C., Goodman, R. S., and Majewski, R. M. *Spotlight synthetic aperture radar: signal processing algorithms.* Boston, USA: Artech House, 1995.

[Che+20] Chen, C. et al. "Point Spread Function Formation in Plane-Wave Imaging: A Theoretical Approximation in Fourier Migration". In: *IEEE Trans. Ultrason., Ferroelectr., Freq. Control* vol. 67, no. 2 (Feb. 2020), pp. 296–307.

[CLR95] Conte, E., Lops, M., and Ricci, G. "Asymptotically optimum radar detection in compound-Gaussian clutter". In: *IEEE Trans. Aerosp. Electron. Syst.* vol. 31, no. 2 (Apr. 1995), pp. 617–625.

[CLR96] Conte, E., Lops, M., and Ricci, G. "Adaptive matched filter detection in spherically invariant noise". In: *IEEE Signal Process. Lett.* vol. 3, no. 8 (Aug. 1996), pp. 248–250.

[Cob07] Cobbold, R. S. C. *Foundations in Biomedical Ultrasound.* Oxford University Press, 2007.

[CPF09a] Camacho, J., Parrilla, M., and Fritsch, C. "Grating-lobes reduction by application of Phase Coherence Factors". In: *Proc. IEEE Int. Ultrason. Symp. (IUS).* Sept. 2009, pp. 341–344.

[CPF09b] Camacho, J., Parrilla, M., and Fritsch, C. “Phase Coherence Imaging”. In: *IEEE Trans. Ultrason., Ferroelectr., Freq. Control* vol. 56, no. 5 (May 2009), pp. 958–974.

[Dah+11] Dahl, J. J. et al. “Lesion detectability in diagnostic ultrasound with short-lag spatial coherence imaging”. In: *Ultrason. Imaging* vol. 33, no. 2 (Apr. 2011), pp. 119–133.

[Den+13] Denarie, B. et al. “Coherent Plane Wave Compounding for Very High Frame Rate Ultrasonography of Rapidly Moving Targets”. In: *IEEE Trans. Med. Imag.* vol. 32, no. 7 (July 2013), pp. 1265–1276.

[DFP09] De Maio, A., Fornaro, G., and Pauciullo, A. “Detection of Single Scatterers in Multidimensional SAR Imaging”. In: *IEEE Trans. on Geosci. Remote Sens.* vol. 47, no. 7 (Apr. 2009), pp. 2284–2297.

[EG05] Ewens, W. J. and Grant, G. R. *Statistical Methods in Bioinformatics: An Introduction.* II. Springer, 2005.

[Fed+03] Fedewa, R. et al. “Spatial coherence of the nonlinearly generated second harmonic portion of backscatter for a clinical imaging system”. In: *IEEE Trans. Ultrason., Ferroelectr., Freq. Control* vol. 50, no. 8 (Aug. 2003), pp. 1010–1022.

[Fer+03] Ferro-Famil, L. et al. “Scene characterization using subaperture polarimetric SAR data”. In: *IEEE Trans. Geosci. Remote Sens.* vol. 41, no. 10 (Oct. 2003), pp. 2264–2276.

[Gol+21] Golfetto, C. et al. “Retrospective Transmit Beamforming and Coherent Plane-Wave Compounding for Microvascular Doppler Imaging: A Comparison Study”. In: *IEEE Trans. Ultrason., Ferroelectr., Freq. Control* vol. 68, no. 4 (Apr. 2021), pp. 1105–1116.

[GW10] Gonzales, R. C. and Woods, R. E. *Digital Image Processing*. III. Pearson, 2010.

[Han+22] Hansen, R. E. et al. “Detection of Coherent Scatterers in Synthetic Aperture Sonar Using Multilook Coherence”. In: *Proc. Eur. Conf. Synth. Aperture Radar (EUSAR).* VDE Verlag, July 2022, pp. 1–6.

[Har78] Harris, F. J. “On the use of windows for harmonic analysis with the discrete Fourier transform”. In: *Proc. IEEE* vol. 66 (1 Jan. 1978), pp. 51–83.

[HM82] Hanley, J. A. and McNeil, B. J. “The Meaning and Use of the Area under a Receiver Operating Characteristic (ROC) Curve”. In: *Radiology* vol. 143, no. 1 (Apr. 1982), pp. 29–36.

[Hol19] Holm, S. *Waves with Power-Law Attenuation.* Cham, Switzerland: Springer, 2019.

[HTu+92] H.Turnbull, D. et al. “Simulation of B-scan images from two-dimensional transducer arrays: Part I — Methods and quantitative contrast measurements”. In: *Ultrason. Imaging* vol. 14, no. 4 (Oct. 1992), pp. 323–343.

[HV14] Hunter, A. J. and Vossen, R. van. “Sonar target enhancement by shrinkage of incoherent wavelet coefficients”. In: *J. Acoust. Soc. Am.* vol. 135, no. 1 (Jan. 2014), pp. 262–268.

[Hve+17] Hverven, S. M. et al. “The influence of speckle statistics on contrast metrics in ultrasound imaging”. In: *Proc. IEEE Int. Ultrason. Symp. (IUS).* Sept. 2017, pp. 1–4.

[IH94] Insana, M. F. and Hall, T. J. “Visual detection efficiency in ultrasonic imaging: A framework for objective assessment of image quality”. In: *J. Acoust. Soc. Am.* vol. 95, no. 4 (Apr. 1994), pp. 2081–2090.

[Jak+96] Jakowatz, J. C. V. et al. *Spotlight-Mode Synthetic Aperture Radar: A Signal Processing Approach.* Boston, MA: Springer, 1996.

[JD93] Johnson, D. H. and Dudgeon, D. E. *Array signal processing: concepts and techniques.* Vol. XIII. Upper Saddle River, NJ: PTR Prentice Hall, 1993.

[Jen+06] Jensen, J. A. et al. “Synthetic aperture ultrasound imaging”. In: *Ultrasonics* vol. 44 (Dec. 2006), e5–e15.

[Jen96] Jensen, J. A. “FIELD: A Program for Simulating Ultrasound Systems”. In: *Proc. 10th Nordicbaltic Conf. Biomed. Imag., Suppl. 1, Part 1.* Vol. 4. 1996, pp. 351–353.

[JS92] Jensen, J. A. and Svendsen, N. B. “Calculation of Pressure Fields from Arbitrarily Shaped, Apodized, and Excited Ultrasound Transducers”. In: *IEEE Trans. Ultrason., Ferroelectr., Freq. Control* vol. 39, no. 2 (Mar. 1992), pp. 262–267.

[Kay13] Kay, S. M. *Fundamentals of Statistical Signal Processing, Volume III: Practical Algorithm Development.* Vol. III. Pearson, 2013.

[Kay98] Kay, S. M. *Fundamentals of Statistical Signal Processing, Volume II: Detection Theory.* Vol. II. Prentice-Hall PTR, 1998.

[Kel86] Kelly, E. J. “An Adaptive Detection Algorithm”. In: *IEEE Trans. Aerosp. Electron.* vol. 22, no. 2 (Mar. 1986), pp. 115–127.

[KK99] Koivunen, A. C. and Kostinski, A. B. “The Feasibility of Data Whitening to Improve Performance of Weather Radar”. In: *J. Appl. Meteorol. (1988-2005)* vol. 38, no. 6 (June 1999), pp. 741–749.

[KLS18] Kessy, A., Lewin, A., and Strimmer, K. “Optimal Whitening and Decorrelation”. In: *Am. Stat.* vol. 72, no. 4 (2018), pp. 309–314.

[Lev08] Levy, B. C. *Principles of Signal Detection and Parameter Estimation.* Springer, 2008.

[LL03] Li, P. C. and Li, M. L. “Adaptive imaging using the generalized coherence factor”. In: *IEEE Trans. Ultrason., Ferroelectr., Freq. Control* vol. 50, no. 2 (Feb. 2003), pp. 128–141.

[LPW04] Lacefield, J. C., Pilkington, W. C., and Waag, R. C. “Comparisons of lesion detectability in ultrasound images acquired using time-shift compensation and spatial compounding”. In: *IEEE Trans. Ultrason., Ferroelectr., Freq. Control* vol. 51, no. 12 (Dec. 2004), pp. 1649–1659.

[Mat+15] Matrone, G. et al. “The Delay Multiply and Sum Beamforming Algorithm in Ultrasound B - Mode Medical Imaging”. In: *IEEE Trans. Med. Imag.* vol. 34, no. 4 (2015), pp. 1–10.

[MF94] Mallart, R. and Fink, M. “Adaptive focusing in scattering media through sound-speed inhomogeneities: The van Cittert Zernike approach and focusing criterion”. In: *J. Acoust. Soc. Am.* vol. 96, no. 6 (Dec. 1994), pp. 3721–3732.

[MI11] Manolakis, D. G. and Ingle, V. K. *Applied Digital Signal Processing: Theory and Practice.* Cambridge, UK: Cambridge University Press, 2011.

[Mon+09] Montaldo, G. et al. “Coherent plane-wave compounding for very high frame rate ultrasonography and transient elastography”. In: *IEEE Trans. Ultrason., Ferroelectr., Freq. Control* vol. 56, no. 3 (Mar. 2009), pp. 489–506.

[NH13] Näsholm, S. and Holm, S. “On a fractional Zener elastic wave equation”. In: *Fract. Calc. Appl. Anal.* vol. 16, no. 1 (Mar. 2013), pp. 26–50.

[OQ98] Oliver, C. and Quegan, S. *Understanding Synthetic Aperture Radar Images.* Artech house, Inc., 1998.

[Ouy+19] Ouyang, Y. et al. “A review of ultrasound detection methods for breast microcalcification”. In: *Math. Biosci. Eng.* vol. 16 (4 Mar. 2019), pp. 1761–1785.

[PF83] Patterson, M. S. and Foster, F. S. “The Improvement and quantitative assessment of b-mode images produced by an annular array/cone hybrid”. In: *Ultrason. Imaging* vol. 5, no. 3 (July 1983), pp. 195–213.

[PM90] Perona, P. and Malik, J. “Scale-space and edge detection using anisotropic diffusion”. In: *IEEE Trans. Pattern Anal. Mach. Intell.* vol. 12, no. 7 (July 1990), pp. 629–639.

[PRA18] Prieur, F., Rindal, O. M. H., and Austeng, A. “Signal Coherence and Image Amplitude With the Filtered Delay Multiply and Sum Beamformer”. In: vol. 65. 7. July 2018, pp. 1133–1140.

[Pri+17] Prieur, F. et al. “Influence of the Delay-Multiply-And-Sum beamformer on the ultrasound image amplitude”. In: *Proc. IEEE Int. Ultrason. Symp. (IUS).* Sept. 2017, pp. 1–4.

[Rin+19] Rindal, O. M. H. et al. “The Effect of Dynamic Range Alterations in the Estimation of Contrast”. In: *IEEE Trans. Ultrason., Ferroelectr., Freq. Control* vol. 66, no. 7 (July 2019), pp. 1198–1208.

[Rin19] Rindal, O. M. H. “Software Beamforming in Medical Ultrasound Imaging- a blessing and a curse”. Accessed on: Nov. 19, 2019. PhD thesis. Oslo, Norway: Univ. of Oslo, Nov. 2019.

[Rod+17] Rodriguez-Molares, A. et al. “The UltraSound ToolBox”. In: *Proc. IEEE Int. Ultrason. Symp. (IUS).* Sept. 2017, pp. 1–4.

[Rod+20] Rodriguez-Molares, A. et al. “The Generalized Contrast-to-Noise Ratio: A Formal Definition for Lesion Detectability”. In: *IEEE Trans. Ultrason., Ferroelectr., Freq. Control* vol. 67, no. 4 (Apr. 2020), pp. 745–759.

[RRA17] Rindal, O. M. H., Rodriguez-Molares, A., and Austeng, A. “The dark region artifact in adaptive ultrasound beamforming”. In: *Proc. IEEE Int. Ultrason. Symp. (IUS).* Sept. 2017, pp. 1–4.

[SAH07] Synnevåg, J.-F., Austeng, A., and Holm, S. “Adaptive Beamforming Applied to Medical Ultrasound Imaging”. In: *IEEE Trans. Ultrason., Ferroelectr., Freq. Control* vol. 54, no. 8 (Aug. 2007).

[SAH09] Synnevåg, J.-F., Austeng, A., and Holm, S. “Benefits of minimum-variance beamforming in medical ultrasound imaging”. In: *IEEE Trans. Ultrason., Ferroelectr., Freq. Control* vol. 56, no. 9 (Sept. 2009), pp. 1868–1879.

[San+15] Sanjuan-Ferrer, M. J. et al. “A New Detection Algorithm for Coherent Scatterers in SAR Data”. In: *IEEE Trans. on Geosci. Remote Sens.* vol. 53, no. 11 (June 2015), pp. 6293–6307.

[San14] Sanjuan-Ferrer, M. J. “Detection of coherent scatterers in SAR data Algorithms and applications”. PhD thesis. ETH Zürich, Jan. 2014.

[Smi+83] Smith, S. W. et al. “Low Contrast Detectability and Contrast/Detail Analysis in Medical Ultrasound”. In: *IEEE Trans. Sonics Ultrason.* vol. 30, no. 3 (May 1983), pp. 164–173.

[SW84] Smith, S. W. and Wagner, R. F. “Ultrasound speckle size and lesion signal to noise ratio: verification of theory”. In: *Ultrason. Imaging* vol. 6, no. 2 (Apr. 1984), pp. 174–180.

[Sza14] Szabo, T. L. *Diagnostic Ultrasound Imaging: Inside Out.* Second. Elsevier Academic Press, 2014.

[THA22] Thon, S. H., Hansen, R. E., and Austeng, A. “Detection of Point Scatterers in Medical Ultrasound”. In: *IEEE Trans. Ultrason., Ferroelectr., Freq. Control* vol. 69, no. 2 (Feb. 2022), pp. 617–628.

[TM98] Tomasi, C. and Manduchi, R. “Bilateral filtering for gray and color images”. In: *Proc. IEEE Int. Conf. Comput. Vis.* Jan. 1998, pp. 839–846.

[TRL15] Torp, H., Rodriguez-Molares, A., and Løvstakken, L. “Optimum beamformer strategy for detecting signals in clutter noise”. In: *Proc. IEEE Int. Ultrason. Symp. (IUS).* Oct. 2015, pp. 1–4.

[Wag+83] Wagner, R. F. et al. “Statistics of Speckle in Ultrasound B-Scans”. In: *IEEE Trans. Sonics Ultrason.* vol. 30, no. 3 (May 1983), pp. 156–163.

[Zem+05] Zemp, R. J. et al. “Detection performance theory for ultrasound imaging systems”. In: *IEEE Trans. Med. Imag.* vol. 24, no. 3 (Mar. 2005), pp. 300–310.

Papers

Paper I

The Influence of Speckle Statistics on Contrast Metrics in Ultrasound Imaging

Stine Myhre Hverven, Ole Marius Hoel Rindal, Alfonso Rodriguez-Molares, and Andreas Austeng

Published in *IEEE International Ultrasonics Symposium (IUS)*, Washington, DC, 2017, pp. 1-4, DOI: 10.1109/ULTSYM.2017.8091875

Abstract

Adaptive beamformers aim for improved resolution and contrast in the ultrasound images, and their performance is typically benchmarked using metrics such as contrast ratio (CR) and contrast-to-noise ratio (CNR). Using synthetic aperture Field II simulations, we show that certain beamformers alter speckle statistics and that this opens up for cherry picking of contrast metrics.

I.1 Introduction

Quality assessment of ultrasound images is difficult since image quality is subjective to the human observer. Nevertheless, image quality metrics are imperative when benchmarking different beamforming techniques. If we do not know how a beamformer alters an image, a quality metric might give an incorrect measurement of the actual image quality. Using the standard Delay-And-Sum (DAS) beamformer as a reference, we examine several adaptive beamformers presented in literature; Capon's Minimum Variance (MV), Eigenspace Based Minimum Variance (EBMV), Coherence Factor (CF), Generalized Coherence Factor (GCF), Phase Coherence Factor (PCF), and Delay-Multiply-And-Sum (DMAS). We show that the speckle statistics for some of these adaptive beamformers are dependent on both scattering intensity and location of the region of interest, resulting in contradicting measurements of standard contrast metrics.

I.2 Background

In this section we briefly introduce the theory for the following beamforming methods; DAS, MV, EBMV, CF, GCF, PCF and DMAS. We refer to [Rin+16] and [RRA17] for full description of the implementation of the beamformers and the parameters used in this study.

I.2.1 Conventional Delay-And-Sum (DAS)

Conventional DAS for image pixel $[z, x]$ is defined as:

$$S_{\text{DAS}}[z, x] = \sum_{m=0}^{M-1} w_m y_m[z, x] \tag{I.1}$$

where M is the number of elements, $y_m[z, x]$ is the delayed signal received at element m, and w_m is a predefined weight for element m.

I.2.2 Minimum Variance Beamforming

Capon's Minimum Variance (MV) beamformer calculates for each pixel a data dependent set of weights $w^T = \{w_0, w_1, \ldots, w_{M-1}\}$ that minimizes power while maintaining unity gain in the steering direction [SAH07]. The solution found with Lagrange multipliers turns out to be dependent on the spatial covariance matrix. The MV weights are used in the summation in (I.1).

The Eigenspace Based Minimum Variance (EBMV) beamformer is an extension of the MV beamformer which utilizes the eigenstructure of the covariance matrix to enhance performance [AM10]. The covariance matrix is eigendecomposed into a signal and noise subspace, and the conventional MV weights are projected onto the signal subspace.

I.2.3 Coherence Based Beamforming

The Coherence Factor (CF) beamformer calculates the ratio between coherent and incoherent energy across the aperture [MF94]. It is used as an adaptive weight to the DAS image [LL03].

The Generalized Coherence Factor (GCF) beamformer is an extension of CF which utilizes the Fourier-spectrum over the receive aperture of the delayed channel data [LL03]. The GCF is calculated as the ratio between the energy in a small angular sector around the direction of interest divided by the total energy of the Fourier-spectrum. It is also used as an adaptive weight to the DAS image.

The Phase Coherence Factor (PCF) beamformer [CPF09] calculates for each pixel an adaptive weight based on the phase of the receive data. The weights are multiplied with the DAS image.

The Delay-Multiply-And-Sum (DMAS) [Mat+15] multiplies the delayed RF-signals using a "signed" square root. The sum of these signals is band-pass filtered around an "artificial second harmonic" signal before conventional envelope detection and log-compression of the signal results in the final image. It is not obvious that this is a "coherence based beamformer". However, it has been shown that "The DMAS enhances signal coherence and can be seen as an intermediate solution between the DAS beamformer and the coherence factor method" [Pri+17].

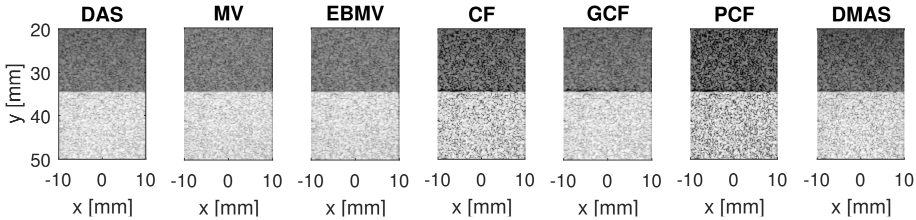

(a) vertical orientation

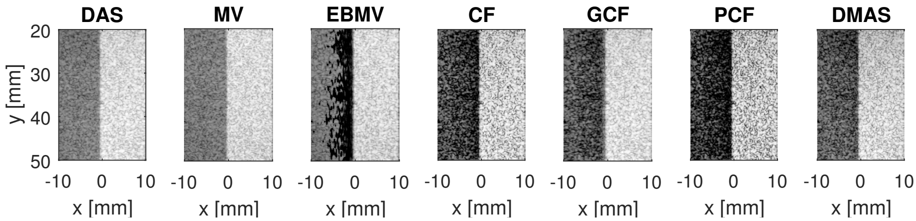

(b) horizontal orientation

Figure I.1: Ultrasound images for the seven different beamformers. The vertical orientation of the speckle phantom is in (a), and the horizontal orientation is in (b). The images are shown with a dynamic range of 80 dB.

Synthetic transmit aperture datasets were simulated in Field II [JS92][Jen96] using a 128 element, λ pitch, linear array with 5 MHz center frequency (L11-4v). The simulated phantom consists of two speckle regions with intensity at -30 dB and 0 dB, using at least 43 scatterers per resolution cell. To investigate any spatial dependency of the beamformer's speckle statistics, two different phantoms were designed. The first phantom has the speckle regions in vertical orientation, where the low intensity region is above the high intensity region as shown in Figure I.1(a). The other phantom is horizontally oriented with the speckle regions located side-by-side as shown in Figure I.1(b).

The beamforming was performed in MATLAB (Mathworks, Natick, MA) using The UltraSound ToolBox (USTB) [Rod+17]. Each transmit sequence was combined before applying the different beamforming methods briefly described above on the combined receive aperture.

The two most common contrast metrics are contrast ratio (CR) and contrast-to-noise ratio (CNR). CR is defined as [HTu+92]:

$$\mathrm{CR} = 20\log_{10}\left(\frac{\mu_1}{\mu_2}\right),$$

where μ_1 and μ_2 are the mean intensity values of the two rectangular speckle regions. The values for the region are calculated with a 0.9 mm margin from the other speckle region, and horizontal and vertical edge margins of 1.5 mm and 3.0 mm. CNR weighs the intensity difference between the two regions with the average variance [PF83]:

$$\text{CNR} = \frac{|\mu_1 - \mu_2|}{\sqrt{(\sigma_1^2 + \sigma_2^2)/2}},$$

where μ_i is the mean intensity value and σ_i^2 is the variance of speckle region i.

I.3 Results

Images created with the DAS, MV, EBMV, CF, GCF, PCF and DMAS beamformers for the vertical speckle phantom are shown in Figure I.1(a) and images for the horizontal phantom are shown in Figure I.1(b). To measure the speckle statistics for the different beamformers in Figure I.1, the normalized probability distribution function (PDF) of each speckle region was estimated. Figure I.2 shows the estimated PDFs of the horizontally oriented phantom shown in Figure I.1, together with the corresponding signal-to-noise ratio (SNR=μ/σ). The estimated PDFs of the speckle region with high intensity is presented in Figure I.2(a). The theoretical Rayleigh distribution for DAS, with SNR = 1.91 [Wag+83], is plotted for comparison. Figure I.2(b) presents the statistics of the low intensity speckle region.

Figure I.3 shows the estimated PDFs of the images after log-compression of the intensity values. Figure I.3(a) shows the vertical speckle phantom and Figure I.3(b) shows for the horizontal speckle phantom. In both plots the estimated PDFs of the low intensity regions are plotted with a solid line, while the estimated PDFs of the high intensity regions are plotted with a dashed line. The SNR, measured from the envelope before log-compression, is indicated in the legend. Figure I.4 shows the CR and CNR measurements for both phantom orientations for the different beamformers.

I.4 Discussion

Figure I.1 shows the different beamformed images for our simulation with 30 dB intensity difference between the speckle regions and two phantom orientations. From the images, we notice how especially the CF and PCF images have higher variance than the DAS image. When the two speckle regions are side-by-side , i.e. horizontally oriented, the adaptive beamformers EBMV, CF and PCF seem to darken the low intensity speckle region in the transition between the two regions.

We can observe in Figure I.2(a) that DAS, MV, EBMV and GCF seem to approximately follow the theoretical Rayleigh distribution. The above beamformers have SNR values close to theoretical Rayleigh, i.e. SNR ≈ 1.91, whereas the CF, PCF and DMAS beamformers have very different distributions and much lower SNR values. However, for the low intensity region presented in Figure I.2(b), only the DAS and MV beamformers are Rayleigh distributed with SNR close to 1.91. The SNR values for the EBMV and GCF beamformers are significantly lower for the low intensity region than the high intensity region. This signifies that the beamformers alter the statistics of the two regions differently. For the CF and PCF beamformers, the SNR was much lower than 1.91 in both cases.

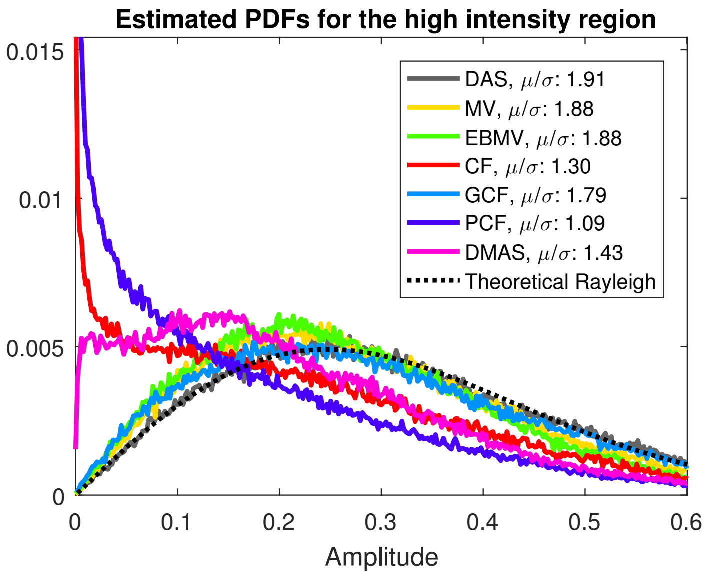

(a)

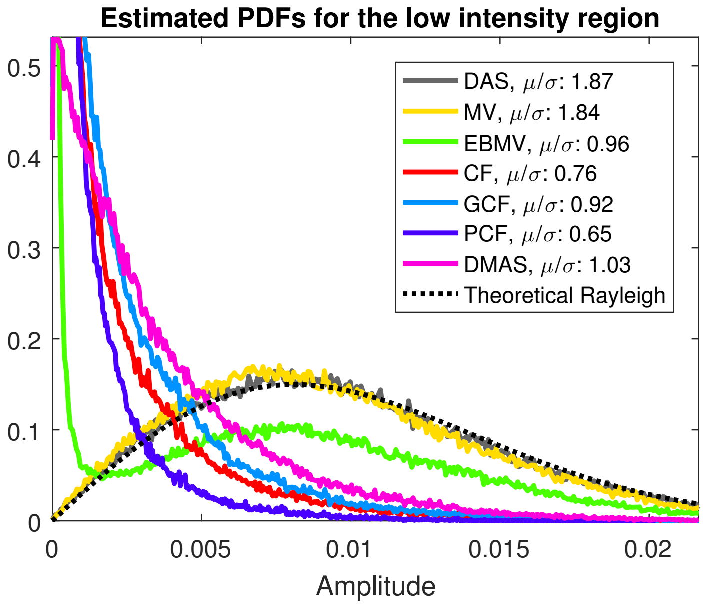

(b)

Figure I.2: Estimated probability distributions (PDF) of the two speckle regions in the horizontal phantom orientation, shown for all beamformers. DAS is compared to its respective theoretical Rayleigh distribution.

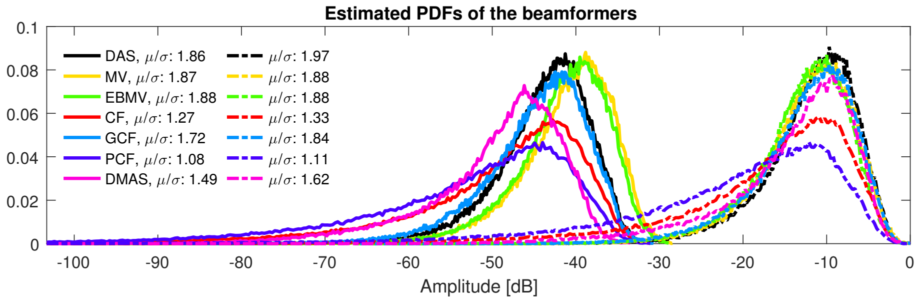

(a) Estimated PDF of dB-scaled image data, vertical orientation

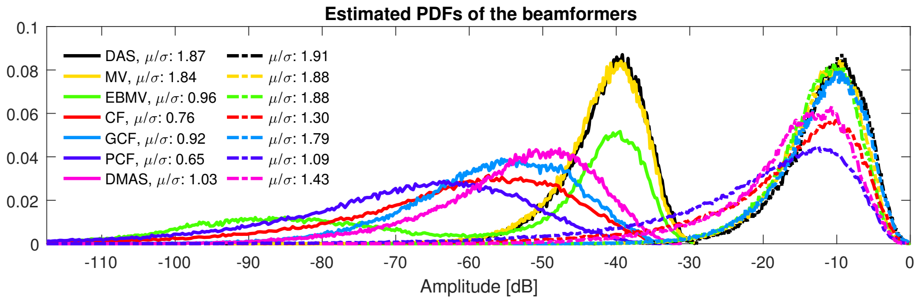

(b) Estimated PDF of dB-scaled image data, horizontal orientation

Figure I.3: Estimated PDFs of the log-compressed images for each speckle region, shown for all beamformers. When the speckle regions are in horizontal orientation, the statistics of the low intensity region is altered compared to the high intensity region.

Figure I.3 shows the estimated PDFs of the beamformed log-compressed images for both phantom orientations. When the speckle regions are orientated one on top of the other, i.e. vertical phantom orientation, the speckle statistics for each region within the same image are similar. However, when the speckle regions are horizontally oriented, several of the adaptive beamformers have different distributions for the two regions. The CF, PCF and DMAS beamformers, which had distributions far from theoretical Rayleigh in Figure I.2, have heavy left-tailed distributions for both phantom orientations. However, for the horizontally oriented phantom there is a clear difference between the low intensity region (solid line) and the high intensity region (dashed line). The EBMV, CF, GCF and PCF beamformers have much more heavy-tailed distributions for the low intensity region, which corresponds to increased variance. The DMAS beamformer has a deformed PDF for the low intensity region with a second peak emerging at very low intensity.

This leads to the results presented in Figure I.4, where we show that a beamformer may have high CR and simultaneously low CNR compared to DAS. The CR measurements in Figure I.4(b) indicate that the CF, GCF, PCF and DMAS beamformers have

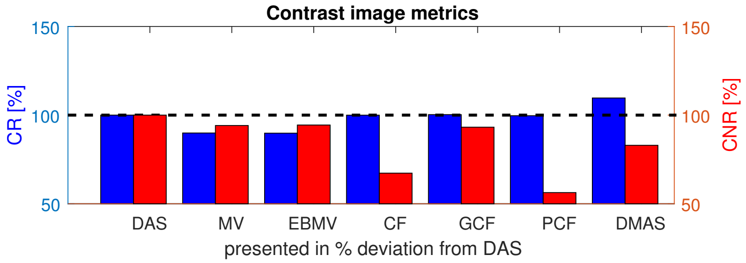

(a) Vertical orientation

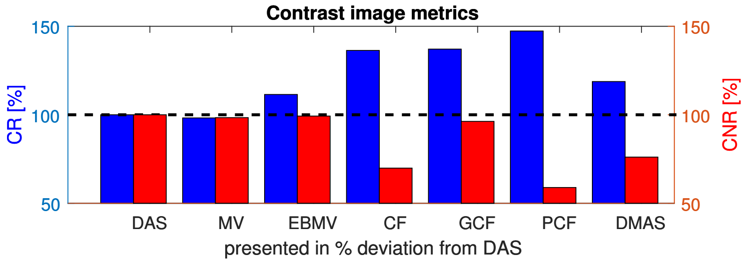

(b) Horizontal orientation

Figure I.4: Contrast metrics for the different adaptive beamformers compared to DAS, given different phantom orientations.

higher contrast than DAS, but concurrently lower CNR compared to DAS. This is consistent with what we observe in Figure I.3 where the EBMV, CF, PCF, GCF and DMAS beamformers have both increased the variance and the intensity difference between the regions. This means that apparent contrast enhancement can be due to alterations of the speckle statistics or the dynamic range. When a beamformer increases the contrast between the speckle regions while also increasing the intensity variance, it is not sufficient to only present one contrast metric when analyzing the beamformer's performance. Presenting only CR as a quality metric would not adequately describe the performance of for example the PCF beamformer when compared to conventional DAS.

The results show that several of the adaptive beamformers are spatially and intensity dependent when altering the speckle statistics of the image data. Further investigation of the intensity dependency should include varying the intensity difference between the regions. Benchmarking the performance of an adaptive beamformer by only using one contrast metric will not sufficiently address any possible spatial or intensity dependent behavior.

I.5 Conclusions

We have shown that the effect of adaptive beamformers on the speckle statistics vary for different beamformers. The effect varies also with regard to spatial location of the speckle regions examined. When evaluating a beamformer's performance in comparison to conventional DAS, both the contrast and contrast-to-noise metrics should be presented. Since an adaptive beamformer can alter the speckle statistics, it is imperative that a performance comparison also includes a statistical discussion.

References

[AM10] Asl, B. M. and Mahloojifar, A. “Eigenspace-based minimum variance beamforming applied to medical ultrasound imaging”. In: *IEEE Trans. Ultrason., Ferroelectr., Freq. Control* vol. 57, no. 11 (Nov. 2010), pp. 2381–2390.

[CPF09] Camacho, J., Parrilla, M., and Fritsch, C. “Phase Coherence Imaging”. In: *IEEE Trans. Ultrason., Ferroelectr., Freq. Control* vol. 56, no. 5 (May 2009), pp. 958–974.

[HTu+92] H.Turnbull, D. et al. “Simulation of B-scan images from two-dimensional transducer arrays: Part I — Methods and quantitative contrast measurements”. In: *Ultrason. Imaging* vol. 14, no. 4 (Oct. 1992), pp. 323–343.

[Jen96] Jensen, J. A. “FIELD: A Program for Simulating Ultrasound Systems”. In: *Proc. 10th Nordicbaltic Conf. Biomed. Imag., Suppl. 1, Part 1.* Vol. 4. 1996, pp. 351–353.

[JS92] Jensen, J. A. and Svendsen, N. B. “Calculation of Pressure Fields from Arbitrarily Shaped, Apodized, and Excited Ultrasound Transducers”. In: *IEEE Trans. Ultrason., Ferroelectr., Freq. Control* vol. 39, no. 2 (Mar. 1992), pp. 262–267.

[LL03] Li, P. C. and Li, M. L. “Adaptive imaging using the generalized coherence factor”. In: *IEEE Trans. Ultrason., Ferroelectr., Freq. Control* vol. 50, no. 2 (Feb. 2003), pp. 128–141.

[Mat+15] Matrone, G. et al. “The Delay Multiply and Sum Beamforming Algorithm in Ultrasound B - Mode Medical Imaging”. In: *IEEE Trans. Med. Imag.* vol. 34, no. 4 (2015), pp. 1–10.

[MF94] Mallart, R. and Fink, M. “Adaptive focusing in scattering media through sound-speed inhomogeneities: The van Cittert Zernike approach and focusing criterion”. In: *J. Acoust. Soc. Am.* vol. 96, no. 6 (Dec. 1994), pp. 3721–3732.

[PF83] Patterson, M. S. and Foster, F. S. “The Improvement and quantitative assessment of b-mode images produced by an annular array/cone hybrid”. In: *Ultrason. Imaging* vol. 5, no. 3 (July 1983), pp. 195–213.

[Pri+17] Prieur, F. et al. “Influence of the Delay-Multiply-And-Sum beamformer on the ultrasound image amplitude”. In: *Proc. IEEE Int. Ultrason. Symp. (IUS).* Sept. 2017, pp. 1–4.

[Rin+16] Rindal, O. M. H. et al. “The dynamic range of adaptive beamformers”. In: *Proc. IEEE Int. Ultrason. Symp. (IUS)* (Sept. 2016), pp. 1–4.

[Rod+17] Rodriguez-Molares, A. et al. “The UltraSound ToolBox”. In: *Proc. IEEE Int. Ultrason. Symp. (IUS).* Sept. 2017, pp. 1–4.

[RRA17] Rindal, O. M. H., Rodriguez-Molares, A., and Austeng, A. “The dark region artifact in adaptive ultrasound beamforming”. In: *Proc. IEEE Int. Ultrason. Symp. (IUS).* Sept. 2017, pp. 1–4.

[SAH07] Synnevåg, J.-F., Austeng, A., and Holm, S. "Adaptive Beamforming Applied to Medical Ultrasound Imaging". In: *IEEE Trans. Ultrason., Ferroelectr., Freq. Control* vol. 54, no. 8 (Aug. 2007).

[Wag+83] Wagner, R. F. et al. "Statistics of Speckle in Ultrasound B-Scans". In: *IEEE Trans. Sonics Ultrason.* vol. 30, no. 3 (May 1983), pp. 156–163.

Paper II

Detection of Point Scatterers in Medical Ultrasound

Stine Hverven Thon, Roy Edgar Hansen, and Andreas Austeng

Published in *IEEE Transactions on Ultrasonics, Ferroelectrics, and Frequency Control*, Feb. 2022, 69 (2): 617-628. DOI: 10.1109/TUFFC.2021.3129619

II

Abstract

We present an overview of the detection of point scatterers in ultrasound images and suggest strategies for evaluating and measuring the detection performance. We use synthetic aperture Field II simulations of a point scatterer in speckle background and evaluate how common imaging techniques affect point target detectability. We discuss how to compare different methods and calculate confidence intervals. In general, applying speckle reduction methods reduces the point detection performance. However, the results show that it is possible to smooth the speckle background and preserve relatively high performance with a suitable and optimized method. The different detection performances of the advanced beamforming methods Coherence Factor (CF), Phase Coherence Factor (PCF), and Capon's Minimum Variance (MV) are presented and benchmarked with standard Delay-and-Sum (DAS). The results show that CF achieves slightly better detection performance than DAS for weak point scatterers, whereas PCF and MV perform worse than DAS. Choice of apodization window and adaptive aperture size affects the probability of detection. Results show that methods that preserve spatial resolution have better detection performance of point scatterers.

II.1 Introduction

Detection of point scatterers in ultrasound images can be challenging due to peaks in the speckle background. Point scatterers are small, highly coherent targets, and there are several applications in medical ultrasound in which their detection is essential. Breast microcalcifications are small, hard calcium deposits in soft tissue that behave as point scatterers in an ultrasound image and can be an early indicator for cancer [And+97; AST00; AST98; Flø+17; Mac+18]. Ultrasound can detect kidney stones, but accurate sizing and diagnosis can be difficult due to background clutter [Ray+10; Tie+18]. Point tracking, use of contrast microbubbles, and biopsy needle tracking are other examples where detection of point targets is crucial [Dia+18; Mat+19; MBR20].

Point scatterers are also of interest in other fields, such as radar [OQ98] and sonar [Abr19].

Detection of a point scatterer in speckle can be viewed as a classical binary detection problem [Abr19; EG05; Kay13; Kay98; Lev08]. In 1983, Smith et al. [Smi+83] developed a statistical model for image quality by connecting contrast and lesion detection. Lesion detectability using contrast is now well established in medical ultrasound [Dah+11; IH94; LPW04; Rod+20; SW84; Zem+05]. However, the statistical properties of a lesion area are different from a point scatterer. In 1997, Anderson et al. [And+97] studied the effects of aperture geometry and phase aberration on point detection performance. In [AST98], they conclude that frequency and spatial compounding slightly improve point target detectability. They summarize their findings on the effect of phase aberration, sound speed errors, array aperture size, transducer center frequency, speckle reduction by compounding, and logarithmic compression in [AST00]. In [Ouy+19], Ouyang et al. reviewed many ultrasound methods for microcalcification detection. Huang et al. [Hua+14] created a detection algorithm based on coherence factor. Torp et al. [TRL15] applied detection theory to create a beamformer (BF) for signal detection.

In this paper, we present an overview and framework for the detection of point scatterers in ultrasound images. The motivation for this paper is to present strategies for calculating the detection performance for point scatterers in speckle, how to compare detection performance between different methods, and how common techniques in ultrasound affect the point detection performance. We discuss how to measure the detection performance and calculate confidence intervals. We establish an optimal intensity threshold detector based on standard Delay-And-Sum (DAS) beamforming. Using synthetic aperture Field II simulations [Jen+06; Jen96; JS92], we create images with a point scatterer in uniform speckle background. We vary the applied apodization, aperture size, beamforming, and speckle reduction method. We wish to evaluate how these common ultrasound techniques affect point detection performance. We apply the same detection strategy to the different images and measure the overall detection performances.

Applying an apodization window on the received channel echoes is a common approach to reduce sidelobes at the cost of spatial resolution [Sza14, p. 178] [JD93, p. 322]. Changes in aperture geometry are expected to give changes in detection performance [And+97]. We study aperture size to establish how reduced resolution degrades detection.

Speckle reduction methods are often applied on ultrasound images to improve contrast [Sza14, ch. 8.4.6]. Our results show that such methods reduce point detection performance, but the effect varies depending on the chosen method. A suitable speckle reduction method may retain high performance while still applying some smoothing to the background. However, an increased amount of smoothing degrades both the resolution and the detection performance.

Adaptive BFs are applied to improve image quality, and they affect the point detection performance. Using DAS as a reference, we examine several adaptive BFs presented in literature; Coherence Factor (CF) [MF94], Phase Coherence Factor (PCF) [CPF09b], and Capon's Minimum Variance (MV) [Cap69]. Our results show that CF achieves slightly better detection performance than DAS for weak point scatterers, whereas the other two perform worse than DAS.

The following chapter presents classical detection theory for point scatterers and strategies for calculating point detection performance. We then introduce the background theory for the BFs. Section II.4 presents the different choices for spatial resolution, apodization, and speckle reduction. Section II.5 shows the results, and in Section II.6 we discuss the effects on detection performance.

II.2 Background - Detection Theory

In this section, we present the background theory for how to measure and evaluate detection performance and introduce general detection theory as presented in [Abr19; Kay98; Lev08]. We reduce the case to its simplest form and study the detection of a single point scatterer in uniform speckle background. Speckle is caused by interference in the echoes from many random scatterers within a resolution cell [Cob07, ch. 8.2.1], whereas point scatterers are small and highly coherent targets. The objective is to decide between two hypotheses: speckle background without ($\mathcal{H}_0$) or with ($\mathcal{H}_1$) a point signal present.

II.2.1 Point Target Detection Strategies

The probability of false alarm P_{FA} is estimated on sequences containing only speckle and the probability of detection P_{D} is estimated on sequences containing one point scatter in speckle. We count the number of intensity values above threshold γ in each scenario to find the number of false alarms and true positives. By comparing them to the total number of realizations R, we get P_{FA} and P_{D}. There is a choice in the type of strategy to use when calculating point detection performance. When presented with an ultrasound image, one assumes the strongest scatterer is the most likely point target candidate. However, the measured probability when picking the maximum point target will depend on how many independent pixels we consider. We can check if the chosen location is correct and the point is an actual true positive in a simulated environment. The overall detection performance depends on how we choose to count false alarms and true positives. In this section, we present the theory behind the five possible detection strategies listed in Table II.1. Based on the results, we choose which strategy to use when measuring the detection performance of the different 2-D ultrasound imaging methods.

The probability distribution of an ideal point signal in additive white Gaussian noise in complex sequences is statistically equivalent to an ideal point in a critically sampled, fully developed speckle scene. To illustrate the detection theory, we consider a simple one-dimensional (1-D) speckle sequence constructed as the complex sum of two normally distributed sequences. Under hypothesis $\mathcal{H}_1$, we add a point scatterer with intensity i_p at a discrete, random location. We estimate expressions for the detection probabilities of the different strategies using this ideal 1-D case.

As a measure of the point's intensity relative to the speckle background, we calculate the point's SNR metric as

$$\text{SNR} = 10 \log_{10} \left(\frac{i_p}{\beta} \right), \tag{II.1}$$

Table II.1: Point Detection Strategies

Strategy	Description
A	Consider each pixel in the image when counting false alarms and only known point pixel when counting true positives.
B	Consider only the maximum value in the image when counting both false alarms and true positives.
C	Consider the maximum value within a small image search window around the known point location when counting both false alarms and true positives.
D	Consider only the maximum value in the image when counting false alarms and only known point pixel when counting true positives.
E	Consider only the maximum value in the image, but additionally check if the chosen maximum is an actual true point when counting true positives.

where i_p is the point scatterer intensity, and β is the average speckle intensity. In this ideal 1-D study, $\beta = 2$.

II.2.2 Probability of False Alarm

The probability density function (PDF) for speckle in an ultrasound image is Rayleigh distributed in amplitude a [Bur78] [OQ98, p. 88] [Kay98, p. 30]

$$p(a)_{\text{Rayleigh}} = \begin{cases} \frac{a}{\sigma^2}\exp(-\frac{a^2}{2\sigma^2}) & \text{if } a > 0 \\ 0 & \text{if } a < 0. \end{cases} \tag{II.2}$$

Here σ is the scale parameter and $\sigma\sqrt{\pi/2}$ is the mean value. When searching for a point target, one assumes the point has a higher intensity than the surrounding background. To find candidate points, we apply a threshold on the intensity image [OQ98, ch. 10]. Intensity $i = a^2$ has a negative exponential PDF [Abr19, p. 261] [OQ98, p. 88][Cob07, p. 502]

$$p(i)_{\text{neg.exp.}} = \frac{1}{\beta}\exp\left(-\frac{i}{\beta}\right), \tag{II.3}$$

where β is the mean intensity value and $\beta = 2\sigma^2 = 2$. The threshold γ can be found by integrating the PDF for observation t of hypothesis $\mathcal{H}_0$ to the chosen P_{FA} value [Kay98, p. 30]

$$P_{\text{FA}} = \int_{\gamma}^{\infty} p(t;\mathcal{H}_0)dt. \tag{II.4}$$

Inserting (II.3) into (II.4), we get

$$P_{\text{FA}}(\gamma) = \exp\left(-\gamma/\beta\right), \tag{II.5}$$

where γ is the chosen intensity threshold. When measuring the $P_{FA}(\gamma)$, we simply count the number of false alarms above the threshold γ compared to the total number of realizations.

II.2.3 Probability of False Alarm for Maximum Intensity Value

Strategies B-E selects the maximum value for false alarm calculation. The maximum value of speckle increases however with the number of independent pixels N considered. This increases or inflates the P_{FA} for a given threshold, as shown in Figure II.1. Following [EG05, ch. 2.11], the probability is such that $Pr\{i_{max} \leq \gamma\} = (Pr\{i \leq \gamma\})^N$. The P_{FA} for the maximum of N random independent variables then becomes [EG05, ch. 2.11], [Kay98, p. 283], [Abr19, p. 587]

$$P_{FA}(\gamma)_{max} = 1-(1-P_{FA}(\gamma))^N = 1-(1-\exp(-\gamma/\beta))^N. \tag{II.6}$$

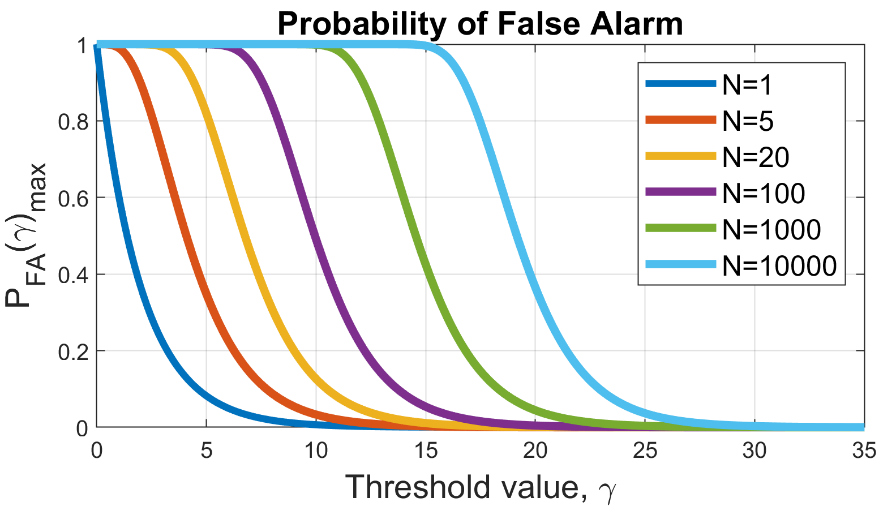

Figure II.1: Theoretical $P_{FA}(\gamma)_{max}$ vs. threshold values. The maximum value of a speckle sequence increases with sequence length. The theoretical mean value β is 2.

II.2.4 Probability of Detection

When a signal from a point scatterer is added to a speckle background, the PDF becomes Rician [Kay98, p. 31], [OQ98, p. 113]

$$p(a)_{\text{Rician}} = \begin{cases} \frac{a}{\sigma^2} \exp\left(-\frac{(a^2+\alpha^2)}{2\sigma^2}\right) I_0\left(\frac{\alpha a}{\sigma^2}\right) & \text{if } a > 0 \\ 0 & \text{if } a < 0, \end{cases} \tag{II.7}$$

where $\mathrm{I}_0(u)$ is the modified Bessel function of the first kind and zeroth order, and α^2 equals the point scatterer intensity i_p. If $\alpha = 0$, the PDF reduces back to Rayleigh. The right-tail probability can be shown to be related to that of the noncentral χ^2 random variable and must be evaluated numerically [Kay98, App. 2D] [Kay13, ch. 6.4]. The theoretical P_{D} for threshold γ can be estimated as [Kay98, p. 283]

$$P_{\mathrm{D}}(\gamma) \approx \mathcal{Q}_{\chi_2'^2(\tau)}\left(\frac{2\gamma}{\beta}\right), \tag{II.8}$$

where $\mathcal{Q}_{\chi_2'^2(\tau)}$ is the right-tail probability or complementary cumulative distribution function related to a noncentral χ^2 variable. P_{D} is estimated using $\tau = \frac{2i_p}{\beta}$, and it is therefore dependent on point SNR. By combining (II.5) with (II.8), P_{D} can be expressed in terms of P_{FA} as

$$P_{\mathrm{D}}(\gamma) \approx \mathcal{Q}_{\chi_2'^2(\tau)}\left(2\ln\frac{1}{P_{\mathrm{FA}}(\gamma)}\right). \tag{II.9}$$

By combining (II.6) with (II.8), P_{D} given by $P_{\mathrm{FA}}(\gamma)_{\max}$ is

$$P_{\mathrm{D}}(\gamma) \approx \mathcal{Q}_{\chi_2'^2(\tau)}\left(-2\ln\left(1-(1-P_{\mathrm{FA}}(\gamma)_{\max})^{\frac{1}{N}}\right)\right). \tag{II.10}$$

The P_{D} of the maximum value can be found as [Abr19, p. 588]

$$P_{\mathrm{D}}(\gamma)_{\max} = 1-(1-P_{\mathrm{D}}(\gamma))(1-P_{\mathrm{FA}}(\gamma)_{\max})^{\left(1-\frac{1}{N}\right)}. \tag{II.11}$$

Scalloping loss occurs when signals arrive between two samples [Har78]. A slight shift in location can cause a reduction in amplitude and energy leakage to the nearby pixels. Oversampling can help reduce this loss and ensure that the maximum achievable resolution is retained [MI11, ch. 6.7]. The increase in $P_{\mathrm{FA}}(\gamma)_{\max}$ when N increases is less than the alternative loss in signal-to-noise ratio (SNR), and oversampling is therefore beneficial for detection [Abr19, p. 497].

As with $P_{\mathrm{FA}}(\gamma)_{\max}$, $P_{\mathrm{D}}(\gamma)_{\max}$ also increases with N. Figure II.2 shows the different methods for calculating P_{D}. One can consider the known true point location, pick the maximum intensity peak of the whole vector, or pick the maximum within a small search window at the known point position. Since the maximum intensity peak may be in the background for low point SNRs, an option is to additionally check if the found candidate is the true point target. For weak point scatterers, the found candidate may be false, and $P_{\mathrm{D}}(\gamma)_{\text{true max}}$ will consequently not converge to 1 for low thresholds.

In Table II.2, we summarize the theoretical formulae corresponding to the five strategies in Table II.1. The formulae are for ideal signals in additive white Gaussian noise in complex sequences, which is statistically equivalent to ideal points in fully developed speckle and corresponds to DAS beamforming.

II.2.5 Evaluation of Detection Performance

A Receiver Operating Characteristics (ROC) curve is a standard method of displaying detection performance. It compares P_{D} to P_{FA} for a given threshold γ. By increasing γ, a lower P_{FA} can be obtained, but then P_{D} will also decrease. All points on the ROC

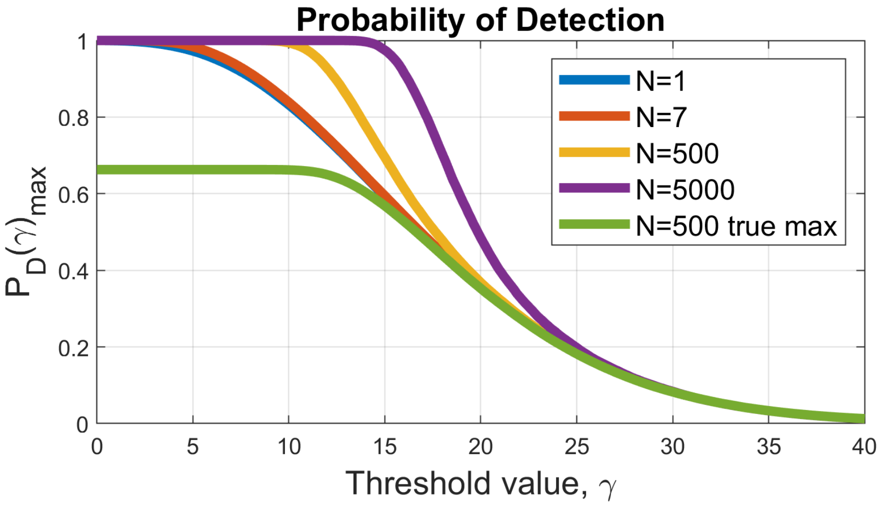

Figure II.2: Theoretical $P_{\mathrm{D}}(\gamma)_{\mathrm{max}}$ vs. threshold values and varying sequence length. Point SNR is 12 dB. The theoretical mean value β is 2. $P_{\mathrm{D}}(\gamma)_{\mathrm{max}}$ finds the maximum intensity point within the sequence. $N = 1$ signifies P_{D} calculated using known true point position only, $N = 7$ corresponds to a ± 3 pixel search window, and $N = 500$ signifies picking the maximum out of 500 pixels. $P_{\mathrm{D}}(\gamma)_{\text{true max}}$ additionally checks if the found maximum has correct position, and for weak point scatterers it will not converge to 1.

Table II.2: Summary of Theoretical Formulae for the Strategies

Strategy	Theoretical Formulae for P_{FA} and P_{D}
A	(II.5), (II.8) and (II.9).
B	(II.6) and (II.11).
C	(II.6) and (II.11) with a small number of independent pixels N.
D	(II.6), (II.8) and (II.10).
E	(II.6).

curve should satisfy $P_{\mathrm{D}} \geq P_{\mathrm{FA}}$ [Lev08, ch. 2.4.2] [Kay98, p. 74]. Figure II.3 presents theoretical ROC curves for the strategies in Table II.1, applied to a random vector of length 500 and a point scatterer placed at random position with 12 dB SNR. Strategy C applied a ± 3 pixel search window ($N = 7$ independent pixels).

Tabulating Area Under the Curve (AUC) is also a way to present ROC results [Abr19, p. 315]. AUC for a diagonal line with $P_{\mathrm{D}} = P_{\mathrm{FA}}$ is 0.5. Another way to present detection performance is to plot P_{D} as a function of SNR for a fixed P_{FA} value [Kay13, ch. 7.3.2]. From Figure II.4 we can see that the detection performance of strategy C varies quite a lot in the range SNR $= [8, 14]$ dB. When testing the detection performance of different methods, the SNR-range where P_{D} varies greatly is the most interesting to analyze. Tabulating P_{D} for a chosen P_{FA} value, for example $P_{\mathrm{FA}} = 1\,\%$, is another way to compare detection performance.

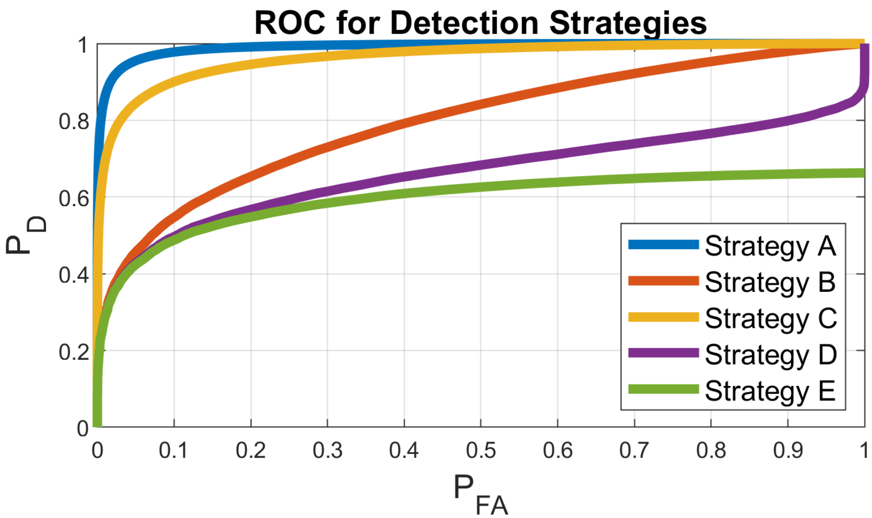

Figure II.3: ROC curves for the different strategies for calculating point detection performance.

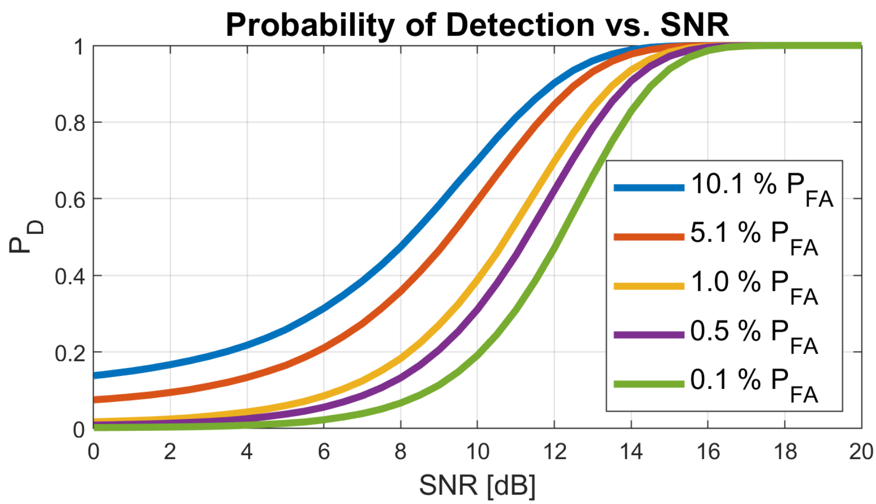

Figure II.4: The P_{D} increases with point SNR. P_{D} is shown for five P_{FA} values and calculated using strategy C with a ± 3 pixel search window.

II.2.6 Choice of Point Target Detection Strategy

Strategy A considers only the known point location for detection and can be vulnerable when imaging effects slightly alter the point target's location. Picking the maximum intensity is the natural choice when searching for a point target in speckle background. Strategy A does not pick the maximum value. Strategy B uses maximum for both P_{FA} and P_{D}, but ignores the fact that the found maximum might not be the true point target. Strategies D and E pick the maximum intensity peak of the entire image for P_{FA}. Two downsides of strategy D are that we ignore false detections when the maximum is not in the correct position, and only P_{FA} is inflated by maximum. Strategy E resembles what we would apply in practice if searching for one point scatterer in an image. However, it has the disadvantage that P_{D} does not converge to 1 for $P_{\text{FA}} = 1$ in the ROC curve if the SNR is low. As such, strategy E does not fulfill the properties of a valid ROC curve [Lev08, ch. 2.4.2].

Strategy C stands out as the optimal choice, a combination of strategies A and B. It resembles a realistic, practical approach the most and gives valid ROC curves. It evaluates a search window around the known point location and picks the maximum value for both false alarm and true positive detection. Figure II.2 shows how P_{D} for a small search window only slightly deviates from P_{D} at the known point position. At the same time, evaluating an image selection will give some inflation of P_{FA} due to the number of pixels considered, as shown in Figure II.1. Picking the maximum gives dependence on N and reduces R compared to using all the pixels.

In the 2-D study, we set the size of the search window to be twice the -6 dB spatial resolution for the DAS image. The probability of detecting the true point target as the maximum is high within such a small window, even when scalloping loss or other imaging effects cause a slight shift in pixel location. We also evaluate how the imaging method affects the speckle background and corresponding false alarms by applying a search window. For detection studies with experimental images, we can fit the search window size to the confidence interval of the known point location. Strategy C can be applied if the detection of several point scatterers is of interest. However, we must note that the choice of search window size relates to the separability of detected point scatterers. If two point targets are located within the same search window, only one detection will be registered. With nonuniform backgrounds, we can apply a form of constant false alarm rate detection with local adaptive thresholding [Abr19; Lev08]. In our study, we only consider a single point scatterer in homogeneous background speckle.

II.2.7 Number of Required Realizations and Confidence Interval

The number of realizations R will affect the accuracy of the measured performance results. If the true probability is small, for example $P_{\text{FA}} = 0.1$ %, only one in a thousand realizations is expected to exceed the threshold. In such a case, R must be much larger than a thousand to ensure an accurate probability estimate. As presented in [Kay98, p. 37], if we wish to have a relative absolute error ϵ for probability P for $100(1-b)$ % of the time, then the required number of realizations R_{req} is

$$R_{req} \geq \frac{(\mathcal{Q}^{-1}(b/2))^2\ (1-P)}{\epsilon^2 P}. \tag{II.12}$$

Here $\mathcal{Q}^{-1}(b/2)$ is the inverse right-tail probability function of a standard normal distribution evaluated at $b/2$. For very small values such as $P_{\text{FA}} = 10^{-3}$, a $10\ \%$ relative accuracy for $80\ \%$ of the time requires $R = 164070$ and it can be difficult or impractical to get enough data. On the other hand, if we wish to analyze a probability of $P = 0.05$ for $80\ \%$ of the time and have $R = 6500$, we get an error of $\epsilon = 7\ \%$. Confidence intervals for the ROC curve can be plotted by calculating the relative error for both P_{FA} and P_{D} at each threshold value using (II.12). The coefficient of variation of the estimated probability P, i.e. the ratio of the standard deviation (STD) to the mean of the estimate, is a similar quantity used to express R_{req} [Abr19, p. 314].

As presented by Hanley and McNeil [HM82], we can compute the confidence interval for the AUC. For large samples, the distribution of AUC is approximately normal. A $100(1-b)\ \%$ confidence interval for sample AUC-value θ may be computed using the standard error (SE) as follows

$$\theta \ \pm \ \mathcal{Q}^{-1}(b/2)\ \text{SE}(\theta), \tag{II.13}$$

where

$$\text{SE}(\theta) = \sqrt{\frac{\theta(1-\theta) + (R_p-1)(Q_1-\theta^2) + (R_s-1)(Q_2-\theta^2)}{R_s R_p}}.$$

It is worth noting that $\text{SE}(\theta)$ is inversely proportional to $\sqrt{R}$. Quadrupling R only reduces $\text{SE}(\theta)$ by a factor of two. $\text{SE}(\theta)$ is small for high θ values close to 1. The number of realizations with and without a point scatterer present is R_p and R_s respectively. Q_1 and Q_2 are distribution-specific quantities expressed as functions of θ and give a conservative estimate of $\text{SE}(\theta)$ [HM82].

$$Q_1 = \frac{\theta}{2-\theta}\ , \qquad Q_2 = \frac{2\theta^2}{1+\theta}. \tag{II.14}$$

II.2.8 Practical Detection Performance in Ultrasound Images

The theoretical formulae for detection performance in this section are for ideal signals in additive white Gaussian noise in complex sequences. This is statistically equivalent to ideal points in fully developed speckle. In practical ultrasound imaging, several factors that potentially affect detection:

- Additive noise on channel data. The effect of noise causes the SNR to vary with depth.
- Finite probe size causes targets positioned far off-center not to be as well represented as centered point targets.
- The spatial resolution is determined by the aperture size and transmitted pulse bandwidth. It typically varies for depth and angle, and oversampling is common.

- Scalloping loss can cause a reduction in amplitude and leakage in energy to nearby pixels.
- Apodization changes resolution and reduces side lobes.
- Speckle reduction methods are often applied on ultrasound images and alter the statistics.
- Advanced beamforming methods alter both the speckle statistics [Hve+17b] and the point-plus-speckle statistics.

In the 2-D study, we evaluate how common imaging techniques affect the detection performance of point scatterers.

II.3 Background - Advanced Beamforming

This section briefly introduces the theory for the following beamforming methods: DAS, MV, CF, and PCF. See The Ultrasound Toolbox (USTB) [Rod+17] for implementation.

II.3.1 Conventional Delay-And-Sum (DAS)

Conventional DAS consists of applying a delay and an amplitude weight to the output of each sensor, then summing the resulting signals [JD93, ch. 4.1]. DAS for image pixel $[z, x]$ is defined as

$$S_{\text{DAS}}[z, x] = \sum_{m=0}^{M-1} w_m y_m[z, x], \tag{II.15}$$

where M is the number of elements, $y_m[z, x]$ is the delayed signal received at element m, and w_m is a predefined weight. DAS is the oldest and simplest array signal processing algorithm but remains a powerful approach today [JD93, ch. 4.1].

II.3.2 Capon's Minimum Variance (MV)

Capon's Minimum Variance (MV) [Cap69] calculates for each pixel a data dependent set of weights $\boldsymbol{w} = [w_0, w_1, \ldots, w_{M'-1}]^T$ that minimizes power while maintaining unity gain in the steering direction [SAH07]. To calculate the weights, the spatial covariance matrix needs to be estimated for each pixel. To do this, we apply spatial averaging with subarrays $\boldsymbol{y}_l[z, x] = [y_l, y_{l+1}, \ldots, y_{l+L-1}]^T$, $l \in [0, M' - L - 1]$, where M' is the length of the active receive aperture and $L = M'/2$. We apply time averaging with 1.5λ range (λ being the wavelength), a diagonal loading factor of $1/100$, and the steering vector as a vector of ones [SAH09]. The MV weights are used in (II.15) and the final image becomes

$$S_{MV}[z, x] = \frac{1}{M' - L + 1} \sum_{l=0}^{M'-L} \boldsymbol{w}^H[z, x]\, \boldsymbol{y}_l[z, x]. \tag{II.16}$$

MV can achieve low sidelobe levels and a narrow beamwidth, increasing the spatial resolution of closely spaced point scatterers. See [SAH09] for a discussion on the parameters.

II.3.3 Mallart-Fink Coherence Factor (CF)

The Coherence Factor (CF) calculates the ratio between coherent and incoherent energy across the aperture [MF94]

$$\mathrm{CF}[z,x] = \frac{\left|\sum y_m[z,x]\right|^2}{M \sum \left|y_m[z,x]\right|^2}. \tag{II.17}$$

It has the potential to give increased contrast and resolution when applied as an adaptive weight to the DAS image [LL03]

$$S_{\mathrm{CF}} = S_{\mathrm{DAS}}[z,x]\ \mathrm{CF}. \tag{II.18}$$

II.3.4 Camacho-Fritsch Phase Coherence Factor (PCF)

The Phase Coherence Factor (PCF) [CPF09b] calculates for each pixel an adaptive weight based on the phase of the receive data. It is a method proposed to improve resolution [CPF09a]

$$\mathrm{PCF}[z,x] = \max\left\{0, 1 - \frac{\gamma^*}{\sigma_0} f[z,x]\right\}, \tag{II.19}$$

where γ^* is a parameter *provided to adjust the sensitivity of PCF to out-of-focus signals* [CPF09b], and $\sigma_0 = \pi/\sqrt{3}$ is the STD of a uniform distribution between $-\pi$ and π [Rod+17]. The function $f[z,x]$ calculates the minimum STD of the instantaneous phase across the aperture. PCF is applied as an adaptive weight to the DAS image

$$S_{\mathrm{PCF}} = S_{\mathrm{DAS}}[z,x]\ \mathrm{PCF}. \tag{II.20}$$

II.4 Methods

In this section, we describe the simulation, processing, and test setups in our study. We used Field II to generate raw channel data and USTB to beamform the data, as illustrated in Figure II.5. We varied the following: the simulated phantom, the point data intensity, the aperture size, the apodization, the speckle reduction, and the BF.

II.4.1 Synthetic Transmit Setup and Image Reconstruction

We designed the phantom as a simple scenario of a single point scatterer in speckle background to establish a baseline detection. We simulated synthetic transmit aperture datasets in Field II to obtain synthetic focus and uniform resolution for all pixels. We used a 128 element, λ pitch, linear array with 5.1 MHz center frequency (L11-4v). We added white Gaussian noise to the channel data at 10 dB *channel SNR*. We kept

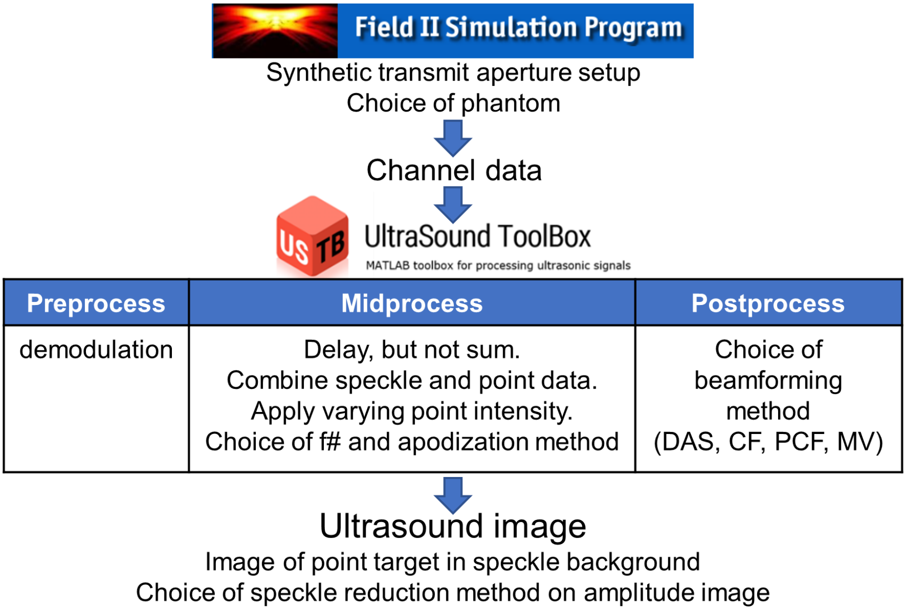

Figure II.5: Overview of the acquisition and processing stage for producing simulated ultrasound images. We use Field II to produce channel data and USTB to beamform the data.

the additive channel noise fixed and below the speckle background level and instead varied the point intensity relative to the combined speckle and noise background. The speed of sound in the medium was 1540 m/s, the transmitted pulse bandwidth was 65 % of the center frequency, the wavelength λ was 0.3 mm, and the aperture size was 38.1 mm.

We simulated 200 speckle realizations, each consisting of 91000 point scatterers and at least 20 scatterers per resolution cell. The speckle pattern is considered well developed if the number of scatterers per resolution cell is larger than ten [Wag+83] [Rin19, ch. 2.9]. We simulated one point scatterer at 65 image positions (13×5 matrix grid), chosen to ensure varying straddle loss. To reduce the number of Field II simulations, we simulated radio frequency channel data for the point scatterers and the speckle background separately. Afterward, we combined the channel data such that we could change the point intensity and position. For a given method and point SNR value, we created and analyzed 65×100 images. To improve the statistical accuracy at low P_{FA} values, we additionally analyzed 100 speckle images. With detection strategy C, this corresponds to 6500 realizations for P_{D} calculation and 13000 realizations for P_{FA} calculation. To ensure uniform average background intensity, we calculated correction maps from the average of all speckle background realizations for each advanced BF and apodization method and applied them to the images before detection. The beamforming was performed in MATLAB (Mathworks, Natick, MA) using USTB.

The reconstructed image scene was 20 mm wide and 40 mm deep. We oversampled the images to ensure full gain and top performance for the high-resolution adaptive BFs. The -6 dB theoretical and measured spatial resolution for a center point scatterer in DAS with hamming transmit apodization corresponded to approximately 5×7 pixels. The total image size was 512×256. For the detection search, we applied a search window grid size two times the spatial resolution. The window ensured we would not miss a detection due to straddle loss or a slight shift in pixel location and also caught some of the method's effect on detected false alarms.

We calculate the point's SNR metric using (II.1) with the average maximum point intensity and the average intensity of the speckle region around center focus depth without the point scatterer present. SNR was calculated for the point scatterer positioned in the center of the image scene, beamformed by the DAS method. By varying the point's intensity, we tested three SNR values in the range SNR $= [10, 14]$ dB. Detection performance in this range varied greatly and signified relatively weak point scatterers in speckle. Note that the choice of point detection strategy and search area affects which SNR interval to choose.

II.4.2 Adaptive Aperture Size and Spatial Resolution

The ratio between imaging depth z and size of active aperture D is termed *F-number* or $f_{\#} = z/D$. Uniform resolution in the final image can be ensured by having a constant $f_{\#}$. It ensures a range-independent beamwidth by increasing the active aperture with increasing range z [Sza14, p. 381]. For pixels close to the edges, the active aperture will be reduced since the physical aperture has finite size. We used $f_{\#} = 1.75$ in this study unless otherwise described. The two-way -6 dB lateral resolution with fixed $f_{\#}$ and rectangular apodization can be approximated as [Rin19, p. 12][Har78]

$$x_{\text{res}} \approx \frac{1.21}{\sqrt{2}} \lambda f_{\#}. \tag{II.21}$$

We compared three different $f_{\#}$ values to establish how image resolution affects the detection performance.

II.4.3 Apodization

In medical ultrasound, applying an apodization window is standard practice for reducing sidelobe levels [Sza14, p. 178] [JD93, p. 322]. Windowing is always a trade-off between resolution and contrast [Har78]. We applied the following apodization methods to study the effect on detection: rectangular, Hamming only on transmit, and Hamming on both transmit and receive. Excepting the apodization study, we applied the same apodization for all simulations; hamming apodization on transmit and rectangular on receive.

II.4.4 Speckle Reduction

Speckle reduction or noise suppression is often applied on medical ultrasound images to improve contrast [Sza14, ch. 8.4.6]. Speckle reduction using filters can greatly improve the contrast between grayscale tissue areas but simultaneously reduce the the point scatterer's resolution. In this study, we analyzed the effect of common denoising filters on the detection of point scatterers. We studied the following filters: Wiener, non-local means, bilateral, anisotropic diffusion, and simple block averaging. Table II.5 in App. II.A presents the filter settings used in this study. Speckle reduction can be applied on the intensity or log-intensity images, but we applied it on the amplitude DAS image for this study [AB07; Bre+07; YA02]. Based on visual inspection, we chose filter settings giving a mild background smoothing. For all methods, we found parameter settings giving in approximately 0.3 STD vs. mean μ of the speckle background. A detailed study on optimal parameters for each filter was not performed.

The *Wiener filter* is also referred to as the minimum mean square error filter or the least square error filter [GW10, ch. 5.8]. The method assumes that noise and image are uncorrelated, tailoring itself to the local image variance. We tested four window sizes with an increasing amount of speckle reduction. We also tested four window sizes for simple block averaging.

A *non-local means filter* removes noise from an image while preserving the sharpness of strong edges [BCM05]. We used the technique first implemented by Buades et al. [BCM05], but for computational efficiency omitted to convolve the Euclidean distance between two comparison windows with a Gaussian kernel. We varied the degree of smoothing with respect to the STD of the image. We present four filters with an increasing amount of speckle reduction.

An *anisotropic diffusion filter* also tries to denoise an image while still preserving the sharpness of edges. It is a technique presented by Perona and Malik [PM90]. We tested several filters by varying the number of iterations used in the diffusion process and the gradient threshold value with respect to STD of the image. The threshold value controls the conduction process by classifying gradient values as edges or noise, and increasing the value smooths the image more.

A *bilateral filter* applies an edge-preserving Gaussian filter. It was presented by Tomasi and Manduchi [TM98]. We varied the degree of smoothing with respect to the image variance and the STD of the spatial Gaussian smoothing kernel. The value of the degree of smoothing corresponds to the variance of the Range Gaussian kernel of the bilateral filter [TM98]. The Range Gaussian is applied on the Euclidean distance of a pixel value from the values of its neighbors.

II.4.5 Advanced Beamforming Methods

We analyzed the four BFs presented in Section II.3 and will refer to them as DAS, MV, CF, and PCF. The input to all the methods was identical. We applied Hamming window on transmit and uniform apodization on receive. The point SNR value was calculated from the DAS images.

II.5 Results

II.5.1 Spatial Resolution and Apodization

Figure II.6 presents the detection performance of three adaptive aperture sizes. As seen from the results, increasing the $f_{\#}$ degrades the detection performance. The

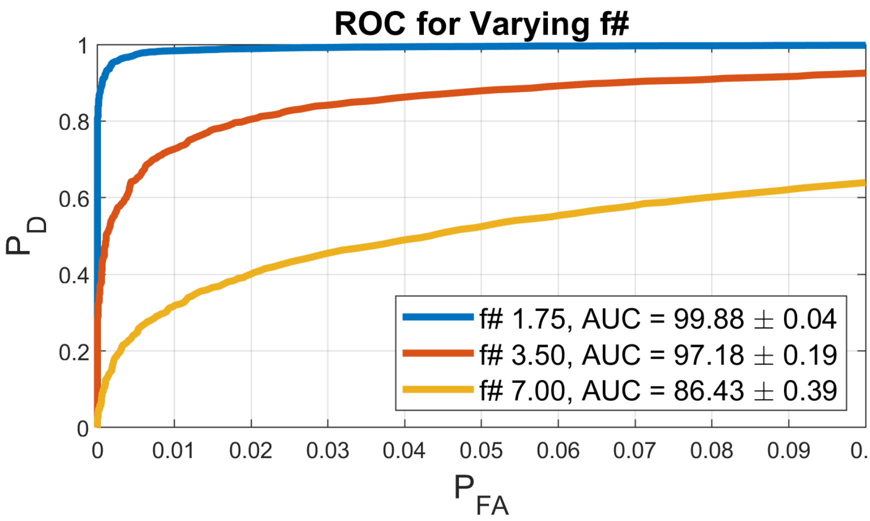

Figure II.6: ROC curve for DAS using three adaptive aperture sizes, giving different spatial resolutions. P_{FA} is shown up to 0.1.

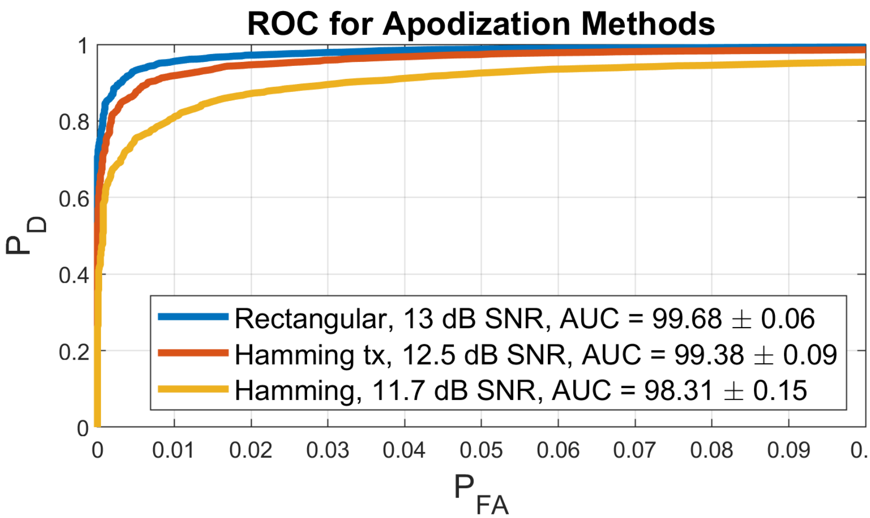

Figure II.7: ROC curve for DAS using different apodization methods: rectangular, Hamming only on transmit (tx), and Hamming on both directions. The input data is the same for all methods, but the different windows alter the spatial resolution and the final point SNR values. P_{FA} is shown up to 0.1.

performance difference between $f_\# = 7$ and $f_\# = 3.5$ illustrates how doubling the adaptive aperture greatly improves point detectability. We applied hamming apodization on transmit and rectangular on receive for all $f_\#$s. Figure II.7 shows the ROC curve for DAS using different apodization schemes: rectangular, Hamming only on transmit, and Hamming on both transmit and receive. Applying a uniform rectangular window gives the highest probability of point detection. A nonuniform window reduces resolution and slightly alters the measured point SNR value. The three methods have final SNR values of 13.0, 12.5, and 11.7 dB.

II.5.2 Speckle Reduction

Figure II.8 shows speckle-reduced images of a sample speckle realization with a point scatterer. Figure II.9 presents AUC results for the methods with respect to STD vs. the mean of the smoothed speckle background. The images in Figure II.8 correspond to the bars with $\sigma/\mu \approx 0.3$ in Figure II.9. Figure II.10 shows the corresponding ROC curves. We can see that some speckle reduction methods perform very close to the original DAS image, and all perform better than simple block averaging. The ROC curves for the bilateral and Wiener filters have partially overlapping confidence intervals. The differences in the ROC curves for the other filters are statistically significant since the separations between the curves are larger than the individual confidence intervals. 80 % confidence intervals were calculated using (II.12) with 6500 and 13000 realizations for P_{D} and P_{FA}.

II.5.3 Advanced Beamforming Methods

Figure II.11 shows beamformed image scenes where the point scatterer is located in the center. The figure visually compares the effect of the BFs. Figure II.12 presents ROC curves for three SNR values. Tabulated performance statistics are shown in Table II.3 and II.4. Confidence intervals for the ROC curves were calculated using (II.12) at each threshold value, with 6500 realizations for P_{D}, 13000 realizations for P_{FA} and an 80 % confidence interval. Confidence intervals for the tabulated AUC values were calculated similarly using (II.13).

Table II.3: AUC for Beamforming Methods

BF	10.3 dB SNR	12.5 dB SNR	13.7 dB SNR
DAS	94.1 ± 0.3	99.4 ± 0.1	99.9 ± 0.04
CF	94.1 ± 0.3	99.4 ± 0.1	99.9 ± 0.04
PCF	93.5 ± 0.3	99.2 ± 0.1	99.8 ± 0.05
MV	91.9 ± 0.3	98.4 ± 0.1	99.4 ± 0.09

Table II.4: P_{D} for Beamforming Methods

BF	10.3 dB SNR	12.5 dB SNR	13.7 dB SNR
DAS	62.2 ± 0.8	94.7 ± 0.4	98.9 ± 0.2
CF	63.6 ± 0.8	94.6 ± 0.4	98.9 ± 0.2
PCF	59.8 ± 0.8	93.4 ± 0.4	98.6 ± 0.2
MV	53.4 ± 0.8	87.2 ± 0.5	95.3 ± 0.3

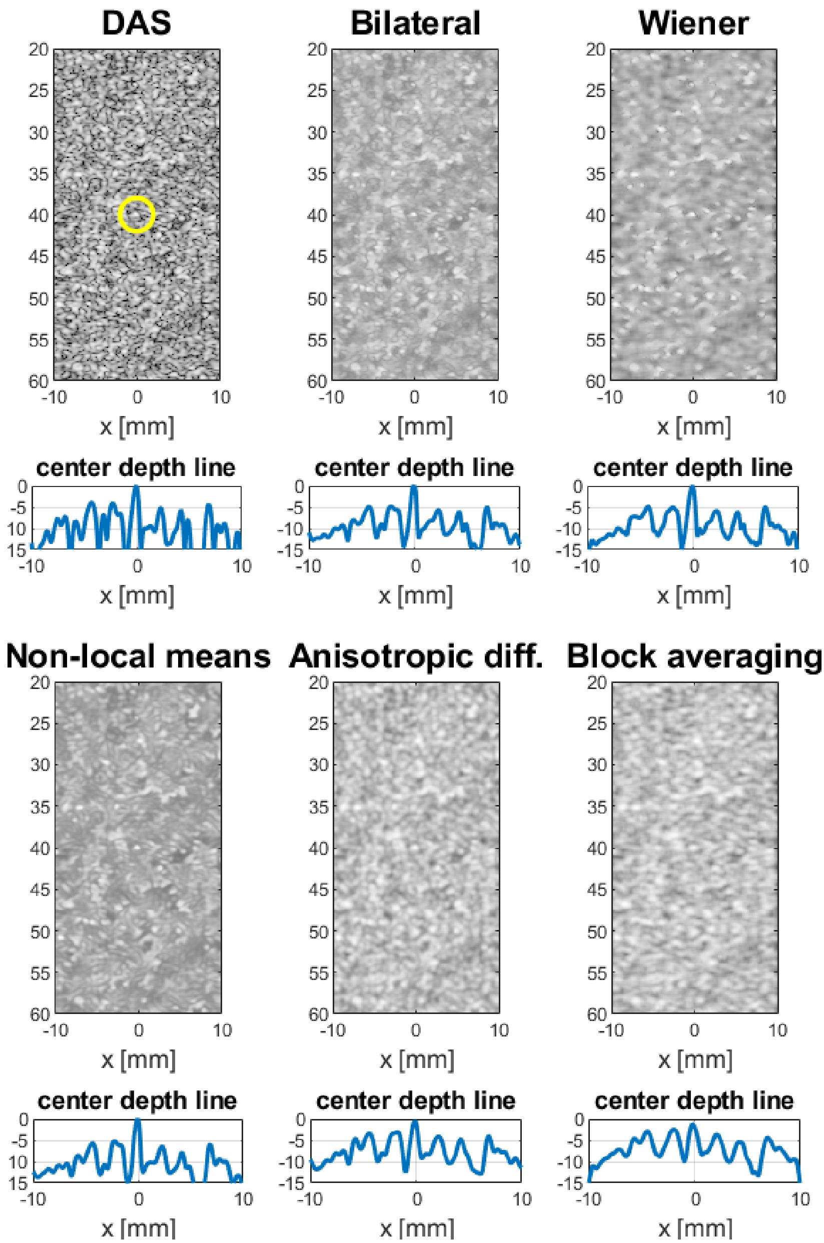

Figure II.8: Speckle reduction methods applied on an image with a point located at $[z, x] = [40, 0]$ mm, indicated by the yellow circle. Point SNR is 10.3 dB. All images are normalized by maximum and presented with -35 dB dynamic range. A center depth cut is presented below each image. The filters have speckle backgrounds with $\sigma/\mu \approx 0.3$. Thresholding the DAS image at -3 dB corresponds to 10 % P_{FA} and 84 % P_{D}. For this specific DAS image, thresholding at 2 % P_{FA} gives eight false alarms.

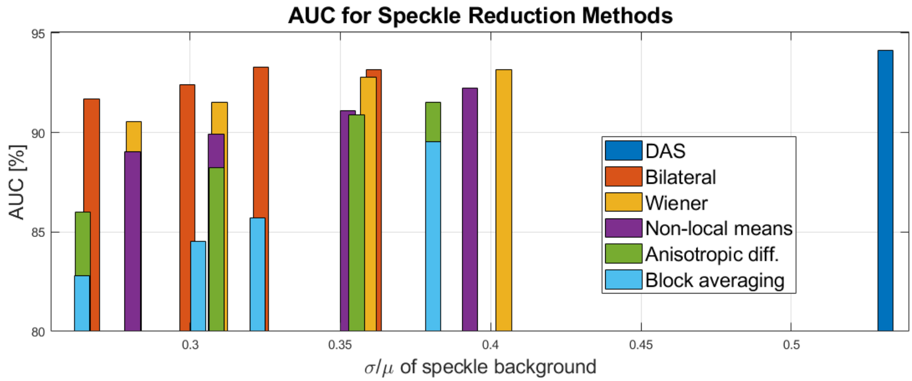

Figure II.9: Tabulated performance results for the speckle reduction methods with 10.3 dB point SNR. The bars present the filter parameters giving high AUC with respect to STD vs. mean of the speckle background.

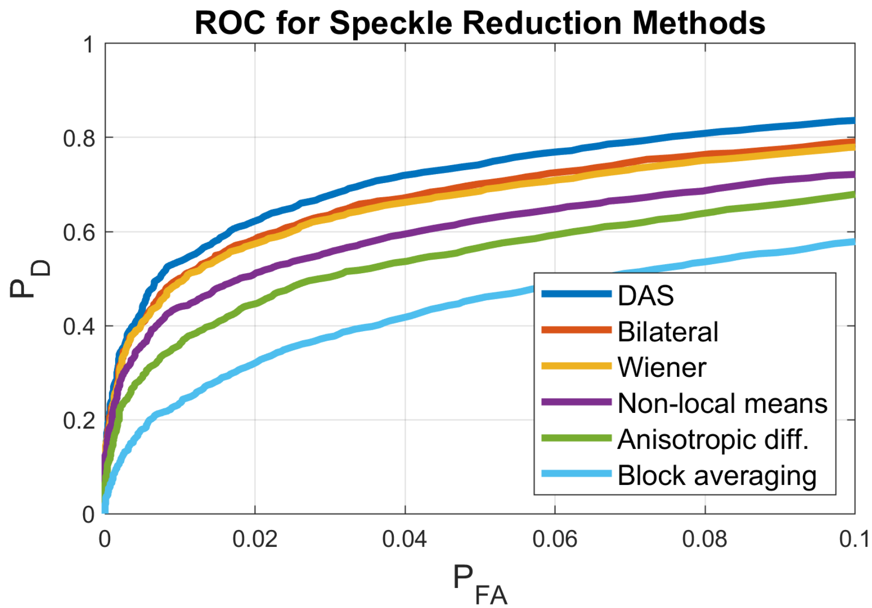

Figure II.10: ROC curves for speckle reduction methods compared to DAS with 10.3 dB point SNR. P_{FA} is shown up to 0.1. The filters give speckle backgrounds with $\sigma/\mu \approx 0.3$. The bilateral and Wiener filter have partially overlapping confidence intervals.

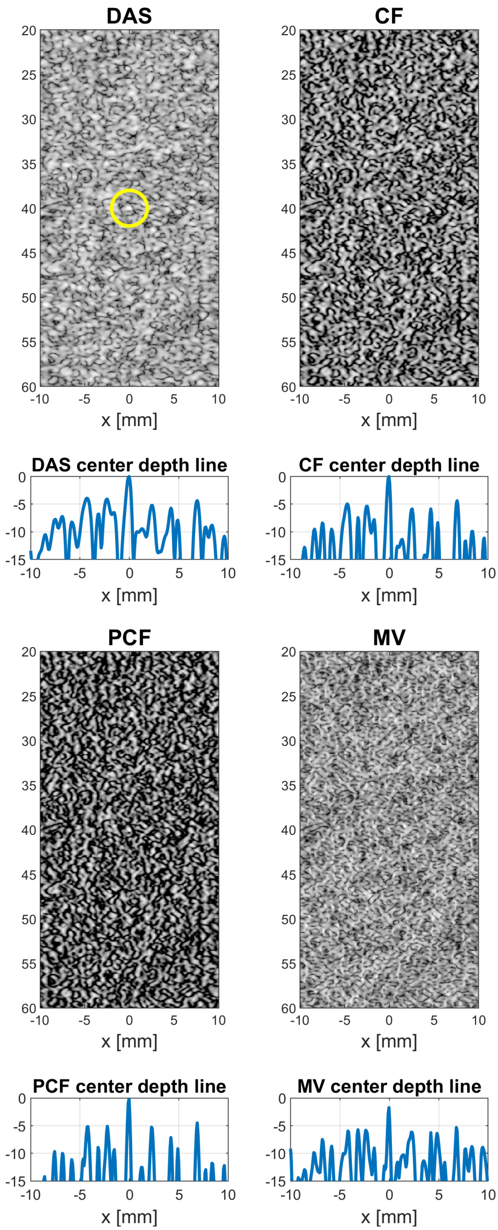

Figure II.11: Four BFs applied on image scene with a point located in center at $x = 0$ mm and $z = 40$ mm depth. The yellow circle indicates the point location. We analyzed 65 different point locations for each speckle background, resulting in 6500 images per beamforming method per SNR value. Point SNR is 10.3 dB here. All images are normalized by maximum and presented with a -35 dB dynamic range to be comparable for the detectability of the point scatterer. A center depth cut is presented below each image to visualize how much the point stands out in log-intensity from peaks in the surrounding speckle background.

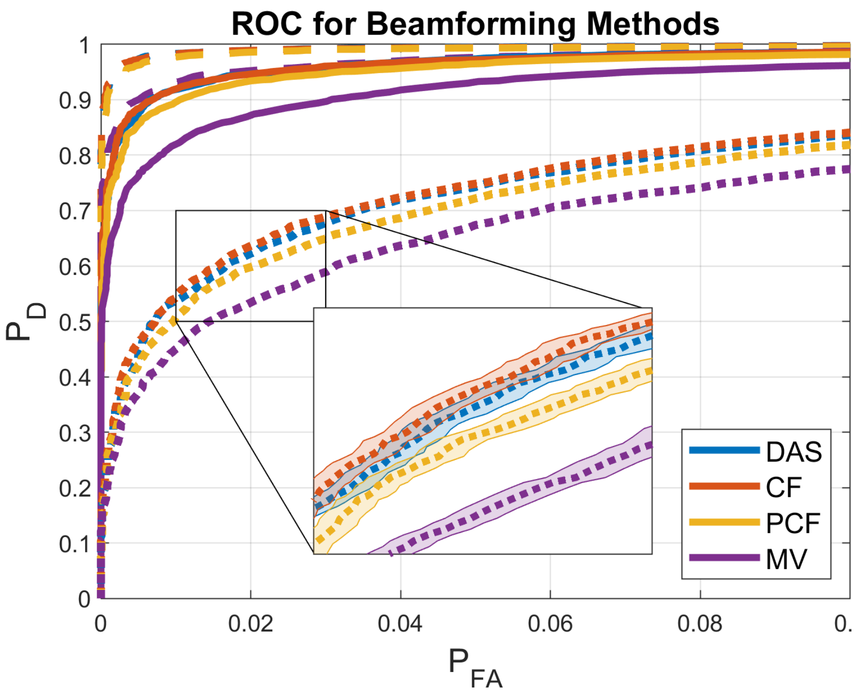

Figure II.12: ROC curves for advanced BFs compared to DAS. Three SNR values are presented; 10.3 dB (dotted), 12.5 dB (solid), and 13.7 dB (dashed). P_{FA} is shown up to 0.1. $80\ \%$ confidence intervals are also shown for a rectangular section of the graph, calculated using 6500 realizations for P_{D} and 13000 realizations for P_{FA}.

II.6 Discussion

II.6.1 Spatial Resolution and Apodization

Reducing the size of the aperture degrades the spatial resolution of the image. From Section II.2, we know that reducing the number of independent pixels lowers $P_{\mathrm{FA}}(\gamma)_{\mathrm{max}}$. Increasing the size of the resolution cell will change the point signal to speckle level within the cell. A loss in resolution is accordingly a loss in point SNR. Figure II.6 shows how reducing the aperture size degrades the detection, as also found in [And+97]. The effect is substantial compared to the other methods in this study. We conclude that it is ideal to have high spatial resolution and high point SNR in terms of detection performance. Techniques that trade-off spatial resolution to obtain better contrast resolution will therefore degrade point detection.

Similarly, we can conclude from the results in Figure II.7 that when we mainly wish to detect point scatterers, the ideal method is to apply uniform apodization. Applying a nonuniform window will suppress some probe elements and thereby reduce the resolution and the maximum point intensity. Apodization with a nonuniform window results in lower point detection performance, though general contrast in the final image might have improved. It is also worth noting that point scatterers at the edges can be more challenging to detect since the edges may not have full aperture coverage.

II.6.2 Speckle Reduction

Applying any speckle reduction will smooth the background, but unfortunately also degrade the image resolution [JD93, p. 322]. This signifies a reduction in point SNR. Based on our results, speckle reduction depletes the number of false alarms but reduces P_{D} even more. In general, speckle reduction thereby degrades the overall point detection performance.

However, the results also show it is possible to smooth the background and keep detection performance close to the original. In this study, the bilateral, Wiener, and non-local means filters outperformed the others and managed to preserve relatively high detection performance even for a high degree of background smoothing. Optimal parameter choices improve detection performance, but from our experience, it is not likely that this will do better than DAS. The anisotropic diffusion filter did not perform as well as the non-local means and bilateral methods. Block averaging significantly reduced the detection performance and is a poor choice if point targets are of interest. When choosing a method for reducing speckle, one should consider that different methods have different performances concerning point detection.

II.6.3 Advanced Beamforming Methods

Figure II.12 shows how CF performs slightly better than DAS for low SNR and P_{FA} values, though the confidence intervals are partially overlapping. Unweighted DAS is the best detector unless prior knowledge is included in the analysis. Point scatterers are small, bright, and highly coherent targets. We can expect high measurable coherence in the signal from a point scatterer, and point detection algorithms can exploit this [Hua+14; Hve+17a]. CF matches prior knowledge about point targets well since it differentiates between coherent and incoherent energy. Speckle background alone is known [MF94] to have an expected mean coherence value of $2/3$, though this theoretical value is affected by specific circumstances in ultrasound imaging [LW95]. Since this is the average, the weights of CF will also enhance some pointlike coherent scatterers in the speckle background. It can be difficult to distinguish true point targets from these peaks at low SNRs based on the weights alone. However, since CF uses image weighting, it can achieve slightly better performance than DAS. The difference in detection performance is distinguishable at low SNR and P_{FA} values. However, we do not have enough realizations to state that the difference is statistically significant since the confidence intervals are partially overlapping in Figure II.12.

The tabulated values for P_{D} in Table II.4 show higher values for CF than DAS with statistical significance with 75 % confidence. The confidence interval curves in Figure II.12 is still a better way to illustrate the accuracy of the results since it shows several measurements. In general, AUC is a more robust method than tabulating P_{D} for a given P_{FA} since it integrates several measurements and is thereby less vulnerable to limited amount of realizations. Tabulating AUC will not catch the slight difference between CF and DAS here since it is calculated over all P_{FA} values, and the difference is only distinguishable for low P_{FA} values.

The results indicate that CF is a promising method to use when point scatterers are of interest, especially in imaging scenes with low SNR values. The DAS image shown in Figure II.11 is an example of such a weak point scatterer. Thresholding the image at -3 dB below the maximum intensity retains many false alarms. An example of a practical application is an ultrasound image with small macrocalcifications in early development. The points will then have low SNR values relative to the background. In such a medical scenario, we wish to have few false alarms. A P_{FA} value of 1 % or lower can be applicable. Referring to the ROC curve in Figure II.12, 1 % P_{FA} corresponds to detecting half of the weak point scatterers, and the results show that CF is a promising alternative to DAS.

The three adaptive BFs have different PDFs from DAS [Hve+17b]. The PDFs of CF and PCF resemble intensity distributions, and in Figure II.11 they appear darker with fewer bright peaks. The difference in PDF affects both P_{FA} and P_{D}. The difference in ROC for PCF in Figure II.12 is statistically significant since the difference between the other curves is larger than the particular confidence interval. PCF has a statistically significant lower detection performance than CF and DAS, but the difference in performance decreases with increasing SNR. PCF is calculated from the STD of the phase. A possible explanation for its performance is that PCF disregards amplitude and thereby retains less information about the point target and the speckle background than CF.

In our analysis, MV has lower detection performance than the other methods. The difference is statistically significant for all three SNR values. MV is known to have good spatial resolution and high separability of point targets [HAR20]. MV is designed for optimum performance for signal in interference and noise. We observe more false alarms for MV, as illustrated in Figure II.11 where the true point in the MV image is not the maximum intensity in the image. A possible cause is the strong dependence on the estimate of the spatial covariance matrix. With a true covariance matrix, its performance should meet DAS for our scenario. With parameter choices that have shown to be robust in ultrasound imaging [SAH09], MV enhances more of the speckle background peaks and attains a poorer detection performance. In the case of multiple point scatterers in speckle, we expect MV to distinguish itself in separating weak point scatterers in the presence of other strong point scatterers.

II.7 Conclusions

In this paper, we have presented an overview of the detection of point scatterers in ultrasound images. Based on classical detection theory, we presented five main strategies to measure and evaluate detection performance. We showed how the choice of detection strategy affects the performance and gives very different ROC curves. We showed how to compare the effect of different imaging methods and calculate confidence intervals for the detection performance.

We simulate many images of a point target in speckle and apply a set of common ultrasound techniques to form the images. Our study shows that uniform apodization gives the best performance when detecting a point scatterer in speckle. Applying a Hamming window or similar suppresses information from some probe elements. It reduces the spatial resolution and thereby degrades the detection performance. Similarly, a large aperture will have better spatial resolution and higher detection performance than a smaller one.

In general, applying speckle reduction to an image will reduce the detection performance of point targets. However, our results show that it is possible to smooth the speckle background while still having detection performance quite close to the original, provided one applies a suitable speckle reduction method with optimal parameters.

The advanced BFs PCF and MV have lower point detection performance than DAS. Unweighted DAS is the best detector unless prior knowledge is included in the analysis. However, CF matches prior knowledge about point targets well. Since it differentiates between coherent and incoherent energy across the aperture, its weights accentuate signals from point scatterers. Our detection performance results show that CF has a positive weighting scheme to the DAS image at low SNR and P_{FA} values.

Appendix II.A

For the speckle reduction methods in Section II.4.4, we chose to use the built-in versions in MATLAB: *wiener2*, *imnlmfilt*, *imdiffusefilt*, *imbilatfilt*, and *filter2*. Table II.5 presents the filter settings we used in this study. The parameter values corresponding to speckle background smoothing of $\sigma/\mu \approx 0.3$ are emphasized in bold.

Table II.5: Speckle Reduction Parameter Settings

Method	Parameter Names	Parameter Values
Wiener	Window sizes	5×7, 7×9 $\mathbf{9{\times}13}$, 11×15
Non-local means	DegreeOfSmoothing ($\times$STD), ComparisonWindowSize, SearchWindowSize	[1,5,11], [1,7,13] **[1,7,23]**, [1,9,21]
Anisotropic diffusion	NumberOfIterations, GradientThreshold ($\times$STD)	[7,1.5], [9,1.5] **[13,2]**, [20,2]
Bilateral	DegreeOfSmoothing ($\times$STD^2), spatialSigma	[1,5], [1,9] **[2,5]**, [3,5]
Block averaging	Window sizes	5×7, 7×9 $\mathbf{7{\times}11}$, 9×13

Acknowledgment

The authors would like to thank O. M. H. Rindal for discussions regarding The UltraSound Toolbox (USTB) [Rod+17].

References

[AB07] Aysal, T. C. and Barner, K. E. "Rayleigh-Maximum-Likelihood Filtering for Speckle Reduction of Ultrasound Images". In: *IEEE Trans. Med. Imag.* vol. 26, no. 5 (May 2007), pp. 712–727.

[Abr19] Abraham, D. A. *Underwater Acoustic Signal Processing: Modeling, Detection, and Estimation.* Springer, 2019.

[And+97] Anderson, M. E. et al. "The detection of breast microcalcifications with medical ultrasound". In: *J. Acoust. Soc. Am.* vol. 101, no. 1 (Jan. 1997), pp. 29–39.

[AST00] Anderson, M. E., Soo, M. S. C., and Trahey, G. E. "Optimizing visualization of breast microcalcifications". In: *Proc. IEEE Int. Ultrason. Symp. (IUS).* Vol. 2. Oct. 2000, pp. 1315–1320.

[AST98] Anderson, M. E., Soo, M. S. C., and Trahey, G. E. "Microcalcifications as elastic scatterers under ultrasound". In: *IEEE Trans. Ultrason., Ferroelectr., Freq. Control* vol. 45, no. 4 (July 1998), pp. 925–934.

[BCM05] Buades, A., Coll, B., and Morel, J.-M. "A Non-Local Algorithm for Image Denoising". In: *Proc. IEEE Comput. Soc. Conf. Comput. Vis. Pattern Recognit.* Vol. 2. June 2005, pp. 60–65.

[Bre+07] Breivik, L. H. et al. "Real-Time Nonlocal Means-Based Despeckling". In: *IEEE Trans. Ultrason., Ferroelectr., Freq. Control* vol. 64, no. 6 (June 2007), pp. 959–977.

[Bur78] Burckhardt, C. B. "Speckle in Ultrasound B-Mode Scans". In: *IEEE Trans. Sonics Ultrason.* vol. 25 (1 Jan. 1978), pp. 1–6.

[Cap69] Capon, J. "High-resolution frequency-wavenumber spectrum analysis". In: *Proc. IEEE* vol. 57 (8 Aug. 1969), pp. 1408–1418.

[Cob07] Cobbold, R. S. C. *Foundations in Biomedical Ultrasound.* Oxford University Press, 2007.

[CPF09a] Camacho, J., Parrilla, M., and Fritsch, C. "Grating-lobes reduction by application of Phase Coherence Factors". In: *Proc. IEEE Int. Ultrason. Symp. (IUS).* Sept. 2009, pp. 341–344.

[CPF09b] Camacho, J., Parrilla, M., and Fritsch, C. "Phase Coherence Imaging". In: *IEEE Trans. Ultrason., Ferroelectr., Freq. Control* vol. 56, no. 5 (May 2009), pp. 958–974.

[Dah+11] Dahl, J. J. et al. "Lesion detectability in diagnostic ultrasound with short-lag spatial coherence imaging". In: *Ultrason. Imaging* vol. 33, no. 2 (Apr. 2011), pp. 119–133.

[Dia+18] Diamantis, K. et al. "Super-Resolution Axial Localization of Ultrasound Scatter Using Multi-Focal Imaging". In: *IEEE Trans. Biomed. Eng.* vol. 65, no. 8 (Aug. 2018), pp. 1840–1851.

[EG05] Ewens, W. J. and Grant, G. R. *Statistical Methods in Bioinformatics: An Introduction.* II. Springer, 2005.

[Flø+17] Flørenæs, E. et al. “In vitro detection of microcalcifications using dual band ultrasound”. In: *Proc. IEEE Int. Ultrason. Symp. (IUS)*. Sept. 2017, pp. 1–4.

[GW10] Gonzales, R. C. and Woods, R. E. *Digital Image Processing*. III. Pearson, 2010.

[HAR20] Hoel Rindal, O. M., Austeng, A., and Rodriguez-Molares, A. “Resolution Measured as Separability Compared to Full Width Half Maximum for Adaptive Beamformers”. In: *Proc. IEEE Int. Ultrason. Symp. (IUS)*. Sept. 2020, pp. 1–4.

[Har78] Harris, F. J. “On the use of windows for harmonic analysis with the discrete Fourier transform”. In: *Proc. IEEE* vol. 66 (1 Jan. 1978), pp. 51–83.

[HM82] Hanley, J. A. and McNeil, B. J. “The Meaning and Use of the Area under a Receiver Operating Characteristic (ROC) Curve”. In: *Radiology* vol. 143, no. 1 (Apr. 1982), pp. 29–36.

[Hua+14] Huang, S. et al. “Beamforming techniques for ultrasound microcalcification detection”. In: *Proc. IEEE Int. Ultrason. Symp. (IUS)*. Sept. 2014, pp. 2193–2196.

[Hve+17a] Hverven, S. M. et al. “Point scatterer enhancement in ultrasound by wavelet coefficient shrinkage”. In: *Proc. IEEE Int. Ultrason. Symp. (IUS)*. Sept. 2017, pp. 1–4.

[Hve+17b] Hverven, S. M. et al. “The influence of speckle statistics on contrast metrics in ultrasound imaging”. In: *Proc. IEEE Int. Ultrason. Symp. (IUS)*. Sept. 2017, pp. 1–4.

[IH94] Insana, M. F. and Hall, T. J. “Visual detection efficiency in ultrasonic imaging: A framework for objective assessment of image quality”. In: *J. Acoust. Soc. Am.* vol. 95, no. 4 (Apr. 1994), pp. 2081–2090.

[JD93] Johnson, D. H. and Dudgeon, D. E. *Array signal processing: concepts and techniques*. Vol. XIII. Upper Saddle River, NJ: PTR Prentice Hall, 1993.

[Jen+06] Jensen, J. A. et al. “Synthetic aperture ultrasound imaging”. In: *Ultrasonics* vol. 44 (Dec. 2006), e5–e15.

[Jen96] Jensen, J. A. “FIELD: A Program for Simulating Ultrasound Systems”. In: *Proc. 10th Nordicbaltic Conf. Biomed. Imag., Suppl. 1, Part 1*. Vol. 4. 1996, pp. 351–353.

[JS92] Jensen, J. A. and Svendsen, N. B. “Calculation of Pressure Fields from Arbitrarily Shaped, Apodized, and Excited Ultrasound Transducers”. In: *IEEE Trans. Ultrason., Ferroelectr., Freq. Control* vol. 39, no. 2 (Mar. 1992), pp. 262–267.

[Kay13] Kay, S. M. *Fundamentals of Statistical Signal Processing, Volume III: Practical Algorithm Development*. Vol. III. Pearson, 2013.

[Kay98] Kay, S. M. *Fundamentals of Statistical Signal Processing, Volume II: Detection Theory*. Vol. II. Prentice-Hall PTR, 1998.

[Lev08] Levy, B. C. *Principles of Signal Detection and Parameter Estimation.* Springer, 2008.

[LL03] Li, P. C. and Li, M. L. "Adaptive imaging using the generalized coherence factor". In: *IEEE Trans. Ultrason., Ferroelectr., Freq. Control* vol. 50, no. 2 (Feb. 2003), pp. 128–141.

[LPW04] Lacefield, J. C., Pilkington, W. C., and Waag, R. C. "Comparisons of lesion detectability in ultrasound images acquired using time-shift compensation and spatial compounding". In: *IEEE Trans. Ultrason., Ferroelectr., Freq. Control* vol. 51, no. 12 (Dec. 2004), pp. 1649–1659.

[LW95] Liu, D.-L. and Waag, R. C. "About the Application of the Van Cittert-Zernike Theorem in Ultrasonic Imaging". In: *IEEE Trans. Ultrason., Ferroelectr., Freq. Control* vol. 42, no. 4 (July 1995), pp. 590–601.

[Mac+18] Machado, P. et al. "Ultrasound Detection of Microcalcifications in Surgical Breast Specimens". In: *Ultrasound Med. Biol.* vol. 44 (6 Mar. 2018), pp. 1286–1290.

[Mat+19] Matrone, G. et al. "Short-lag spatial coherence imaging with multi-line transmission to improve needle visibility in ultrasound images". In: *J. Acoust. Soc. Am.* vol. 146 (Oct. 2019), pp. 2861–2861.

[MBR20] Matrone, G., Bell, M. A. L., and Ramalli, A. "Improving the Detectability of Highly Coherent Targets in Short-Lag Spatial Coherence Images with Multi-Line Transmission". In: *Proc. IEEE Int. Ultrason. Symp. (IUS).* Sept. 2020, pp. 1–4.

[MF94] Mallart, R. and Fink, M. "Adaptive focusing in scattering media through sound-speed inhomogeneities: The van Cittert Zernike approach and focusing criterion". In: *J. Acoust. Soc. Am.* vol. 96, no. 6 (Dec. 1994), pp. 3721–3732.

[MI11] Manolakis, D. G. and Ingle, V. K. *Applied Digital Signal Processing: Theory and Practice.* Cambridge, UK: Cambridge University Press, 2011.

[OQ98] Oliver, C. and Quegan, S. *Understanding Synthetic Aperture Radar Images.* Artech house, Inc., 1998.

[Ouy+19] Ouyang, Y. et al. "A review of ultrasound detection methods for breast microcalcification". In: *Math. Biosci. Eng.* vol. 16 (4 Mar. 2019), pp. 1761–1785.

[PM90] Perona, P. and Malik, J. "Scale-space and edge detection using anisotropic diffusion". In: *IEEE Trans. Pattern Anal. Mach. Intell.* vol. 12, no. 7 (July 1990), pp. 629–639.

[Ray+10] Ray, A. A. et al. "Limitations to Ultrasound in the Detection and Measurement of Urinary Tract Calculi". In: *Urology* vol. 76, no. 2 (Mar. 2010), pp. 295–300.

[Rin19] Rindal, O. M. H. "Software Beamforming in Medical Ultrasound Imaging-a blessing and a curse". Accessed on: Nov. 19, 2019. PhD thesis. Oslo, Norway: Univ. of Oslo, Nov. 2019.

[Rod+17] Rodriguez-Molares, A. et al. "The UltraSound ToolBox". In: *Proc. IEEE Int. Ultrason. Symp. (IUS)*. Sept. 2017, pp. 1–4.

[Rod+20] Rodriguez-Molares, A. et al. "The Generalized Contrast-to-Noise Ratio: A Formal Definition for Lesion Detectability". In: *IEEE Trans. Ultrason., Ferroelectr., Freq. Control* vol. 67, no. 4 (Apr. 2020), pp. 745–759.

[SAH07] Synnevåg, J.-F., Austeng, A., and Holm, S. "Adaptive Beamforming Applied to Medical Ultrasound Imaging". In: *IEEE Trans. Ultrason., Ferroelectr., Freq. Control* vol. 54, no. 8 (Aug. 2007).

[SAH09] Synnevåg, J.-F., Austeng, A., and Holm, S. "Benefits of minimum-variance beamforming in medical ultrasound imaging". In: *IEEE Trans. Ultrason., Ferroelectr., Freq. Control* vol. 56, no. 9 (Sept. 2009), pp. 1868–1879.

[Smi+83] Smith, S. W. et al. "Low Contrast Detectability and Contrast/Detail Analysis in Medical Ultrasound". In: *IEEE Trans. Sonics Ultrason.* vol. 30, no. 3 (May 1983), pp. 164–173.

[SW84] Smith, S. W. and Wagner, R. F. "Ultrasound speckle size and lesion signal to noise ratio: verification of theory". In: *Ultrason. Imaging* vol. 6, no. 2 (Apr. 1984), pp. 174–180.

[Sza14] Szabo, T. L. *Diagnostic Ultrasound Imaging: Inside Out.* Second. Elsevier Academic Press, 2014.

[Tie+18] Tierney, J. E. et al. "In vitro feasibility of next generation non-linear beamforming ultrasound methods to characterize and size kidney stones". In: *Urolithiasis* vol. 47 (Jan. 2018), pp. 181–188.

[TM98] Tomasi, C. and Manduchi, R. "Bilateral filtering for gray and color images". In: *Proc. IEEE Int. Conf. Comput. Vis.* Jan. 1998, pp. 839–846.

[TRL15] Torp, H., Rodriguez-Molares, A., and Løvstakken, L. "Optimum beamformer strategy for detecting signals in clutter noise". In: *Proc. IEEE Int. Ultrason. Symp. (IUS)*. Oct. 2015, pp. 1–4.

[Wag+83] Wagner, R. F. et al. "Statistics of Speckle in Ultrasound B-Scans". In: *IEEE Trans. Sonics Ultrason.* vol. 30, no. 3 (May 1983), pp. 156–163.

[YA02] Yu, Y. and Acton, S. T. "Speckle reducing anisotropic diffusion". In: *IEEE Trans. Image Process.* vol. 11, no. 11 (Nov. 2002), pp. 1260–1270.

[Zem+05] Zemp, R. J. et al. "Detection performance theory for ultrasound imaging systems". In: *IEEE Trans. Med. Imag.* vol. 24, no. 3 (Mar. 2005), pp. 300–310.

Paper III

Point scatterer enhancement in ultrasound by wavelet coefficient shrinkage

Stine Myhre Hverven, Ole Marius Hoel Rindal, Alan J. Hunter, and Andreas Austeng

Published in *IEEE International Ultrasonics Symposium (IUS)*, Washington, DC, 2017, pp. 1-4, DOI: 10.1109/ULTSYM.2017.8092971

III

Abstract

Background speckle can often obscure objects of interest in an ultrasound image. The probability of detection and classification of point scatterers is highly affected by background speckle. The proposed algorithm uses a coherence-based wavelet coefficient shrinkage method. Point scatterers in the ultrasound image are enhanced by separating coherent point targets from incoherent background speckle. Results using Field II ultrasound simulations show how the algorithm retains the point scatterers and increases their conspicuity. The algorithm has potential to detect microcalcifications in breast tissue.

III.1 Introduction

The size, distribution and morphology of microcalcifications in breasts can for some cases be considered an early indicator of breast cancer. Microcalcifications are small, hard calcium deposits in soft breast tissue and behave as point scatterers in an ultrasound image. However, detection of microcalcifications in ultrasound images is challenging as they are often obscured by background speckle.

The proposed algorithm uses a coherence-based wavelet shrinkage method to suppress speckle background in order to enhance point scatterers. From the original image, the algorithm creates multiple images or looks with statistically independent noise realizations and retained wavenumber resolution. The algorithm then utilizes a coherence metric to determine the similarity of the wavelet coefficients between these looks. The wavelet coefficients with low coherence are attenuated to produce an image with reduced speckle. The method has previously been applied on sonar images to separate coherent targets from incoherent background reverberation noise [HV14].

III.2 Methods

III.2.1 Phantom Data Sets

A phantom with three point scatterers in speckle was designed to test the algorithm's ability to enhance point scatterers. The simulation for the point scatterers and the speckle were run separately in order to vary the speckle intensity level more easily. Each data set was normalized by its maximum intensity, but the speckle data was further intensity scaled relative to the point scatterers using the relative values of 50, 70, and 95 %. The scaled speckle data was then added to the other data to create images with varying speckle intensity. The synthetic aperture dataset was simulated using Field II [JS92][Jen96] and a linear array with 128 elements, 5 MHz center frequency and λ pitch (properties of Philips L11-4v). Beamforming was performed using The Ultrasound Toolbox (USTB) [Rod+17].

The method was also verified on an ultrasound image of a real tissue-mimicking phantom (CIRS 054GS) with a hyperechoic area and several point scatterers. A coherently compounded plane wave ultrasound image was acquired with the Verasonics Vantage system using a linear probe (Philips L7-4, 128 elements, 75 angles, 5.2 MHz, f# = 1.75). As with the simulated data, an image of only speckle was also recorded and used to create an image with extra 70 % speckle intensity.

III.2.2 Algorithm Description

Figure III.1 shows a flowchart of the algorithm. The edges of the original image are first tapered down to reduce Gibbs phenomenon in the discrete Fourier transform of the images. Two complimentary looks are then generated as described below. These looks are subsequently decomposed into wavelet coefficients. The coherence between the wavelet transforms is estimated, and after p realizations an averaged estimate of the coherence is thresholded. This is multiplied with the wavelet transform of the original image to generate the final image.

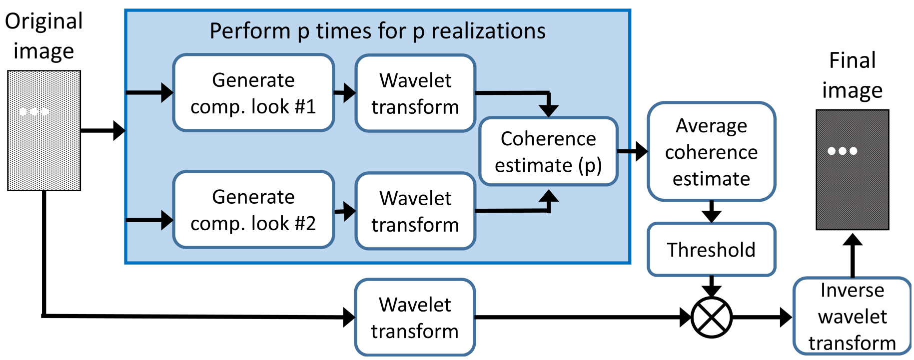

Figure III.1: Flowchart of the wavelet coefficient shrinkage algorithm.

Complimentary looks of the original image are first generated by partitioning the frequency space, i.e. the 2-D FFT of the image into two sets. This is accomplished by applying a 2-D grid to the space where blocks are randomly assigned to either of the two sets, see Figure III.2. The size of the blocks in the grid is chosen so that information of the point scatterers is preserved over several blocks, while the speckle background is correlated on a much smaller scale than the block size [HV14]. The point scatterers will then be persistent in both of the resulting two complimentary looks, whereas the speckle will ideally not have high coherence between the looks.

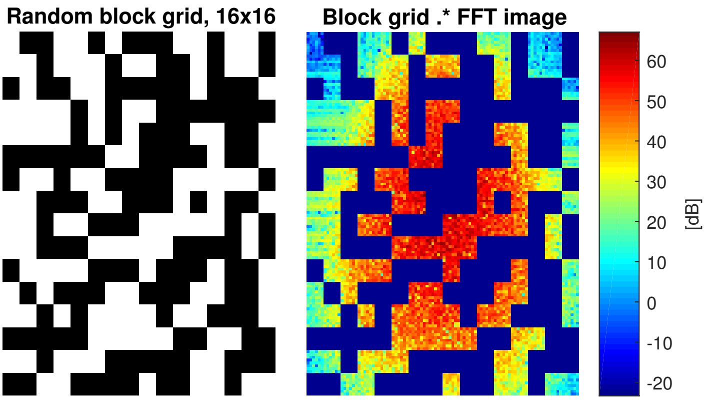

(a) Block grid (b) Partitioned FFT

Figure III.2: Generation of complimentary looks by partitioning frequency space using a random block grid (a). The partitioned frequency space shown here (b) creates one look, and the other is created using the inverse block grid.

Wavelets can be used to de-noise images while preserving resolution. The target information can be described using a few wavelet coefficients, whereas noise is more evenly distributed [HV14]. Thresholding these wavelet coefficients will give a final inverse wavelet transformed image which has retained target information and suppressed noise.

The multilevel 2-D wavelet decomposition was performed with a symmetric biorthogonal wavelet base [Dau92]. The discrete wavelet transform decomposes an image into high and low frequencies. From the high-pass filtered image, three detail images are created, each describing directional local changes in the image. The low-pass filtered image is further downscaled and yields what is known as an approximation image. This image is further high-pass filtered to produce the three smaller detail images of the next level, and so on.

The coherence between two looks is estimated as:

$$\mathrm{C}(x,y,l,p) = \left| \frac{\sum\limits_{m,n=-\frac{N-1}{2}}^{\frac{N-1}{2}} \mathrm{W}_1 \mathrm{W}_2^*}{\sqrt{\sum\limits_{m,n=-\frac{N-1}{2}}^{\frac{N-1}{2}} |\mathrm{W}_1|^2} \sqrt{\sum\limits_{m,n=-\frac{N-1}{2}}^{\frac{N-1}{2}} |\mathrm{W}_2|^2}} \right|$$

$$\text{given } \mathrm{W}_i = \mathrm{W}_i(x + m\Delta x, y + n\Delta y, l, p) \tag{III.1}$$

where (x,y) is the pixel location in the wavelet transformed image, l is the decomposition level, p is the realization number, and Δx and Δy are the pixel dimensions. W_i is the wavelet transform of complementary look i and W_i^* denotes its conjugate. NxN is the sliding window size over which the coherence for pixel location (x,y) is calculated. A hanning window with $N = 5$ was used. A large window size will reduce variance, but also reduce spatial resolution. The average coherence estimate for each level l is obtained by averaging the coherence estimate between two looks over all P realizations.

$$\mathrm{C_{av}}(x,y,l) = \frac{1}{P} \sum_{p=1}^{P} |\mathrm{C}(x,y,l,p)| \tag{III.2}$$

The average coherence estimate is thresholded by a simple weighting scheme where coefficients with values less than t_{min} are completely suppressed, values greater than t_{max} are retained, and between these two there is a linear transition.

$$\mathrm{C_{th}}(x,y,l) = \begin{cases} 1, & \text{if } C_{\text{av}}(x,y,l) > t_{\text{max}} \\ 0, & \text{if } C_{\text{av}}(x,y,l) < t_{\text{min}} \\ \frac{\mathrm{C_{av}}(x,y,l) - t_{\text{min}}}{t_{\text{max}} - t_{\text{min}}}, & \text{otherwise} \end{cases} \tag{III.3}$$

These thresholded coefficients are multiplied with the wavelet coefficients of the original image, and the inverse wavelet transform of the adjusted coefficients yield the final image.

III.2.3 Evaluation Criteria

As a visibility metric for the point scatterers, the metrics conspicuity (Cp) and Peak$_{\text{point}}$-to-Peak$_{\text{speckle}}$ ratio (PP) are presented. Cp is a measure of how clearly discernible a point is from the background at same depth and it is defined as [Dah+11]:

$$\text{Conspicuity} = \frac{\max_{\text{point}} - \mu_{\text{speckle}}}{\sigma_{\text{speckle}}}. \tag{III.4}$$

PP measures the intensity difference between the point scatterers and peaks in the speckle background:

$$\text{PP} = 20 \log_{10} \left(\frac{\max_{\text{point}}}{\max_{\text{speckle}}} \right) \tag{III.5}$$

where $\max_{point}$ and $\max_{speckle}$ are the maximum intensity values. We call PP_1 the ratio calculated within the areas depicted by the solid white lines in Figure III.3, i.e. areas at same depth. PP_2 is calculated when the maximum speckle intensity is within the area depicted by the dotted white lines.

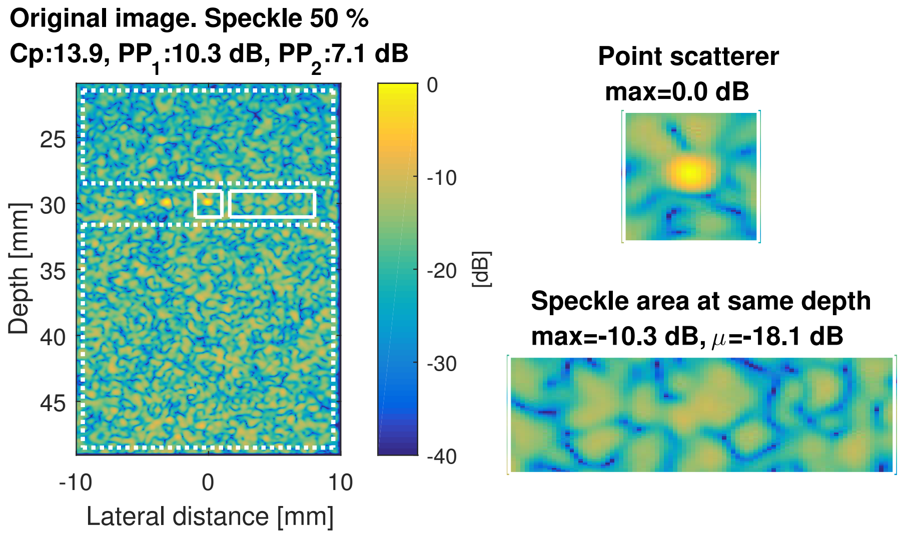

Figure III.3: Conspicuity (Cp) and Peak_{point}-to-$\text{Peak}_{speckle}$ ratio (PP) metrics calculated using (III.4) and (III.5).

III.3 Results

Figure III.4 shows the results when the method is applied to a plane wave image of a real tissue-mimicking phantom. Conspicuity of the point scatterers in the wavelet shrunk image is around 14-17 times higher than in the original. A more detailed analysis is presented for the simulated phantom.

The threshold levels for the simulated phantom were chosen based on the average coherence estimates for each level, shown in Figure III.5. The three point scatterers are easily discernible in the first level decomposition images with coherence values around 0.6. The points are somewhat discernible in the second level with coherence values above 0.35. Further decomposition does not include much of the target information. The approximate coherence values found in Figure III.5 were used as initial threshold limits and were further adjusted. Mild threshold limits are more likely to retain all point scatterers, but will also include more of the speckle background and increase the possibility of false positives in the final image. Three different threshold limits were used to create the thresholded average coherence estimates shown in Figure III.6.

Figure III.7 shows the results from the simulated phantom when the speckle background intensity is varied (50, 70 and 95 %). All three point scatterers are retained when their intensity is above maximum speckle intensity, and the conspicuity values

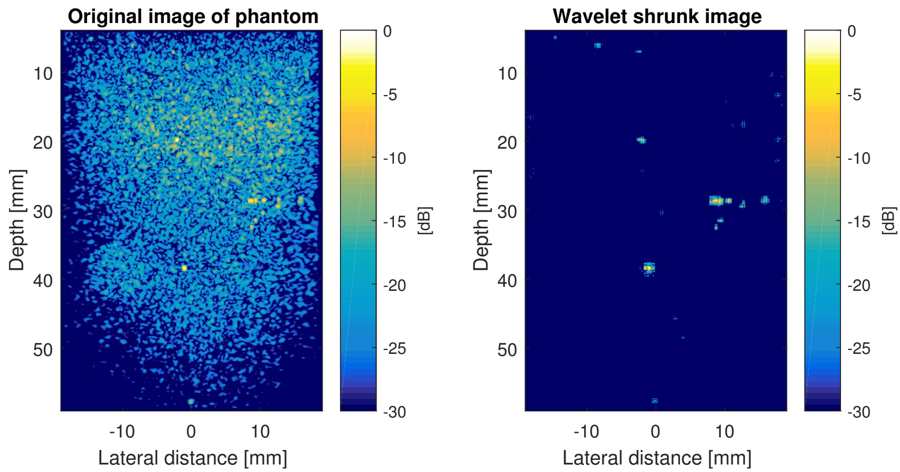

Figure III.4: Results on an image of a real tissue-mimicking phantom. Cp is 14-17 times higher in the wavelet shrunk image.

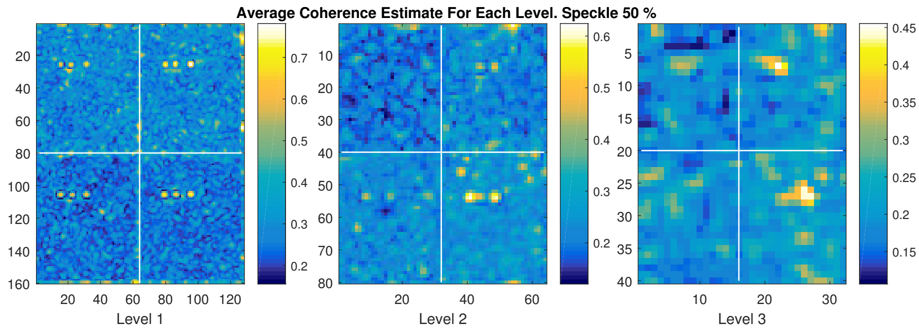

Figure III.5: Average coherence estimates for the simulated phantom. The four coefficient images are shown together for each wavelet decomposition level. The upper left corner shows the approximation image. The other three corners show the three detail images; horizontal (top right), vertical (bottom left) and diagonal (bottom right).

Table III.1: Cp and PP measurements corresponding to Figure III.7, calculated using (III.4) and (III.5).

Speckle [%]	**Cp**		**PP_1**		**PP_2**	
	Original	**Final**	**Original**	**Final**	**Original**	**Final**
50	13.9	247.9	10.3 dB	33.3 dB	7.1 dB	18.3 dB
70	9.3	301.2	7.3 dB	35.7 dB	4.1 dB	12.3 dB
95	6.2	359.4	4.6 dB	36.6 dB	1.4 dB	6.5 dB

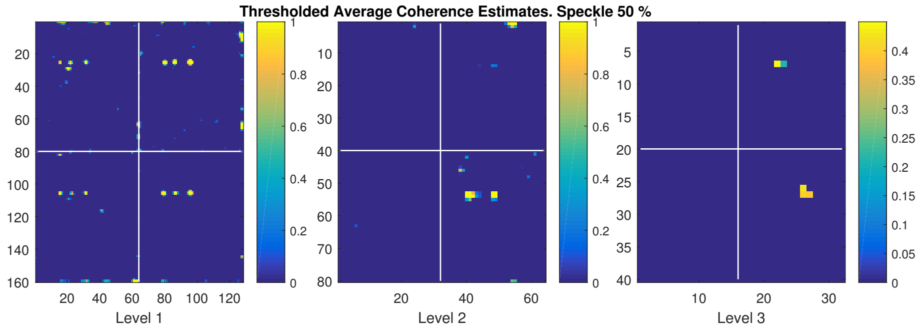

(a) Threshold limits: (0.5-0.65, 0.45-0.55, 0.4-0.5). Speckle 50 %

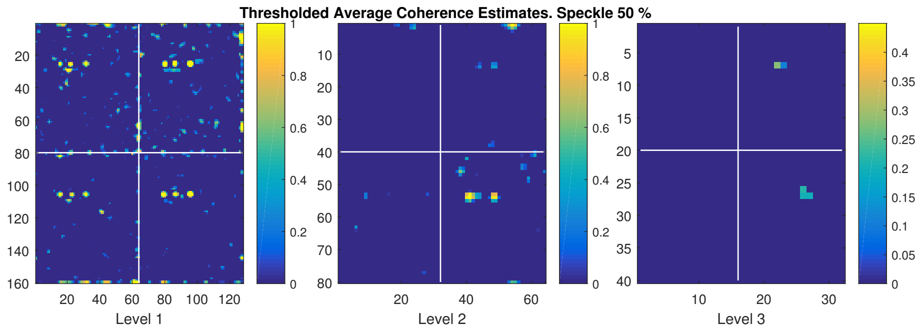

(b) Threshold limits: (0.4-0.6, 0.4-0.6, 0.4-0.6). Speckle 50 %

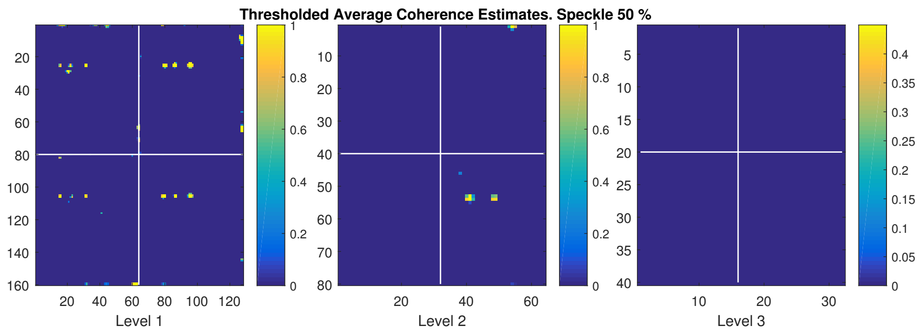

(c) Threshold limits: (0.55-0.65, 0.5-0.6, 0.5-0.6). Speckle 50 %

Figure III.6: Thresholded average coherence estimates using different threshold limits, applied on the images in Figure III.5. The top image (a) corresponds to results shown in Figure III.7(a), and (b) and (c) correspond to Figure III.8.

are around 18-58 times larger than in the original image. Table III.1 summarizes these results. Figure III.8 shows the results when using two different threshold limits for the 50 % speckle image.

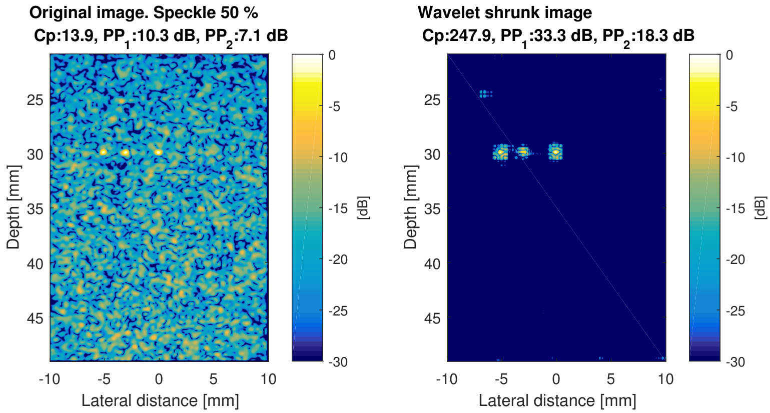

(a) Speckle 50 %. Threshold limits: (0.5-0.65, 0.45-0.55, 0.4-0.5)

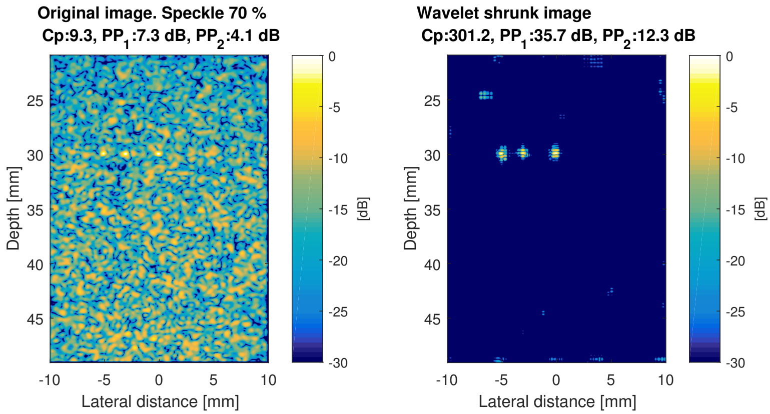

(b) Speckle 70 %. Threshold limits: (0.5-0.65, 0.45-0.55, 0.4-0.5)

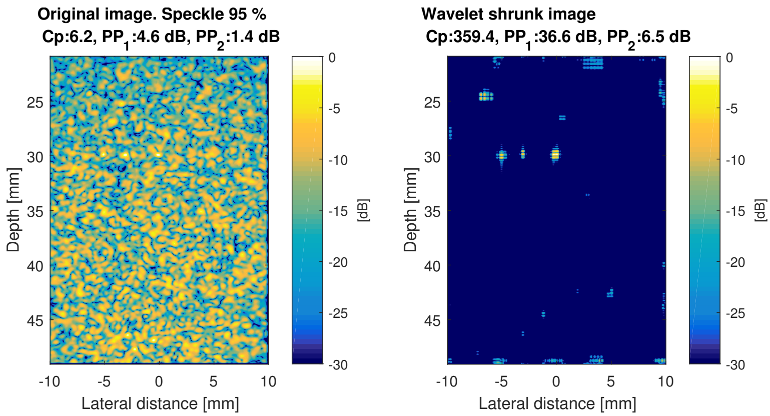

(c) Speckle 95 %. Threshold limits: (0.5-0.65, 0.45-0.55, 0.4-0.5)

Figure III.7: Results with varying speckle background intensity (50, 70 & 95 %). Cp and PP measurements are summarized in Table III.1.

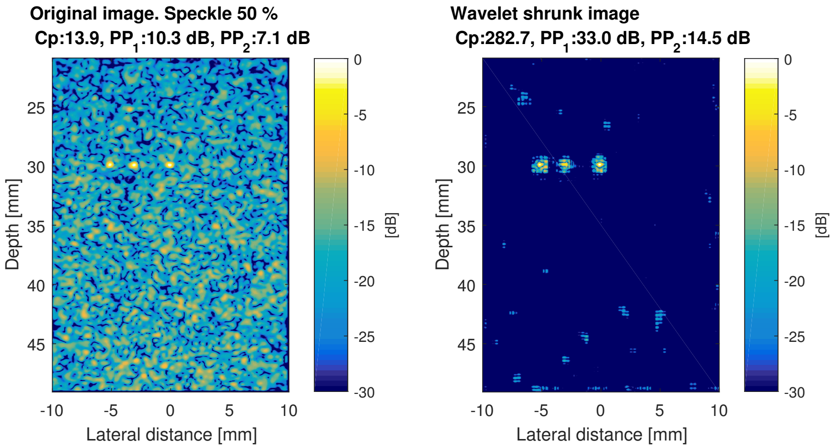

(a) Results using threshold limits: (0.4-0.6, 0.4-0.6, 0.4-0.6).

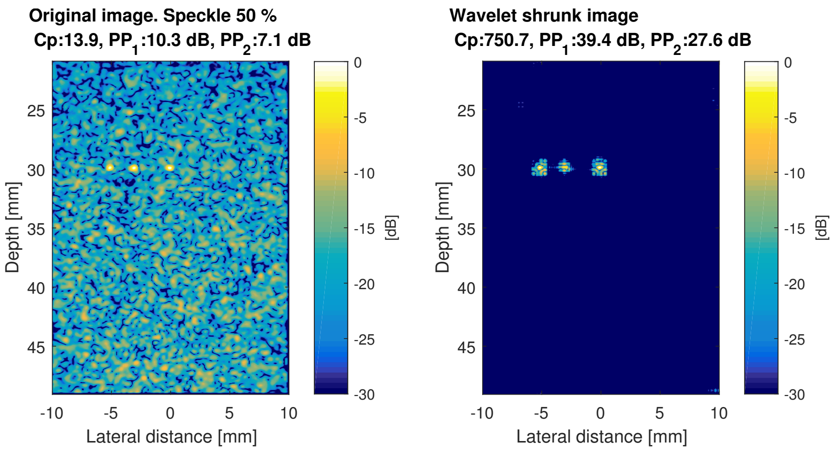

(b) Results using threshold limits: (0.55-0.65, 0.5-0.6, 0.5-0.6).

Figure III.8: Results when applying the threshold limits shown in Figure III.6(b) and III.6(c).

III.4 Discussion

Results on both the tissue-mimicking phantom in Figure III.4 and the simulated data in Figure III.7 show how the method can suppress speckle background. From Figure III.6 we expect best results when threshold values for the first and second level are relatively strict, since this excludes coefficients describing only speckle background. Decomposing with mild threshold limits to more than three levels resulted in the inclusion of more background speckle in the final image. From results shown in Figure III.8 we see that the best result for the 50 % speckle intensity is obtained when the threshold limits are so strict that the last level is completely attenuated, corresponding to an actual two-level decomposition.

Results presented in Figure III.7 and summarized in Table III.1 illustrate how the algorithm increases conspicuity by around 18-58 times more than in the original image. The method retains all of the point scatterers, even when intensity peaks in the speckle background are almost at the same level. When the speckle intensity increases, the chance of false positives in the final image also increases. The high speckle values in the shallow and deep depth range seen in the 95 % speckle results are assumed edge artifacts caused by Gibbs effect.

The results show it is essential to choose threshold limits for each level based on the coherence estimate values, which in turn are related to the size of the target objects and the intensity of the speckle background in the original image. When the speckle intensity is almost at the same level as the point scatterers, a strict thresholding can exclude too much information. With high relative speckle intensity, the method can be beneficial as a supplement to the conventional ultrasound image.

It is expected that a large number of realizations reduces the variance in the final image. However, results showed no difference between using P=100 or P=10000 realizations. P=12 was similar to P=100 when using the same parameters. When P was reduced to six realizations a little more of the speckle background was visible in the final image. This indicates that few realizations are required to produce a final image with well suppressed speckle background. The results when varying the threshold limits show how it is also not necessary to decompose into many levels and that even two levels might suffice. The fact that the algorithm works well with a low number of realizations and few levels is very positive for its computation time. The initial results indicate that the algorithm can enhance point scatterers that are almost buried in speckle, a situation quite similar to microcalcifications in breasts.

III.5 Conclusions

We have shown that the wavelet coefficient shrinkage algorithm manages to suppress speckle background and enhance point scatterers in an ultrasound image. The conspicuity of the point scatterers are greatly increased. The method retains the point scatterers even when intensity peaks in the speckle background are almost at the same intensity level. The method was tested for a variety of wavelet decomposition levels, thresholding schemes and number of realizations. Results show that few levels and number of realizations are necessary. The algorithm has potential to detect microcalcifications in breast tissue.

References

[Dah+11] Dahl, J. J. et al. “Lesion detectability in diagnostic ultrasound with short-lag spatial coherence imaging”. In: *Ultrason. Imaging* vol. 33, no. 2 (Apr. 2011), pp. 119–133.

[Dau92] Daubechies, I. “Symmetry for Compactly Supported Wavelet Bases”. In: *Ten Lectures on Wavelets*. 1992. Chap. 8, pp. 251–287.

[HV14] Hunter, A. J. and Vossen, R. van. “Sonar target enhancement by shrinkage of incoherent wavelet coefficients”. In: *J. Acoust. Soc. Am.* vol. 135, no. 1 (Jan. 2014), pp. 262–268.

[Jen96] Jensen, J. A. “FIELD: A Program for Simulating Ultrasound Systems”. In: *Proc. 10th Nordicbaltic Conf. Biomed. Imag., Suppl. 1, Part 1*. Vol. 4. 1996, pp. 351–353.

[JS92] Jensen, J. A. and Svendsen, N. B. “Calculation of Pressure Fields from Arbitrarily Shaped, Apodized, and Excited Ultrasound Transducers”. In: *IEEE Trans. Ultrason., Ferroelectr., Freq. Control* vol. 39, no. 2 (Mar. 1992), pp. 262–267.

[Rod+17] Rodriguez-Molares, A. et al. “The UltraSound ToolBox”. In: *Proc. IEEE Int. Ultrason. Symp. (IUS)*. Sept. 2017, pp. 1–4.

Paper IV

Point Detection in Ultrasound Using Prewhitening and Multilook Optimization

Stine Hverven Thon, Roy Edgar Hansen, and Andreas Austeng

Published in *IEEE Transactions on Ultrasonics, Ferroelectrics, and Frequency Control*, June 2022, 69 (6): 2085-2097. DOI: 10.1109/TUFFC.2022.3167923.

Abstract

We investigate methods to improve the detection of point scatterers in ultrasound imaging using the standard Delay-and-Sum (DAS) image as our starting point. An optimized whitening transform can increase the spatial resolution of the image. By splitting an image's frequency spectrum into many subsets using the multilook technique, we can exploit the coherent properties of a point scatterer. We present three new multilook methods and evaluate their effect on point detection. The performances are compared to DAS using synthetic aperture Field II simulations of a point scatterer in uniform speckle background. The results show that optimized prewhitening of the images can significantly improve point detection. The multilook methods have the potential to improve the detection performance further when a sufficient number of looks are used. If prior knowledge about the optimal spectrum limits is unavailable and a nonoptimal prewhitening is applied, applying the new multilook methods can considerably improve the point detection.

IV.1 Introduction

Point scatterers are small, highly coherent targets that can be challenging to detect due to peaks in the speckle background. There are several applications in medical ultrasound in which their detection is of importance, such as breast microcalcifications, kidney stones, and point tracking [And+97; AST00; AST98; Dia+18; Flø+17; Mac+18; Mat+19; MBR20; Ray+10; Tie+18]. Point targets are also of interest in other fields of study, such as radar [OQ98] and sonar [Abr19]. In the same way as [Ste07], this study is inspired by synthetic aperture imaging techniques in the radar community. We take the standard Delay-and-Sum (DAS) image as our starting point and investigate methods to improve point detection. The techniques presented in this paper are a continuation of the work in [THA22] and inspired by the multilook technique established in the radar community [CLR95; CLR96; Kel86; San+15]. We can view the detection of a point scatterer in speckle as a classical binary detection problem [Abr19; EG05; Kay13; Kay98; Lev08]. For a given image region, the objective is to decide between two hypotheses: speckle background *with* or *without* a point signal present. In [THA22] we discussed how to measure and evaluate the detection performance of various common ultrasound techniques.

Czerwinski et al. studied boundary and line detection on ultrasound images in [CJO98; CJO99]. They tested the Sticks detector and found that the performance of this technique could be significantly improved by prewhitening the speckle field. A whitening transform converts the covariance matrix of a set of random variables into the identity matrix [Kel86; KK99; KLS18], which consequently raises the frequency amplitudes to the same average level. Applying an optimized whitening transform to the ultrasound image increases the effective spatial frequency coverage and correspondingly the spatial resolution since resolution is inversely proportional to bandwidth. Increased resolution corresponds to increased point signal intensity compared to the speckle background (point SNR), and this significantly improves the probability of detection [THA22]. We study different whitening filter limits and evaluate their improved point detection performance. To get measurable and statistically significant results, we need many images with specific point scatterer intensity, known point location, and varying speckle background. To achieve this, we simulated many images of a point scatterer in uniform speckle background using Field II [Jen+06; Jen96; JS92]. This study is the first work in ultrasound to combine prewhitening with the multilook technique.

The multilook technique is a widely used technique in synthetic aperture radar (SAR) imaging to reduce speckle [Jak+96, ch. 3.3] [OQ98, p. 29]. It creates several *subimages* or *looks* from the original DAS image by splitting the entire frequency bandwidth into several subsets with different central frequencies. The *normalized matched filter* (NMF) multilook method is well established in the radar field [CLR95; CLR96; Kel86; San+15]. Based on the known response from a point scatterer, it imposes higher weighting on the contribution from the important looks to maximize point detection. We present three new heuristic methods to improve point detection using multilook optimization. Our three new methods are inspired by the NMF method. The *normalized matched filter weighted* (NMFW) method applies NMF as an image weighting scheme. It combines optimized look weighting with the actual point intensity to ensure that we enhance points with intensities higher than the surrounding background. The *multilook coherence factor* (MLCF) is a simplification of the NMF method. MLCF omits the look weighting and instead calculates the ratio between the coherent and incoherent sum of all the looks weighed equally. The *multilook coherence factor weighted* (MLCFW) method applies the MLCF method as a weighting scheme.

We evaluate the detection performance of the multilook methods and compare them to original DAS and optimized prewhitening. Our results show that applying a multilook method can improve the point detection, provided we use many divisions in the sublooking process. We also evaluate the methods using *nonoptimal* prewhitening to test the methods when prior knowledge about the optimal whitening limits is unavailable. The new methods MLCF and MLCFW significantly improve the detection performance for weak point scatterers and can also be applied without prior knowledge about the theoretical point signal response.

The following section briefly presents how to calculate point detection performance. We then introduce the whitening transform and the sublooking process. We present results from a one-dimensional (1-D) study to establish the potential of prewhitening and sublooking. Section IV.5 presents the different choices for the whitening filter limits and the setup for applying the multilook methods on the 2-D ultrasound DAS images. Section IV.6 shows the results, and in Section IV.7 we discuss how the methods affect the point detection performance.

IV.2 Background - Detection Theory

IV.2.1 Measuring Probability of False Alarm and Detection

Detection performance is measured in terms of probability of false alarm P_{FA} and probability of detection P_{D}. P_{FA} is estimated using images containing only speckle, and P_{D} is estimated using images with a point scatterer present [Kay98, ch. 3.3]. We classify the intensity values above threshold γ as correct detections and false alarms. We find the measured probabilities P_{D} and P_{FA} by counting the number of values and comparing them to the number of realizations R. When presented with an ultrasound image, we assume that the most likely target candidate is the scatterer with the highest intensity [Abr19; THA22]. We detect within a search window if the pixel is a point scatterer. Since we have a simulated environment, we can adopt the detection strategy from [THA22] and evaluate a search window around the known point location. We pick the maximum value within the search window for the false alarm and true positive. The search window size affects the separability of point targets. If there are two point targets within a search window, we will only detect the strongest point. As in [THA22], we study a simplified but statistically equivalent 1-D scenario to establish and illustrate the different methods. We apply the same search window sizes as in [THA22] for the detection studies, which for the 1-D study is a ± 3 independent pixels window size.

P_{D} depends on the point's intensity relative to the background. We calculate the point's SNR metric as

$$\text{SNR} = 10 \log_{10} \left(\frac{i_p}{i_s} \right), \tag{IV.1}$$

where i_p is the average maximum point intensity, and i_s is the average intensity of the speckle region around this location without the point scatterer present.

IV.2.2 Evaluation of Detection Performance

A Receiver Operating Characteristics (ROC) curve compares P_{D} to P_{FA} for a given threshold γ. It is a conventional method of displaying detection performance. We can achieve a lower P_{FA} by increasing γ, but then P_{D} is also expected to decrease. All points on the ROC curve should satisfy $P_{\text{D}} \geq P_{\text{FA}}$ [Lev08, ch. 2.4.2] [Kay98, p. 74]. Area Under the Curve (AUC) is another way to present ROC results [Abr19, p. 315]. AUC for a diagonal line with $P_{\text{D}} = P_{\text{FA}}$ equals 0.5. We can also present P_{D} for a chosen P_{FA} value, for example $P_{\text{FA}} = 5\%$, or plot P_{D} as a function of SNR for a fixed P_{FA} value

[Kay13, ch. 7.3.2]. The SNR-range where P_{D} varies greatly is the most interesting to analyze when comparing the detection performance of different methods. Since detection performance given high P_{FA} values is not of much practical interest, we present ROC curves for P_{FA} values up to 0.1.

The accuracy of the measured performance results is affected by the number of realizations R [Kay98, p. 37]. We can plot confidence intervals for the ROC curve by calculating the relative absolute error for P_{FA} and P_{D} at each γ value. In [HM82], Hanley and McNeil present how to compute a conservative estimate of the confidence interval for the AUC. It is proportional to $\sqrt{R}$ and depends on the number of speckle realizations with and without a point scatterer present.

IV.3 The Whitening Transform

A *whitening transform* is defined as a decorrelation transform that converts a set of random variables having a known covariance matrix into a set of new random variables whose covariance is the identity matrix [Kel86; KK99; KLS18]. The transformation is called *whitening* because it changes the input vector into a white noise vector. Prewhitening boosts the frequency amplitudes to the same average level. To obtain a whitening transform, we can estimate a smoothed average of the frequency image data. We calculate such an estimate based on secondary data or by applying an adaptive method. This study estimated a smoothed average and applied its inverse to the frequency data.

To study the effect of whitening, we first present results on ideal 1-D sequences of a point scatterer with a random position in speckle. We first create 500 realizations of a 1-D speckle sequence, constructed as a complex sum of two normally distributed sequences. We add a point scatterer to the sequence with a chosen point SNR value. To obtain statistically significant results, we tested 200 different random positions for the point scatterer for each speckle sequence. The sequence is further bandpass filtered with a raised cosine filter and oversampled by a factor of three. Since a realistic ultrasound frequency spectrum always includes some noise, we add random noise with intensity -15 dB below the average speckle level to the 1-D sequence. The spectrum in Figure IV.1 has a similar shape to the magnitude frequency spectrum of an oversampled, basebanded ultrasound signal in one direction.

Figure IV.1 shows the magnitude spectrum of a speckle sequence before and after whitening. To obtain a whitening filter, we first calculate a smoothed average of the magnitude of the Fourier transform of the speckle vector. The whitening filter is the inverse of this smoothed average. The whitening filter is set to zero outside the valid frequencies, which for the 1-D study depends on the amount of oversampling. The frequencies after the whitening transform are raised to the same mean amplitude level while retaining the randomness. We obtain the whitening filter for the 2-D images by calculating a smoothed average of the magnitude of the 2-D Fourier transform of all the complex speckle images.

The spectrum does not have an ideal rectangular shape with clear cutoff limits between the signal and noise. We have used a priori knowledge of the spectrum shape to set the prewhitening filter limits. The whitening filter that optimizes detection

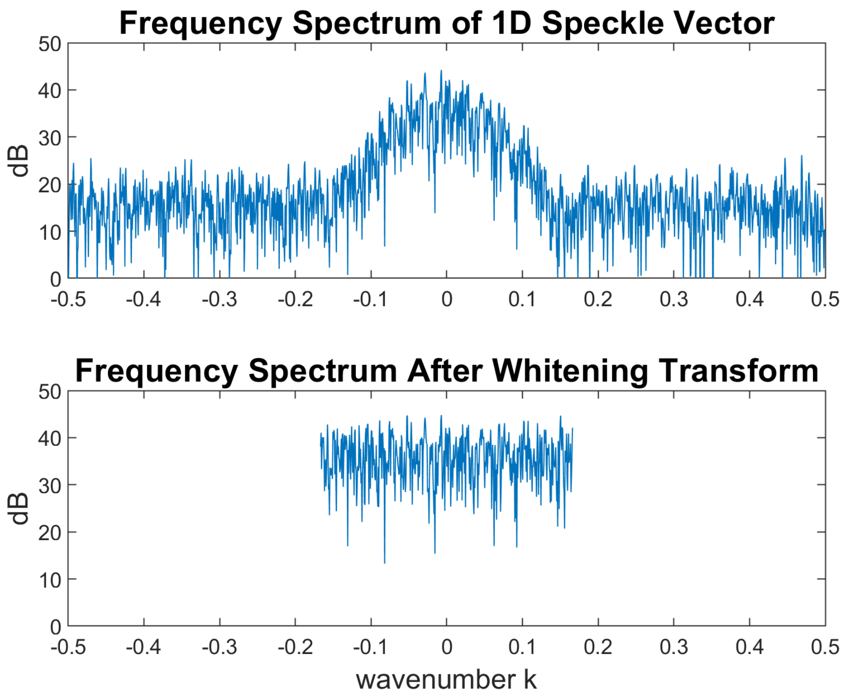

Figure IV.1: The spatial frequency spectrum of a bandpass filtered, oversampled 1-D speckle sequence with some added noise. The same spectrum is also shown after applying an optimized whitening transform, and the transform only retains and enhances the valid frequencies.

performance depends however on both image resolution and point SNR since the spectrum is nonuniform. Consider a uniform frequency spectrum for both signal and noise with the same bandwidth B. Doubling the effective spatial frequency coverage by whitening corresponds to doubling the resolution since resolution is inversely proportional to bandwidth. Decreasing the size of the resolution cell means the point scatterer is combined with fewer diffusive scatterers within the cell. This improves the point SNR and consequently the detection performance [THA22]. The noise contribution reduces and this consequently improves the point's SNR. P_{D} is therefore proportional to both bandwidth B and point SNR,

$$P_D \text{ for fixed } P_{FA} \quad \propto \quad B \cdot \text{SNR}. \tag{IV.2}$$

The *optimal* whitening filter limits maximize (IV.2) and are therefore dependent on where we have *both* large bandwidth and positive SNR. In Figure IV.1 we have used a signal vector oversampled by a factor of three with accordingly narrowed whitening filter limits. Increasing the filter limits outside the area of positive SNR will effectively decrease the P_{D}. Similarly, if we narrow the filter limits to enclose the portion of the frequency spectrum with known high point SNR, the reduced bandwidth causes a decrease in P_D. Figure IV.2 shows the great improvement in ROC that we can achieve by prewhitening the data. It should be noted that the detection improvement is a function of the signal spectrum and the noise spectrum.

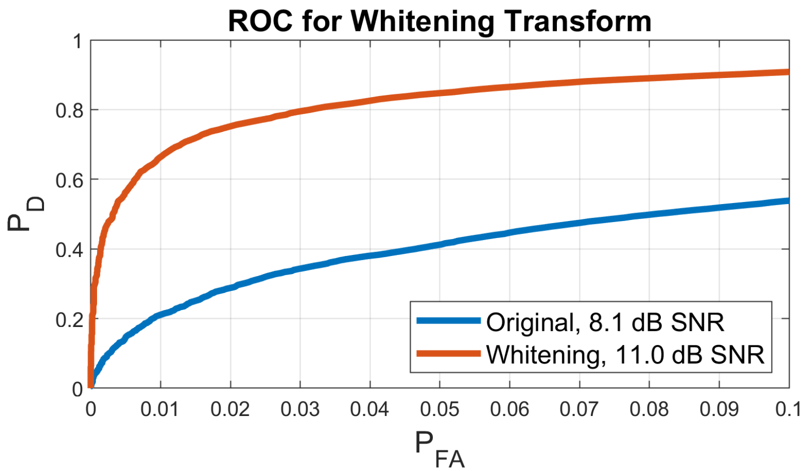

Figure IV.2: ROC for a whitening transform applied on 1-D speckle sequences with or without a point target. Applying an optimized whitening increases the measured point SNR.

IV.4 The Sublooking Process

The multilook technique splits the entire frequency bandwidth of the image into several adjacent subsets [Jak+96, ch. 3.3] [OQ98, p. 29]. Each subset has a different central frequency. We can create a separate image, known as a *sublook* or *look*, by computing the inverse Fourier transform of a subset. Splitting into L non-overlapping subsets reduces the frequency bandwidth by a factor L and thus similarly degrades the final image resolution of the looks. We can create several sublooks by either having independent subset bandwidths or allowing a partial overlap [San+15].

IV.4.1 Point Signal Response in a Sublook

A point target is a coherent scatterer that is a dominant scatterer within a resolution cell. Some scattering loss occurs when the point scatterer is not in the center of the resolution cell. The Point Spread Function (PSF) describes the response of an imaging system to a point source. To obtain the PSF for each point position in the 1-D study, we started with the PSF of a point in the center, and then shifted the phase with respect to each pixel position. We can retrieve the response of a coherent scatterer in each sublook by adjusting the PSF for the sublook center frequency and bandwidth. We now evaluate the ideal 1-D point scatterer signal from Sect. IV.2 and IV.3. The complex amplitude of this original point scatterer is $C = C_0 e^{j\phi}$ if we assume it is in the center of the resolution cell. Following [San+15], we start with a point scatterer positioned at a distance z_0 and its sinc-response

$$a_{\text{point}}(z) = C_0 e^{j\phi} e^{-j\frac{4\pi f_0}{c}z_0} \operatorname{sinc}\left(\frac{2B(z-z_0)}{c}\right). \tag{IV.3}$$

Here f_0 is the transducer center frequency, c is the wave speed, and B is the frequency bandwidth. We create L sublooks of equal bandwidth $B_S = B/L$ by applying rectangular window filters over the different central frequencies $f_c^{(n)}$, for $n = 1, ..., L$. Each sublook response $a^{(n)}$ is thus

$$a^{(n)}(z) = \mathcal{F}^{-1}\left\{\mathcal{F}\{a_{\text{point}}(z)\}\operatorname{rect}\left(\frac{f - f_c^{(n)}}{B_S}\right)\right\} \tag{IV.4}$$

where $\mathcal{F}$ represents the Fourier transform. We can express the point signal response in each sublook n as [San+15]

$$a^{(n)}(z) = \frac{B_S}{B} C_0 e^{j\phi} e^{-j\frac{4\pi f_0}{c}z_0} e^{j\frac{4\pi f_c^{(n)}}{c}(z-z_0)} \operatorname{sinc}\left(\frac{2B_S(z-z_0)}{c}\right). \tag{IV.5}$$

From the expression, we see that the new bandwidth B_S creates a broader sinc and thus degrades the range resolution to $\Delta z_S = c/(2B_S)$. The final 2-D response depends on the bandwidth in both directions. For the 2-D images in [San+15], the response in the other direction was similarly calculated and multiplied to the above expression.

Chen et al. present a theoretical model to depict the PSF for varying point scatterer positions and apodization settings for plane-wave ultrasound imaging in [Che+20]. The PSF is affected by the point scatterer's position, the transducer characteristics, and beamforming setting [Che+20]. The PSF is horizontally symmetric when the point scatterer is in the center, as illustrated in Figure IV.3, but asymmetric when the point is shifted away from the center[Che+20]. Since many aspects affect the PSF, we simulated the actual response of a point scatterer placed in each pixel position to obtain the true PSF per pixel position for our 2-D setup. The frequency response was further prewhitened and divided into subsets to create the theoretical point signal response per sublook per pixel position.

IV.4.2 Spatial Frequency Limits

The spatial frequency coverage or wavenumber support for an ultrasound imaging system is defined by the finite aperture size, the band-limited pulse, and centered on $2k_0 = 4\pi f_0/c$ [AT00, ch. 3]. In the k_x direction, the support region's lateral width increases linearly with increasing frequency. The PSF has a shape resembling a slice cut of a circular arc, as illustrated in Figure IV.3. The system cannot image objects with spatial frequencies outside the PSF limits. The spectrum in Figure IV.3 has been bandpass filtered ($f_L \leq f \leq f_H$) and demodulated by the estimated center spatial frequency k_D ($k_D \approx 2k_0$). The spectrum shown in Figure IV.3 is normalized such that

$$\kappa_{zmax} = \frac{k_H - k_D}{k_D} = \frac{f_H - f_D}{f_D}. \tag{IV.6}$$

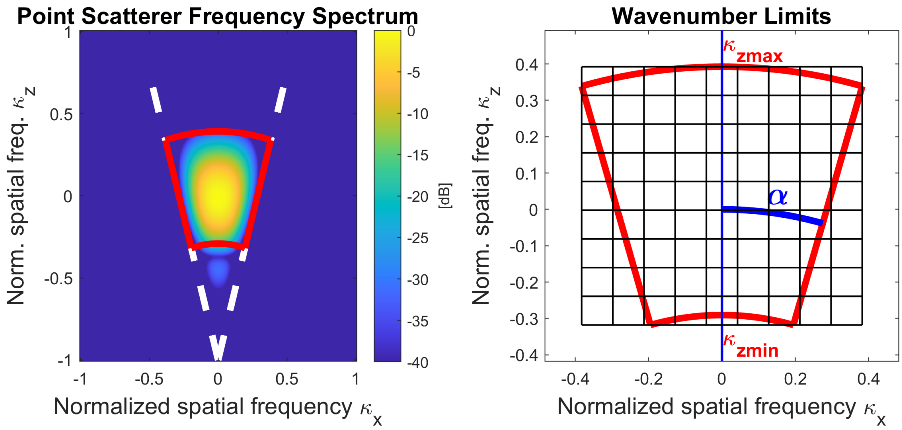

Figure IV.3: The frequency spectrum of a point scatterer, shown with a 40 dB dynamic range. The spatial frequencies are normalized by the estimated center frequency k_D ($\approx 2k_0$). The critical angle α is 16°. The region shown is divided into 9×9 subsets.

With an adaptive aperture setting, we can ensure uniform image resolution by applying a range-independent beamwidth by increasing the active aperture with increasing range z [Sza14, p. 381]. The *F-number* or $f_{\#}$ is the ratio between imaging depth z and active aperture size D^*, i.e., $f_{\#} = z/D^*$. The adaptive aperture settings limit the lateral spatial frequency k_x. The receiving angle is the angle between the depth z and the lateral distance from the origin x. The critical angle is the largest probe-to-object angle the system can image. It is confined to the transducer aperture range, i.e., $x_{\max} = D/2$ [Che+20]. With equal transmit and receive aperture D^*, the critical angle α is [Gol+21][Den+13]

$$\alpha = \text{atan}\left(\frac{D^*/2}{z}\right) = \text{atan}\left(\frac{1}{2f_{\#}}\right). \tag{IV.7}$$

A small $f_{\#}$ results in a wide frequency response in the k_x-direction. Figure IV.3 illustrates the relation between angle α and the normalized spatial frequency limits:

$$\text{limits for } \kappa_x \quad = \pm\frac{k_H \sin(\alpha)}{k_D}. \tag{IV.8}$$

The lower limit for κ_z is

$$\kappa_{zmin} = \frac{k_L \cos(\alpha) - k_D}{k_D}. \tag{IV.9}$$

IV.4.3 The Multilook Methods

The Generalized Likelihood Ratio Test (GLRT) is the basis for the formulae for the multilook techniques and its derivation is shown in detail in the Appendix. The

GLRT test for sublooks evaluates each specific image pixel and its corresponding L-dimensional sublook vector $\boldsymbol{y}$. The detector is also known as the *normalized matched filter* (NMF) and it is well-known in the radar community [CLR95; CLR96; DFP09]. The NMF decision rule with respect to threshold γ is [CLR95; CLR96; Kel86; San+15] [San14, ch. 3.4.4]

$$\mathrm{NMF}(\boldsymbol{y}) = \frac{|\boldsymbol{a}^{\mathrm{H}}\mathrm{M}^{-1}\boldsymbol{y}|^2}{(\boldsymbol{y}^{\mathrm{H}}\mathrm{M}^{-1}\boldsymbol{y})(\boldsymbol{a}^{\mathrm{H}}\mathrm{M}^{-1}\boldsymbol{a})} > \gamma. \tag{IV.10}$$

Here $\boldsymbol{a}^{\mathrm{H}}$ is the Hermitian conjugate of the sublook vector of a theoretical point scatterer at the specific pixel position. The correlation among speckle samples belonging to the different sublooks is described by the sublook covariance matrix M. The whitening process can be incorporated into M as in [CLR95; CLR96; Kel86], but in this study we prewhiten the images prior to subset division and therefore M only depends on the subset bandwidth overlap [San+15]. M is equal to the identity matrix I in the case of independent, non-overlapping subsets. With $L = L_z L_x$ number of sublooks, the dimension of M is $L \times L$.

The numerator of (IV.10) corresponds to the power output of matched filtering of the sublook vector $\boldsymbol{y}$ with the theoretical vector $\boldsymbol{a}$, calculated per pixel. Note that the numerator effectively is a weighted coherent sum of all looks such that we retain the full image resolution in the final image. The NMF method is a normalized method due to the denominator. The denominator is essential in the case of textured backgrounds, where the number and resolution of the sublooks influence how well the denominator estimates the background.

We simplify (IV.10) for independent sublooks ($\mathrm{M} = \mathrm{I}$) and get

$$\mathrm{NMF}(\boldsymbol{y})\bigg|_{\mathrm{M}=\mathrm{I}} = \frac{|\boldsymbol{a}^{\mathrm{H}}\boldsymbol{y}|^2}{(\boldsymbol{y}^{\mathrm{H}}\boldsymbol{y})(\boldsymbol{a}^{\mathrm{H}}\boldsymbol{a})} > \gamma. \tag{IV.11}$$

If we weight all sublooks equally, i.e., $\boldsymbol{a} = 1$'s, the numerator becomes a coherent sum of all looks. The numerator is then the same as only applying prewhitening. Again, the numerator ensures we retain the full image resolution in the final image. The test in (IV.11) changes to a ratio of the coherent and incoherent sum of all the sublooks. We term the new multilook method *multilook coherence factor* (MLCF).

$$\mathrm{MLCF}(\boldsymbol{y}) = \frac{|\mathbf{1}^{\mathrm{H}}\boldsymbol{y}|^2}{(\boldsymbol{y}^{\mathrm{H}}\boldsymbol{y})L} = \frac{|\sum_{n=1}^{L} y(n)|^2}{L\sum_{n=1}^{L} |(y(n)|^2} > \gamma. \tag{IV.12}$$

The simplification of $\boldsymbol{a} = 1$'s drastically reduces the computational complexity as the method does not require prior knowledge of the theoretical point signal response per sublook. The ratio in MLCF is reminiscent of Coherence Factor (CF) beamforming in ultrasound. The CF *beamformer* calculates the ratio between coherent and incoherent energy across the aperture [MF94]. It is used as an adaptive weight to the DAS image [LL03]. This study takes the DAS image as its starting point and investigates methods to improve point detection. The MLCF method is a new 2-D CF method since we divide the spatial frequencies over two dimensions and calculate the coherence over the resulting sublooks. Traditional CF has overlapping spatial frequency areas, whereas MLCF has non-overlapping spatial frequency areas in both spatial direction and frequency.

The image weighting is inspired by adaptive coherence-based beamformers that apply weights to the DAS image. Since image weighting with the CF weights gave an improvement in the ROC results in [THA22], it was interesting to explore if we could obtain the same improvement using the multilook methods as weighting schemes. We therefore create two new multilook methods by applying NMF and MLCF as weighting schemes to the prewhitened image. NMF is not applied as an image weighting in the radar community. We term the new image created by NMF weighting as a *NMF weighted* image (NMFW).

$$\mathrm{NMFW}(\boldsymbol{y}) = \mathrm{NMF}(\boldsymbol{y}) \cdot \left| \sum_{n=1}^{L} y(n) \right| > \gamma. \tag{IV.13}$$

We correspondingly apply MLCF as a weighting scheme and refer to the new multilook image as a *MLCF weighted* (MLCFW) image.

$$\mathrm{MLCFW}(\boldsymbol{y}) = \mathrm{MLCF}(\boldsymbol{y}) \cdot \left| \sum_{n=1}^{L} y(n) \right| > \gamma. \tag{IV.14}$$

It should be noted that (IV.10) and (IV.12) produce normalized results, and (IV.13) and (IV.14) do not. Table IV.1 summarizes the differences in computational complexity of the suggested methods.

Table IV.1: Computational Complexity of the Suggested Methods

Prewhitening	MLCF & MLCFW	NMF & NMFW
Low computational complexity. Preferable with prior knowledge of the critical angle and pulse bandwidth.	Medium computational complexity. Prewhitening and sublook division.	High computational complexity. Prewhitening and sublook division. Requires prior knowledge of the theoretical point signal response per sublook.

Figure IV.4 shows an example ultrasound image scene with three point scatterers. The same image scene is shown after prewhitening and the four multilook methods, but before any detection thresholding. The multilook methods seem to increase the threshold between the point scatterers and the peaks in the speckle background. However, it could be that the methods simply stretch the dynamic range [Rin+19]. The brightest points in the image, whether speckle or point targets, will then become more distinct from the background. Since both speckle peaks and point targets are enhanced, a detection strategy picking the maximum value within a search window for false alarm and true positive will not measure an improvement in detection. To fully evaluate the detection performance, we need to perform a full ROC analysis.

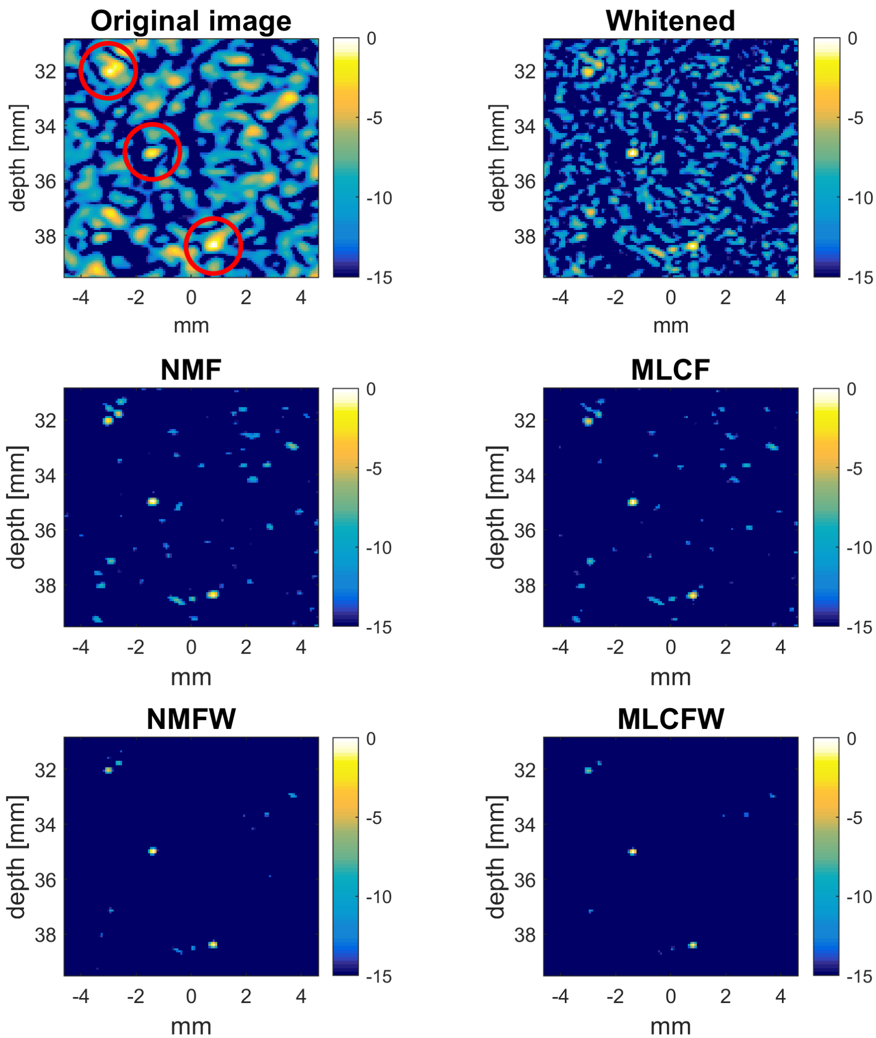

Figure IV.4: Example of an ultrasound image with three point scatterers shown for prewhitening and the four multillook methods. All images are normalized by the maximum value to be comparable, and shown with a 15 dB dynamic range. The red circles indicate the locations of the three point scatterers.

IV.4.4 Number of sublooks

The NMF is shown to be asymptotically optimum for a large number of sublooks $L \gg 1$ [CLR95]. Even for a moderate number such as $L \geq 8$, the deviation to the optimum is relatively small except when P_{D} is high. Figure IV.5 shows the ROC curves for the multilook methods using 19 and 141 sublooks. Figure IV.6 shows how the AUC for NMF and NMFW increases with increasing L but also observe how it starts to

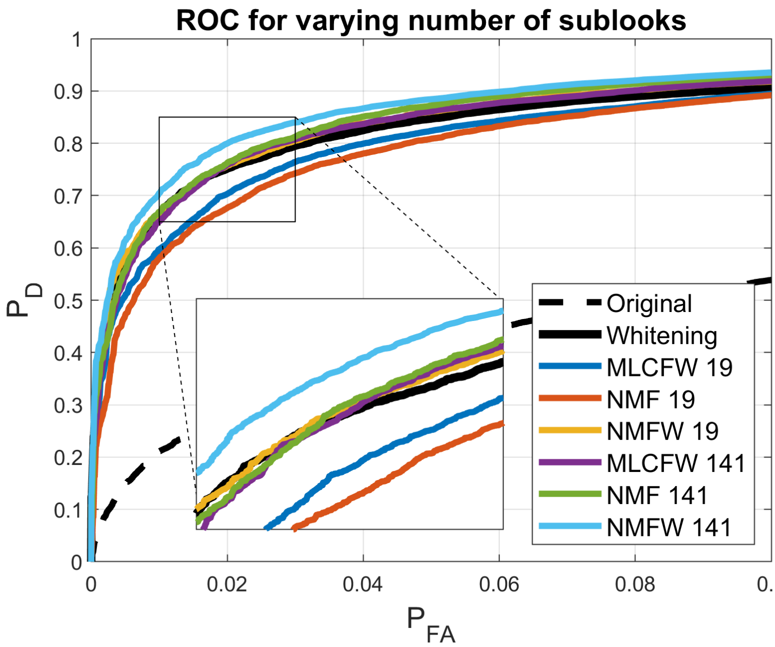

Figure IV.5: ROC for the multilook methods applied on ideal 1-D speckle sequences with or without a point target. We analyzed 2500 speckle realizations, each with 200 random point scatterer positions. Point SNR is 8 dB. Here are the results using 19 and 141 sublooks.

saturate at a high number of sublooks. With increasing L, the denominator in (IV.12) improves its estimate of the speckle power, and the ROC curve for MLCFW approaches NMFW. The results indicate a saturation around three independent pixels per sublook in the whitened case. To achieve sufficient variation in each sublook image, it must contain information from some independent pixels. The results in [San14] also show improved detection performance with increasing number of sublooks. Increasing the number of sublooks increases the computational load, so the practical number to use will be situation-dependent.

IV.5 Methods

This section describes the simulation and test setups in our study. We used Field II software to generate raw channel data. Figure IV.7 illustrates the setup of the detection analysis. The DAS beamforming was performed in MATLAB (Mathworks, Natick, MA) using the Ultrasound Toolbox (USTB)[Rod+17].

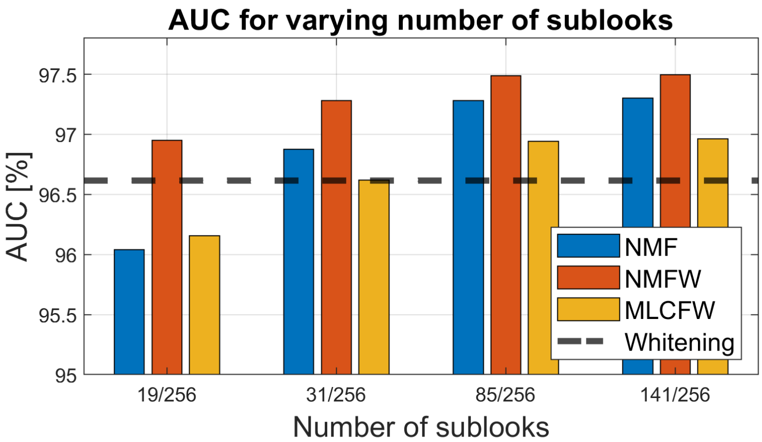

Figure IV.6: AUC for the multilook methods using a varying number of sublooks. Point SNR is 8 dB. Using $L = 85$ sublooks corresponds to approximately three independent pixels per sublook ($85/256 \approx 1/3$).

IV.5.1 Synthetic Transmit Setup and Image Reconstruction

In order to establish a baseline for detection, we designed the phantom as a simple scenario of a single point scatterer in uniform speckle background. The setup was the same as in [THA22]. We acquired images with focused, uniform resolution for all pixels using synthetic transmit aperture imaging. We used a 128 element, λ pitch, linear array with 5.1 MHz center frequency. The transmitted pulse bandwidth was 65 $\%$ of the center frequency, the wavelength λ was 0.3 mm, the aperture size was 38.1 mm, and the speed of sound was 1540 m/s. We added white Gaussian noise to the channel data at 10 dB *channel SNR*, assuring the additive channel noise fixed and below the speckle background level. The data was basebanded before further processing. We varied the point scatterer intensity relative to the combined speckle and noise background to obtain different point SNR values.

We simulated 243 speckle realizations, consisting of 91000 point scatterers and at least 20 scatterers per resolution cell. This ensured fully developed speckle statistics [Wag+83]. For the 2-D study with different whitening filter limits, we simulated one point scatterer at 65 image positions (13×5 matrix grid). For the 2-D multilook study, we simulated one point scatterer at 117 image positions (13×9 matrix grid). We chose the point positions to ensure varying scalloping loss [Har78]. We simulated radio frequency channel data separately for the point scatterer and the speckle background. DAS beamforming is a linear process, and we could therefore coherently combine the data images to get varying point locations and SNR values. For a given point SNR value in the multilook study, we created and analyzed 117×243 images. Using detection strategy C in [THA22], this corresponds to 28431 realizations for P_{D} and P_{FA} calculation.

We ensured uniform average background intensity by calculating correction maps

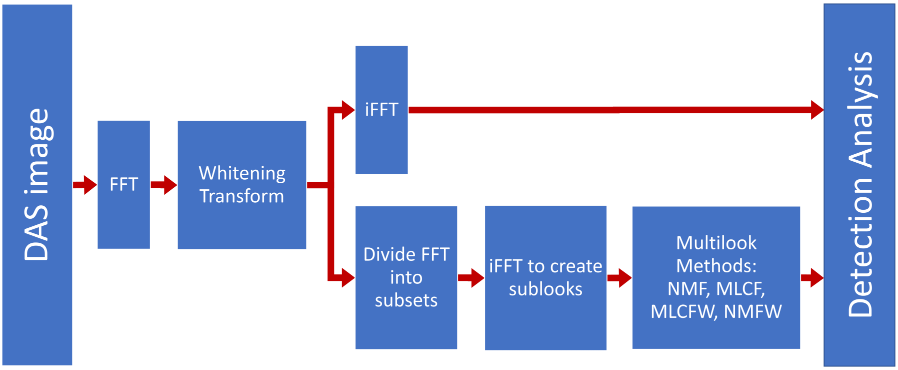

Figure IV.7: Setup of the detection analysis in this study. We start with the DAS image in the spatial frequency domain (FFT) and apply a whitening transform. We then divide the frequency domain into subsets over two dimensions and create *sublooks*. We apply the multilook methods on these sublooks and finally analyze the point detection performance.

from the average of all speckle backgrounds and applying them to the images before detection. The reconstructed image scene is the same as in [THA22], a 20 mm wide and 40 mm deep scene of 512×256 pixel size. The -6 dB spatial resolution for a center point scatterer with hamming transmit apodization and $f_{\#} = 1.75$ corresponded to approximately 5×7 pixels [THA22]. The detection strategy applied a search window of size two times the spatial resolution. Point SNR was calculated using (IV.1) for the point scatterer positioned in the center of the DAS image scene. We tested SNR values that correspond to relatively weak point scatterers in speckle.

IV.5.2 Whitening Transform

In this study, we applied the same whitening transform to all the DAS images. The whitening transform was estimated using many speckle realizations. As presented in Section IV.4, the limits for the spatial frequencies are defined by the critical angle α and the pulse bandwidth. The optimal limits of the whitening filter transform depends on the image resolution and the point SNR. We studied the following eight different whitening transform limits:

- Box region $\{k_{zmax}, k_{zmin}, k_{xmin}, k_{xmax}\}$
- Angle α with frequencies $\{f_L, f_H\}$
- Angles $\alpha \pm 10\%$ with frequencies $\{f_L, f_H\}$

- Angle α -20% with frequencies $\{f_L, f_H\}$
- Angle α with frequencies $\{+5\%\ f_L, -5\%\ f_H\}$
- Angle α with frequencies $\{-5\%\ f_L, +5\%\ f_H\}$
- Angle α $+10\%$ with frequencies $\{-5\%\ f_L, +5\%\ f_H\}$

The inverse whitening filter is tapered with a small Gaussian filter to reduce edge effects. Figure IV.8 illustrates the different whitening filter limits. The optimal angle for the whitening transform depends on both SNR and the geometry and system setup.

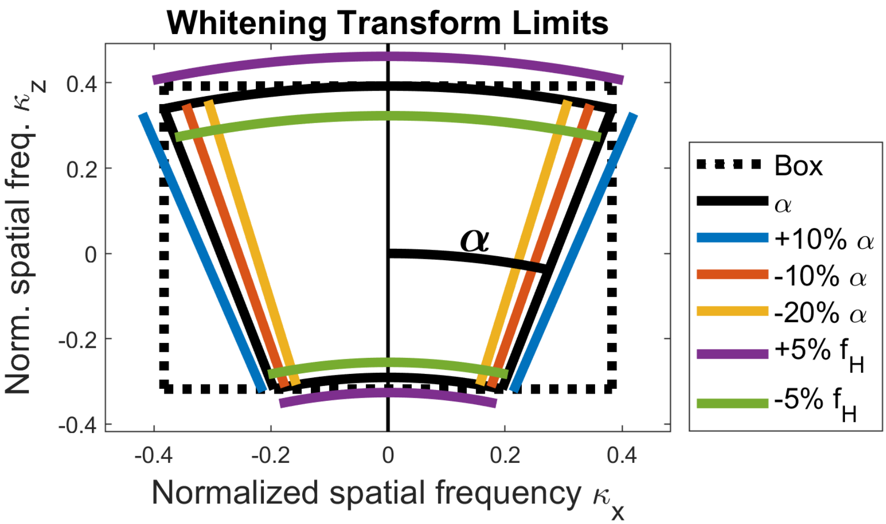

Figure IV.8: Illustration of seven whitening filter limits defined by the critical angle α and the pulse bandwidth. $+5\%$ f_H corresponds to a 5% increase in f_H and -5% in f_L .

IV.5.3 Multilook Method

To get the same resolution for all sublooks, we chose a rectangular grid for the subsets, as depicted in Figure IV.3. We applied a steep exponential decay, $exp(-(2|k|/B_S)^4$, to the edges of the subset filters to suppress any edge effects. We applied prewhitening using the critical angle α with the known pulse bandwidth frequencies $\{f_L, f_H\}$ as whitening limits. The α-whitening limits ensure that the sublooks created from the subsets outside the critical angle α are suppressed. The theoretical point scatterer look vectors in NMF will also suppress these sublooks. We simulated the actual response of a point scatterer placed in each pixel and the pixel's corresponding look vector to ensure correct theoretical vectors. We can also determine the theoretical look vectors using the frequency response of a point scatterer in the center, shifting the phase with respect to each pixel position, and calculating the corresponding look vector. The latter technique was applied for the 1-D study in Section IV.4. For simplicity, (IV.20) and (IV.10) assume the point scatterer is in the center of the pixel. ROC-analyses on simulated SAR images have shown that this approximation has negligible effects provided L is large (in the order of 30) and $SCR > 10$ dB [San14, p. 125].

We performed ROC analysis for NMF, NMFW, MLCF, and MLCFW. Since sublook overlap does not contribute more overall information [San14], we chose to apply independent, non-overlapping, and uniformly spaced subsets. The covariance matrix M in (IV.10) simplifies to a diagonal matrix since the input images are prewhitened. In comparison, [San+15] also used prewhitened images for NMF but chose to use uniformly spaced, rectangular, and partially overlapping sublook bandwidths. We tested 13×13, 19×15, and 45×25 subset block grids, dividing the frequency spectrum into 169, 285, and 1125 subsets, respectively.

In addition to the optimized α-whitening limits, we also tested the multilook methods combined with a *nonoptimal* prewhitening. We applied angle $\alpha + 10\%$ and frequencies $\{-5\%\ f_L, +5\%\ f_H\}$ as the nonoptimal, wide whitening limits. The limits are illustrated by the blue and purple lines in Figure IV.8.

IV.6 Results

Figure IV.9 compares the ROC curves for the original and α-whitened images for two different point SNR values. The measured point SNR values of the images *after* whitening is also presented in the legend to show how an optimized whitening can drastically increase the point SNR.

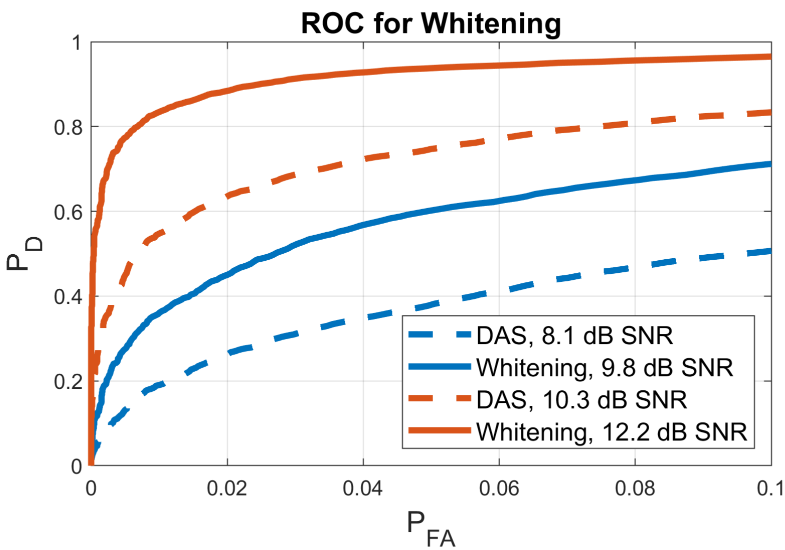

Figure IV.9: ROC curves for two point SNR values with or without α-whitening the images before detection analysis.

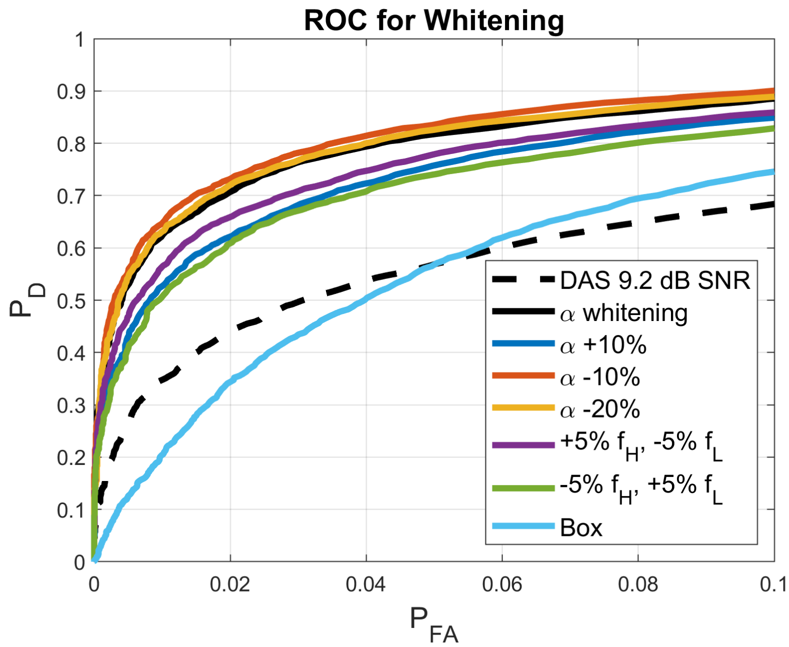

Figure IV.10: ROC curves for the images before and after whitening. The seven whitening filter limits correspond to varying angle and frequency limits.

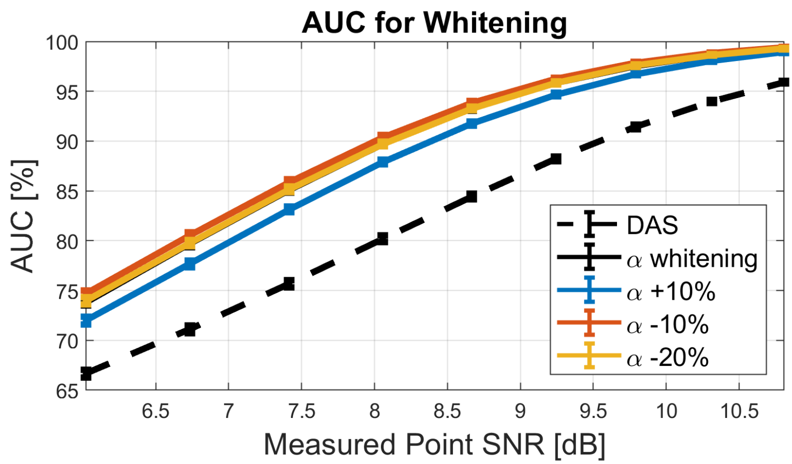

Figure IV.11: AUC for the images before and after whitening, shown with respect to the measured SNR of the original DAS images. Error bars show the 80 % confidence intervals. The black α curve lies underneath the yellow $\alpha - 20\%$ curve.

Figure IV.10 compares the ROC curves for the original and whitened images using seven different filter limits. Figure IV.8 illustrates the varying angle and frequency limits. Only filtering the image using the filter limits $\{\alpha,\ f_L,\ f_H\}$ and without prewhitening, results in the same ROC curve as the original unfiltered DAS image due to relatively little added channel noise. Figure IV.11 shows the effect of whitening on the AUC. Whitening the images drastically increases the AUC. The small error bars indicate the 80% confidence intervals. The effect of whitening is more significant at lower SNR values.

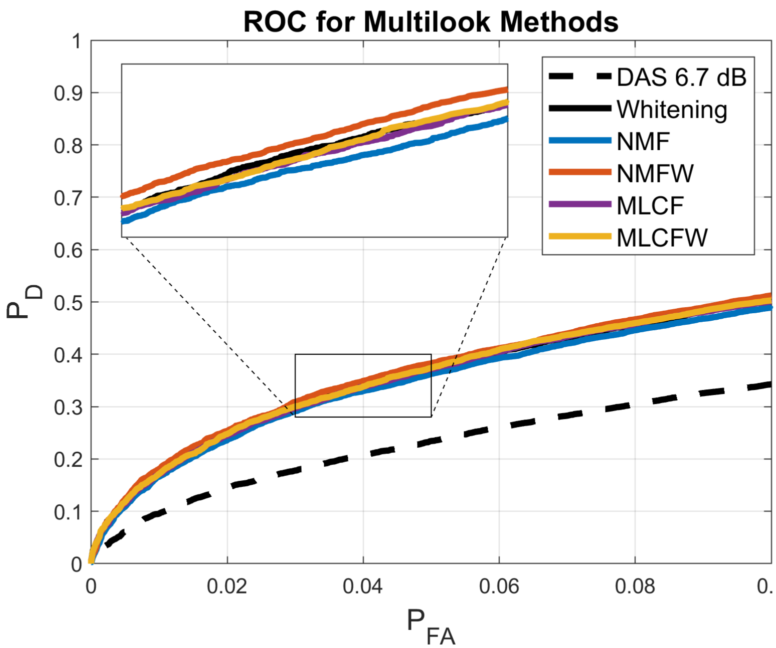

Figure IV.12: ROC curves for the multilook methods NMF, NMFW, MLCF, and MLCFW using 45×25 sublooks. The curves are compared to the original DAS and the optimized α-prewhitened DAS. Point SNR is 6.7 dB.

Figure IV.12 compares the ROC curves for α-whitened images and the four multilook methods NMF, NMFW, MLCF and MLCFW. We studied 28431 images using a 45×25 sublook division. Coherent sum of all looks has a similar ROC curve as only prewhitening. Figures IV.13 and IV.14 shows the corresponding AUC and P_{D} values. The 80% confidence intervals are shown by the error bars. NMFW has a significantly higher P_{D} value than α-whitening in Figure IV.14. Though NMFW has higher P_{D} than whitening at low P_{FA} values, its overall AUC is not significantly higher than that of prewhitening. This is because the slope of the ROC curve for the multilook method slightly reduces at high P_{FA} values compared to whitening. Figure IV.15 shows the P_{D} values for three multilook methods with varying number of sublooks. P_{D} increases with an increasing number of sublooks for NMF and NMFW. At 45×25 sublooks,

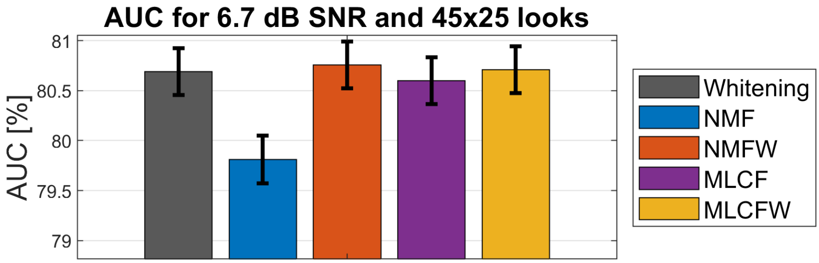

Figure IV.13: AUC for α-whitening and the four multilook methods; NMF, NMFW, MLCF, and MLCFW. The 80% confidence interval is $\pm 0.23\%$ for these AUC values.

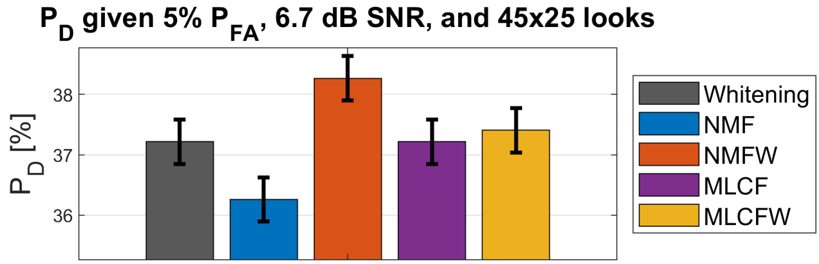

Figure IV.14: P_{D} given 5% P_{FA} for NMF, NMFW, MLCF and MLCFW compared to α-whitening. The 80% confidence interval is $\pm 0.37\%$.

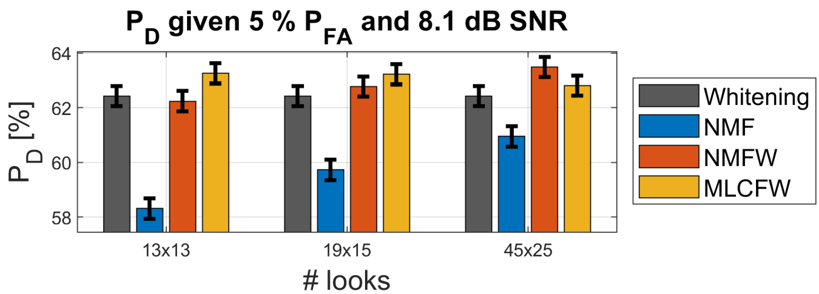

Figure IV.15: P_{D} given 5% P_{FA} for NMF, NMFW, and MLCFW compared to α-whitening and using a varying number of sublooks. The 80% confidence interval is $\pm 0.37\%$.

NMFW has a significantly higher P_{D} value than α-whitening. The results of this study show it is beneficial to use many sublooks for point detection. However, increasing the sublook division also increases the computational load.

Figure IV.16 compares the ROC curves for *nonoptimal* whitened images and the four multilook methods NMF, NMFW, MLCF and MLCFW using 45×25 sublooks. The wide whitening limits reduces the detection performance compared to the optimized α-whitening limits. Figure IV.17 shows the corresponding P_{D} values given 5% P_{FA}.

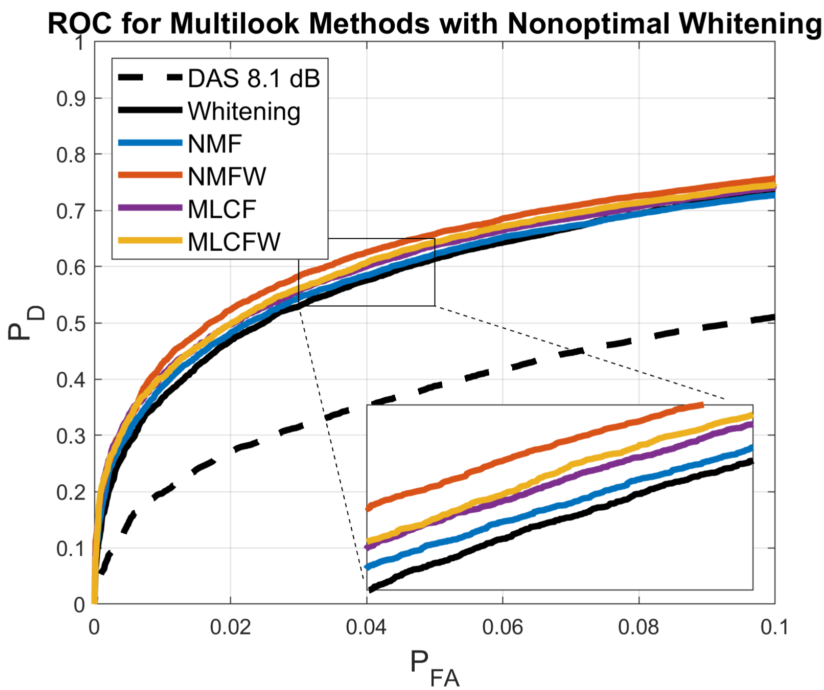

Figure IV.16: ROC curves for the multilook methods NMF, NMFW, MLCF, and MLCFW using 45×25 sublooks and *nonoptimal* prewhitening. The curves are compared to original DAS and the *nonoptimal* prewhitened DAS. Point SNR is 8.1 dB.

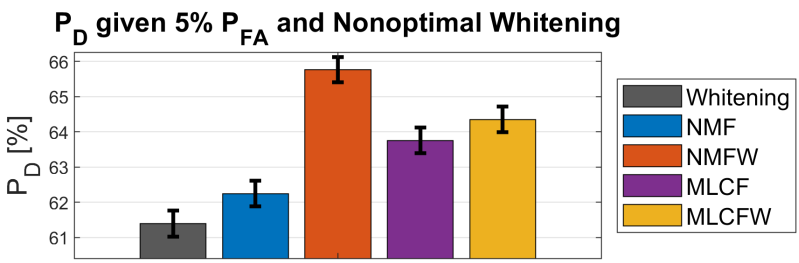

Figure IV.17: P_{D} given 5% P_{FA} for NMF, NMFW, MLCF, and MLCFW using 45×25 sublooks and *nonoptimal* prewhitening. The 80% confidence intervals are approximately $\pm 0.36\%$.

IV.7 Discussion

The steady increase in software processing power and the shift towards software beamforming make it possible to generate both the standard display image and images that are preferable for analysis. Therefore, the image used for detection analysis can differ from the image displayed on the machine for the medical personnel. In [THA22], we showed how rectangular apodization was beneficial for point detection, although a more Gaussian-shaped apodization produces a more visually pleasing image. In this study, we propose using a whitened image for point detection. The results in Figures IV.9 to IV.11 show that whitening the images has a significantly positive effect on point detection. As discussed in Section IV.3, optimized whitening of the data is comparable to increasing the bandwidth and consequently image resolution. Increased resolution corresponds to increased SNR, as also shown by the measured point SNR values in both Figure IV.2 and IV.9. We use the same search window size for the detection strategy corresponding to two times the measured -6 dB spatial resolution in the original image. The whitened image has therefore more independent pixels within the applied search window. As long as the window is relatively small, this will not disqualify whitened versus unwhitened [THA22].

The performances of the different whitening filter limits in Figures IV.10 and IV.11 show that narrowing the angular limits can be beneficial as regions with low SNR are suppressed. However, with increasing SNR, the optimal filter limits converge towards the critical angle α. The ROC curves also emphasize that the optimal frequency limits are well estimated from the pulse bandwidth limits $\{f_L, f_H\}$. Increasing or decreasing the frequency limits by $\pm 5\%$ degrades the overall detection performance.

The detection of point scatterers is strongly dependent of spatial resolution [THA22]. We have therefore chosen to use ultrasound images with uniform resolution in our study. This gives us the possibility to place point scatterers randomly in the image and be ensured the same point SNR value. We chose to use synthetic transmit aperture imaging with constant $f_\#$ to obtain such images. This detection study starts with a complex DAS image with uniform resolution and Rayleigh distributed speckle. We have chosen to use uniform apodization at receive in our study. The speckle statistics is not changed by tapering on receive or even harmonic imaging [Fed+03]. The sidelobe levels and the spatial resolution will change though. Our approach to improve detection performance is therefore also valid in these cases, but the actual detection performance changes due to the change in resolution.

Images with varying spatial resolution will have a location dependent detection performance since the point SNR value then depends on where the point is located. The optimal size of the search window is also affected by resolution. An image with uniform resolution has the same wavenumber coverage for all pixels. If we have an image with varying spatial resolution, the wavenumber coverage will vary at different pixel positions. We would then need to vary the prewhitening transform and possibly vary the sublook resolution based on the position in the image. We have chosen a simplified scenario, but the results are transferable to images with varying spatial resolution.

The AUC increases for all multilook methods with an increasing number of sublooks in the 1-D and 2-D studies. These findings are consistent with [CLR95], where a large L is suggested since a small L can cause a deviation from the optimum at high P_D values. The NMFW method with 13×13 sublooks follows whitening at low P_D and P_{FA} values, but the whitening curve is marginally better than NMFW at high P_D and P_{FA} values. Increasing the sublook division to 45×25 increases both P_D and AUC for

NMFW. NMFW has a significantly higher P_{D} value than α-whitening in Figures IV.14 and IV.15. It slightly reduces the slope of its ROC curve at high P_{FA} values compared to whitening. Therefore, NMFW gives better detection performance at low P_{FA} values but similar overall AUC values as whitening. Note that detection performance at high P_{FA} values is not of much practical interest. The results also indicate saturation of P_{D} and AUC at an increasing number of sublooks, similar to results in [San+15]. The number of possible sublooks depends on the spatial wavenumber coverage of the system, as the minimum subset bandwidth is governed by the resolution and number of independent pixels. Dividing into many sublooks increases the computational load, so there is a trade-off between the maximum exploitation of the sublook information and the computational load.

From the initial 1-D simulations, it was surprising that NMF did not perform better than prewhitening on the 2-D ultrasound images. The 2-D images consist of a uniform speckle background with a frequency spectrum similar to that of a point scatterer. The added channel noise was beamformed and demodulated in the same way as the speckle and point signal. The speckle scenes used in the 1-D study include some added noise at -15 dB below the average speckle level. The added noise in Figure IV.1 has a flat frequency spectrum and is different from the Gaussian-shaped speckle frequency spectrum. In the 1-D study, the NMF method suppressed the noise contribution and improved the detection performance using many sublooks. The 1-D whitening filter is not fully optimal and should ideally be tighter. Compared to the 2-D noise, the 1-D noise has a flat spectrum and is also more uncorrelated. This can explain the observed differences in the 1-D and 2-D results for NMF.

Figure IV.10 shows that slightly shrinking the whitening limits only provides small improvements in the ROC curves for the 2-D images. The potential of the multilook methods to adjust and weight the wavenumber coverage is similarly small for such images. However, the multilook methods have great potential for 2-D images where the optimal whitening limits are unknown or where the frequency spectrum of the noise is different from the PSF. Quantization or range-dependent noise will provide a noise spectrum with a different shape than the PSF. Since the NMF method uses prior knowledge of the PSF per pixel position, it should then manage to suppress more of the unwanted, noisy parts of the spatial spectrum. The application of NMF on SAR images has proved to be especially beneficial for image scenes with compound-Gaussian clutter backgrounds. The NMF method is a normalized method that does not require texture correction prior to point detection. The denominator in the NMF equation estimates the background and normalizes the output. Therefore, the authors believe the NMF method will perform well for point scatterer detection in ultrasound images with textured backgrounds. A possible next step is to study these multilook methods on textured ultrasound images. Quantization noise or range-dependent noise will also provide a noise spectrum of a different shape than the PSF.

The new multilook method NMFW performed better than NMF in this study. This is similar to the observations in [THA22], where coherence-based beamforming methods performed best when applied as weighting schemes to the original image. We found that coherence-based methods that exploit both amplitude and phase information perform best. In the radar community, NMF is not applied as an image weighting. The coherent scatterers of interest are often of SNR > 10 dB and in heavily textured image scenes [San14, p. 125]. The benefit of NMF being bounded and normalized is therefore of importance. Note also that our whitening transform utilized information about the spatial frequency limits. In that sense, we included part of the benefits of the NMF and NMFW methods into the whitening transform, as these methods also suppress the same regions in the frequency domain.

The calculation of the new method MLCF is more straightforward than NMF, as it sums all the sublooks without applying the matched filter weighting. The AUC result for MLCF is better than NMF in Figure IV.13. Therefore, the MLCF results indicate a good potential for textured or noisy image scenes where background normalization is essential. The results for the new method MLCFW are similar to the observations in [THA22] where CF beamforming improved the detection performance of weak point scatterers compared to conventional DAS beamforming. Point scatterers are small, bright, and highly coherent targets. MLCFW matches prior knowledge about point targets well since it differentiates between coherent and incoherent energy across the frequency spectrum. Combined with a whitening transform that suppresses the frequency spectrum outside the critical angle and pulse bandwidth, the coherence-based weights accentuate signals from point scatterers. The MLCFW method does not need as many sublooks as NMF and NMFW to have the same detection performance as prewhitening in the 2-D study. The results for MLCFW can indicate saturation of P_{D} towards the α-whitening level at a high number of sublooks, but we cannot declare this tendency with sufficient statistical significance.

The results using *nonoptimal* whitening in Figures IV.16 and IV.17 show how the multilook methods can improve the detection performance when the optimal whitening limits are unknown or wrong. This corresponds to the results in the 1-D study where tightened whitening limits would have been more optimal. The multilook methods are able to suppress the sublooks generated from areas without true point target information. The NMF method contains the known point signal response in each sublook. The theoretical response might not be exactly known or difficult to obtain for some setups. The results show that the new methods MLCF and MLCFW greatly improve the detection performance for weak point scatterers and do not require prior knowledge.

IV.8 Conclusions

This paper has studied methods to improve point detection performance in ultrasound images. Our study shows that whitening can significantly improve the detectability of point scatterers. Optimized whitening of the data is comparable to increasing the image resolution. We applied an optimized whitening transform that included filtering at the critical angle and pulse bandwidth limits. We also show that narrowing the angular limits can be beneficial in the presence of noisy backgrounds and weak point scatterers since we then suppress spatial frequency regions with low SNR values.

We introduce three new multilook methods based on the NMF method commonly used for point detection in SAR images. We term the new methods NMFW, MLCF, and MLCFW and evaluate their performance. The results show that the multilook methods have the potential to improve the detection performance, provided the number of sublooks is high. The NMF method matches the received signal in each pixel by the theoretical signal from a point scatterer over the sublooks. We apply NMF as a weighting scheme, and the new multilook method NMFW improves the detectability of weak point scatterers. The results indicate a potential gain in utilizing coherence over looks when detecting point scatterers. MLCF is a new, simplified version of NMF, and MLCFW is the image-weighted version. The MLCF and MLCFW methods accentuate signals from point scatterers by differentiating between coherent and incoherent energy over the sublooks.

The results on uniform speckle backgrounds indicate that optimized prewhitening is the preferred method to use before point detection. However, the results on multilook methods using nonoptimal prewhitening show that MLCF and MLCFW can significantly improve the detection performance when prior knowledge about the optimal whitening limits is unavailable. The application of NMF on SAR images has proved to be especially beneficial for image scenes with compound-Gaussian clutter backgrounds. Therefore, we expect the NMF and MLCF methods will perform well for point scatterer detection in ultrasound images with textured backgrounds. However, if computational efficiency is essential and we have uniform speckle backgrounds, we recommend only applying an optimized prewhitening of the data.

Appendix IV.A The Generalized Likelihood Ratio Test (GLRT) for Sublooks

The Generalized Likelihood Ratio Test (GLRT) is the basis for the formulae for the multilook techniques. We present the derivation of the GLRT expression in this section. To give a complete and detailed presentation, we follow and combine the derivations in [Kel86], [CLR95], [San14, ch. 3.4.4], and [San+15], and fill in steps in between. We start with a binary test to decide if we have speckle (hypothesis $\mathcal{H}_0$) or signal + speckle (hypothesis $\mathcal{H}_1$) [TRL15]. The point scatterer is present in the pixel under test when the L-dimensional sublook vector $\boldsymbol{y}$ contains the point signal response $\boldsymbol{a}$.

$$\begin{cases} \mathcal{H}_0: & \boldsymbol{y} = \boldsymbol{w} \\ \mathcal{H}_1: & \boldsymbol{y} = C\boldsymbol{a} + \boldsymbol{w}. \end{cases} \tag{IV.15}$$

The complex amplitude of the point scatterer is $C = C_0 e^{j\phi}$, and $\boldsymbol{w}$ signifies only speckle.

The Neyman-Pearson (NP) theorem states that the Likelihood Ratio Test (LRT) maximizes P_{D} for a given P_{FA} [Kay98, ch. 3.3]

$$\text{LRT}(\boldsymbol{y}) = \frac{p(\boldsymbol{y}; \mathcal{H}_1)}{p(\boldsymbol{y}; \mathcal{H}_0)} > \gamma, \tag{IV.16}$$

where p is the probability density function (PDF) for observation $\boldsymbol{y}$. The threshold γ can be found by integrating the PDF for observation y of hypothesis $\mathcal{H}_0$ to the chosen P_{FA} value [Kay98, p. 30],

$$P_{\text{FA}} = \int_{\gamma}^{\infty} p(y; \mathcal{H}_0) dy. \tag{IV.17}$$

If the speckle background is modeled as a zero-mean complex Gaussian random vector, the PDF of the sublook vector $\boldsymbol{y}$ given hypothesis $\mathcal{H}_0$ is [San+15]

$$p(\boldsymbol{y};\mathcal{H}_0) = \frac{1}{\pi^L(\sigma^2)^L|\mathrm{M}|}\exp\left(-\frac{\boldsymbol{y}^H\mathrm{M}^{-1}\boldsymbol{y}}{\sigma^2}\right), \tag{IV.18}$$

where $\boldsymbol{a}^H$ is the conjugate transpose of the point signal response and M is the normalized covariance matrix. Note that the notation in [San+15] refers to normalized covariance matrix, while the notations in [Kel86] and [CLR95] uses the covariance matrix $\mathrm{M} = 2\sigma^2\Sigma$ where Σ is the normalized covariance matrix after the whitening transformation ($|\mathrm{M}| = |2\sigma^2\Sigma| = (2\sigma^2)^L|\Sigma|$). Under the $\mathcal{H}_1$ hypothesis, the background $\boldsymbol{w}$ has the same PDF as under $\mathcal{H}_0$, and we find the PDF of $\boldsymbol{y}$ by substituting $\boldsymbol{w}$ with $\boldsymbol{y} - C\boldsymbol{a}$ [Kel86]

$$p(\boldsymbol{y};\mathcal{H}_1) = \frac{1}{\pi^L(\sigma^2)^L|\mathrm{M}|}\exp\left(\frac{-(\boldsymbol{y}-C\boldsymbol{a})^H\mathrm{M}^{-1}(\boldsymbol{y}-C\boldsymbol{a})}{\sigma^2}\right). \tag{IV.19}$$

The LRT is thus the ratio between (IV.19) and (IV.18), and the NP test becomes a matched filter [San14, ch. 3.4].

The LRT is the optimal detector for a known signal in noise when the PDFs of both hypotheses are known. However, in our case, we wish to detect a signal with unknown amplitude, phase, and position in a speckle background of unknown level. Following classical detection theory [Kay98, ch. 6], the GLRT replaces the unknown parameters by their maximum likelihood estimates (MLE) before performing hypothesis testing as in (IV.16). The GLRT takes the form

$$\mathrm{GLRT}(y) = \frac{\max\limits_{C,\sigma^2}\ p(\boldsymbol{y}|C,\sigma^2;\mathcal{H}_1)}{\max\limits_{\sigma^2}\ p(\boldsymbol{y}|\sigma^2;\mathcal{H}_0)} > \gamma, \tag{IV.20}$$

where the speckle power σ^2 is the variance of the speckle and noise background, and C is the complex signal amplitude $C_0e^{j\phi}$. For simplicity, we assume the point scatterer inside the resolution cell is centered. In [San14, ch. 4.2.5], the formulae was extended to the case of unknown position, and the mismatch was shown to be small but noticeable for low point SNR values. The results indicate that using many sublooks decreases the mismatch and makes it possible to avoid optimizing the formulae for unknown position.

We now derive the maximizations in (IV.20) using the PDFs in IV.19 and IV.18, and following [Kel86], [CLR95], [San14, ch. 3.4.4], and [San+15]. Even though the solution is derived in the case of white Gaussian background, the formulation remains valid also for the more complex case of compound-Gaussian clutter[San14, ch. 3.4.4]. To derive the GLRT, it is necessary to calculate the MLEs of the unknown parameters σ^2 and C.

We first derive the MLE of σ^2 under $\mathcal{H}_0$ and start by taking the natural logarithm of the PDF. The exponential function goes away and the expression becomes the sum

$$\ln(p(\boldsymbol{y};\mathcal{H}_0)) = -\ln\pi - L\ln\sigma^2 - \ln|\mathrm{M}| - \sigma^2\boldsymbol{y}^H\mathrm{M}^{-1}\boldsymbol{y}. \tag{IV.21}$$

Derivation of (IV.21) gives

$$\frac{d}{d\sigma^2}\left\{\ln(p(\boldsymbol{y};\mathcal{H}_0))\right\} = -\frac{L}{\sigma^2} - \boldsymbol{y}^H \mathrm{M}^{-1}\boldsymbol{y}. \tag{IV.22}$$

By setting (IV.22) equal to zero, we get the final expression for the MLE of σ^2 as

$$\hat{\sigma^2}\,|_{\mathcal{H}_0}= \frac{\boldsymbol{y}^H \mathrm{M}^{-1}\boldsymbol{y}}{L}. \tag{IV.23}$$

Inserting M as the identity matrix in (IV.23) simplifies the expression to $\boldsymbol{y}^H\boldsymbol{y}/L$. With the MLE $\hat{\sigma^2}$, the denominator in (IV.20) becomes

$$\max_{\sigma^2} p(\boldsymbol{y};\mathcal{H}_0) = \frac{\exp(-L)}{\pi^L\left(\frac{\boldsymbol{y}^H\mathrm{M}^{-1}\boldsymbol{y}}{L}\right)^L|\mathrm{M}|}. \tag{IV.24}$$

The MLEs under hypothesis $\mathcal{H}_1$ must also be found. We start by first supposing the parameter C is known [San14, ch. 3.4.4]. Using the same parameter substitution on (IV.23) as we did moving from (IV.18) to (IV.19), the MLE under $\mathcal{H}_1$ can be expressed as

$$\hat{\sigma^2}\,|_{\mathcal{H}_1}= \frac{1}{L}(\boldsymbol{y}-C\boldsymbol{a})^H\mathrm{M}^{-1}(\boldsymbol{y}-C\boldsymbol{a}). \tag{IV.25}$$

We now insert (IV.25) into (IV.19) to get

$$\max_{\sigma^2} p(\boldsymbol{y};\mathcal{H}_1) = \frac{\exp(-L)}{\pi^L(\frac{1}{L}(\boldsymbol{y}-C\boldsymbol{a})^H\mathrm{M}^{-1}(\boldsymbol{y}-C\boldsymbol{a}))^L|\mathrm{M}|}, \tag{IV.26}$$

We must also obtain the MLE for $\hat{C}$ to maximize the PDF for C. To maximize this term, we follow the procedure E. J. Kelly presented in [Kel86] by rewriting

$$\begin{aligned}(\boldsymbol{y}-C\boldsymbol{a})^H\mathrm{M}^{-1}(\boldsymbol{y}-C\boldsymbol{a}) =&(\boldsymbol{y}^H\mathrm{M}^{-1}\boldsymbol{y}) + |C|^2(\boldsymbol{a}^H\mathrm{M}^{-1}\boldsymbol{a})\\ &-2\mathrm{Re}\{C(\boldsymbol{y}^H\mathrm{M}^{-1}\boldsymbol{a})\}\\ &= (\boldsymbol{y}^H\mathrm{M}^{-1}\boldsymbol{y}) - \frac{|(\boldsymbol{a}^H\mathrm{M}^{-1}\boldsymbol{y})|^2}{(\boldsymbol{a}^H\mathrm{M}^{-1}\boldsymbol{a})}\\ &+(\boldsymbol{a}^H\mathrm{M}^{-1}\boldsymbol{a})\times\left|C-\frac{(\boldsymbol{a}^H\mathrm{M}^{-1}\boldsymbol{y})}{(\boldsymbol{a}^H\mathrm{M}^{-1}\boldsymbol{a})}\right|^2.\end{aligned} \tag{IV.27}$$

We maximize the PDF by minimizing the quantity in (IV.27). The minimum is clearly attained when the positive term containing C is made to vanish [Kel86]. The MLE for C is therefore

$$\hat{C} = \frac{\boldsymbol{a}^H\mathrm{M}^{-1}\boldsymbol{y}}{\boldsymbol{a}^H\mathrm{M}^{-1}\boldsymbol{a}}. \tag{IV.28}$$

Using this expression for $\hat{C}$, we can now find $\hat{\sigma^2}$ under hypothesis $\mathcal{H}_1$ by inserting (IV.28) into (IV.25) [San+15]. We get

$$\begin{aligned}\hat{\sigma^2}\,|_{\mathcal{H}_1} &= \frac{1}{L}(\boldsymbol{y}-\frac{\boldsymbol{a}^H\mathrm{M}^{-1}\boldsymbol{y}}{\boldsymbol{a}^H\mathrm{M}^{-1}\boldsymbol{a}}\boldsymbol{a})^H\mathrm{M}^{-1}(\boldsymbol{y}-\frac{\boldsymbol{a}^H\mathrm{M}^{-1}\boldsymbol{y}}{\boldsymbol{a}^H\mathrm{M}^{-1}\boldsymbol{a}}\boldsymbol{a})\\ &= \frac{1}{L}\left((\boldsymbol{y}^H\mathrm{M}^{-1}\boldsymbol{y}) - \frac{|(\boldsymbol{a}^H\mathrm{M}^{-1}\boldsymbol{y})|^2}{(\boldsymbol{a}^H\mathrm{M}^{-1}\boldsymbol{a})}\right).\end{aligned} \tag{IV.29}$$

Finally, we have $\hat{\sigma^2}$ and $\hat{C}$ under $\mathcal{H}_1$ and we can rewrite the numerator in (IV.20) as

$$\max_{\sigma^2, C} p(\boldsymbol{y}; \mathcal{H}_1) = \frac{\exp(-L)}{\pi^L \left(\frac{1}{L} \left((\boldsymbol{y}^H \mathrm{M}^{-1} \boldsymbol{y}) - \frac{|(\boldsymbol{a}^H \mathrm{M}^{-1} \boldsymbol{y})|^2}{(\boldsymbol{a}^H \mathrm{M}^{-1} \boldsymbol{a})} \right) \right)^L |\mathrm{M}|}. \tag{IV.30}$$

Inserting (IV.30) and (IV.24) into (IV.20), we express the GLRT as

$$\begin{aligned} \mathrm{GLRT}(\boldsymbol{y}) &= \frac{\left(\frac{\exp(-L)}{\pi^L \left(\frac{1}{L} \left((\boldsymbol{y}^H \mathrm{M}^{-1} \boldsymbol{y}) - \frac{|(\boldsymbol{a}^H \mathrm{M}^{-1} \boldsymbol{y})|^2}{(\boldsymbol{a}^H \mathrm{M}^{-1} \boldsymbol{a})} \right) \right)^L |\mathrm{M}|} \right)}{\left(\frac{\exp(-L)}{\pi^L \left(\frac{\boldsymbol{y}^H \mathrm{M}^{-1} \boldsymbol{y}}{L} \right)^L |\mathrm{M}|} \right)}, \\ &= \frac{\left(\boldsymbol{y}^H \mathrm{M}^{-1} \boldsymbol{y} \right)^L}{\left((\boldsymbol{y}^H \mathrm{M}^{-1} \boldsymbol{y}) - \frac{|(\boldsymbol{a}^H \mathrm{M}^{-1} \boldsymbol{y})|^2}{(\boldsymbol{a}^H \mathrm{M}^{-1} \boldsymbol{a})} \right)^L} > \gamma. \end{aligned} \tag{IV.31}$$

Adjusting the threshold and simplifying (IV.31) further gives

$$\mathrm{GLRT}(\boldsymbol{y}) = \frac{1}{\left(1 - \frac{|(\boldsymbol{a}^H \mathrm{M}^{-1} \boldsymbol{y})|^2}{(\boldsymbol{y}^H \mathrm{M}^{-1} \boldsymbol{y})(\boldsymbol{a}^H \mathrm{M}^{-1} \boldsymbol{a})} \right)} > \gamma, \tag{IV.32}$$

or equivalently [CLR95]

$$\mathrm{GLRT}(\boldsymbol{y}) = \frac{|\boldsymbol{a}^{\mathrm{H}} \mathrm{M}^{-1} \boldsymbol{y}|^2}{(\boldsymbol{y}^{\mathrm{H}} \mathrm{M}^{-1} \boldsymbol{y})(\boldsymbol{a}^{\mathrm{H}} \mathrm{M}^{-1} \boldsymbol{a})} > \gamma. \tag{IV.33}$$

References

[Abr19] Abraham, D. A. *Underwater Acoustic Signal Processing: Modeling, Detection, and Estimation*. Springer, 2019.

[And+97] Anderson, M. E. et al. "The detection of breast microcalcifications with medical ultrasound". In: *J. Acoust. Soc. Am.* vol. 101, no. 1 (Jan. 1997), pp. 29–39.

[AST00] Anderson, M. E., Soo, M. S. C., and Trahey, G. E. "Optimizing visualization of breast microcalcifications". In: *Proc. IEEE Int. Ultrason. Symp. (IUS)*. Vol. 2. Oct. 2000, pp. 1315–1320.

[AST98] Anderson, M. E., Soo, M. S. C., and Trahey, G. E. "Microcalcifications as elastic scatterers under ultrasound". In: *IEEE Trans. Ultrason., Ferroelectr., Freq. Control* vol. 45, no. 4 (July 1998), pp. 925–934.

[AT00] Anderson, M. E. and Trahey, G. E. *A seminar on k-space applied to medical ultrasound*. Duke Univ., Apr. 2000.

[Che+20] Chen, C. et al. "Point Spread Function Formation in Plane-Wave Imaging: A Theoretical Approximation in Fourier Migration". In: *IEEE Trans. Ultrason., Ferroelectr., Freq. Control* vol. 67, no. 2 (Feb. 2020), pp. 296–307.

[CJO98] Czerwinski, R., Jones, D., and O'Brien, W. "Line and boundary detection in speckle images". In: *IEEE Trans. Image Process.* vol. 7, no. 12 (Dec. 1998), pp. 1700–1714.

[CJO99] Czerwinski, R., Jones, D., and O'Brien, W. "Detection of lines and boundaries in speckle images-application to medical ultrasound". In: *IEEE Trans. Med. Imag.* vol. 18, no. 2 (Feb. 1999), pp. 126–136.

[CLR95] Conte, E., Lops, M., and Ricci, G. "Asymptotically optimum radar detection in compound-Gaussian clutter". In: *IEEE Trans. Aerosp. Electron. Syst.* vol. 31, no. 2 (Apr. 1995), pp. 617–625.

[CLR96] Conte, E., Lops, M., and Ricci, G. "Adaptive matched filter detection in spherically invariant noise". In: *IEEE Signal Process. Lett.* vol. 3, no. 8 (Aug. 1996), pp. 248–250.

[Den+13] Denarie, B. et al. "Coherent Plane Wave Compounding for Very High Frame Rate Ultrasonography of Rapidly Moving Targets". In: *IEEE Trans. Med. Imag.* vol. 32, no. 7 (July 2013), pp. 1265–1276.

[DFP09] De Maio, A., Fornaro, G., and Pauciullo, A. "Detection of Single Scatterers in Multidimensional SAR Imaging". In: *IEEE Trans. on Geosci. Remote Sens.* vol. 47, no. 7 (Apr. 2009), pp. 2284–2297.

[Dia+18] Diamantis, K. et al. "Super-Resolution Axial Localization of Ultrasound Scatter Using Multi-Focal Imaging". In: *IEEE Trans. Biomed. Eng.* vol. 65, no. 8 (Aug. 2018), pp. 1840–1851.

[EG05] Ewens, W. J. and Grant, G. R. *Statistical Methods in Bioinformatics: An Introduction*. II. Springer, 2005.

[Fed+03] Fedewa, R. et al. “Spatial coherence of the nonlinearly generated second harmonic portion of backscatter for a clinical imaging system”. In: *IEEE Trans. Ultrason., Ferroelectr., Freq. Control* vol. 50, no. 8 (Aug. 2003), pp. 1010–1022.

[Flø+17] Flørenæs, E. et al. “In vitro detection of microcalcifications using dual band ultrasound”. In: *Proc. IEEE Int. Ultrason. Symp. (IUS).* Sept. 2017, pp. 1–4.

[Gol+21] Golfetto, C. et al. “Retrospective Transmit Beamforming and Coherent Plane-Wave Compounding for Microvascular Doppler Imaging: A Comparison Study”. In: *IEEE Trans. Ultrason., Ferroelectr., Freq. Control* vol. 68, no. 4 (Apr. 2021), pp. 1105–1116.

[Har78] Harris, F. J. “On the use of windows for harmonic analysis with the discrete Fourier transform”. In: *Proc. IEEE* vol. 66 (1 Jan. 1978), pp. 51–83.

[HM82] Hanley, J. A. and McNeil, B. J. “The Meaning and Use of the Area under a Receiver Operating Characteristic (ROC) Curve”. In: *Radiology* vol. 143, no. 1 (Apr. 1982), pp. 29–36.

[Jak+96] Jakowatz, J. C. V. et al. *Spotlight-Mode Synthetic Aperture Radar: A Signal Processing Approach.* Boston, MA: Springer, 1996.

[Jen+06] Jensen, J. A. et al. “Synthetic aperture ultrasound imaging”. In: *Ultrasonics* vol. 44 (Dec. 2006), e5–e15.

[Jen96] Jensen, J. A. “FIELD: A Program for Simulating Ultrasound Systems”. In: *Proc. 10th Nordicbaltic Conf. Biomed. Imag., Suppl. 1, Part 1.* Vol. 4. 1996, pp. 351–353.

[JS92] Jensen, J. A. and Svendsen, N. B. “Calculation of Pressure Fields from Arbitrarily Shaped, Apodized, and Excited Ultrasound Transducers”. In: *IEEE Trans. Ultrason., Ferroelectr., Freq. Control* vol. 39, no. 2 (Mar. 1992), pp. 262–267.

[Kay13] Kay, S. M. *Fundamentals of Statistical Signal Processing, Volume III: Practical Algorithm Development.* Vol. III. Pearson, 2013.

[Kay98] Kay, S. M. *Fundamentals of Statistical Signal Processing, Volume II: Detection Theory.* Vol. II. Prentice-Hall PTR, 1998.

[Kel86] Kelly, E. J. “An Adaptive Detection Algorithm”. In: *IEEE Trans. Aerosp. Electron.* vol. 22, no. 2 (Mar. 1986), pp. 115–127.

[KK99] Koivunen, A. C. and Kostinski, A. B. “The Feasibility of Data Whitening to Improve Performance of Weather Radar”. In: *J. Appl. Meteorol. (1988-2005)* vol. 38, no. 6 (June 1999), pp. 741–749.

[KLS18] Kessy, A., Lewin, A., and Strimmer, K. “Optimal Whitening and Decorrelation”. In: *Am. Stat.* vol. 72, no. 4 (2018), pp. 309–314.

[Lev08] Levy, B. C. *Principles of Signal Detection and Parameter Estimation.* Springer, 2008.

[LL03] Li, P. C. and Li, M. L. “Adaptive imaging using the generalized coherence factor”. In: *IEEE Trans. Ultrason., Ferroelectr., Freq. Control* vol. 50, no. 2 (Feb. 2003), pp. 128–141.

[Mac+18] Machado, P. et al. “Ultrasound Detection of Microcalcifications in Surgical Breast Specimens”. In: *Ultrasound Med. Biol.* vol. 44 (6 Mar. 2018), pp. 1286–1290.

[Mat+19] Matrone, G. et al. “Short-lag spatial coherence imaging with multi-line transmission to improve needle visibility in ultrasound images”. In: *J. Acoust. Soc. Am.* vol. 146 (Oct. 2019), pp. 2861–2861.

[MBR20] Matrone, G., Bell, M. A. L., and Ramalli, A. “Improving the Detectability of Highly Coherent Targets in Short-Lag Spatial Coherence Images with Multi-Line Transmission”. In: *Proc. IEEE Int. Ultrason. Symp. (IUS)*. Sept. 2020, pp. 1–4.

[MF94] Mallart, R. and Fink, M. “Adaptive focusing in scattering media through sound-speed inhomogeneities: The van Cittert Zernike approach and focusing criterion”. In: *J. Acoust. Soc. Am.* vol. 96, no. 6 (Dec. 1994), pp. 3721–3732.

[OQ98] Oliver, C. and Quegan, S. *Understanding Synthetic Aperture Radar Images*. Artech house, Inc., 1998.

[Ray+10] Ray, A. A. et al. “Limitations to Ultrasound in the Detection and Measurement of Urinary Tract Calculi”. In: *Urology* vol. 76, no. 2 (Mar. 2010), pp. 295–300.

[Rin+19] Rindal, O. M. H. et al. “The Effect of Dynamic Range Alterations in the Estimation of Contrast”. In: *IEEE Trans. Ultrason., Ferroelectr., Freq. Control* vol. 66, no. 7 (July 2019), pp. 1198–1208.

[Rod+17] Rodriguez-Molares, A. et al. “The UltraSound ToolBox”. In: *Proc. IEEE Int. Ultrason. Symp. (IUS)*. Sept. 2017, pp. 1–4.

[San+15] Sanjuan-Ferrer, M. J. et al. “A New Detection Algorithm for Coherent Scatterers in SAR Data”. In: *IEEE Trans. on Geosci. Remote Sens.* vol. 53, no. 11 (June 2015), pp. 6293–6307.

[San14] Sanjuan-Ferrer, M. J. “Detection of coherent scatterers in SAR data Algorithms and applications”. PhD thesis. ETH Zürich, Jan. 2014.

[Ste07] Stepinski, T. “An Implementation of Synthetic Aperture Focusing Technique in Frequency Domain”. In: *IEEE Trans. Ultrason., Ferroelectr., Freq. Control* vol. 54, no. 7 (July 2007), pp. 1399–1408.

[Sza14] Szabo, T. L. *Diagnostic Ultrasound Imaging: Inside Out*. Second. Elsevier Academic Press, 2014.

[THA22] Thon, S. H., Hansen, R. E., and Austeng, A. “Detection of Point Scatterers in Medical Ultrasound”. In: *IEEE Trans. Ultrason., Ferroelectr., Freq. Control* vol. 69, no. 2 (Feb. 2022), pp. 617–628.

[Tie+18] Tierney, J. E. et al. “In vitro feasibility of next generation non-linear beamforming ultrasound methods to characterize and size kidney stones”. In: *Urolithiasis* vol. 47 (Jan. 2018), pp. 181–188.

[TRL15] Torp, H., Rodriguez-Molares, A., and Løvstakken, L. “Optimum beamformer strategy for detecting signals in clutter noise”. In: *Proc. IEEE Int. Ultrason. Symp. (IUS).* Oct. 2015, pp. 1–4.

[Wag+83] Wagner, R. F. et al. “Statistics of Speckle in Ultrasound B-Scans”. In: *IEEE Trans. Sonics Ultrason.* vol. 30, no. 3 (May 1983), pp. 156–163.

Paper V

Point Detection in Textured Ultrasound Images

Stine Hverven Thon, Andreas Austeng, and Roy Edgar Hansen

in *Elsevier Ultrasonics*, May 2023, volume 131, pages 106968. DOI: 10.1016/j.ultras.2023.106968.

Abstract

Detection of point scatterers in textured ultrasound images can be challenging. This paper investigates how four multilook methods can improve the detection. We analyze many images with known point scatterer locations and randomly textured backgrounds. The *normalized matched filter* (NMF) and *multilook coherence factor* (MLCF) methods are normalized methods that do not require any texture correction prior to detection analysis. They are especially propitious when optimal texture correction of the ultrasound images is difficult to obtain. The results show *significant* improvement in detection performance when the MLCF method is weighted with the prewhitened and texture corrected image. The method can be applied even when we do not have prior knowledge about the optimal prewhitening limits. The multilook methods NMF and *NMF weighted* (NMFW) are very favorable methods to apply on images where acoustic noise dominates the speckle background.

V.1 Introduction

Detection of point scatterers in medical ultrasound is essential in several applications. Some example applications are detection of breast microcalcifications [And+97; AST00; AST98; Flø+17; Guo+18; Mac+18], kidney stones [Ray+10; Tie+18], microbubbles [Bro+19; Pel+21], and point tracking [Dia+18; Mat+19; MBR20]. Peaks in the textured speckle background can make it very challenging to detect point targets. This paper investigates if four multilook methods have the potential to improve the point detection of a textured, standard Delay-and-Sum (DAS) image. The four multilook methods are introduced in [THA22b], which studied uniform speckle backgrounds. We now assess the point detection performance of these methods on textured ultrasound images.

We can adjust the aperture weightings of the ultrasound array to optimize the signal to noise ratio (SNR) versus the peak sidelobe levels [SMM06]. The results in [THA22b] show how we can significantly improve the detection probability and increase the effective spatial resolution of the image if we apply an optimized *whitening* transform. Whitening has previously been used in ultrasound to improve detection of edges [CJO98; CJO99] or point scatterers in uniform speckle backgrounds [THA22b]. This work studies the point detection performance of prewhitening combined with texture correction. To get measurable and statistically significant results, we simulate several images of a point scatterer in inhomogeneous speckle backgrounds using the Field II software [Jen+06; Jen96; JS92]. An inhomogeneous texture predominantly has the same tissue type with some fluctuations about a mean value [Sza14, ch. 9.2].

The methods in this paper are inspired by multilook techniques from the radar field [CLR95; CLR96; Kel86; San+15]. In a similar fashion, Masoom et al. detect simulated spherical targets in textured ultrasound images by combining an algorithm from radio astronomy with constant false alarm rate (CFAR) processing from the radar field in [MAC13]. The multilook technique is used on synthetic aperture radar (SAR) images and has the potential to reduce speckle [Jak+96, ch. 3.3] [OQ98, p.29]. The method splits the entire frequency bandwidth of the original image into subsets. The subsets do not have the same central frequencies. We can in this way get many images or *sublooks* from one original image. The contribution from some of the sublooks are more important in terms of point detection. The *normalized matched filter* (NMF) multilook method maximizes point detection by imposing higher weighting on these sublooks [CLR95; CLR96; Kel86; San+15]. We presented three new multilook methods to improve point detection in [THA22b]. The *multilook coherence factor* (MLCF) [THA22b] calculates the ratio between the coherent and incoherent sum of the sublooks with equal sublook weighting. It is a simpler method than the NMF method. The NMF and MLCF are normalized methods and do not require texture correction prior to detection analysis. The *normalized matched filter weighted* (NMFW) and the *multilook coherence factor weighted* (MLCFW) methods weight the NMF and MLCF methods with the prewhitened *and* texture corrected DAS image.

The performance of the multilook methods is benchmarked against texture corrected versions of the original and prewhitened DAS image. The MLCF and MLCFW methods do not need prior knowledge of the theoretical point signal response. By using suboptimal or wide prewhitening limits, we test the methods when the optimal whitening limits are unknown. We also evaluate the methods when a successful texture correction is difficult to obtain. Finally, we evaluate the multilook methods on images where acoustic noise dominates the speckle background.

Section V.2 briefly describes how to measure point detection performance, and how to apply prewhitening and the multilook methods. We discuss how to estimate and correct for texture in Section V.3. Section V.4 presents the setup for the simulation and detection study. Section V.5 presents the detection results for the methods and Section V.6 discusses the observed performances on textured backgrounds.

V.2 Background

V.2.1 Point Detection

We measure detection performance using the probability of false alarm P_{FA} and the probability of detection P_{D}. We estimate P_{FA} using images containing only speckle, and we estimate P_{D} using images with a point scatterer present [Kay98, ch. 3.3]. We have a simulated environment with known location for the point scatterer and adopt the detection strategy from [THA22a]. We evaluate a search window around the known point location, and pick the maximum value within it. The point's SNR metric [THA22a; THA22b] is the point's relative intensity compared to the background and it greatly affects P_{D}. We calculate the average intensity of the background around the point location using the speckle images without the point scatterer present.

A Receiver Operating Characteristics (ROC) curve displays detection performance by comparing P_{D} to P_{FA} for a given threshold γ [Lev08, ch. 2.4.2] [Kay98, p. 74]. As in [THA22a; THA22b], this paper presents ROC curves for P_{FA} values up to 0.1. ROC results can also be presented by tabulating P_{D} for a chosen P_{FA} value or the Area Under the Curve (AUC) [Abr19, p. 315]. The accuracy of the ROC and AUC depend on the number of realizations [Kay98, p. 37][HM82; THA22a].

V.2.2 The Whitening Transform and Spatial Frequency Limits

Whitening or prewhitening is an operation performed on a signal to make it more similar to white noise, and thus more suitable to be analyzed by statistics-based methods [Ale16, p. 399]. A whitening transform can be estimated using a secondary data set or by applying an adaptive method. In this study we have simulated many realizations of speckle background images. We estimate the smoothed average of the spatial frequency spectrum used in the whitening transform from the simulated realizations. For most of the scenarios in this study, we estimated the average spectrum using the image speckle scenes without texture or after texture correction. A texture corrected image is an image where the amplitude variation of the speckle is estimated and corrected for, i.e., an image with almost uniform speckle background. We then apply the inverse of the smoothed average to the Fourier transform of the image in question. We refer to the resulting image as a whitened or prewhitened image in this study. The results in [THA22b] illustrate the *significant* improvement in point detection obtained with an optimized whitening transformed image.

A system's imaging capability is governed by the point spread function (PSF) and many parameters affect it [Che+20; Shi+09]. The spatial frequency spectrum is centered on $2k_0 = 4\pi f_0/c$ [AT00, ch. 3], where f_0 is the center frequency and c is the speed of sound. The aperture size limits the lateral spatial frequency k_x and the critical angle α [Che+20; Den+13; Gol+21; THA22b]. The images in this study are bandpass filtered using lower and upper frequency limits f_L and f_H, i.e., $f_L \leq f \leq f_H$, and demodulated using the estimated center spatial frequency k_D ($k_D \approx 2k_0$). As in [THA22b], we ensure uniform image resolution by applying an adaptive aperture setting with a range- independent beamwidth. The $f_{\#}$ is the ratio between imaging depth and active aperture size [Sza14, p. 381]. We used an $f_{\#}$ of 1.75, and the reconstructed images are 20 mm wide with imaging depth of 20 mm to 60 mm. We use the notation κ_x and κ_z for the normalized spatial frequencies in the lateral and depth direction.

V.2.3 The Multilook Methods

The multilook technique is widely used on synthetic aperture radar (SAR) images [Jak+96, ch. 3.3] [OQ98, p. 29]. It splits the frequency bandwidth of the original image into many subsets. The subsets have different central frequencies and they can either be independent or partially overlapping [San+15]. We create a sublook by computing the inverse Fourier transform of a subset. As in [THA22b], we choose to apply L independent, non-overlapping, and uniformly spaced subsets to create sublooks with equal image resolution. The multilook methods evaluate the L-dimensional sublook vector $\boldsymbol{y}$ that corresponds to each image pixel. The *normalized matched filter* (NMF) [CLR95; CLR96; DFP09] and the *multilook coherence factor* (MLCF) [THA22b] are calculated on prewhitened images and do *not* require any texture correction prior to detection analysis. For the case of independent sublooks, NMF is [THA22b]

$$\mathrm{NMF}(\boldsymbol{y}) = \frac{|\boldsymbol{a}^{\mathrm{H}}\boldsymbol{y}|^2}{(\boldsymbol{y}^{\mathrm{H}}\boldsymbol{y})(\boldsymbol{a}^{\mathrm{H}}\boldsymbol{a})}. \tag{V.1}$$

NMF weights the sublooks according to the theoretical point signal response $\boldsymbol{a}$ for each pixel in each sublook. If we weight all sublooks equally, the test in (V.1) changes to the ratio of the coherent and incoherent sum of all sublooks, i.e., MLCF [THA22b]:

$$\mathrm{MLCF}(\boldsymbol{y}) = \frac{|\mathbf{1}^{\mathrm{H}}\boldsymbol{y}|^2}{(\boldsymbol{y}^{\mathrm{H}}\boldsymbol{y})L} = \frac{|\sum_{n=1}^{L} y(n)|^2}{L\sum_{n=1}^{L}|y(n)|^2}. \tag{V.2}$$

We also apply NMF and MLCF as a weighting schemes to the prewhitened *and* texture corrected image, $\mathrm{DAS}_{\text{whitened+TC}}$. We refer to these two methods as *NMF weighted* (NMFW) and *MLCF weighted* (MLCFW) images.

$$\mathrm{NMFW}(\boldsymbol{y}) = \mathrm{NMF}(\boldsymbol{y}) \cdot \mathrm{DAS}_{\text{whitened+TC}}. \tag{V.3}$$

$$\mathrm{MLCFW}(\boldsymbol{y}) = \mathrm{MLCF}(\boldsymbol{y}) \cdot \mathrm{DAS}_{\text{whitened+TC}}. \tag{V.4}$$

V.3 Textured Scenes

V.3.1 Creating Textured Backgrounds

Ultrasound images typically include varying echo intensities in the tissue speckle. Living tissue is full of structure, movement, and organization on several length scales [Sza14, ch. 9.1]. An *inhomogeneous* texture has the same type of tissue with small fluctuations about a mean value, while a region enclosing a group of regions with different characteristics is called *heterogeneous* [Sza14, ch. 9.2]. An ultrasound image can have edges caused by transitions between interfaces or lines caused by anisotropic muscle fibers, making it more difficult to discern small point scatterers. An optimal point scatterer detector needs to handle nonuniform backgrounds.

As in [THA22b], we simulate a huge number of images containing a single point scatterer at different positions and images containing uniform speckle. By combining all the different point only images with every speckle only image we produce a

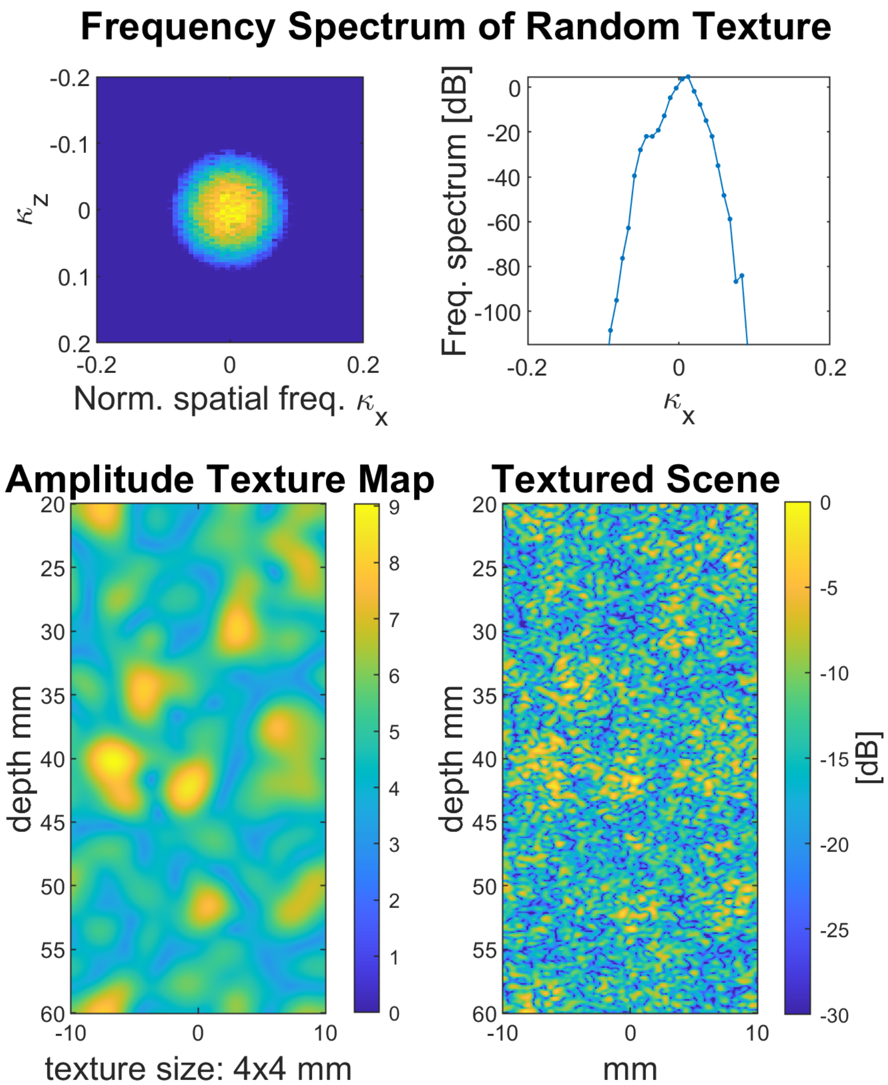

Figure V.1: Example of a random texture map. We first create a frequency spectrum with a Gaussian distribution and multiply this with a complex random frequency spectrum. An example is shown to the upper left, and a cut through the spectrum at κ_z is shown to the upper right. We form the amplitude texture map shown to the lower left by inverting the created spectrum. To get the textured scene to the lower right, we multiply the amplitude texture map with the original image. The final DAS image is normalized by its maximum value and shown with a 30 dB dynamic range.

set of images of a point at different locations in speckle. By scaling the point only images we control the point SNR value in the final images. Combining the images is mathematically equivalent to combining the raw channel data since DAS is a linear process. We can also combine the DAS images with random texture maps to simulate textured backgrounds. The point scatterer will retain its point SNR compared to the immediate surrounding background. Point detection is particularly of interest within a tissue area, such as a liver or a cyst. We choose to model the tissue backgrounds with random texture fluctuations of a specific scale such that the size of the texture is larger than that of a point scatterer but substantially smaller than the image scene.

We create a frequency spectrum with a steep Gaussian profile with maximum value in the center. With a Gaussian texture profile, it is easy to set a specific scale for the texture blobs as the shape is of the form $e^{-(k_z^2+k_x^2)/s_t}$, where s_t sets the scale of the texture fluctuations. We multiply this Gaussian profile with a complex random frequency spectrum and get the frequency spectrum shown in the upper subimages in Figure V.1. Since we simulate the texture, we can measure the texture's size using the frequency spectrum. The -6 dB width Δk_x in spatial frequency is related to the -6 dB width in the image domain

$$\Delta x_{\text{texture}} = \frac{2\pi}{\Delta k_x}. \tag{V.5}$$

Inversion back to the image domain creates the amplitude texture map. Figure V.1, bottom left, shows an example texture map with texture size is $4\,\mathrm{mm} \times 4\,\mathrm{mm}$, which we refer to as small texture size. We then multiply the amplitude texture map with the original DAS image to get the final textured image shown to the bottom right in Figure V.1. The left subimage in Figure V.2 shows a scene with large texture size of $8\,\mathrm{mm} \times 9\,\mathrm{mm}$.

V.3.2 Texture Estimation and Correction

Texture correction finds slowly varying changes in the amplitude of the textured image and removes them. This is a necessary step for simple threshold detection to work. Another option is to have the detector locally estimate the speckle level [Kay98, ch. 9]. We find a texture estimate by first applying background smoothing with a sufficiently large window. The size of the texture must typically be estimated, which is not always easy to do. Since this is not a study about texture correction, we choose the texture scale estimated from the texture map to get the best possible texture correction. We start with median filtering and continue with a Gaussian smoothing kernel with filter size set to the measured -6 dB texture size. We obtain a texture corrected image by dividing the original image with the texture estimate. Figure V.2 shows the texture estimate of an image and the resulting texture corrected image.

The optimal texture correction depends on the scale of the texture. The ultrasound image can have varying texture, and we must use adaptive filtering in such instances. This is not included in this study since we simplify the study to the same texture size in the whole image scene. The window size for texture estimation must be sufficiently large to avoid suppressing point scatterers but at the same time small enough to capture small scale texture variations. It can be challenging to estimate large texture variations

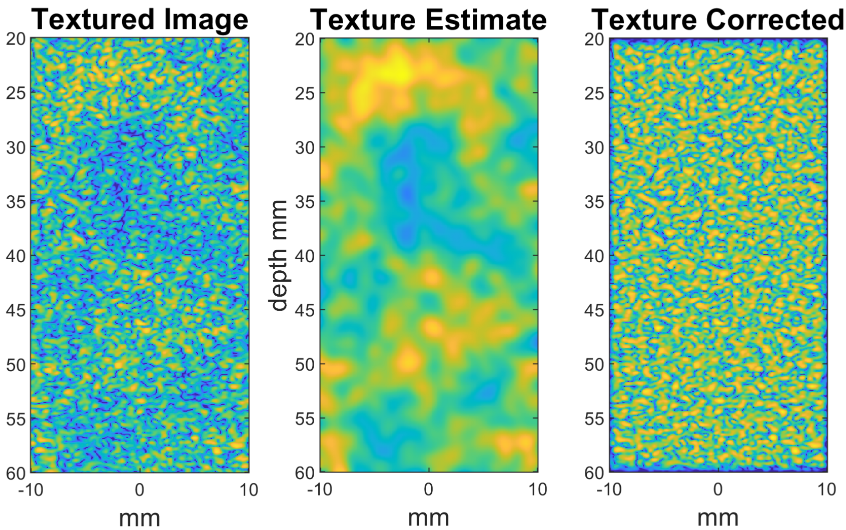

Figure V.2: Texture correction of the DAS image ("DAS TC") shown to the left. A texture estimate as shown in the middle is found by applying background smoothing with a large window. We obtain a texture corrected image as shown to the right by dividing the original image with the texture estimate. The texture estimate is shown with a 15 dB dynamic range, while the other images have a 30 dB dynamic range. The images are normalized by their maximum value to be comparable.

of small scale. Figure V.3 compares the ROC results using varying window sizes to the original DAS images *without* texture and point SNR of 8.7 dB. Figure V.3 shows how texture degrades the ROC. Texture correction can improve the detection performance but will not entirely reach the same performance as non-textured backgrounds. Using a too small window size reduces P_D and creates a ROC curve only slightly better than applying no texture correction.

V.4 Methods

We created raw channel data using the Field II software, and performed the DAS beamforming using the Ultrasound Toolbox (USTB) [Rod+17] in MATLAB (Mathworks, Natick, MA). The simulation setup is a replica of the setup used in [THA22a; THA22b]. We used a linear array with $38.1\ \mathrm{mm}$ aperture size, consisting of 128 elements with λ pitch. The center frequency f_0 was 5.1 MHz, the speed of sound was $1540\ \mathrm{m/s}$ and the transmitted pulse had a frequency bandwidth of 65% of f_0. Hamming apodization was applied on transmit.

As in [THA22a; THA22b], we simulated radio frequency channel data separately for the point scatterer and the speckle background. We simulated the speckle image using at least 20 scatterers per resolution cell, corresponding to 91 000 point scatterers

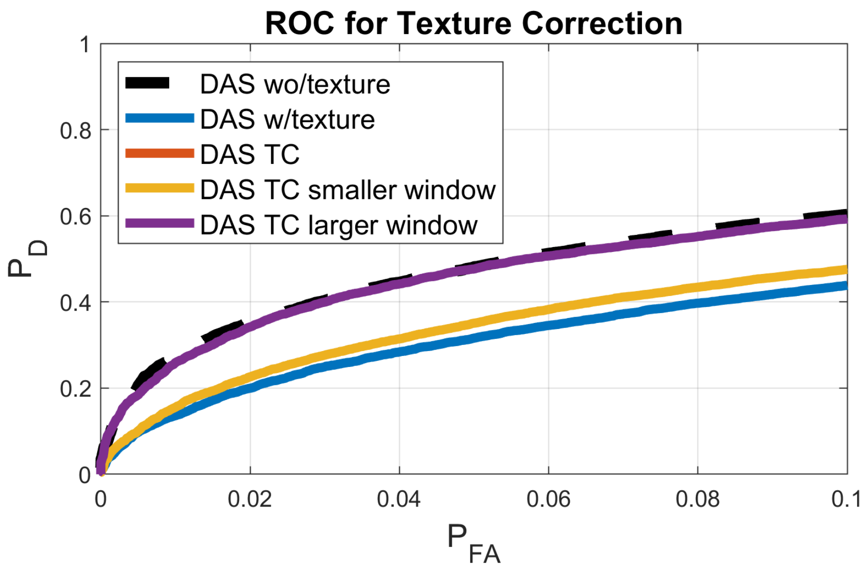

Figure V.3: ROC for texture corrected (TC) images using three window filter sizes compared to original DAS *with* and *without* texture. P_{FA} is shown up to 0.1. The red curve signifies TC using the measured -6 dB texture size. The red curve lies directly beneath the purple curve. The purple curve corresponds to 50% larger window size.

in total per speckle realization. To obtain images with high, uniform spatial resolution, we used a synthetic transmit aperture setup with constant $f_{\#}$. Such a setup transmits from every consecutive element, receives on all elements, and synthesizes focus at every pixel. We do not include frequency dependent attenuation in the simulations. We coherently combine the resulting point and speckle images to obtain a final DAS image with a specific point SNR value. Using focused, uniform amplitude speckle scenes ensures the same point SNR value regardless of where in the scene the point target is located.

Figure V.4 shows the detection analysis setup. We simulated 243 focused, constant resolution, uniform amplitude speckle scenes and 117 single point images that were coherently combined to form 28 431 speckle scenes with a single point target. This defines our sample size for P_{D} and P_{FA} calculation in our detection performance study. Different from [THA22b], this study uses textured backgrounds that more closely resembles a real-world situation. With uniform resolution, we can simplify the prewhitening process by assuming the same wavenumber coverage for all pixels. We calculated the point SNR value using the point scatterer in the center of the *untextured* DAS image. We chose a point SNR value signifying relatively weak point scatterers for the detection studies. The point SNR is 8.7 dB for the original untextured DAS image for all the scenarios under study except the dominant additive acoustic noise scenario. In the latter case, the original intensity of the point scatterer had to be increased to 9.5 dB for it not to be buried by the noise. Each ROC curve represents

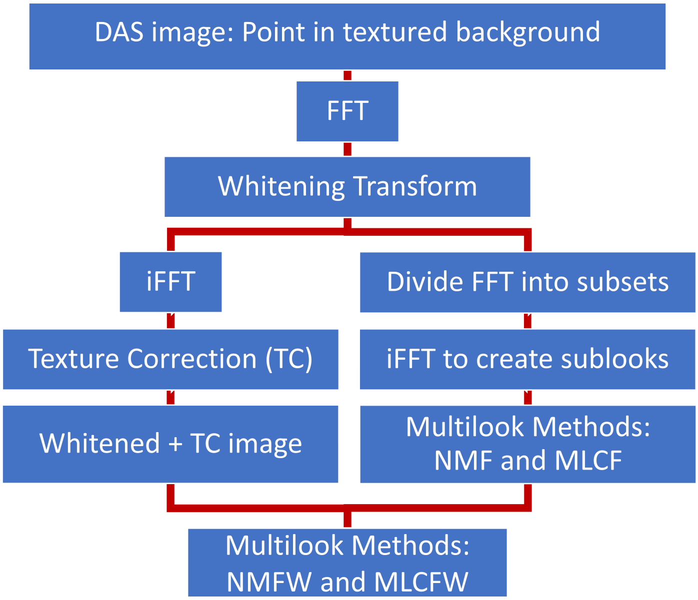

Figure V.4: Illustration of the detection analysis setup of this study on textured images. We first apply a whitening transform to the original, textured DAS image while in the spatial frequency (FFT) domain. We divide the frequency spectrum into subsets and create *sublooks*. We apply the multilook methods NMF and MLCF on these sublooks. To create the NMFW and MLCFW images, we multiply the multilook weights to the prewhitened *and* texture corrected image. We assess the point detection performance of the various methods.

28 431 realizations of one choice of point SNR value.

Before adding texture, we calculated correction maps from the average of all speckle backgrounds to ensure uniform average background intensity. The texture in this study is of two different sizes; $4\,\mathrm{mm} \times 4\,\mathrm{mm}$ and $8\,\mathrm{mm} \times 9\,\mathrm{mm}$. We varied the texture amplitude to find an amplitude fluctuation that distinctly reduces the point detection performance. The distinct drop in ROC after multiplying the original image with the amplitude texture map is shown in Figure V.3 by the black and blue curves. The texture map in Figure V.1 shows the applied amplitude map that we multiplied to the original image. We also varied the window size for the texture estimation, as illustrated in Figure V.3.

The *optimal* whitening limits depend on the geometry, system setup, and the SNR [THA22b]. We also tested the multilook methods combined with *suboptimal* or *wide* whitening limits. Prewhitening suppresses subsets outside the whitening limits. We applied the following three whitening limits:

- Optimized: angle α with frequency limits $\{f_L, f_H\}$
- Suboptimal: $\alpha + 10\%$ with $\{-5\%\, f_L, +5\%\, f_H\}$

- Wide: $\alpha + 30\%$ with $\{-10\%\, f_L, +10\%\, f_H\}$

Acoustic noise is a realistic scenario as the imaging depth increases. As mentioned, a ROC study was also performed for dominant acoustic noise. To simulate the noise, we created channel data consisting of white Gaussian noise and basebanded it before beamforming. We then coherently combined the resulting noise image with the speckle background image. We applied an adaptive prewhitening for the noisy background scenario, where we estimated a smoothed average version of each image's spatial frequency spectrum and applied the optimal whitening limits. We created the point scatterer look vectors for the NMF method by simulating the actual response of a point scatterer placed in each pixel and the pixel's corresponding look vector [THA22b]. We studied the following cases corresponding to realistic scenarios:

- Prewhitening before or after texture correction.
- Optimal prewhitening and texture correction. The optimal prewhitening limits and the optimal window size for texture estimation are both known.
- Varying texture size. How do the methods perform on small versus large texture size? Using optimal prewhitening and texture correction.
- Varying number of sublooks for the multilook methods. Using optimal prewhitening and texture correction.
- Suboptimal/wide prewhitening. The whitening limits are approximately known or estimated from the frequency spectrum of the image. Using optimal texture correction.
- Suboptimal texture correction. The optimal window size for texture estimation is not known. Using optimal prewhitening.
- Dominant additive acoustic noise. Using optimal texture correction and adaptive prewhitening with optimal whitening limits.

MLCF and MLCFW are especially of interest in the case of suboptimal prewhitening since they do not require any prior knowledge about the optimal limits and the theoretical point signal response in each sublook.

In Section V.5.2, we present an example image of the methods applied on an experimental image acquisition of a CIRS 054GS tissue-mimicking phantom. The phantom is imaged with a Verasonics linear probe (L7-4) with 5.2 MHz center frequency and $f_{\#} = 1.7$. We note that we only include this example for illustrative purposes. The optimal spatial frequency bandwidth limits are unknown in this example case. The frequency bandwidth is estimated from the image's frequency spectrum, and the angular whitening limit is based on the imaging setup's $f_{\#}$. The more straightforward methods MLCF and MLCFW are compelling to use in this scenario since they do not need prior knowledge about the theoretical point signal response. The multilook methods used 19×15 sublooks.

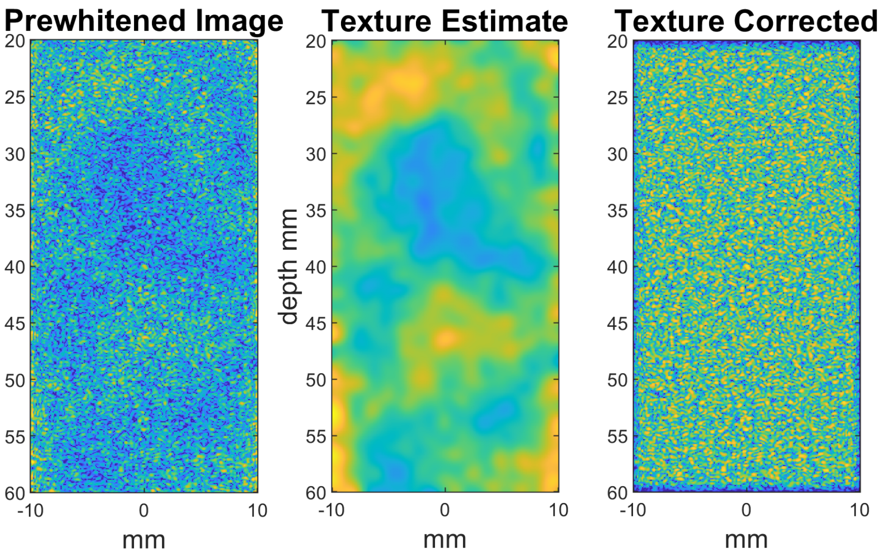

Figure V.5: Texture correction on a whitened image ("Whitening + TC”). We obtain the texture corrected image shown to the right by dividing the whitened image shown to the left with the texture estimate shown in the middle. The texture estimate is shown with a 15 dB dynamic range, while the other images have 30 dB dynamic range. The images are normalized by their maximum value to be comparable.

V.5 Results

V.5.1 Prewhitening Before or After Texture Correction

Figure V.2 illustrates texture correction of the DAS image, termed ”DAS TC”. Figure V.5 shows the results when the textured image is whitened *prior* to texture correction. We refer to this as "Whitening + TC” in the result figures.

Figure V.6 shows the difference in detection performance when whitening is applied before or after texture correction, termed "Whitening + TC” and "TC + Whitening”. The red curve shows the ROC results of only applying texture correction to the DAS images, termed "DAS TC”.

V.5.2 Example Images

We present two example images to illustrate the multilook methods on textured backgrounds. The first example is the textured ultrasound image in Figure V.7 with several point scatterers simulated using Field II software with the same setup as in the detection study. The optimal prewhitening limits and the optimal window size for texture estimation are both known in this example. Based on this image alone, it would seem the multilook methods are better suited for point detection. For example,

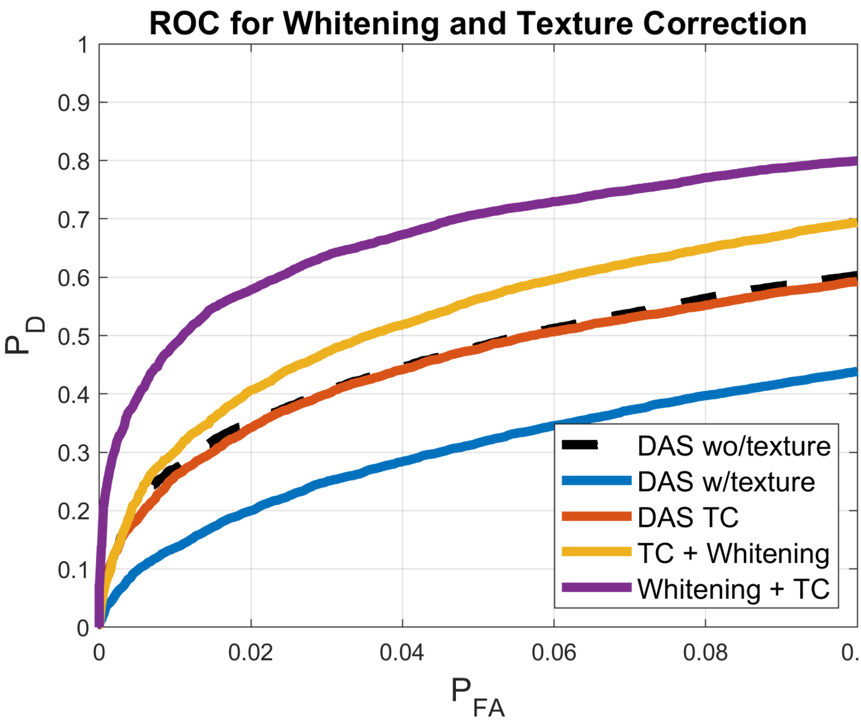

Figure V.6: ROC for texture corrected (TC) images compared to original DAS *with* and *without* texture. P_{FA} is shown up to 0.1. "DAS TC" signifies applying texture correction to the DAS image, whereas "Whitening + TC" signifies prewhitening and then texture correction.

at the -16.9 dB threshold, the MLCFW image has zero false alarms and retains all true positives. In comparison, the whitened image has zero false alarms at the -4.9 dB threshold. However, the methods could be stretching the dynamic range [Rin+19] and not actually improving the point detection. As discussed in [THA22b], we must for this reason measure the detection performance using many independent images or realizations with known point scatterer locations.

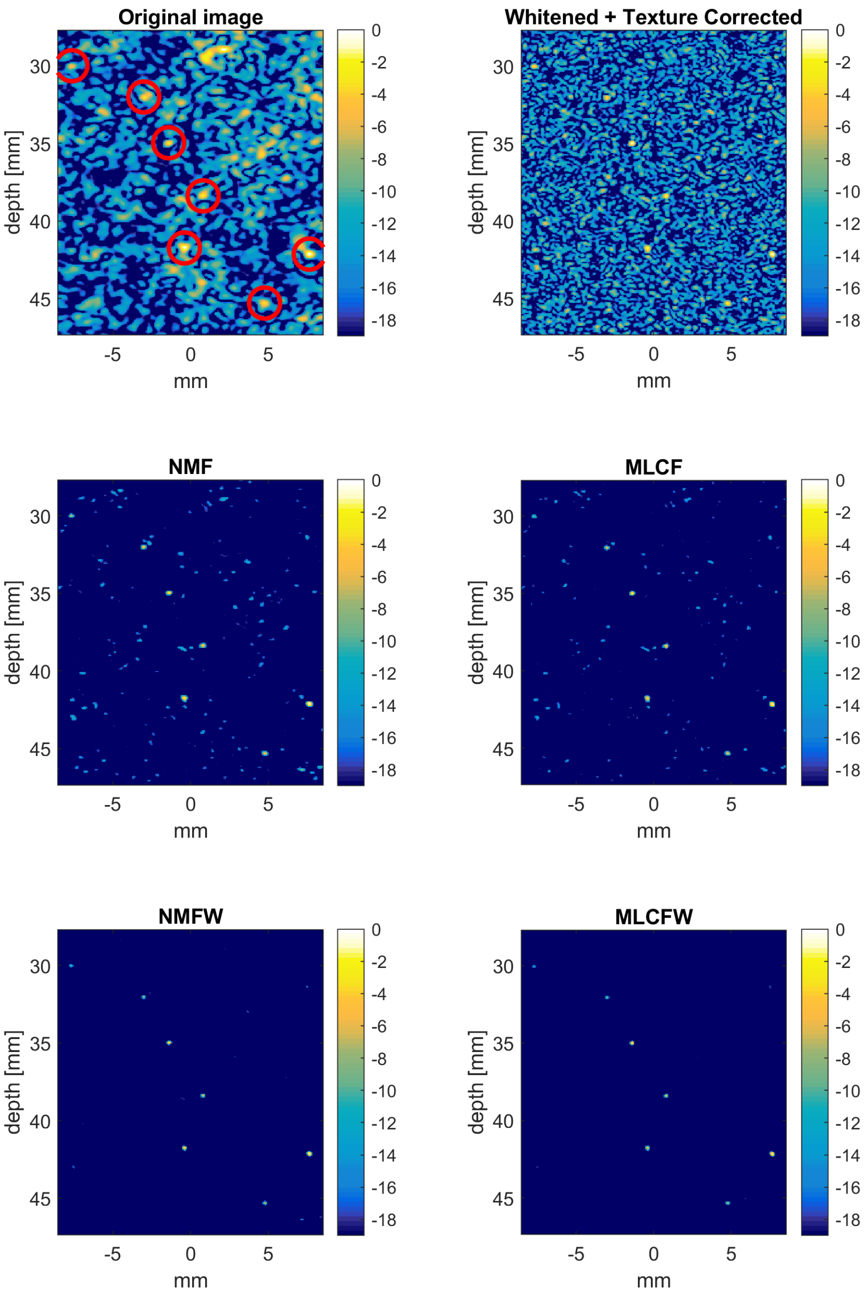

Figure V.7: Ultrasound image with seven point scatterers in a textured background. The red circles in the original DAS image indicate the locations of the true point scatterers. The multilook methods NMF, MLCF, NMFW, and MLCFW used 19×15 sublooks and α-prewhitening. To be visually comparable, the images are normalized by maximum and shown with a 19 dB dynamic range.

The second example is an image of a tissue-mimicking phantom imaged and shown in Figures V.8 and V.9. The original image is highly speckled and all four images are shown with a 21 dB dynamic range to be visually comparable. In the original DAS image, the amplitude difference between the two point targets is slight. However, the whitening process increases the intensity difference between the points to 5.6 dB. We note that the optimal whitening filter was unknown and instead estimated from the frequency spectrum of the image. The multilook methods use the prewhitened image as input and the resulting figures further increase the difference between the points. As an example, the MLCF image has a 10 dB difference between the two point targets and thereby indicate that the bottom point scatterer is more likely to be a true point target. The MLCFW image has zero false alarms and retains both point scatterers at the shown −21 dB threshold. Again, we cannot ascertain which method is better suited for point detection from a few image examples. A detailed detection study requires many images with known point target locations and point SNR values.

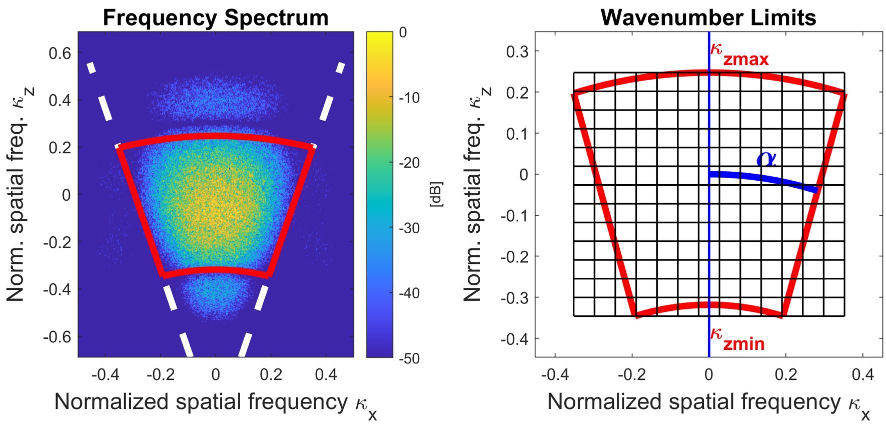

Figure V.8: Whitening filter limits for an ultrasound image of a tissue-mimicking phantom where the optimal frequency limits are unknown and must be estimated from the image's frequency spectrum. The angular limit is based on the $f_{\#}$. The chosen area is divided into subsets for the multilook methods.

V.5.3 Detection Results on Simulated Images

The dashed black curve in Figure V.10 represents the texture corrected (TC) DAS images, as illustrated in Figure V.2. Point SNR is 8.7 dB for the original *untextured* DAS image for all the scenarios under study except the dominant additive acoustic noise scenario. The solid black curve shows the ROC curve for the prewhitened and textured corrected images ("Whitening + TC"), as illustrated in Figure V.5. The colored ROC curves represent the four multilook methods. Since low P_{FA} values are of interest, the ROC curves are shown for P_{FA} values up to 0.1. Figure V.10 presents the results for the multilook methods using 13 $\times$ 13 sublooks on images with large texture

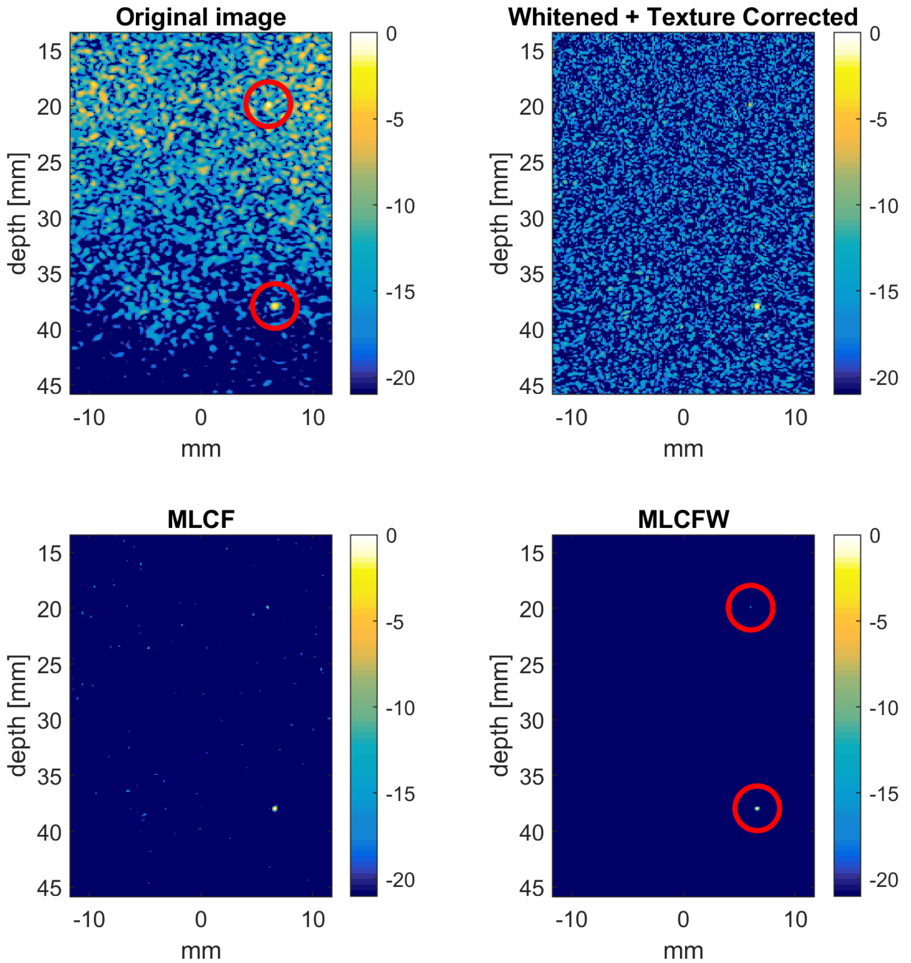

Figure V.9: An ultrasound image of a tissue-mimicking phantom with point scatterers in a highly speckled background. The original image is shown with the whitened and texture corrected image and the multilook methods MLCF and MLCFW. The whitening limits are estimated from the image's frequency spectrum. The red circles indicate the true point scatterers. To be visually comparable, the images are normalized by maximum and shown with a 21 dB dynamic range.

variations. This ROC study applied optimal α-prewhitening and optimal texture correction. Figure V.11 presents the corresponding AUC results.

Figure V.12 presents the detection performance of MLCFW using varying number of sublooks. Optimal prewhitening and optimal texture correction are applied in these cases. The optimal number of sublooks for the multilook methods on large texture is around 19×15, while the optimal on small texture is around 13×13 sublooks.

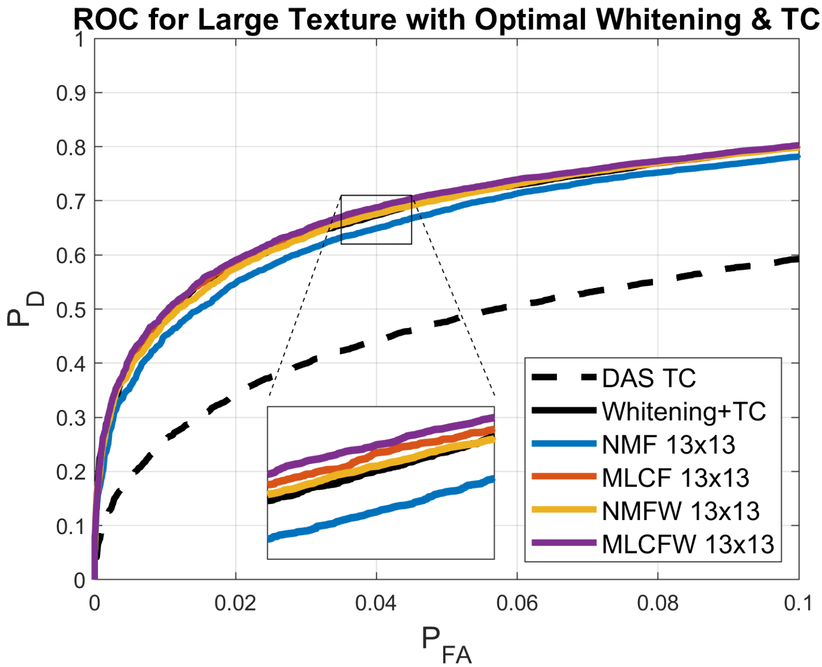

Figure V.10: ROC for the four multilook methods using 13 × 13 sublooks on images with large texture variations. Optimal α-prewhitening and optimal texture correction are applied.

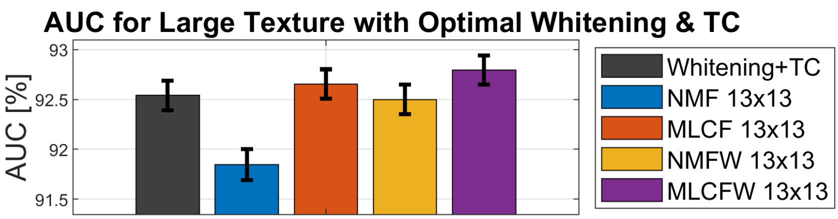

Figure V.11: AUC for the four multilook methods using 13 × 13 sublooks on images with large texture variations. Optimal α-prewhitening and optimal texture correction are applied.

Figure V.13 presents the ROC results for the four multilook methods using suboptimal texture correction. The number of sublooks is 13 × 13, and the texture size is small. The window size used in texture correction is smaller than the actual texture size, and it therefore slightly degrades the overall detection performance of "Whitening+TC". All four multilook methods outperform prewhitening. Figure V.14

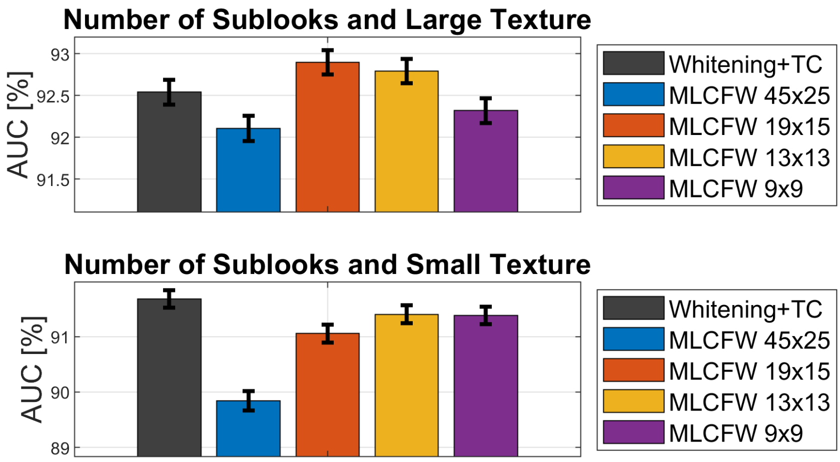

Figure V.12: AUC for the multilook method MLCFW using optimal "Whitening + TC" and a varying number of sublooks on images with small and large texture variations.

presents the corresponding AUC results. The multilook methods NMFW and MLCFW have the highest AUC values. Figure V.15 shows the P_{D} values given 3% P_{FA} for the multilook methods when a suboptimal, slightly wider whitening filter was used. Figure V.15 shows the P_{D} values when a filter with very wide whitening limits was used.

Figure V.17 presents the ROC results for the four multilook methods on images where additive acoustic noise dominates the speckle background. We applied adaptive prewhitening of the images. Optimal whitening limits and optimal window size for texture correction are both known. All four multilook methods perform better than prewhitening, especially the multilook methods NMFW and NMF. The number of sublooks is 19×15, and the texture size is large. The dotted, black ROC curve represents the original noisy DAS images without prewhitening and texture correction. The point SNR is 9.5 dB for the original *untextured* images. Figure V.18 presents the corresponding AUC results.

V.6 Discussion

Optimized prewhitening significantly improves the detection performance when combined with texture correction. Prewhitening prior to texture correction achieves a much higher detection performance than applying texture correction first, as shown in Figure V.6. This is because prewhitening improves spatial resolution, giving a larger scale difference between point scatterers and texture. This again allows for better texture correction without negatively affecting the point scatterer response. The AUC results for prewhitening are higher in the case of large texture. An optimal texture estimate is easier to achieve with slowly varying texture, such as in Figure V.5.

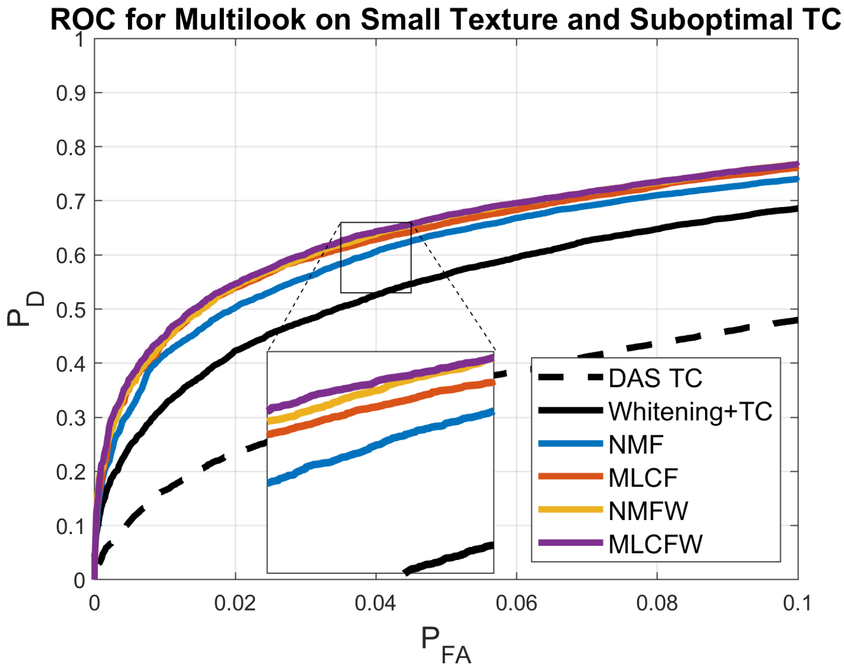

Figure V.13: ROC for the multilook methods on DAS images with suboptimal texture correction (TC). The texture size is small. The methods used 13 $\times$ 13 sublooks and optimal whitening.

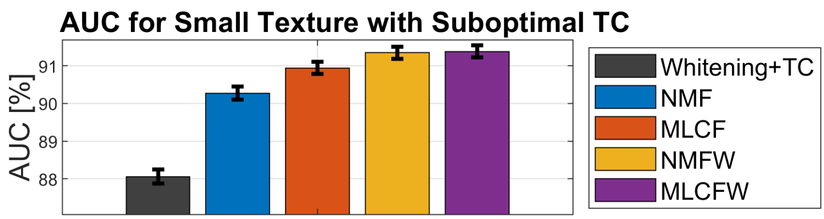

Figure V.14: AUC for the multilook methods when using suboptimal texture correction (TC). The texture size is small. The methods used 13 $\times$ 13 sublooks and optimal α-whitening.

Prewhitening uses a classical spectral estimator, which requires that the input signal is stationary and ergodic [Ale16, p. 399]. An amplitude trend in the data as a function of depth can be compensated by applying a time-varying gain or depth correction to remove the transmission loss effects before entering the spectral domain and applying prewhitening. When the spectrum shape changes with depth, the signal

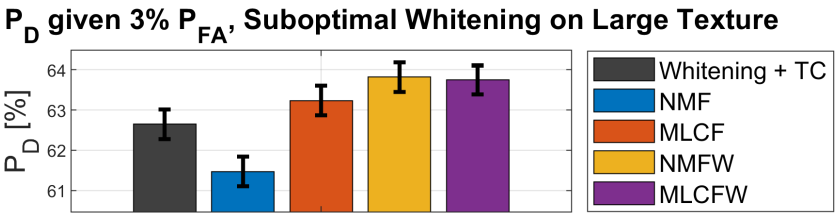

Figure V.15: P_{D} given 3% P_{FA} for the multilook methods using 19×15 sublooks combined with suboptimal prewhitening and optimal texture correction (TC).

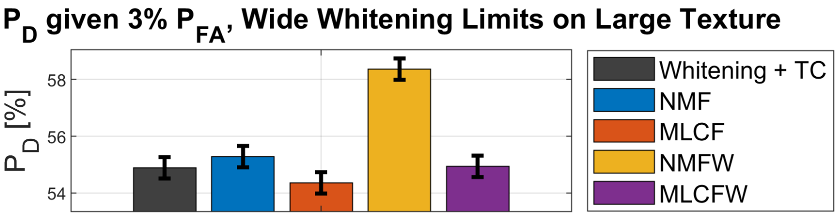

Figure V.16: P_{D} given 3% P_{FA} for the multilook methods using 25×21 sublooks combined with very wide whitening limits and optimal texture correction (TC).

is strictly non-stationary even after depth correction. A fixed prewhitening filter is then suboptimum, and a depth-dependent prewhitening filter can be applied. We expect the multilook methods to do better than prewhitening and texture correction in such cases. If the amplitude variations in the ultrasound image are considerable, it may be beneficial first to apply texture correction to achieve stationarity before applying prewhitening.

By comparing the AUC results in Figure V.12, it is evident that both prewhitening and the multilook methods perform better when the texture size is large. The results in Figure V.12 show how the multilook method improves its detection performance when the number of sublooks decreases. Table V.1 summarizes the observed behavior of the multilook methods using a varying number of sublooks when applied to different image backgrounds. Fewer sublooks increases the calculation speed of the multilook method. Textured scenes require sublooks with higher image resolution than the uniform speckle backgrounds previously studied in [THA22b]. The numerator in (7.26) retains full image resolution regardless of the number of sublooks. However, the denominator improves its background estimate when the sublooks are many but have high image resolution. Therefore, the optimal number of sublooks depends on the texture size. A small texture size requires subsets with larger bandwidth to be discernible in the resulting sublooks. The results for the multilook methods are better for slowly varying texture since we then can use a higher number of sublooks, which improves the denominator's estimate.

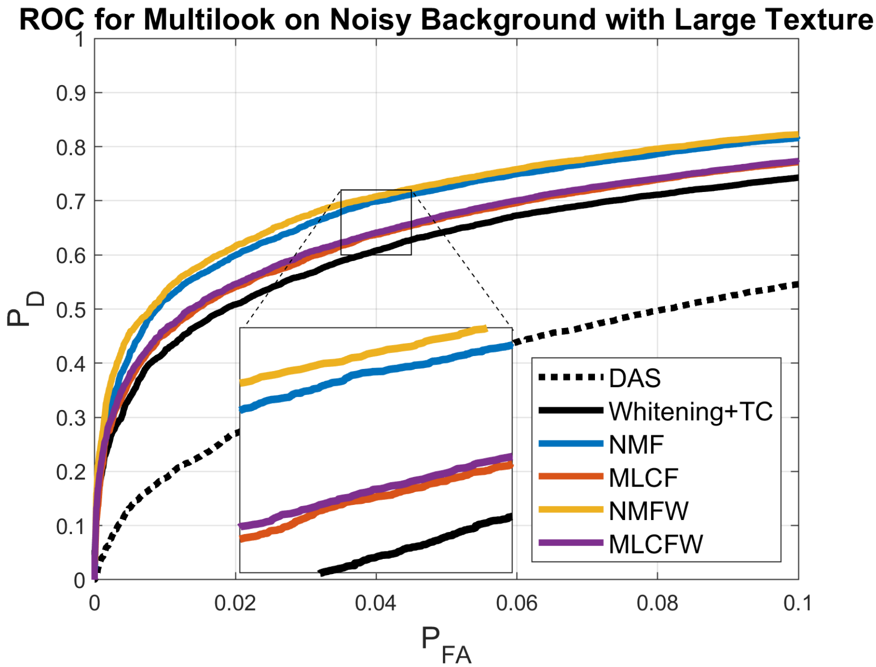

Figure V.17: ROC for the multilook methods on DAS images with dominant acoustic noise and optimal texture correction. The texture size is large. The methods are calculated using 19 $\times$ 15 sublooks and adaptive prewhitening with optimal limits.

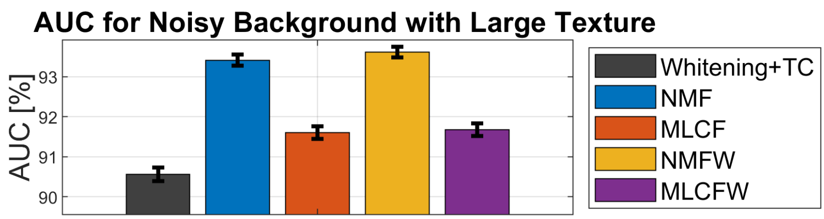

Figure V.18: AUC for the multilook methods on DAS images with dominant acoustic noise and optimal texture correction. The texture size is large. The methods are calculated using 19 $\times$ 15 sublooks and adaptive prewhitening with optimal limits.

The results in Figures V.10, V.14, and V.18 show significant improvement in detection performance using the image weighted MCFW multilook method. The benefit of MLCFW is that it can be applied even when prior knowledge about the theoretical point signal response and the optimal prewhitening limits is unavailable. Even for the scenario of optimal prewhitening and optimal texture correction in

Table V.1: Summary of Number of Sublooks

Background	Number of sublooks			
	9x9	13x13	19x15	45x25
Homogenous	Poor	Poor	Moderate	Best
Large texture	Moderate	Good	Best	Poor
Small texture	Good	Best	Good	Poor

Figure V.10, the ROC curves for the MLCF and MLCFW methods slightly outperform prewhitening at low P_{FA} values.

The ROC study on suboptimal prewhitening in [THA22b] found a significant improvement in detection performance for the multilook methods using 45×25 sublooks. The NMFW method performs better than MLCFW in the case of suboptimal whitening since it incorporates extra knowledge about the correct point signal response per sublook and can suppress more unwanted subsets at the edges of the spectrum. However, the inclusion of texture in this study causes the optimal number of sublooks to decrease. As a consequence, the multilook methods cannot suppress as many unwanted edge subsets, and therefore they cannot achieve the same amount of improvement as found in [THA22b]. The results on suboptimal prewhitening on textured image scenes show that NMFW and MLCFW performs slightly better than prewhitening at low P_{FA} values, as illustrated by the P_{D} values in Figure V.15. The difference is however too small to give the multilook methods higher overall AUC values. Prewhitening is a robust method even when applied suboptimal limits. Figure V.16 illustrates a scenario when the whitening limits are poorly estimated and chosen too wide. The NMFW method performs much better than the other methods in this case. The number of sublooks is 25×21 to give subsets of similar size as when using the optimal prewhitening limits.

The image example in Figure V.7 makes it evident that the multilook methods can increase the threshold difference between false alarms and true positives. It is more challenging to visually extract the point scatterers in the whitened image than the multilook weighted images. Therefore, it can be preferable for an ultrasound operator to see the multilook images when searching for point scatterers.

The improvements in detection performance for the multilook methods compared to prewhitening are especially large for image backgrounds where optimal texture correction is difficult to obtain. This is shown in Figures V.13 and V.14. An ultrasound image can have a varying texture scale, making it more challenging to obtain an optimal texture estimate. The image weighting methods NMFW and MLCFW perform best in Figure V.13 since the applied texture correction still provides some improvement to the detection performance. However, the NMF and MLCF methods show great potential when an optimal texture correction is difficult to obtain, or a normalized method is wanted.

The improvements in detection performance for the multilook methods compared to prewhitening are significant when acoustic noise dominates speckle, as illustrated in Figures V.17 and V.18. Such a scenario is realistic as the imaging depth increases. The

NMFW and NMF methods perform especially well in this scenario. They incorporate prior knowledge about the theoretical point signal response in each sublook and can weight the sublook accordingly.

Table V.2 summarizes the observed benefits and setbacks of the suggested methods in this study.

V.7 Conclusions

We have studied four multilook methods with the aim of improving point detection in textured ultrasound images. The results show *significant* improvement in detection performance using optimized prewhitening on images where an optimal texture correction is easily obtained. An improvement in detection performance is also found for the image weighting multilook method MLCFW. When detecting point targets in textured backgrounds, the multilook methods require sublooks with higher image resolution than in uniform backgrounds. In general, the methods perform best when using many sublooks with high image resolution. The optimal number of sublooks depend on the texture size. The methods in this study perform best on the images with slowly varying texture. The NMF and MLCF methods are normalized and perform better than prewhitening when an optimal texture correction is difficult to obtain. The multilook methods perform better than prewhitening when acoustic noise dominates the speckle background.

Table V.2: Summary of Observed Potential Benefits and Setbacks of the Suggested Methods

Scenario	Method				
	Prewhitening	MLCF	MLCFW	NMF	NMFW
Optimal whitening & optimal TC	Large improvement in detection performance.	Similar performance as whitening.	Similar performance as whitening. Slightly better than whitening in the case of large texture.	Setback compared to whitening.	Similar performance as whitening.
Suboptimal prewhitening wo/texture	Some reduction in detection performance, but still a robust method.	Performs slightly better than whitening.	Performs slightly better than whitening.	Performs slightly better than whitening.	Performs better than whitening.
Suboptimal prewhitening w/texture	Some reduction in detection performance, but still a robust method.	Similar performance as whitening.	Performs slightly better than whitening at low P_{FA} values.	Some setback compared to whitening.	Performs slightly better than whitening at low P_{FA} values.
Wide prewhitening w/texture	Reduction in detection performance.	Similar performance as whitening.	Similar performance as whitening.	Performs slightly better than whitening at low P_{FA} values.	Performs better than whitening.
Suboptimal TC	Much affected by suboptimal TC.	Not affected by TC.	Improvement due to weighting with MLCF.	Not affected by TC.	Improvement due to weighting with NMF.
Poor TC	Much affected by poor TC.	Not affected by TC.	Affected by poor TC.	Not affected by TC.	Affected by poor TC.
Dominant additive acoustic noise	Improvement compared to only TC, but method enhances much of the noise.	Method weights sublooks using coherence.	Method weights sublooks using coherence.	Method weights sublooks according to theoretical point signal response.	Method weights sublooks according to theoretical point signal response.
Computational complexity	Low	Medium	Medium	High	High

Color coding:	Poor	Good	Great

References

[Abr19] Abraham, D. A. *Underwater Acoustic Signal Processing: Modeling, Detection, and Estimation.* Springer, 2019.

[Ale16] Alessio, S. M. *Digital Signal Processing and Spectral Analysis for Scientists.* Cham, Switzerland: Springer, 2016.

[And+97] Anderson, M. E. et al. "The detection of breast microcalcifications with medical ultrasound". In: *J. Acoust. Soc. Am.* vol. 101, no. 1 (Jan. 1997), pp. 29–39.

[AST00] Anderson, M. E., Soo, M. S. C., and Trahey, G. E. "Optimizing visualization of breast microcalcifications". In: *Proc. IEEE Int. Ultrason. Symp. (IUS).* Vol. 2. Oct. 2000, pp. 1315–1320.

[AST98] Anderson, M. E., Soo, M. S. C., and Trahey, G. E. "Microcalcifications as elastic scatterers under ultrasound". In: *IEEE Trans. Ultrason., Ferroelectr., Freq. Control* vol. 45, no. 4 (July 1998), pp. 925–934.

[AT00] Anderson, M. E. and Trahey, G. E. *A seminar on k-space applied to medical ultrasound.* Duke Univ., Apr. 2000.

[Bro+19] Browne, J. E. et al. "An investigation of the detection capability of pulsed wave duplex Doppler of low grade stenosis using ultrasound contrast agent microbubbles – An in-vitro study". In: *Ultrasonics* vol. 96 (July 2019), pp. 48–54.

[Che+20] Chen, C. et al. "Point Spread Function Formation in Plane-Wave Imaging: A Theoretical Approximation in Fourier Migration". In: *IEEE Trans. Ultrason., Ferroelectr., Freq. Control* vol. 67, no. 2 (Feb. 2020), pp. 296–307.

[CJO98] Czerwinski, R., Jones, D., and O'Brien, W. "Line and boundary detection in speckle images". In: *IEEE Trans. Image Process.* vol. 7, no. 12 (Dec. 1998), pp. 1700–1714.

[CJO99] Czerwinski, R., Jones, D., and O'Brien, W. "Detection of lines and boundaries in speckle images-application to medical ultrasound". In: *IEEE Trans. Med. Imag.* vol. 18, no. 2 (Feb. 1999), pp. 126–136.

[CLR95] Conte, E., Lops, M., and Ricci, G. "Asymptotically optimum radar detection in compound-Gaussian clutter". In: *IEEE Trans. Aerosp. Electron. Syst.* vol. 31, no. 2 (Apr. 1995), pp. 617–625.

[CLR96] Conte, E., Lops, M., and Ricci, G. "Adaptive matched filter detection in spherically invariant noise". In: *IEEE Signal Process. Lett.* vol. 3, no. 8 (Aug. 1996), pp. 248–250.

[Den+13] Denarie, B. et al. "Coherent Plane Wave Compounding for Very High Frame Rate Ultrasonography of Rapidly Moving Targets". In: *IEEE Trans. Med. Imag.* vol. 32, no. 7 (July 2013), pp. 1265–1276.

[DFP09] De Maio, A., Fornaro, G., and Pauciullo, A. “Detection of Single Scatterers in Multidimensional SAR Imaging”. In: *IEEE Trans. on Geosci. Remote Sens.* vol. 47, no. 7 (Apr. 2009), pp. 2284–2297.

[Dia+18] Diamantis, K. et al. “Super-Resolution Axial Localization of Ultrasound Scatter Using Multi-Focal Imaging”. In: *IEEE Trans. Biomed. Eng.* vol. 65, no. 8 (Aug. 2018), pp. 1840–1851.

[Flø+17] Flørenæs, E. et al. “In vitro detection of microcalcifications using dual band ultrasound”. In: *Proc. IEEE Int. Ultrason. Symp. (IUS).* Sept. 2017, pp. 1–4.

[Gol+21] Golfetto, C. et al. “Retrospective Transmit Beamforming and Coherent Plane-Wave Compounding for Microvascular Doppler Imaging: A Comparison Study”. In: *IEEE Trans. Ultrason., Ferroelectr., Freq. Control* vol. 68, no. 4 (Apr. 2021), pp. 1105–1116.

[Guo+18] Guo, R. et al. “Ultrasound Imaging Technologies for Breast Cancer Detection and Management: A Review”. In: *Ultrasound Med. Biol.* vol. 44, no. 1 (Jan. 2018), pp. 37–70.

[HM82] Hanley, J. A. and McNeil, B. J. “The Meaning and Use of the Area under a Receiver Operating Characteristic (ROC) Curve”. In: *Radiology* vol. 143, no. 1 (Apr. 1982), pp. 29–36.

[Jak+96] Jakowatz, J. C. V. et al. *Spotlight-Mode Synthetic Aperture Radar: A Signal Processing Approach.* Boston, MA: Springer, 1996.

[Jen+06] Jensen, J. A. et al. “Synthetic aperture ultrasound imaging”. In: *Ultrasonics* vol. 44 (Dec. 2006), e5–e15.

[Jen96] Jensen, J. A. “FIELD: A Program for Simulating Ultrasound Systems”. In: *Proc. 10th Nordicbaltic Conf. Biomed. Imag., Suppl. 1, Part 1.* Vol. 4. 1996, pp. 351–353.

[JS92] Jensen, J. A. and Svendsen, N. B. “Calculation of Pressure Fields from Arbitrarily Shaped, Apodized, and Excited Ultrasound Transducers”. In: *IEEE Trans. Ultrason., Ferroelectr., Freq. Control* vol. 39, no. 2 (Mar. 1992), pp. 262–267.

[Kay98] Kay, S. M. *Fundamentals of Statistical Signal Processing, Volume II: Detection Theory.* Vol. II. Prentice-Hall PTR, 1998.

[Kel86] Kelly, E. J. “An Adaptive Detection Algorithm”. In: *IEEE Trans. Aerosp. Electron.* vol. 22, no. 2 (Mar. 1986), pp. 115–127.

[Lev08] Levy, B. C. *Principles of Signal Detection and Parameter Estimation.* Springer, 2008.

[Mac+18] Machado, P. et al. “Ultrasound Detection of Microcalcifications in Surgical Breast Specimens”. In: *Ultrasound Med. Biol.* vol. 44 (6 Mar. 2018), pp. 1286–1290.

[MAC13] Masoom, H., Adve, R. S., and Cobbold, R. S. “Target detection in diagnostic ultrasound: Evaluation of a method based on the CLEAN algorithm”. In: *Ultrasonics* vol. 53, no. 2 (Feb. 2013), pp. 335–344.

[Mat+19] Matrone, G. et al. "Short-lag spatial coherence imaging with multi-line transmission to improve needle visibility in ultrasound images". In: *J. Acoust. Soc. Am.* vol. 146 (Oct. 2019), pp. 2861–2861.

[MBR20] Matrone, G., Bell, M. A. L., and Ramalli, A. "Improving the Detectability of Highly Coherent Targets in Short-Lag Spatial Coherence Images with Multi-Line Transmission". In: *Proc. IEEE Int. Ultrason. Symp. (IUS).* Sept. 2020, pp. 1–4.

[OQ98] Oliver, C. and Quegan, S. *Understanding Synthetic Aperture Radar Images.* Artech house, Inc., 1998.

[Pel+21] Pellow, C. et al. "High frequency ultrasound nonlinear scattering from porphyrin nanobubbles". In: *Ultrasonics* vol. 110 (Feb. 2021), p. 106245.

[Ray+10] Ray, A. A. et al. "Limitations to Ultrasound in the Detection and Measurement of Urinary Tract Calculi". In: *Urology* vol. 76, no. 2 (Mar. 2010), pp. 295–300.

[Rin+19] Rindal, O. M. H. et al. "The Effect of Dynamic Range Alterations in the Estimation of Contrast". In: *IEEE Trans. Ultrason., Ferroelectr., Freq. Control* vol. 66, no. 7 (July 2019), pp. 1198–1208.

[Rod+17] Rodriguez-Molares, A. et al. "The UltraSound ToolBox". In: *Proc. IEEE Int. Ultrason. Symp. (IUS).* Sept. 2017, pp. 1–4.

[San+15] Sanjuan-Ferrer, M. J. et al. "A New Detection Algorithm for Coherent Scatterers in SAR Data". In: *IEEE Trans. on Geosci. Remote Sens.* vol. 53, no. 11 (June 2015), pp. 6293–6307.

[Shi+09] Shin, H.-C. et al. "Sensitivity to point-spread function parameters in medical ultrasound image deconvolution". In: *Ultrasonics* vol. 49, no. 3 (Mar. 2009), pp. 344–357.

[SMM06] Sakhaei, M., Mahloojifar, A., and Malek, A. "Optimization of point spread function in ultrasound arrays". In: *Ultrasonics* vol. 44, no. 2 (Feb. 2006), pp. 159–165.

[Sza14] Szabo, T. L. *Diagnostic Ultrasound Imaging: Inside Out.* Second. Elsevier Academic Press, 2014.

[THA22a] Thon, S. H., Hansen, R. E., and Austeng, A. "Detection of Point Scatterers in Medical Ultrasound". In: *IEEE Trans. Ultrason., Ferroelectr., Freq. Control* vol. 69, no. 2 (Feb. 2022), pp. 617–628.

[THA22b] Thon, S. H., Hansen, R. E., and Austeng, A. "Point Detection in Ultrasound Using Prewhitening and Multilook Optimization". In: *IEEE Trans. Ultrason., Ferroelectr., Freq. Control* vol. 69, no. 6 (June 2022), pp. 2085–2097.

[Tie+18] Tierney, J. E. et al. "In vitro feasibility of next generation non-linear beamforming ultrasound methods to characterize and size kidney stones". In: *Urolithiasis* vol. 47 (Jan. 2018), pp. 181–188.